

# **Three-dimensional Multiscale Modelling and Simulation of Atria and Torso Electrophysiology**

**DOCTORAL THESIS**

Author:

**Ana Ferrer Albero**

Supervisors:

Prof Francisco Javier Saiz Rodríguez

Dr Rafael Sebastián Aguilar

Dr Felipe Atienza Fernández



**UNIVERSITAT  
POLITÈCNICA  
DE VALÈNCIA**

PROGRAMA DE DOCTORADO EN  
TECNOLOGÍAS PARA LA SALUD Y EL BIENESTAR

Valencia, Spain  
July 2017

© 2017 by Ana Ferrer Albero. All rights reserved.

Three-dimensional Multiscale Modelling and Simulation of Atria and Torso Electrophysiology; Ph.D. Thesis, Universitat Politècnica de València.

This book was typeset using word and output as PDF. Cover: Three-dimensional Multiscale Modelling and Simulation of Atria and Torso Electrophysiology; Ph.D. Thesis, Universitat Politècnica de València. Computed with ELVIRA and rendered with Paraview.

# **Three-dimensional Multiscale Modelling and Simulation of Atria and Torso Electrophysiology**

Ana Ferrer Albero

Ph.D. thesis submitted to the Department of Electronic Engineering in the fulfilment of the requirements for the degree of Doctor of Philosophy at the Universitat Politècnica de València, Spain.



**Supervisors:**

Prof Francisco Javier Saiz Rodríguez  
Polytechnic University of Valencia, Spain

Dr Rafael Sebastián Aguilar  
University of Valencia General Study, Spain

Dr Felipe Atienza Fernández  
University Hospital Gregorio Marañón, Madrid, Spain

**External Evaluators:**

Dr Vicente Bodí Peris  
University Clinic Hospital, Valencia, Spain

Prof Pablo Laguna Lasaosa  
University of Zaragoza, Spain

Prof Jose Luis Rojo Álvarez  
University Rey Juan Carlos, Spain

**Reading Committee:**

Prof Francisco Javier Chorro Gascó  
University Clinic Hospital, Valencia, Spain

Prof Pablo Laguna Lasaosa  
University of Zaragoza, Spain

Dr Beatriz Ana Trenor Gomis  
Polytechnic University of Valencia, Spain

This work was conducted at the Research and Innovation Centre of Bioengineering (Universitat Politècnica de València) and at the Computational Multiscale Simulation Lab (Universitat de València Estudi General).



*A mi familia...*



---

# Acknowledgements

This thesis has been conducted at the Research and Innovation Centre of Bioengineering (Universitat Politècnica de València) and at the Computational Multiscale Simulation Lab (Universitat de València). I would like to express my deep and warm gratitude to all persons who helped me, in one way or another, to be in the position of defending my PhD thesis and fulfilling a personal wish. Without their valuable friendship and support, I would not have been able to conduct and conclude my research project.

I would firstly like to extend a heartfelt thanks to my PhD supervisors but not only for their excellent scientific supervision. To Prof Javier Saiz, for giving me the opportunity to work in a stimulating research environment, printing a practical research meaning to all my investigations and for transmitting always the best of his optimism. To Dr Rafael Sebastián, for the commitment in transferring me his knowledge on computational meshing and modelling techniques, for his continuous interest in finding new techniques to improve my work and for all the very nice moments shared beyond the lab walls. Both of them guided me with sense and sensitivity along this hard and long research process. Personally, the journey we shared has touched me greatly, and encourages me to pursuit new goals.

I also want to express my gratitude to Dr José Felix, mechanical engineer from the Politecnico di Milano, for his invaluable understanding of the mathematical fundamentals in cardiac modelling. I deeply thank him for receiving me in his lab during several weeks and for all the endless sessions explaining how to model the cardiac physiology and pathology. I also thank Dr Damián Sanchez-Quintana, pathologist from the Universidad de Extremadura, for providing his knowledge on the atrial histology and guiding me to continuously improve our atrial model. Furthermore, I want to thank Dra Maite Izquierdo, cardiologist from the University Clinic Hospital of Valencia, for her advice during the process of fine-tuning the atrial model. I sincerely thank they three for their continuous warm support.

The colleagues from my lab deserve all my gratitude and friendship. Laura Martínez, Alejandro López, Jordi Cano, Víctor Zena, Juan Francisco Gómez, Eduardo Godoy, Bea Carbonell and Karen Cardona from whom I have always learnt and I always will. Never-

ending lunch times discussing about models, exciting dinner moments talking about everything and incredible life experiences shared on trips. Furthermore, I want to thank all my colleagues from the Health Research Institute INCLIVA for bearing with me this last crazy year. They all have been my balance point and I would not be able to reach this day without their personal involvement.

I would also like to thank all the friends who helped me to overcome hard moments that raised in the past. Marga Linares, Nuria Morata, Jose A. Pérez, Pascual Belda, Teresa Domínguez and Miguel Alamar. All of them were my lifeguard and I would not have graduated without their friendship and support. I am here today because they were then there.

Finally, I want to thank my family for supporting me throughout all my life. My mother, for giving me her strength, courage and love. My two brothers, Alejandro and Alberto, and their partners, Ana and Esther, for always being there, at the right place at the right moment no matter the circumstances. My amazing little sister Cristina, for inspiring me every single day and being my candle in the wind. Herman and Lucia, and all my nephews and nieces, for being my world and, perhaps without knowing, pushing me always to seek out something else.

---

# Abstract

A better understanding of the electrical activity of the heart under physiological and pathological conditions has always been key for clinicians and researchers. Over the last years, the information in the P-wave signals has been extensively analysed to uncover the mechanisms underlying atrial arrhythmias by localizing ectopic foci or high-frequency rotors. However, the relationship between the activation of the different areas of the atria and the characteristics of the P-wave signals or body surface potential maps are still far from being completely understood. Multiscale anatomical and functional models of the heart are a new technological framework that can enable the investigation of the heart as a complex system.

This thesis is centred in the construction of a multiscale framework that allows the realistic simulation of atrial and torso electrophysiology and integrates all the anatomical and functional descriptions described in the literature. The construction of such model involves the development of heterogeneous cellular and tissue electrophysiology models fitted to empirical data. It also requires an accurate 3D representation of the atrial anatomy, including tissue fibre arrangement, and preferential conduction axes. This multiscale model aims to reproduce faithfully the activation of the atria under physiological and pathological conditions. We use the model for two main applications. First, to study the relationship between atrial activation and surface signals in sinus rhythm. This study should reveal the best places for recording P-waves signals in the torso, and which are the regions of the atria that make the most significant contribution to the body surface potential maps and determine the main P-wave characteristics. Second, to spatially cluster and classify ectopic atrial foci into clearly differentiated atrial regions by using the body surface P-wave integral map (BSPiM) as a biomarker. We develop a machine-learning pipeline trained from simulations obtained from the atria-torso model aiming to validate whether ectopic foci with similar BSPiM naturally cluster into differentiated non-intersected atrial regions, and whether new BSPiM could be correctly classified with high accuracy.



---

# Resumen

En la actualidad, una mejor compresión de la actividad eléctrica del corazón en condiciones fisiológicas y patológicas es clave para médicos e investigadores. A lo largo de los últimos años, la información derivada de la onda P se ha utilizado para intentar descubrir los mecanismos subyacentes a las arritmias auriculares mediante la localización de focos ectópicos y rotores de alta frecuencia. Sin embargo, la relación entre la activación de distintas regiones auriculares y las características tanto de las ondas P como de la distribución de potencial en la superficie del torso está lejos de entenderse completamente. Los modelos cardíacos funcionales y anatómicos son una nueva herramienta que puede facilitar la investigación relativa al corazón entendido como sistema complejo.

La presente tesis se centra en la construcción de un modelo multiescala para la simulación realista de la electrofisiología cardíaca tanto a nivel auricular como de torso, integrando toda la información anatómica y funcional disponible en la literatura. La construcción de este modelo implica el desarrollo, en base a datos experimentales, de modelos electrofisiológicos heterogéneos tanto celulares como tisulares. Así mismo, es imprescindible una representación tridimensional precisa de la anatomía auricular, incluyendo la dirección de fibras y los haces de conducción preferentes. Este modelo multiescala busca reproducir fielmente la activación auricular en condiciones fisiológicas y patológicas. Su uso se ha centrado fundamentalmente en dos aplicaciones. En primer lugar, estudiar la relación entre la activación auricular en ritmo sinusal y las señales en la superficie del torso. Este estudio busca definir la mejor ubicación para el registro de las ondas P en el torso así como determinar aquellas regiones auriculares que contribuyen fundamentalmente a la formación y distribución de potenciales superficiales así como a las características de las ondas P. En segundo lugar, agrupar y clasificar espacialmente los focos ectópicos en regiones auriculares claramente diferenciables empleando como biomarcador los mapas superficiales de integral de la onda P (BSPiM). Se ha desarrollado para ello una metodología de aprendizaje automático en la que las simulaciones obtenidas con el modelo multiescala aurícula-torso sirven de entrenamiento, permitiendo validar si los focos ectópicos cuyos BSPiMs son similares se agrupan de forma natural en regiones auriculares no intersectadas y si BSPiMs nuevos podrían ser clasificados prospectivamente con gran precisión.



---

# Resum

Avui en dia, una millor comprensió de l'activitat elèctrica del cor en condicions fisiològiques i patològiques és clau per a metges i investigadors. Al llarg dels últims anys, la informació derivada de l'ona P s'ha utilitzat per intentar descobrir els mecanismes subjacentes a les arítmies auriculars mitjançant la localització de focus ectòpics i rotors d'alta freqüència. No obstant això, la relació entre l'activació de diferents regions auriculars i les característiques tant de les ones P com de la distribució de potencial en la superficie del tors està lluny d'entendre's completament. Els models cardíacs funcionals i anatòmics són una nova eina que pot facilitar la recerca relativa al cor entès com a sistema complex.

La present tesi es centra en la construcció d'un model multiescala per a la simulació realista de la electrofisiologia cardíaca tant a nivell auricular com de tors, integrant tota la informació anatòmica i funcional disponible en la literatura. La construcció d'aquest model implica el desenvolupament, sobre la base de dades experimentals, de models electrofisiològics heterogenis, tant cel·lulars com tissulars. Així mateix, és imprescindible una representació tridimensional precisa de l'anatomia auricular, incloent la direcció de fibres i els feixos de conducció preferents. Aquest model multiescala busca reproduir fidelment l'activació auricular en condicions fisiològiques i patològiques. El seu ús s'ha centralitzat fonamentalment en dues aplicacions. En primer lloc, estudiar la relació entre l'activació auricular en ritme sinusal i els senyals en la superficie del tors. A més a més, amb aquest estudi també es busca definir la millor ubicació per al registre de les ones P en el tors, així com, determinar aquelles regions auriculars que contribueixen fonamentalment a la formació i distribució de potencials superficials a l'hora que es caracteritzen les ones P. En segon lloc, agrupar i classificar espacialment els focus ectòpics en regions auriculars clarament diferenciables emprant com a biomarcador els mapes superficials d'integral de l'ona P (BSPiM). És per això que s'ha desenvolupat una metodologia d'aprenentatge automàtic en la qual les simulacions obtingudes amb el model multiescala auriculars serveixen d'entrenament, la qual cosa permet validar si els focus ectòpics, llurs BSPiMs són similars, s'agrupen de forma natural en regions auriculars no intersectades i si BSPiMs nous podrien ser classificats de manera prospectiva amb precisió.



---

# Contents

ACKNOWLEDGEMENTS .....	I
ABSTRACT .....	III
RESUMEN .....	V
RESUM .....	VII
CONTENTS .....	IX
LIST OF FIGURES .....	XIII
LIST OF TABLES .....	XVII
ABBREVIATIONS .....	XIX
CHAPTER 1 MOTIVATION .....	1
1.1. CLINICAL MOTIVATION .....	1
1.2. TECHNICAL MOTIVATION .....	4
1.3. GENERAL AIM.....	5
1.4. STRUCTURE OF THE THESIS.....	5
CHAPTER 2 CLINICAL BACKGROUND.....	7
2.1. ANATOMY OF THE HUMAN ATRIA AND TORSO .....	7
2.1.1. <i>Atrial anatomy</i> .....	7
2.1.2. <i>Torso anatomy</i> .....	11
2.2. ELECTROPHYSIOLOGY OF THE HUMAN ATRIA AND TORSO.....	15
2.2.1. <i>Atrial electrophysiology</i> .....	15
2.2.2. <i>Torso electrophysiology</i> .....	18
2.3. ATRIAL ELECTRICAL DISORDERS .....	26
2.3.1. <i>Common atrial flutter</i> .....	26
2.3.2. <i>Focal atrial tachycardia (FAT)</i> .....	27
2.3.3. <i>Atrial fibrillation (AF)</i> .....	29
2.4. CLINICAL MANAGEMENT OF ATRIAL ARRHYTHMIAS.....	30

<b>CHAPTER 3 JUSTIFICATION AND OBJECTIVES .....</b>	<b>33</b>
3.1. JUSTIFICATION .....	33
3.2. OBJECTIVES .....	34
3.2.1. <i>Main hypothesis</i> .....	34
3.2.2. <i>General objective</i> .....	34
3.2.3. <i>Specific objectives</i> .....	35
<b>CHAPTER 4 MULTISCALE 3D MODEL OF THE HUMAN ATRIA.....</b>	<b>37</b>
4.1. EXISTING HUMAN ATRIAL MODELS .....	37
4.1.1. <i>Models of atrial myocytes</i> .....	38
4.1.2. <i>Models of atrial tissue and propagation</i> .....	43
4.1.3. <i>Models of the human atrium</i> .....	47
4.2. MODELLING ATRIAL MYOCYTES .....	48
4.3. MODELLING ATRIAL TISSUE .....	53
4.4. MODELLING THE THREE-DIMENSIONAL ATRIA.....	57
4.4.1. <i>Analysis of histological data</i> .....	57
4.4.2. <i>Novel 3D atrial model</i> .....	60
4.4.3. <i>Multiscale anisotropic vs isotropic atrial activation</i> .....	67
4.5. DISCUSSION .....	73
4.5.1. <i>Multiscale anatomical and electrophysiological atrial model</i> .....	73
4.5.2. <i>Multiscale atrial simulations</i> .....	75
4.6. LIMITATIONS .....	76
<b>CHAPTER 5 GENESIS OF P-WAVES: CONTRIBUTION FROM ATRIAL REGIONS.....</b>	<b>79</b>
5.1. EXISTING HUMAN TORSO MODELS.....	79
5.2. MODELLING THE HUMAN TORSO.....	81
5.3. PROPAGATION OF ATRIAL RHYTHMS .....	86
5.3.1. <i>The heat transfer equation</i> .....	88
5.3.2. <i>The Finite Elements Method</i> .....	90
5.4. BODY SURFACE POTENTIAL MAPS (BSPM) .....	92
5.4.1. <i>Study of the P-wave across the torso surface</i> .....	94
5.4.2. <i>Study of determinants for the P-wave characteristics</i> .....	95
5.5. CONTRIBUTION OF INDIVIDUAL ATRIAL REGIONS TO NORMAL ATRIAL BEHAVIOUR.....	97
5.5.1. <i>Study of regions with greatest impact on P-wave morphology</i> .....	97
5.5.2. <i>Study of individual impact on electrocardiographic leads</i> .....	101
5.6. DISCUSSION .....	106
5.6.1. <i>Realistic torso model</i> .....	107
5.6.2. <i>Body Surface Potential Maps and P-waves</i> .....	107
5.7. LIMITATIONS .....	109
<b>CHAPTER 6 NON-INVASIVE LOCALIZATION OF ATRIAL ECTOPIC BEATS .....</b>	<b>111</b>
6.1. EXISTING APPROACHES TO LOCALIZE ATRIAL ECTOPIC TRIGGERS .....	111

6.2.	IMPROVEMENTS OF THE MULTI-SCALE 3D ATRIAL-TORSO MODEL.....	113
6.2.1.	<i>Cellular scale</i> .....	113
6.2.2.	<i>Tissue and atrial scale</i> .....	115
6.2.3.	<i>Torso scale</i> .....	117
6.3.	BIOPHYSICAL SIMULATIONS OF FOCAL ATRIAL TACHYCARDIA.....	117
6.3.1.	<i>Triggering sites of atrial ectopic beats</i> .....	117
6.3.2.	<i>Computation of extracellular potentials</i> .....	119
6.3.3.	<i>Stimulation protocol for triggering ectopic beats</i> .....	120
6.4.	BIOMARKERS TO INTERPRET FOCAL ATRIAL TACHYCARDIA .....	121
6.4.1.	<i>Study of biomarkers on the torso surface</i> .....	121
6.4.2.	<i>Validation of body surface P-wave integral maps (BSPiM)</i> .....	123
6.4.3.	<i>Influence of the CS-LA bridges on the BSPiMs</i> .....	131
6.5.	CLUSTERING AND CLASSIFICATION OF ATRIAL ECTOPIC FOCI FROM BSPiM .....	134
6.5.1.	<i>Methodological pipeline</i> .....	134
6.5.2.	<i>BSPiMs clustering and database</i> .....	135
6.5.3.	<i>Prospective classification of ectopic foci</i> .....	140
6.6.	DISCUSSION .....	141
6.6.1.	<i>Computational modelling and validation</i> .....	141
6.6.2.	<i>Clustering and classification of BSPiM</i> .....	142
6.6.3.	<i>Previous studies</i> .....	142
6.7.	LIMITATIONS.....	145
	<b>CHAPTER 7 GENERAL CONCLUSIONS .....</b>	<b>147</b>
	<b>ANNEX I FUTURE RESEARCH WORK.....</b>	<b>151</b>
	<b>ANNEX II LIST OF SCIENTIFIC PUBLICATIONS.....</b>	<b>153</b>
	<b>REFERENCES .....</b>	<b>155</b>
	<b>CURRICULUM VITAE .....</b>	<b>177</b>



---

# List of Figures

Figure 1.1: Action potentials and electrocardiogram .....	2
Figure 2.1: Cavities of the heart and conduction system.....	7
Figure 2.2: Position of the atria with respect to the other torso structures.....	8
Figure 2.3: Endocardial face of the LA (left) and RA (right) .....	9
Figure 2.4: Structure of the backbone .....	11
Figure 2.5: Bones of the human thorax .....	12
Figure 2.6: Lungs in situ .....	12
Figure 2.7: Computed tomography showing the great blood vessels .....	13
Figure 2.8: Anatomical structure of the liver .....	13
Figure 2.9: Physiological behaviour of the cell membrane .....	16
Figure 2.10: APs registered at different atrial and ventricular areas.....	17
Figure 2.11: Cardiac myocyte.....	18
Figure 2.12: Construction of the vectorcardiogram.....	20
Figure 2.13: ECG under physiological conditions .....	21
Figure 2.14: Position of the electrodes to register the standard and augmented leads ....	22
Figure 2.15: Unipolar precordial leads (V1 to V6).....	23
Figure 2.16: Physiological ECG registered at the 12 standard leads .....	24
Figure 2.17: Placement of the chest leads and interpolated BSPM.....	25
Figure 2.18: Standard 12 leads of common atrial flutter.....	27
Figure 2.19: Standard 12 leads of multifocal atrial tachycardia .....	28
Figure 2.20: Standard 12 leads of atrial fibrillation.....	30
Figure 4.1: Multiscale cardiac model .....	38
Figure 4.2: Schematic representation of the mathematical human atrial cell model .....	39
Figure 4.3: Schematic representation of a gate .....	41
Figure 4.4: Differences in the AP morphology when changing the ODE.....	49
Figure 4.5: Differences in the AP morphology when varying the stabilization time.....	50
Figure 4.6: Differences in AP morphology when varying duration and amplitude.....	50
Figure 4.7: Resulting characteristic APs produced by each subcellular model .....	52
Figure 4.8: Electrophysiological heterogeneity relative to the eight cellular submodels....	52
Figure 4.9: Automatic excitability of the sodium-calcium exchanger.....	53

---

*List of Figures*

---

Figure 4.10: Slab with 50x50x3 linear hexahedra with 300 $\mu\text{m}$ of spatial resolution .....	54
Figure 4.11: Conductivity (S/cm pF) for the eight atrial type of tissues .....	55
Figure 4.12: LATs computed from the simulations performed for each type of tissue.....	55
Figure 4.13: Conduction Velocity (cm/s) associated to each type of atrial tissue.....	57
Figure 4.14: Anatomical atrial regions and principal fibre direction .....	58
Figure 4.15: Rule-based algorithm to assign fibre direction .....	60
Figure 4.16: Atrial multi-layer mesh .....	61
Figure 4.17: Properties of the novel 3D atrial model .....	62
Figure 4.18: Cellular and tissue properties of the atrial model.....	67
Figure 4.19: Threshold current required for triggering the models .....	68
Figure 4.20: APD <sub>90</sub> differences between cellular, tissue slab and atrial scale .....	69
Figure 4.21: Spatial variability of APD <sub>90</sub> across the atrium.....	69
Figure 4.22: Atrial LATs produced by the anisotropic atria with fibre orientation.....	71
Figure 4.23: Atrial depolarization sequence.....	72
Figure 4.24: LAT differences between anisotropic and isotropic atrial model.....	73
Figure 5.1: Examples of previous existing human torso models .....	80
Figure 5.2: Building process of the human torso model .....	82
Figure 5.3: Surface meshes.....	83
Figure 5.4: Tetrahedral torso mesh .....	84
Figure 5.5: Tetrahedral torso model including the most relevant organs.....	85
Figure 5.6: Body surface potential maps over time .....	93
Figure 5.7: Spatial information from the potential root means square (B-RMS) .....	95
Figure 5.8: Effects of the tissue heterogeneity in the P-wave morphology .....	96
Figure 5.9: Contribution from individual atrial regions to the P-wave.....	97
Figure 5.10: Body surface RMS maps from the 21 individualized atrial regions .....	99
Figure 5.11: Added contribution from atrial regions with highest and lowest impact .....	100
Figure 5.12: P-waves registered on precordial and standard leads (V3, V6 and D3) .....	102
Figure 5.13: P-waves produced by the RA structures .....	103
Figure 5.14: P-waves produced by the LA structures .....	104
Figure 5.15: P-waves produced by the RA structures registered on the rear torso .....	105
Figure 5.16: P-waves produced by the LA structures registered on the rear torso .....	106
Figure 6.1: AP's morphologies and distribution across the atria.....	114
Figure 6.2: Atrial depolarization sequence.....	116
Figure 6.3: Transversal cut of the torso, at the height where the atrium is placed .....	117
Figure 6.4: Localization of the 58 ectopic focus sites (including the SAN) .....	118
Figure 6.5: Simulated BSPMs and integral map (BSPiM) computed at the torso surface .	122
Figure 6.6: Comparison between simulated and experimental BSPiMs .....	124
Figure 6.7: Simulated LATs by activating the SAN, the 17 RA and the 14 LA sites .....	126
Figure 6.8: Simulated and experimental BSPiMs for the whole validation set .....	127
Figure 6.9: P-wave morphology in simulated and experimental precordial leads .....	129
Figure 6.10: P-wave morphologies registered for the 30 ectopic sites on the RA .....	130
Figure 6.11: P-wave morphologies registered for the 27 ectopic sites on LA.....	131

*List of Figures*

---

Figure 6.12: In-silico simulations when foci are paced in distal and proximal LA sites.....	132
Figure 6.13: In-vivo clinical BSPiMs.....	133
Figure 6.14: Methodological pipeline to cluster and classify ectopic foci .....	134
Figure 6.15: Simulated normalized additional BSPiMs .....	136
Figure 6.16: Exemplary BSPiMs included in the ECs .....	137
Figure 6.17: Clustering of the BSPiMs.....	138



---

# List of Tables

Table 2.1: Anatomical dimensions of the most relevant atrial structures.....	10
Table 2.2: Anatomical dimensions of thoracic cage and the organs.....	15
Table 4.1: Human biatrial 3D multiscale models .....	48
Table 4.2: Ionic channel conductance and APD <sub>90</sub> for the eight submodels .....	51
Table 4.3: Longitudinal and transversal conduction velocities for the atrial tissues .....	56
Table 4.4: Atrial regions and main electrophysiological cellular and tissue properties.....	63
Table 5.1: Experimental and model values of tissue conductivities .....	86
Table 6.1: Multiplicative factors and APD associated to each sub-model .....	114
Table 6.2: Longitudinal and transversal conduction velocities for atrial tissues .....	115
Table 6.3: Anatomical sites of the 58 foci (including the SAN) .....	119
Table 6.4: Classification of BSPiMs.....	139



---

# Abbreviations

AF	Atrial fibrillation
AP	Action potential
APD	Action potential duration
AVN	Atrioventricular node
AVR	Atrioventricular ring
BB	Bachmann's bundle
BCL	Basic cycle length
Bpm	Beats per minute
B-RMS	Body root means square
BSPiM	Body surface P-wave integral map
BSPM	Body surface potential map
CS	Coronary sinus
CT	Crista terminalis
CV	Cross validation
EAM	Electroanatomical mapping
EC	Ectopic clusters
ECG	Electrocardiogram
ECGI	Electrocardiographic imaging
EGM	Electrogram
FAT	Focal atrial tachycardia
FO	Fossa Ovalis
IB	Intercaval bundle
ICV	Inferior cava vein
IST	Isthmus
LA	Left atrium
LAA	Left atrial appendix
LAS	Left atrial septum
LAT	Local activation time

*Abbreviations*

---

LFO	Limb of Fossa Ovalis
LIPV	Left inferior pulmonary vein
LPW	Left posterior wall
LSPV	Left superior pulmonary vein
LSW	Left superior wall
MRI	Magnetic resonance image
MV	Mitral valve
PM	Pectinate muscle
PSVT	Paroxysmal supraventricular tachycardia
PV	Pulmonary veins
RA	Right Atrium
RAA	Right atrial appendix
RAS	Right atrial septum
RIPV	Right inferior pulmonary vein
RLW	Right lateral wall
RSPV	Right superior pulmonary vein
SAN	Sinoatrial node
SCV	Superior cava vein
SVM	Support vector machine
TV	Tricuspid valve

# CHAPTER 1

---

## Motivation

### 1.1. Clinical motivation

The electrical activity of the heart under physiological and pathological conditions has always been of high scientific and clinical interest. The first studies in the area of cardiac electrophysiology were carried out by (Einthoven et al. 1950) who studied how the position of the heart influences the form of the electrocardiogram (ECG). Today, we know that the ECG is the synchronized sum of the action potentials (APs) produced by the atrial and ventricular myocytes as revealed by the registry of the ionic currents through the cellular membrane (Sachse 2004).

Nowadays, the ECG remains the standard and non-invasive procedure when the aim is focused on the detection and analysis of cardiac disorders provoked by arrhythmias. These are abnormal heart rhythms leading to an ineffective mechanical contraction. The clinical approach intends to interpret the signal registered on the torso surface based on a partial knowledge of the cardiac source. This is the well-known forward problem in electrocardiography (Yasuura 1981; Gulrajani 1998; Shahidi et al. 1994; Burton et al. 2011). The problem gives rise to a unique solution, i.e., a stimulus originated from the SAN at a specific frequency, which activates the atrial and ventricular myocardium generating an electrical wavefront that will move forward through the torso up to its surface. In this way, the ECG depicts a characteristic wave on the torso surface consisting of the four sections shown in Figure 1.1: the P-wave (associated to the atrial depolarization), the QRS complex (relative to the ventricular depolarization and atrial repolarization), the T wave (produced during the ventricular repolarization), and the U-wave (still a subject of debate since it could be produced by a late repolarization of Purkinje fibres, a late repolarization of some other portions of left ventricle, or an alteration in the normal action potential shape by after-potentials).

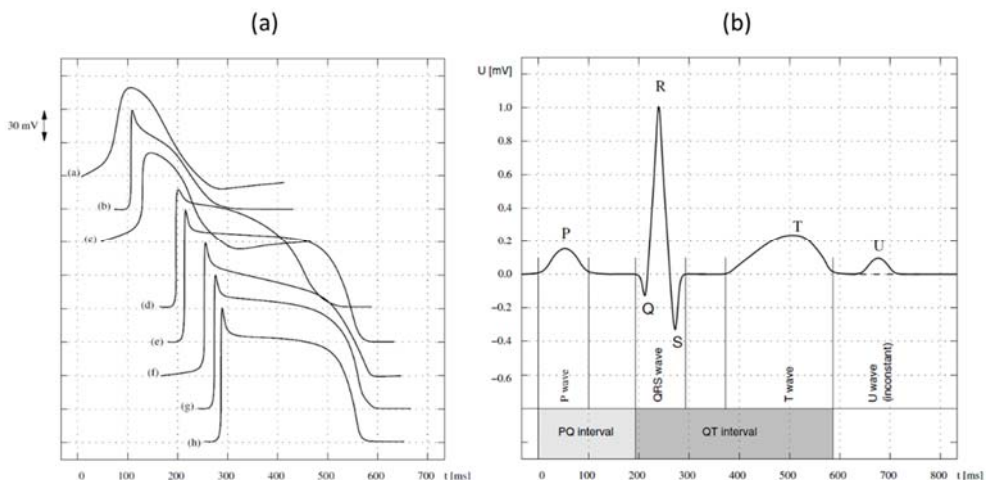


**Figure 1.1: Action potentials and electrocardiogram**

a) APs registered from cardiac myocytes at SAN<sup>a</sup>, atrium<sup>b</sup>, AVN<sup>c</sup>, His bundle<sup>d</sup>, Tawara bundle<sup>e</sup>, Purkinje fibres<sup>f</sup>, subendocardium<sup>g</sup> and subepicardium<sup>h</sup>; b) ECG registered from a physiological propagation in an adult person (Sachse 2004).

Electrical cardiac disorders are produced by alterations in the cardiac rhythm due to a few potential causes: i) an increase in the rhythm above 100 beats per minute in resting state (tachycardia); ii) a reduction in the heart rate, below 60 beats per minute (bradycardia); iii) ectopic beats triggered from wrong areas; iv) unusual conduction pathway described by the cardiac wavefront; or a combination of some of them. In this way, arrhythmias can be classified as: a) supraventricular, when the origin are the atria or the atrial conduction bundles; b) atrioventricular block; and c) ventricular arrhythmias. In either case, physiological or arrhythmic rate, the registry of the signal on the torso surface is feasible since the torso behaves as a passive and three-dimensional conductor, which encapsulates different organs (lungs, ribs, liver, skeletal muscle, blood vessels and the heart). Using the forward problem approach, clinicians may be able to diagnose cardiac disorders depending on their own capacity and expertise to interpret superficial signals in terms of morphology, duration, amplitude and frequency rate of the ECG. A better understanding of cardiac arrhythmias is very relevant for researchers and clinicians.

Focusing the interest on atrial arrhythmias, an in-depth analysis was carried out by (Almendral & Huerta 2001) and more recently by the task force for the management of atrial fibrillation of the (ESC) European Society of Cardiology (Kirchhof et al. 2016) with the contribution of the European Heart Rhythm Association (EHRA) of the ESC. These studies confirm that paroxysmal supraventricular tachycardia (PSVT) together with atrial fibrillation (AF) have the highest incidence and prevalence on a global level.

PSVT has an incidence of 35 out of 100000 person-year in the case of focal atrial tachycardia and 88 out 100000 person-year in the case of atrial flutter. Regarding atrial fibrillation, the estimated numbers of men and women with AF worldwide in 2010 were 20.9 million and 12.6 million, respectively, with higher incidence and prevalence rates in developed countries (Colilla et al. 2013; Chugh et al. 2014; Kirchhof et al. 2016). By 2030, between 14 and 17 million AF patients are anticipated in the European Union, with in between 120000 and 215000 newly diagnosed patients per year (Colilla et al. 2013; Krijthe et al. 2013; Zoni-Berisso et al. 2014). This increase in both the prevalence and incidence of AF is mainly due to the empirical fact of an increasing number of older people. Estimates suggest an AF prevalence of approximately 3% in adults aged 20 years or older (Bjorck et al. 2013; Haim et al. 2015), with greater prevalence in older persons and in patients with other clinical conditions. These cardiac disorders do not represent by themselves an imminent risk for life, but are associated to an increased risk of all-cause comorbidity.

The use of the ECG to diagnose those cardiac disorders present however a main shortcoming. Since the ECG is registered once the arrhythmia is already initiated, it forces the clinical assessment to be based on the analysis of the atrial frequency, the P-wave morphology, localization and polarity with respect the QRS complex in different torso leads (Almendral & Huerta 2001). This procedure lacks therefore of the information about the mechanisms that originate the arrhythmia, as well as the information on why and when the trigger starts, and where the ectopic site is localized.

In those cases, in which it is necessary to identify the mechanism that initiates the arrhythmia, and localize the ectopic trigger to diagnose a cardiac disorder, validated technologies are highly necessary. The most recommended, but invasive approach, is the intracardiac electrophysiological study (Miller & Zipes 2011). This invasive procedure requires the use of a set of intracardiac leads that are directly placed inside the atrial or ventricular cavity. Among the non-invasive techniques, the electrocardiographic imaging (ECGI) and the body surface potential map (BSPM) may allow to localize the arrhythmic heart region to guide an optimal intervention therapy. However, neither of these approaches currently have a widespread use in the clinical practice. ECGI requires solving the bioelectrical inverse problem, which is technically complex and computationally demanding. BSPM may give an overview of the potential distribution on the torso surface but it requires a very high number of leads to be placed on the patient's chest and processing techniques to analyse the surface signals.

Once the diagnose is already performed, the aim during the treatment is to restore the patient to sinoatrial rhythm and to avoid recurrences (Almendral & Huerta 2001). Albeit the first therapy is based on the administration of antiarrhythmic drugs (Kowey 2011), when the arrhythmia persists or secondary effects arise, other procedures like electrical cardioversion, pacemaker implantation or ablation therapy are required.

The abovementioned figures and shortcomings represent the main reason why new approaches are of great importance to first improve the knowledge of the physio-pathological mechanisms of atrial arrhythmias and second to develop and validate non-invasive diagnostic tools and advanced therapies reducing the impact on patients and the cost burden for the health systems.

## **1.2. Technical motivation**

As introduced in the previous section, current techniques and tools used to diagnose and treat atrial arrhythmias represent a risk for the patient's health. Since they are mainly invasive or are not still validated for the clinical practice, a growing interest within the scientific community arises focused on the research and development of new approaches different to the traditional solution of the forward problem.

Biophysical modelling provides a quantitative framework for integrating multiscale and multi-modal clinical data in order to understand arrhythmogenic behaviours that emerge from the complex interactions of multiple pathophysiological factors underlying atrial arrhythmias. Biophysical multiscale models of the heart have the potential to provide new insights into the complex processes underlying AF (Clayton et al. 2011). Detailed electrophysiology cell models have been developed to describe the voltage- and time-dependent currents, in human atrial cells (Courtemanche et al. 1998; Nygren et al. 2001; Maleckar et al. 2009) and in human SAN cells (Chandler et al. 2011). Those models have been integrated into tissue models of the human atria based on partial descriptions from animal experiments and clinical data to reproduce specific AF patterns (Harrild & Henriquez 2000; Seemann et al. 2006; Tobón et al. 2008; Aslanidi et al. 2011; Tobón et al. 2013). To study the spatiotemporal organization of atrial arrhythmias, different techniques are being used, including the analysis of the electrogram morphology, dominant frequency and regularity or organization index (Tobón et al. 2012).

Those computational models, realistically built in terms of anatomy and electrophysiology, have to include all the volumetric properties, regarding all the scales that intervene in the origin and propagation of atrial arrhythmias from the cell to the torso surface. Such an integrative approach is not feasible in an experimental or clinical setting, which indicates the clear need for efficient, quantitative, biophysical models.

The so-called inverse problem in electrocardiography try to determine the electrical activation sequence, which gives rise to the electrical potentials registered on the torso surface. In this regard, the aim is to infer the endocardial and epicardial electrical sources and the propagation from the heart to the torso surface. The solution of this inverse problem is neither simple nor unique mainly due to two factors (Gulrajani 1998; Atienza et al. 2009): first, the low signal amplitude and second, the lack of clinical observations of the cardiac sources provided by electrophysiological studies. The main consequence is that different methodological pipelines are requested which avoid patients from suffering

invasive and risky interventions and that the implementation of such methodology may be carried out without high complex systems.

An in-depth analysis of previous models has been carried out during this PhD thesis and there is an amount of relevant studies related to the multiscale modelling of cardiovascular phenomena. This is a basic research discipline but also a potential source of technology transfers with high interest at international level since it is possible to register and manipulate variables not accessible before, to solve the forward problem as well as come up with solutions for the inverse problem using a non-invasive approach.

### **1.3. General aim**

The main aim of this PhD thesis is to develop a highly detailed computer-based model of the atria that allows simulation of atrial electrophysiology, in health and disease. The model will integrate medical and biological data and allow exploring the interaction of anatomical and electrophysiological factors. The model will be used to study the electrical sources at atrial scale responsible for the potential distribution on the torso surface under physiological and arrhythmogenic conditions. This will also allow developing a novel methodology to solve the inverse problem in electrocardiography. The proposed method tries to overcome the shortcomings associated to those more traditional methods by driving an in-depth analysis of the atrial areas that determine each single section of the P-wave and then, using machine learning techniques to predict the localization of ectopic foci in focal atrial tachycardia (FAT) non-invasively.

Pursuing this general aim, the three-dimensional multiscale atrial-torso model developed in this thesis has been built from experimental images and histological data. We have considered realistic electro-anatomical properties of the cardiac tissue and other body organs as well as the heterogeneous differences between them. This has enabled the use of meshing techniques adapted to the finite elements method with hundreds of thousands of degrees of freedom.

### **1.4. Structure of the Thesis**

This thesis is divided in eight chapters, in which the motivation driving to the present PhD thesis is explained. A detailed clinical background is presented in Chapter 2, which helps to understand and justify the main objective of this thesis, described in Chapter 3. The three central chapters (4, 5 and 6) deeply describe both, the computational models and the in-silico studies carried out. Conclusions drew from these chapters are outlined in Chapter 7, while future research work and scientific publications derived from this thesis are listed in Annexes I and II. Following, there is the outline of each chapter with additional details:

**Chapter 2** explains the anatomical and electrophysiological characteristics of the human atria and torso under physiological conditions. The main atrial electrical disorders are also described as well as how they are currently managed in clinical practice.

**Chapter 3** sets out the justification and the main hypothesis for the present PhD thesis and describes the specific objectives that will lead to achieve the main aim.

**Chapter 4** describes the multiscale atrial model and the mathematical approach used to drive the physiological electrical propagation through the myocardial tissue.

**Chapter 5** introduces the torso model and the mathematical approach to propagate the normal atrial activity towards its surface. This chapter also investigates the atrial regions responsible for the P-wave characteristics.

**Chapter 6** studies the clustering and classification of FAs depending on the body surface distribution of new promising biomarkers.

**Chapter 7** draws significant conclusions that might enable the use of the computational model presented here to help in the clinical diagnosis and treatment of atrial arrhythmias.

**Annex I** outlines the future research work.

**Annex II** gives the list of scientific contributions derived and related to this PhD thesis published in JCR journals and international conferences.

# CHAPTER 2

---

## Clinical background

*This chapter gives an overview of the anatomical and electrophysiological characteristics of the human atria and torso under physiological conditions. The main atrial electrical disorders are also described as well as how they are currently managed in clinical practice.*

### 2.1. Anatomy of the human atria and torso

#### 2.1.1. Atrial anatomy

The atria are two chambers placed at the upper side of the heart, above the two ventricle chambers. They are separated by the interatrial wall, as can be seen in Figure 2.1 and Figure 2.2, and from the ventricles by the atrioventricular septum (Wang et al. 1995; Sachse 2004). Both wall types consist of a connective tissue that isolates the chambers allowing only the communication among them through the tricuspid valve (between right atrium and ventricle) and the mitral valve (between the left atrium and ventricle).

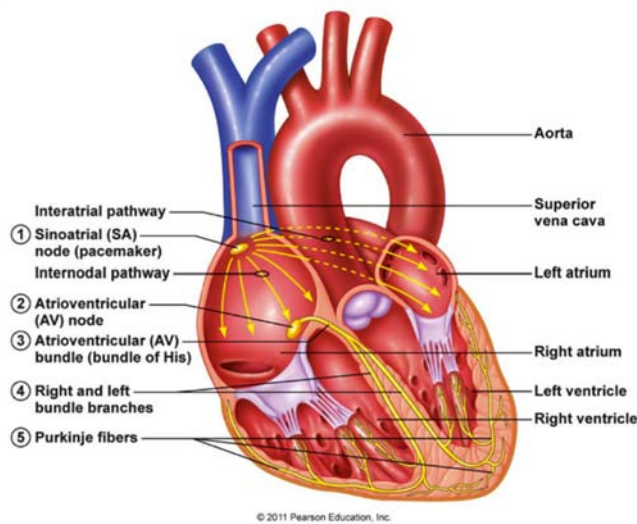
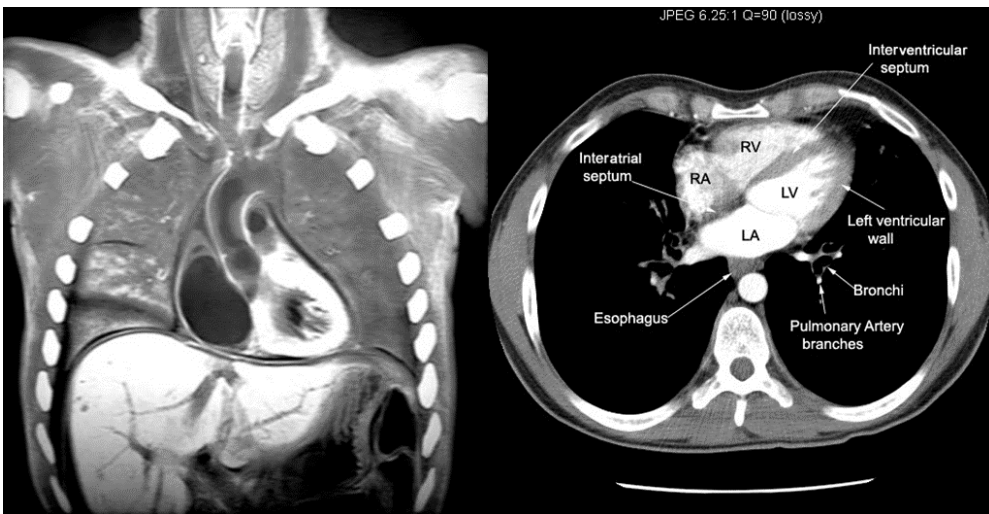


Figure 2.1: Cavities of the heart and conduction system



**Figure 2.2: Position of the atria with respect to the other torso structures**  
Left: frontal plane; Right: transverse plane. (Chandrasekhar & Chandrasekhar 2012).

The left atrium (LA), see Figure 2.3 left panel, connects with left and right pulmonary veins (PV) from the posterior wall and with the left ventricle through the mitral valve (MV). This valve consists of endocardial folds relaying on a stable support of fibrous tissue with a face adhered to the atrioventricular ring and the other side open to the atrial chamber. The atrium shapes the left posterior side and the basement of the heart and is surrounded by the esophagus on the posterior side, with the left bronquial tube and the trunk of the pulmonary arteries.

The right atrium (RA), see Figure 2.3 right panel, connects with superior and inferior cava veins, that dreins the venous blood, and with the right ventricle trough the tricuspid valve (TV). This atrium is in close contact with the right lung on the anterolateral edge, with the left atrium on the left posterior side and with the aortic trunk on the anteromedial face. A triangular-shaped appendix spreads towards the heart front and is held by the pectinate muscles (PM) at the endocardial membrane. These muscles make up a very complex net of parallel ridges linked to the crista terminalis (CT) which spreads from the anterior area of the superior cava vein (SCV) up to the inferior cava vein (ICV) and the TV vestibule (Sánchez-Quintana et al. 2002).

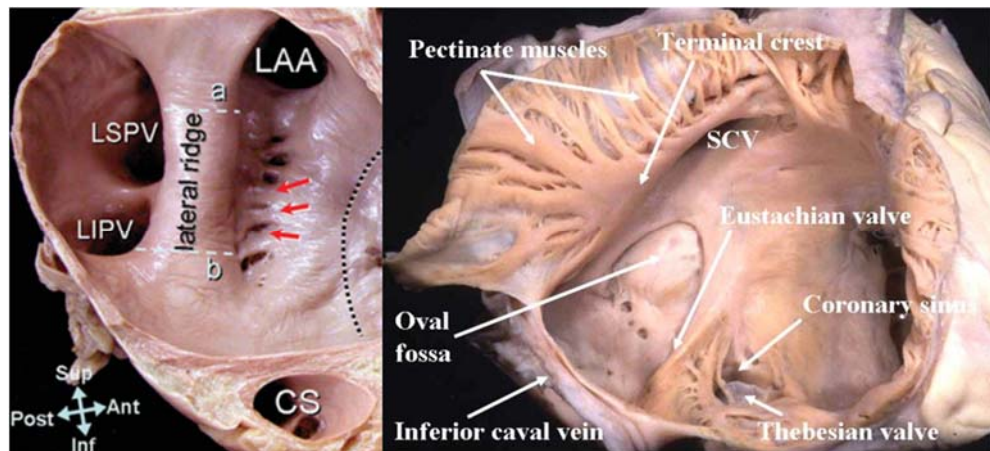


**Figure 2.3: Endocardial face of the LA (left) and RA (right)**

Highlighted on the LA: left atrial appendix (LAA), left superior pulmonary veins (LSPV), left inferior pulmonary veins (LIPV), and muscle trabeculae (red arrows) (Cabrera et al. 2008). Highlighted on the RA: pectinate muscles (PM), crista terminalis (CT), fossa ovalis (FO), superior cava vein (SCV), inferior cava vein (ICV), coronary sinus (CS), among others (Anderson & Cook 2007).

Near the ICV, arising from the lower rear side of the RA and spread along the heart's posterior surface between the left ventricle and left atrium, the coronary sinus (CS, Figure 2.3) collects the majority of the cardiac venous blood and facilitates the movement of this blood into the RA.

Experimental studies carried out by (Kitzman et al. 1988; Wang et al. 1995; Cohen et al. 1995; Lemery et al. 2007; Cabrera et al. 2008) describe the atrial anatomy in further detail as well as all its anatomical parts, such as the right and left appendix (RAA and LAA), the CT, the PMs, the muscle fibers, the CS, the FO and both atrioventricular valves (TV and MV). The dimensions of these regions and anatomical structures have been previously collected in two thesis carried out within our research group (Ruiz-Villa 2010; Tobón 2010) and Table 2.1 shows the most relevant sizes.

Remains to be defined the preferential conduction bundles that guide the electrical impulses under physiological conditions and the pacemaker region. Regarding the bundles, these born in the RA and are aligned with the major muscular RA-LA connexions like the limbus of the FO (Spach et al. 1985) and the Bachmann's bundle (BB) (Bachmann 1916; Wang et al. 1995). BB is the most important bridge, located at the upper anterior face between both atria and forces this direction as the preferential conduction. However, it is also the principal driver of atrial arrhythmias (Lemery et al. 2007) having the highest influence in the distribution of the electrical activity on the torso surface. On the other hand, the electrical activity of the heart, under physiological conditions, is originated in a region called sinoatrial node (SAN). This highly specialized anatomical structure is localized at the upper rightmost side of the RA, just where the

SCV drains to the heart. The SAN is the natural pacemaker of the heart and the responsible for initiating the depolarization phase that subsequently triggers the mechanical contraction of the heart (Guerra & Cinca 2007).

**Table 2.1: Anatomical dimensions of the most relevant atrial structures**

LA			RA		
Region	Size (cm)	Reference	Region	Size (cm)	Reference
Wall width	0.20 0.30-0.50 0.05-0.35	(Wang et al. 1995; Sunderman & Boerner 1950; Coffey et al. 1981)	Wall width	0.05-0.35 0.80-0.12	(Sunderman & Boerner 1950; Hiraoka et al. 1998)
LAA	5.70	(Weigner et al. 1999)	Between anterior and posterior wall	2.80-5.20	(Cohen et al. 1995)
Diameter PV	0.70-1.60	(Cohen et al. 1995)	Between septum and lateral wall	2.90-5.30	(Cohen et al. 1995)
Length PV	0.80-1.50	(Ho et al. 1999)	Between lower and upper faces	4.20-3.60	(Bommer et al. 1979)
External diameter MV	2.00–3.80 2.60-3.20 2.50-3.30	(Cohen et al. 1995; Kitzman et al. 1988; Sunderman & Boerner 1950)	External diameter TV	2.00–4.00 3.20-3.70 3.20-4.00	(Cohen et al. 1995; Kitzman et al. 1988; Sunderman & Boerner 1950)
<b>Interatrial unions</b>			Diameter CS	0.95–1.10 0.60–0.75	(Cohen et al. 1995; Cabrera et al. 1998)
Region	Value (cm)	Reference	Wall CT	0.70-1.60 0.30-0.60	(Cohen et al. 1995; Akcay et al. 2007)
BB	0.40 0.90 1.10	(Lemery et al. 2003)	Length CT	5.10-6.00	(Matsuyama et al. 2004)
FO	0.18-4.40 cm <sup>2</sup>	(Reig et al. 1997)	SAN	0.60 x 0.40	(Negoescu 1991)

### 2.1.2. Torso anatomy

The human torso is the part of the human body that contains the vital organs, with the exception of the brain. It is a semi-rigid structure responsible for facilitating the lifting and downward movements used to breathe as well as for protecting the thoracic viscera.

This rib cage is longitudinally limited by the backbone on his posterior face, by the sternum on the upper and anterior side and transversally by twelve pair of ribs that three-dimensional surround the torso. The vertebral column exercises the function of longitudinal axis for the whole skeleton, leaving the ribs and viscera suspended on its ventral face. This structure consists of 24 vertebrae plus the sacrum and coccyx distributed as shown in Figure 2.4 (Thibodeau et al. 2007). The sternum, Figure 2.5, a solid stretched and flattened bone in which side edges the rib cartilages born closing the thoracic cage, is located almost parallel to the vertebral column but in its anterior face. Finally, the twelve pairs of ribs are independently placed on both sides of the trunk, Figure 2.5, closing the thoracic cage on the anterior part thanks to the connection with the sternum and on the rear side since they are connected to the vertebral column.

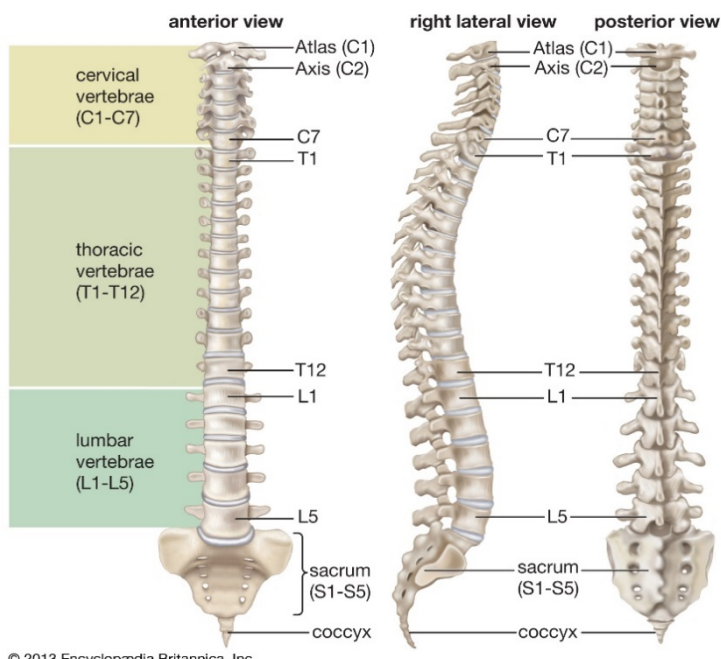
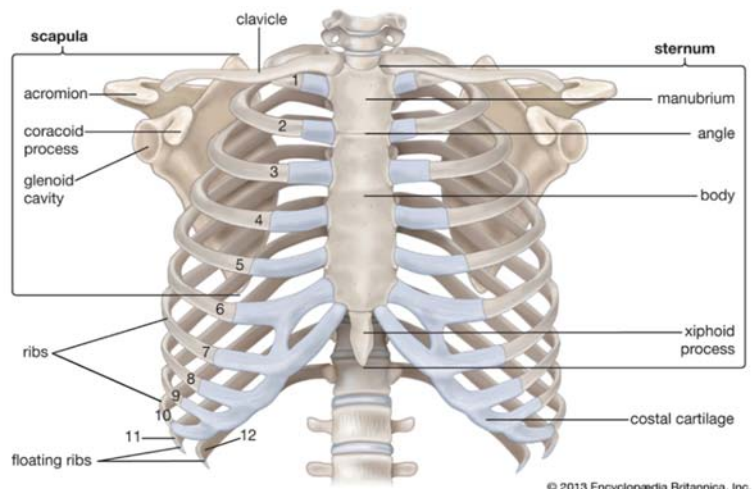


**Figure 2.4: Structure of the backbone**

## Chapter 2

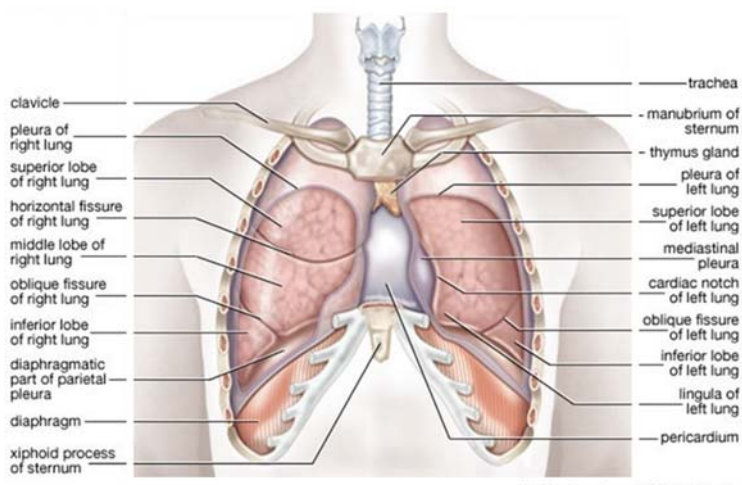
---



© 2013 Encyclopædia Britannica, Inc.

**Figure 2.5: Bones of the human thorax**

Lungs are the essential organs belonging to the respiratory system responsible for the gas exchange. They have a conical shape, Figure 2.6, spread from the diaphragm up to the clavicle and are surrounded by the ribs. Its medial region is concave in shape appropriate to accommodate the heart, being sharply concave on its left side (Thibodeau et al. 2007).



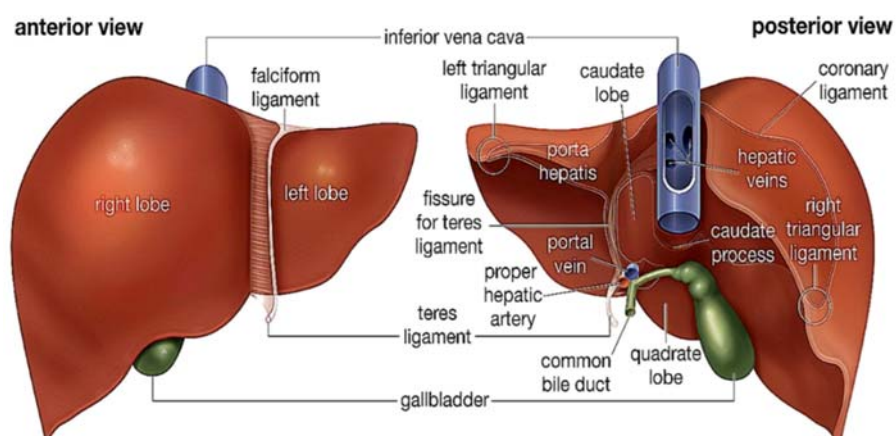
© 2008 Encyclopædia Britannica, Inc.

**Figure 2.6: Lungs in situ**

As already said before, one of the main tasks of the thoracic cage is to protect the great blood vessels, i.e., the aortic artery on his upwards and downwards paths, the trunk of the pulmonary arteries, the superior and inferior cava veins and the pulmonary veins. The aorta is the most relevant artery in the body and is the vehicle for the whole arterial system. It is divided, as shown in Figure 2.7, in several sections named depending on the blood direction and sense.



**Figure 2.7: Computed tomography showing the great blood vessels**  
 Left: ascending aorta (1), SCV (2), pulmonary trunk (3), left pulmonary veins (4). Right: right (5) and left (6) ventricle, ascending aorta (7), aortic arch (8), descending aorta (9) (T.B Moeller 2007).



© 2010 Encyclopædia Britannica, Inc.

**Figure 2.8: Anatomical structure of the liver**

The liver is the biggest gland in the body placed on the diaphragm's lower face, behaving as the heart's floor. It consists of two main lobes as shown in Figure 2.8, each of them subdivided into multiple liver lobules with a shape of small hexagonal or pentagonal cylinders of about 1mm in diameter and 2mm in height (Thibodeau et al. 2007).

It remains to define the dimensions regarding not only the thoracic cage but also each of the organs placed inside. Several experimental studies carried out by (Cormier. et al. 1990; Bellemare et al. 2001; Kratzer et al. 2003; Thibodeau et al. 2007; Busscher et al. 2010; Cassola et al. 2011; Kramer et al. 2012) have allowed summarizing the anatomical dimensions (see Table 2.2).

In a 5-year clinical trial carried out by (Bellemare et al. 2001), the authors involved 64 adult and healthy men and women in order to analyse, among other objectives, the thoracic dimensions. This trial allowed the registry of the anthropometric dimensions related to the thoracic cage to determine the averaged thoracic values of width, depth and height. Later on, in another study carried out by (Bellemare et al. 2003), sex differences between the male and female thoracic dimensions were deeply analysed, concluding that female's thoracic cages are typically a 10-12% smaller than in men. All these dimensions are depicted in Table 2.2.

The lungs' physiological sizing was determined by (Kramer et al. 2012) who analysed 166 patients. This study concluded that factors such as age, height and weight do not influence the lungs' dimensions and then men's and women's lungs have approximately the same size (see Table 2.2).

With respect the vertebral column, (Busscher et al. 2010) compared the dimensions of 6 spines from death adults with the dimensions of pig's spines giving relevant information in terms of anatomical structure and size.

The average sternum sizing was provided by (Selhofer et al. 2006) who studied the dimensions in a pool of 55 men and 35 women with an average of 65 years of age. This morphometric study concludes that there are not significant sex differences with regards the general sternum structure, providing similar results in two thirds of the population under study. Results depicted in Table 2.2 represent the maximum and minimum dimension, totalling the length of the three sections, i.e., the manubrium, the body and the xiphoid appendix.

Finally, (Kratzer et al. 2003) carried out a study where used ultrasounds to determine the liver's dimensions on 2080 individuals, 983 men and 1097 women, aged between 18 and 88. The authors determined that the average diameter of this organ is  $14.0 \pm 1.7$  cm, with an average range depicted in Table 2.2. It is also an outcome of this study the relevant influence of sex, body mass index, height, weight and age on the final liver's dimension.

**Table 2.2: Anatomical dimensions of thoracic cage and the organs**

Torso		
Region	Size (cm)	Ref.
Shoulder breadth	39.90 - 50.50	(Cassola et al. 2011)
Abdomen circumference	70.70 - 110.40	
Average torso breadth	26.35 - 28.61	(Bellemare et al. 2001)
Shoulder depth	17.70 - 25.30	
Waist depth	17.70 - 26.90	(Cassola et al. 2011)
Average torso depth	13.27 - 16.27	
Diaphragm height	20.46 - 26.12	(Bellemare et al. 2001)
Lung height	25.00	
Lungs posteroanterior diameter	16.00	(Kramer et al. 2012)
Lung's bases transverse diameter	10.00 (right) - 7.00 (left)	
Spine length	56.94	(Busscher et al. 2010)
Sternum length	29.36 - 36.54	(Selthofer et al. 2006)
Sternum angle	158.97 - 173.73	
Rib angle	49.15 - 62.75	(Bellemare et al. 2003)
Liver diameter	9.40 - 21.30	(DeLand & North 1968; Kratzer et al. 2003)

## 2.2. Electrophysiology of the human atria and torso

### 2.2.1. Atrial electrophysiology

#### 2.2.1.1 The action potential (AP)

Cardiac cells in general and the atrial cells in particular, are excitable cells so-called myocytes. These cells are cylindrical in shape with approximately 100µm in length and from 10 to 15 µm in diameter (Ilnicki 1987). They are capable of responding to electrical stimuli when these are sufficiently intense to force the cell to move from its resting state. This excitation is mainly due, see Figure 2.9, to the movement of Na<sup>+</sup>, Ca<sup>2+</sup> and K<sup>+</sup> ions through the cell membrane because of the gradients in concentrations and potential on both sides of the lipid bilayer that form the cell membrane (Zipes & Jalife 2004).

In order to make the ionic exchange possible, there exist an amount of membrane proteins, the so-called ion channels, capable of responding to electrical, chemical or mechanical stimuli and, as consequence, facilitating such channels to move towards an open or close state in a selective way depending on the specific ion. Depending on the type of

stimulus that activate the cell, the ion channels can be classified as voltage-gated channels, mechanically-gated channels or ligand-gated channels.

Beyond the type of ionic channels that define the lipid membrane, the myocytes rest in a situation of dynamic equilibrium in which the intracellular domain holds a lower potential than in the extracellular domain. This situation is the so-called resting phase and is characterized by a potential of -80mV approximately. When the stimulus reach the cell, a sequence of openings and closures, see Figure 2.9 left panel, are performed by the ionic channels, and different transport mechanisms, what produce a synchronized incoming and outgoing of ionic currents responsible for the cell activation (depolarization phase) and the return of the cell to its resting state (repolarization phase).

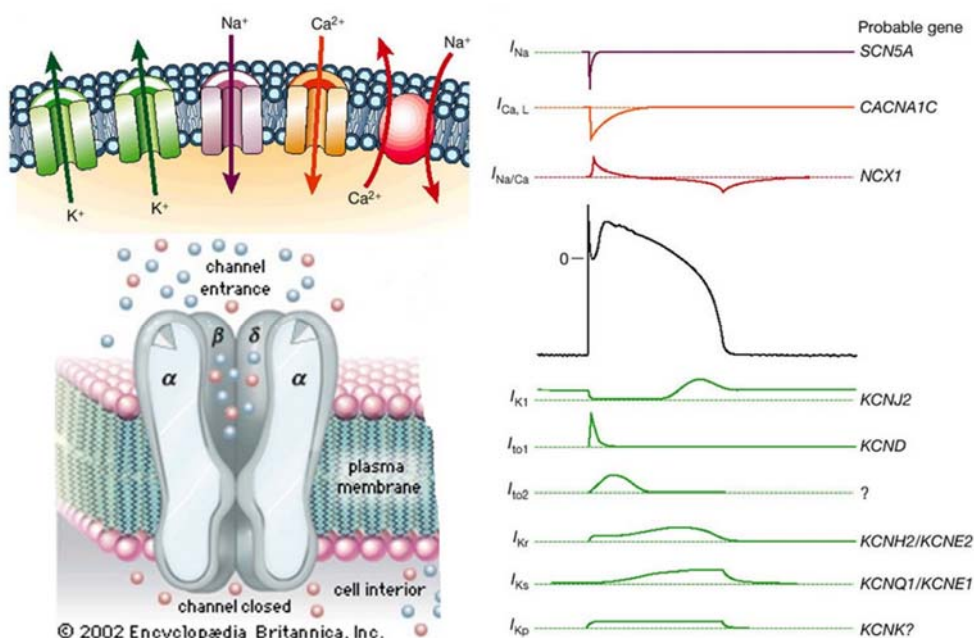


**Figure 2.9: Physiological behaviour of the cell membrane**

Upper left: main ionic channels of potassium  $K^+$ , sodium  $Na^+$ , calcium  $Ca^{2+}$ , sodium-potassium pump  $Na^+/Ca^{2+}$ . Lower left: representation of an ionic channel embedded in the cell membrane. Right panel: main ionic currents responsible for the depolarization phase ( $I_{Na^+}$ ,  $I_{CaL}$ ,  $I_{Na/Ca}$ ), AP (black line), and main ionic currents responsible for the plateau and repolarization phases (Marbán 2002).

The first ionic current in being activated, as can be seen in Figure 2.9 right panel, is the fast sodium current ( $I_{Na^+}$ ). This current starts the depolarization phase, increasing the cellular potential up to approximately +20mV and being deactivated almost immediately (few milliseconds). This current is the main responsible for the fast rising edge in the

AP. Then, the calcium current ( $I_{Ca}^{2+}$ ), with lower intensity, together with the outgoing potassium current ( $I_K^+$ ), produce a slow decrease of the membrane potential giving rise to the plateau phase in the AP. The duration and amplitude of this phase is mainly dependent on the type of cardiac myocyte. In this regard, atrial and ventricular APs are quantitatively different as can be seen in Figure 2.10 (Dawodu et al. 1996). Finally, the activation of additional potassium currents drives the potential drop down towards the cellular resting state.

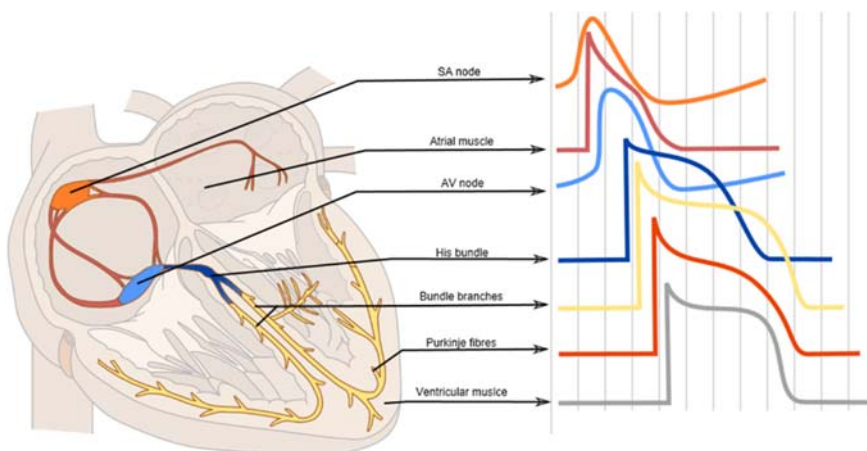


**Figure 2.10: APs registered at different atrial and ventricular areas**

A large number of studies have been carried out throughout history with the aim of analysing the heterogeneity of different atrial regions in both humans and animal species. In the case of humans, studies performed by (Wang et al. 1993; Benardeau et al. 1996) determined the existence of two or three different types of APs, with a characteristic triangular shape and then quite different to the AP morphology when it is generated by ventricular myocytes. Meanwhile, (Feng et al. 1998) carried out experimental measurements in different areas of the dog atrial tissue and determined the presence of heterogeneities in the AP duration (APD) at the CT (270ms), PMs (190ms), RAA (180ms) and the atrioventricular rings (160ms).

#### 2.2.1.2 Tissue heterogeneity

Up to now, we have analysed the electrophysiological behaviour of the cardiac cells. However, the properties at cellular scale are as important as those at tissue scale, i.e., the way muscular fibres are anatomically and electrically interconnected facilitating in such way the activation of the tissue and its mechanical contraction under physiological conditions.

The three-dimensional net of muscular fibres depicts transversal and longitudinal connections, being this last configuration the preferential conduction way (see Figure 2.11). In order to ease the cell communication, the distal ends of the cell hold some kind of transmembrane channels, the so-called gap-junctions, devoted to communicate the adjacent cell cytoplasm by means a low resistivity (400 times lower than in the case of the cell membrane). This structural cell anisotropy nurtures a conduction velocity dependent on the specific cardiac region, which is quantitatively higher in the longitudinal axis, i.e., between 2 and 5 times faster than the transversal velocity.

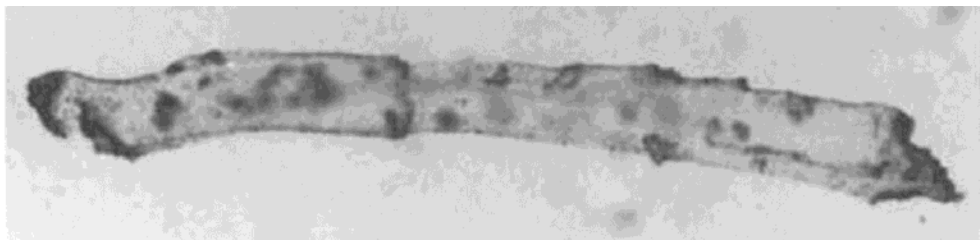


**Figure 2.11: Cardiac myocyte**  
(Kléber et al. 2001).

#### 2.2.1.3 Sinus rhythm and atrial depolarization pattern

Normal electrical activity of the heart under physiological conditions starts at the region of the SAN. From that moment, the electrical activity moves from one myocyte to another, activating the atrial tissue and generating a wavefront that propagates from the RA towards the LA through the preferential conduction bundles described in previous sections, i.e., the BB, the FO and the CS. The main outcome is the information at tissue level that could be registered using an electro-anatomical mapping system. This potential is the so-called electrogram (EGM) and is extremely useful to diagnose the electrical activity of the heart. Its main shortcoming comes from the fact that it is an invasive technique and then it involves some risks for the patient's health.

#### 2.2.2. Torso electrophysiology

One-step forward towards the study of the cardiac electrophysiology addresses the influence of the human torso on the propagation of the electrical potential from the atria to the torso surface. This propagation is already defined through the succession of three phases, i.e., the electrical heart-torso coupling, the propagation through the volumetric conductor and the registration of the electrical potential on the torso surface. All these stages are finally responsible for the external signal that is used to diagnose the electrical activity of the heart, the electrocardiogram (ECG).

### 2.2.2.1 Phase I: Heart-torso coupling

One hypothesis highly discussed by several authors (Tung 1978; Plonsey & Barr 1984; Barr & Plonsey 1984) and lately confirmed by (Ferrero et al. 1994) considers the whole myocardium as a single excitable cell based on the fact that all the myocytes operate under some kind of electrical short circuit. When this excitable cell is in resting state, it does not allow the current to flow towards the extracellular domain and then no potentials arise in the volumetric conductor where the cell is immersed. However, when a strong enough stimulus gets the cell, an ionic exchange through the membrane starts as well as a series of displacement currents associated to its capacitive behaviour. Both sides of the cell membrane can then be considered as a binomial current source-sink.

This simplified model allows resembling each cell membrane to a single current dipole moving aligned to the AP and the cell membrane as a whole to a surface summation of single current dipoles. This simplification allows to calculate the potential in the extracellular potential using the Equation 2.1 defined by (Ferrero et al. 1994):

$$u(\vec{r}) = -\frac{\gamma}{4\pi} \cdot \frac{\sigma_i}{\sigma_e} \iiint \vec{v}' u_m(\vec{r}') \cdot \vec{v}' \left[ \frac{1}{|\vec{r}' - \vec{r}|} \right] dv \quad \text{Equation 2.1}$$

where  $u(\vec{r})$  is the extracellular potential generated by a volumetric distribution of single current dipoles, computed at the point  $\vec{r}$ ,  $\gamma$  is a scale factor smaller than the unit which considers that the volume occupied by the myocardium is bigger than the intracellular volume of the fibres,  $\vec{r}' - \vec{r}$  is the distance between each dipole position vector and the point  $\vec{r}$ ,  $\sigma_i$  and  $\sigma_e$  are the intracellular and extracellular conductivities,  $u_m(\vec{r}')$  is the membrane potential associated to each dipole and  $v$  is the volume.

### 2.2.2.2 Phase II: Propagation of electrical potential through the volumetric conductor

Under this approach, the extracellular domain is represented by the human torso, which behaves as a low resistance volumetric conductor. As though it was an electrical wire, this conductor allows to registry the potential falls in each point within its borders.

If we assume this extracellular domain as infinite and homogeneous, the spatial integration of the electrical field generated by all the single electrical dipoles gives rise to the concept of cardiac dipole as the unit representative of the myocardial propagation (Waller 1889; Gabor & Nelson 1954). The time evolution of such dipole when it is referenced to a single point describes a kind of 3D curves on the space called vectorcardiogram (see Figure 2.12). This curve describes three characteristic loops responsible for the expected waves depicted in the ECG. For this, a vector projection of the dipole will be necessary with respect to the specific leads.

It is worth highlighting the error we assume when considering the torso as a homogeneous and infinite volume. Every realistic analysis must then consider two constrains. On

one side, the torso is finite, limited by its own surface, and highly asymmetric regarding the frontal, lateral and sagittal planes. On the other side, inside the torso there exist regions with different conductivities what produces high heterogeneity. Lungs, as the larger organ inside the torso, have a very low conductivity around  $0.389\text{mS/cm}$ , while blood for example holds the higher value around  $7.000\text{mS/cm}$  or even the torso by itself which stands around  $2.390\text{mS/cm}$  (S. Gabriel et al. 1996).

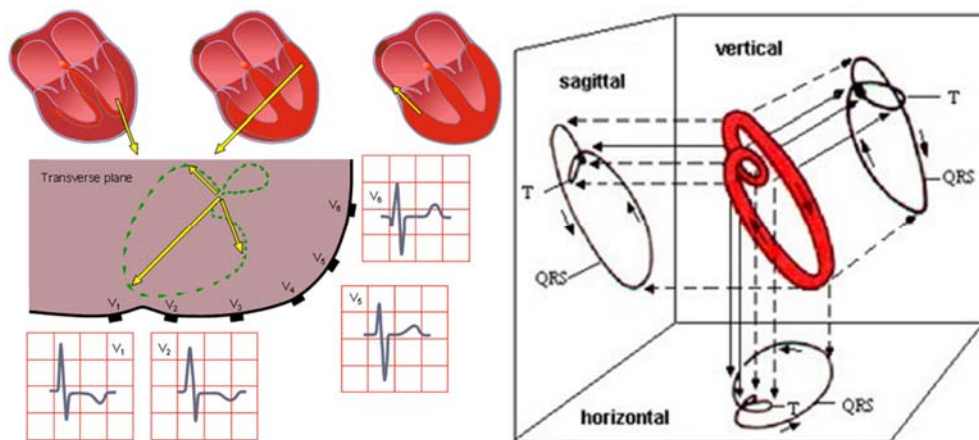


**Figure 2.12: Construction of the vectorcardiogram**

Red line on right panel shows the curve as it moves synchronously with the ventricular depolarization (Krzyminiewski & Grajek 2005).

#### 2.2.2.3 Phase III: Registration of the surface potentials

The morphology of the electrical signal on the torso surface is highly dependent on the configuration used during the registration process. Whatever it is finally used, the ECG shows, under physiological conditions, not only characteristic electrical voltages but also the expected P, Q, R, S and T waves (Guyton 1987) and the controversial in origin U wave.

The P-wave, as depicted in Figure 2.13, holds a duration and amplitude under physiological conditions that very rarely is above 120ms and 0.25mV respectively (Meek & Morris 2002). It is the result of the atrial depolarization and gives rise to the atrial contraction. Approximately 160ms after the starting of the P-wave, the QRS complex arises as the result of the ventricular depolarization and contraction. This part of the signal is normally shorter than 100ms with an amplitude highly dependent on the specific lead where it is recorded. The T-wave lasts approximately 200ms. It is due to the ventricular repolarization and its mechanical relaxation. Both amplitudes corresponding to the QRS

complex and the T-wave mask in fact the atrial repolarization, so this phase is not obvious in the ECG. The source of the U-wave remains unknown. It is frequently associated to the repolarization of the Purkinje fibres, the prolonged repolarization of the M-cells in the midmyocardium and after-potentials, possibly caused by mechanical forces in the ventricular wall (Van Eck et al. 2003). This wave normally shares the same polarity as the T-wave although it is normally less than 25% of its voltage with a maximum amplitude between 1 and 2 mm and a duration of 50ms approximately. In fact, its size is inversely proportional to the heart rate so the most common cause of prominent U-wave is bradycardia.

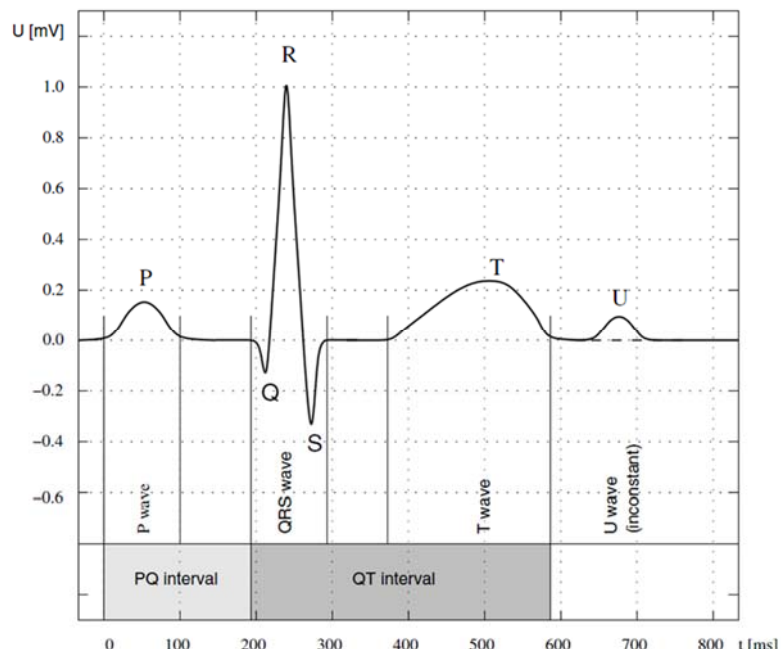


**Figure 2.13: ECG under physiological conditions**

Normal durations are: P-wave around 100ms, PQ segment around 200ms, QRS complex around 100ms (Sachse 2004).

The standard procedure to register the electrical potential on the torso surface consists in placing 12 electrodes on standard leads. The outcome of all these signals is a kind of spatial information about the electrical activity of the heart and how it is propagated through the frontal, lateral and sagittal planes towards the torso surface. Depending on the specific localization of the leads, they are called standard, augmented or precordial leads.

The bipolar standard limb leads (I, II, III) shown in Figure 2.14 are in chronological order the oldest ones used by Einthoven at the beginning of XX century (Einthoven et al. 1950) and are based on the concept of bipolarity. In this way, a positive and negative terminal carefully placed allow to compute the ECG using the Einthoven's law: at any given instant, the potential in lead II is equal to the sum of the potentials in leads I and III (Guyton 1987). The electrodes that form these signals are located on the limbs, one on each arm and one on the left leg, giving rise to Einthoven's triangle.

In the case of the unipolar augmented limb leads, already shown in Figure 2.14, there is a single positive electrode referenced against a combination of the other limb electrodes, with a different combination for each augmented lead. This null point, the so-called Goldberger's central terminal, represents the negative pole and does not register significant variations in electric potential. The positive electrodes are located on the left arm (aVL), the right arm (aVR), and the left leg (aVF) all of them connected to the limbs by means of electric resistances (Guyton 1987). For example, in lead aVR, the electric potential of the right arm is compared to the negative pole, which is obtained by adding together the potential of leads aVL and aVF.

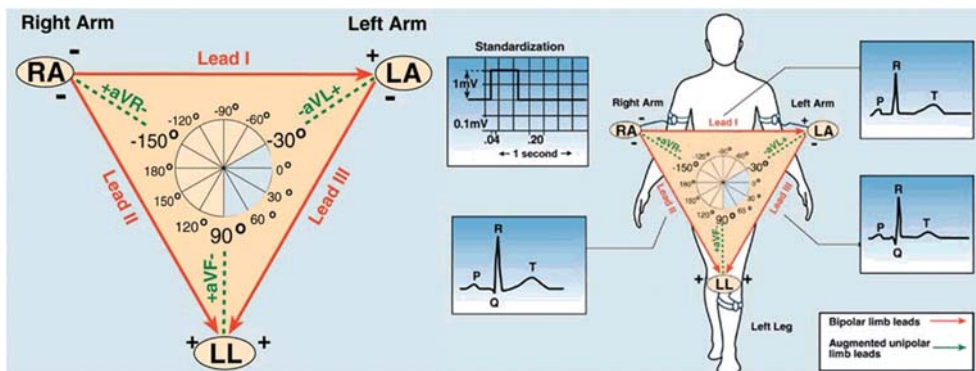


**Figure 2.14: Position of the electrodes to register the standard and augmented leads**  
Standard limb leads (I, II, III); Augmented leads (aVR, aVL, aVF) (Yanowitz 2012).

Finally, the unipolar precordial leads, shown in Figure 2.15, are placed at the central and leftmost side of the frontal torso. The specific placement is as follows: V1 fourth intercostal space to the right of the sternum; V2 fourth intercostal space to the left of the sternum; V3 between leads V2 and V4; V4 fifth intercostal space at left midclavicular line; V5 level with lead V4 at left anterior axillary line; and V6 level with lead V5 at left mid-axillary line. These unipolar leads are compared to a common lead, the so-called Wilson's central terminal, produced by averaging the measurements from the electrodes placed at right and left arms and the left leg to give an average potential across the body.

Among these three possible placements, the most common in clinical practice is the one using the precordial leads since electrodes are very much closer to the heart.

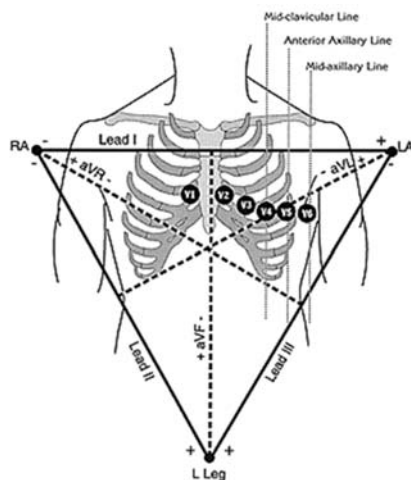


**Figure 2.15: Unipolar precordial leads (V1 to V6)**  
(Yanowitz 2012).

The morphology of the ECG under physiological conditions is shown in Figure 2.16. Standard leads (I, III, III) are quite similar to each other and depict a positive deflection in the P-wave but also in the QRS complex and T-wave. On the other hand, potentials registered at the augmented leads (aVR, aVL, aVF) follow the same trend as the standard leads with the exception of aVR, which is reverse in polarity. Finally, precordial leads (V1 to V6) have in general higher amplitude. In the case of V1 and V2, since are placed above the atria, show a negative deflection meaning the potential is moving away from the lead. On the other side, leads V4 to V6 are placed nearer the apex and receive the potential almost during most of the myocardial depolarization so they normally show a positive deflection.

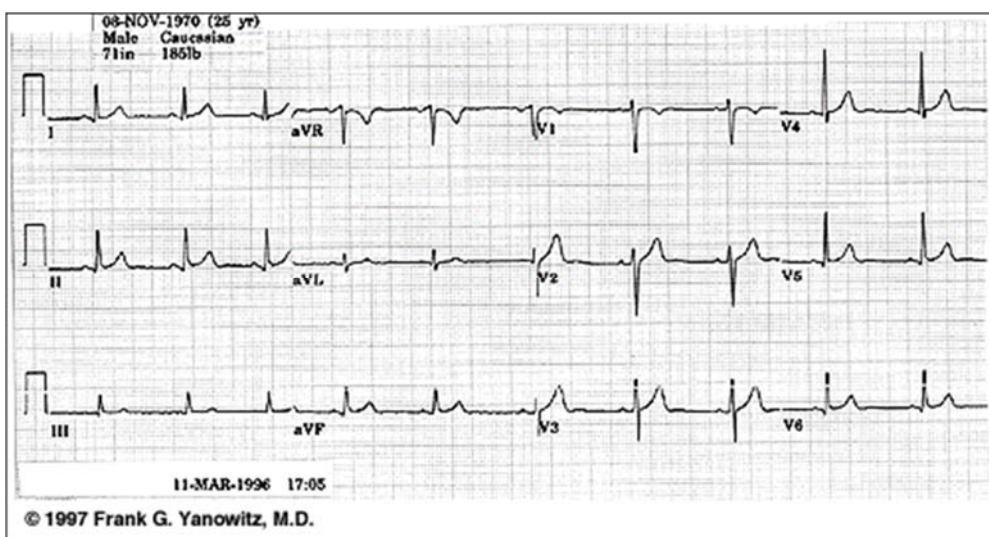
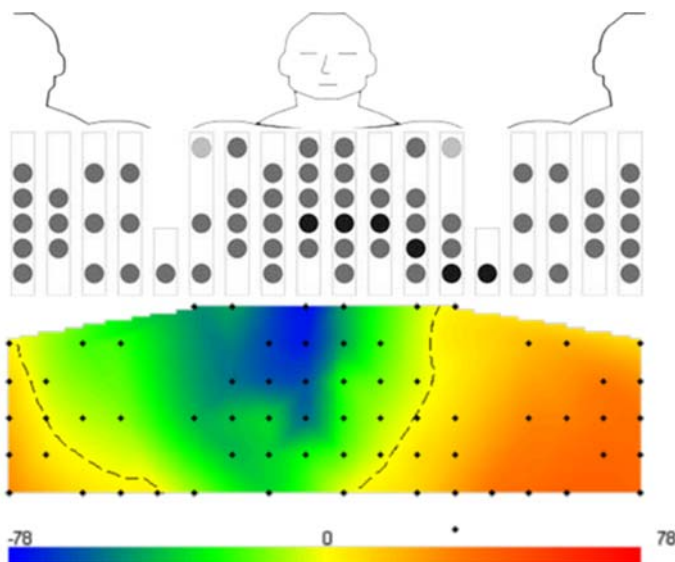


Figure 2.16: Physiological ECG registered at the 12 standard leads

Currently, there exist another technique to study the electrical potentials on the torso surface. It is the so-called body surface potential map or BSPM. It consists in the registration of the electrical potentials in a larger number of leads placed on the torso surface in order to generate maps depicting the distribution of these potentials across the torso surface as shown in Figure 2.17. This technique holds two main advantages in comparison with the traditional ECG. On one hand, larger number of electrodes allow the registration of unseen events during the 12 leads ECG and this may allow to diagnose new pathologies (Carley 2003; Finlay et al. 2005). On the other hand, higher density of information may allow building coloured maps related to the potential range and then facilitate the understanding of the spatio-temporal information by means of more advance signal processing techniques.



**Figure 2.17: Placement of the chest leads and interpolated BSPM**  
(M. S. Guillem et al. 2009).

However, BSPM has still many shortcomings. Regarding the number and placement of the electrodes, there is no single standard or agreement in the field that can be widely used. Indeed, the number of electrodes may vary between 32 and 256 and some authors argue that there exists redundant information when the number of electrodes changes from 30 to 64 (Lux et al. 1978; Hoekema et al. 1999). Furthermore, since the density of electrodes is very high, the process of fixing those electrodes to the torso surface is a time consuming process. Finally, the amount to wires and electrodes introduces noise in the system and then the signal acquisition and its quality can also be worse than it should be expected, forcing to disregard some signals.

All these constraints point out that the BSPM is not yet a widely used technique in the current clinical practice, and then further investigations must be carried out (Pedron-Torrecilla 2010). Over the last decade, the state-of-the-art in cardiac computational modelling has progressed rapidly. The electrophysiological function of the heart can now be simulated with a high degree of detail and accuracy, opening the doors for addressing current clinical problems in cardiac electrophysiology (Trayanova & Chang 2015). In this regard, multiscale human atrial-torso models together with machine learning and signal processing techniques may allow interpreting the genesis of the ECG, understanding how the BSPM or new BSPM-derived biomarkers may guide the localization of ectopic triggers and at the end improving the diagnosis of atrial arrhythmias and the patient-specific therapeutic interventions.

## **2.3. Atrial electrical disorders**

Atrial arrhythmias are the most common supraventricular disorders that arise from improper electrical activity of the heart leading to ineffective mechanical contraction (Kirchhof et al. 2016; Sethi et al. 2017).

Several approaches have been used to classify the atrial arrhythmias. Based on the frequency, arrhythmias may be classified into tachycardia (with frequency higher than 100 beats per minute, bpm) and bradycardias (when frequency is lower than 60 bpm). When the classification criterion is the duration, atrial arrhythmias may be classified into persistent or permanent (if it is permanently present) and paroxysmal (when it is only present on precise moments). Finally, if the aim is to classify in terms of the electrophysiological mechanisms and the anatomical substrate, arrhythmias may be divided into macro-reentrant (including atrial flutter among other macro-reentrant circuits in the RA and LA), focal tachycardia (due to an automatic trigger from a single site) and atrial fibrillation (Lesh et al. 1996).

Reentry is usually confirmed by demonstrating initiation and termination of atrial tachycardia with programmed electrical stimulation and by the presence of manifest or concealed entrainment. It is associated with anatomical or functional regions of block as well as areas of slow conduction (Saoudi et al. 2001).

### **2.3.1. Common atrial flutter**

After atrial fibrillation, atrial flutter is the most important and most common atrial tachyarrhythmia. Common atrial flutter is an organized macro-reentrant (one single reentrant circuit) atrial tachycardia, confined to the RA (Waldo et al. 1977) that can be subdivided based on the rotation of the circuit to counter clockwise (90% of patients) or clockwise atrial flutter (10% of patients) (Sethi et al. 2017). The atrial rate is often around 300 bpm with a resulting ventricular rate of around 150 bpm (Hall & Todd 2006). Other authors however set the rate around 200 and 260 ms cycle length, although it may fluctuate depending on patient's previous treatment (Saoudi et al. 2001).

Typical atrial flutter originates in a circuit around the tricuspid annulus limited by the SCV and ICV, CS and CT as the anatomical barriers. The most common direction of activation in the circuit (90% of clinical cases) is descending the anterior and lateral walls and ascending the septal and posterior walls of the RA. This condition produces continuous electrical activity around the atrial circuit and consequently in the ECG (f waves). In this regard, the ECG shows a saw tooth's pattern in inferior leads (II, III, aVF and V1), with a slow downward slope followed by a fast upward slope explained by electrical forces going through the cavotricuspid isthmus and the septum, and then approaching the inferior leads through the lateral wall (see Figure 2.18) (Almendral & Huerta 2001; Saoudi et al. 2001; Wellens 2002; Doiny & Merino 2013).

The incidence of this kind of common tachyarrhythmia is higher than it was initially considered, affecting to 88 in every 100000 individuals per year, double men than

women, and where the age is a significant risk factor (Granada et al. 2000). Furthermore, typical atrial flutter cases make up around 23% of all 12863 ablation procedures in the Spanish National Ablation's Registry (Pedrote-Martínez et al. 2016). Furthermore, atrial flutter is considered to hold as much risk as atrial fibrillation for thromboembolic events (3-4% per year). Atrial flutter also carries a proarrhythmic risk, and additionally, rhythm control and ventricular rate response can only hardly be achieved with medical treatment (Halligan et al. 2004; Ghali et al. 2005; Doiny & Merino 2013).

Some conditions may make the ECG diagnosis difficult: a) scarred atria with low areas of voltage could mimic isoelectric baseline despite atrial continuous electrical activity; b) concomitant circuits could also change the typical atrial appearance; and c) both high and irregular ventricular rate responses may make the diagnosis difficult (Doiny & Merino 2013).



**Figure 2.18: Standard 12 leads of common atrial flutter**  
(Doiny & Merino 2013).

### 2.3.2. Focal atrial tachycardia (FAT)

This kind of supraventricular disorders is characterized by an atrial activation starting rhythmically at a small focus from which it spreads centrifugally, not requiring the atrioventricular node (AVN) and the ventricle either to remain active (Chen et al. 1994; Almendral & Huerta 2001). Common sites of these foci are CT and PVs (Tang et al. 1995; Kalman et al. 1998; Saoudi et al. 2001). This arrhythmia usually has a cycle length higher than 250ms but it can also be lower than 200ms.

Two main mechanisms can lead to a FAT: automaticity or triggered activity. The enhanced automaticity of the pacemaker cells increase the rate of AP discharge and then the heart rate (Saoudi et al. 2001). Triggered activity results from the premature activation of cardiac tissues by early (January et al. 1991) or delayed (Cranefield 1977) afterdepolarizations. This classification can also lead to just one identifiable P-wave morphology (unifocal tachycardia) or to give rise to different morphologies during a single registry (multifocal tachycardia). In any case, the pseudo P-wave morphologies depicted by FATs are quite different from the physiological sinus P-wave in terms of amplitude, polarity and axis as can be seen in Figure 2.19 (Lee & Fynn 2015).

FAT does not occur randomly and tends to cluster around certain anatomic regions. Common sites of origin in the RA include CT, TV, ostium of CS, perinodal region, and more rarely the RAA. On the other hand, left sided FAT normally occurs in the PVs, MV and more rarely the LAA (Lee & Fynn 2015).

Although FATs are not a life-threatening illness, its importance lies particularly on the morbidity. A study carried out by (Orejarena et al. 1998) defined a prevalence between 1 and 3 in every 1000 individuals, with an incidence of 35 in every 100000 individuals per year. Therefore, they are not frequent, representing around 10-15% of the overall patients seen by a cardiac arrhythmia and electrophysiology unit.

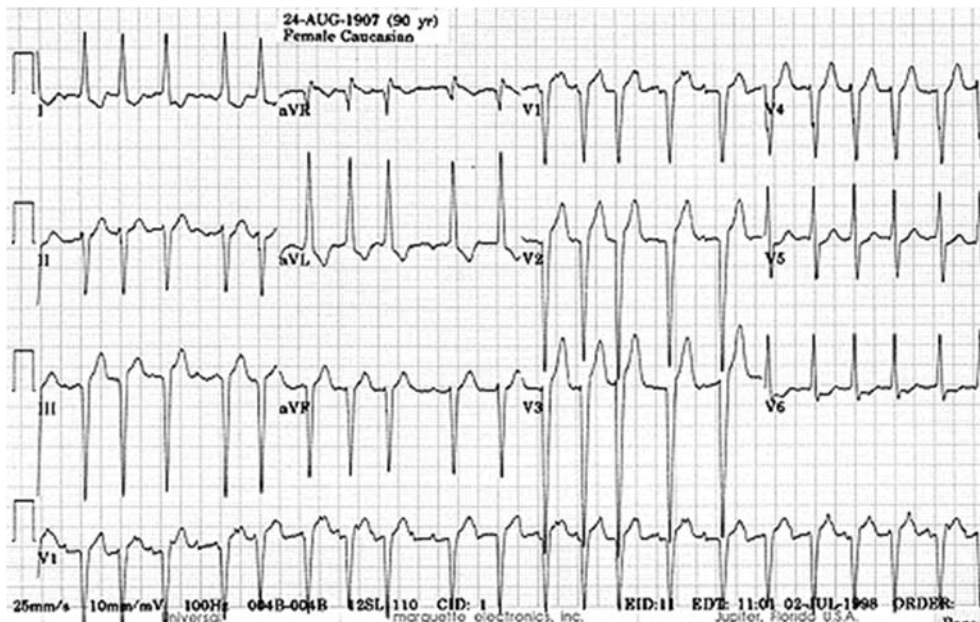


**Figure 2.19: Standard 12 leads of multifocal atrial tachycardia**  
(Yanowitz 2012).

### **2.3.3. Atrial fibrillation (AF)**

Atrial fibrillation consists on a rapid electrical activity behaving chaotically and de-synchronously and unable to effectively contract the atria. AF can be sustained by mechanisms including rapid ectopic activity (usually generated in PVs), reentrant circuits and structural and/or focal changes (Jalife 2003; Haïssaguerre et al. 2009; Sanchez 2014). Under AF, disorganized electrical waves with cycle lengths usually less than 200 ms cause both atria to contract irregularly and at rates higher than 300 bpm and usually of 400 to 600 bpm (Waktare 2002; Goel et al. 2013).

Different approaches have been used regarding the electrical mechanisms of this chaotic activity. On one side, (Moe 1962) suggested the presence of multiple reentrant fragmented waves which spread throughout the excitable atrial tissue blocking a normal propagation of the wavefront. The focal hypothesis was firstly used by (Haïssaguerre et al. 2009) who suggested that AF is maintained by a continuous trigger of very high frequency foci mainly placed in or around the PVs. More recently, the rotor hypothesis by (Jalife 2003) began to gain strength. This approach is based on the belief that AF is triggered by a burst of ectopic beats originated in the pulmonary veins whose wavefronts fragment in the surrounding tissue generating rotating vortices. One of the vortices becomes stable triggering a functional reentry or rotor that acts as the main driver of the chaotic behaviour.

The diagnosis of AF requires the analysis of the irregular RR intervals and no discernible distinct P waves as those shown in Figure 2.20. Based on the presentation, duration, and spontaneous termination of AF episodes in the ECG, five types of AF are traditionally distinguished: first diagnosed episode of AF regardless of duration or presence or absence of symptoms, paroxysmal (2 or more episodes of AF that spontaneously terminate within 7 days), persistent and long-standing persistent (episode lasting longer than paroxysmal AF but not more than 1 year), and permanent AF (episode lasting beyond 1 year) (Goel et al. 2013).

The Framingham Heart Study (Kannel et al. 1982; Onundarson et al. 1987) unveiled that the incidence of this cardiac disorder in population over 22 years of age was about 2% being age a risk factor. On the other hand, the Task Force for the management of atrial fibrillation of the European Society of Cardiology (Kirchhof et al. 2016) published estimates that suggest an AF prevalence of approximately 3% in adults aged 20 years or older. This figure even increases up to 5% in people over 65 years (Furberg et al. 1994; Harada et al. 1996). In 2010, the estimated numbers of men and women with AF worldwide were 20.9 million and 12.6 million, respectively, with higher incidence and prevalence rates in developed countries. By 2030, 14–17 million of AF patients are anticipated in the European Union, with between 120000 and 215000 newly diagnosed patients per year (Krijthe et al. 2013; Zoni-Berisso et al. 2014).

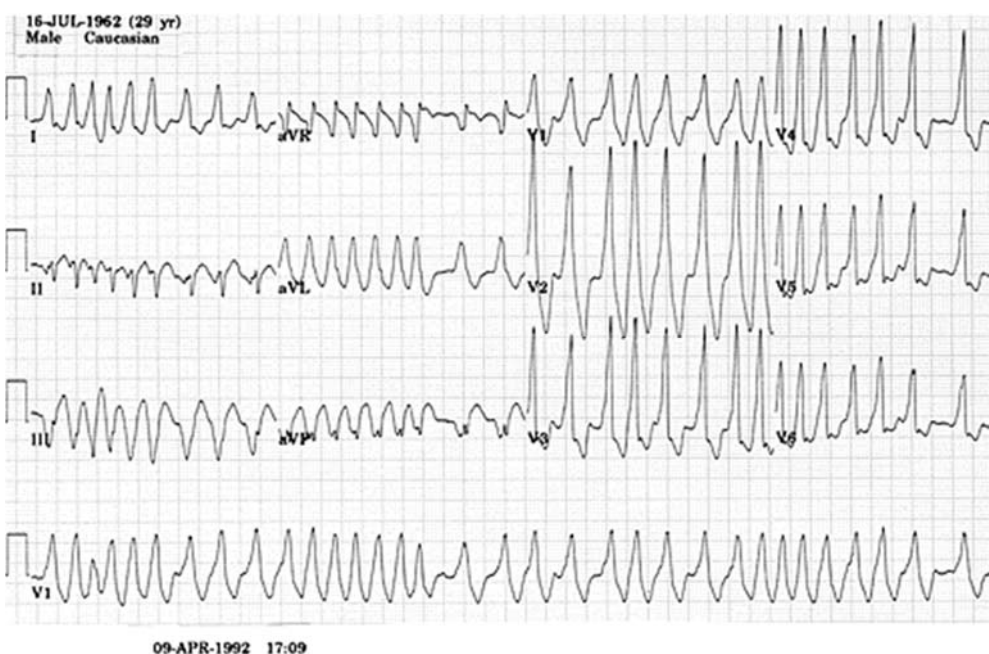


**Figure 2.20: Standard 12 leads of atrial fibrillation**  
(Yanowitz 2012).

## 2.4. Clinical management of atrial arrhythmias

The management of arrhythmias has changed significantly over the past decades (Hebbar & Hueston 2002; Hall & Todd 2006; Liew 2013; Goel et al. 2013; Almendral et al. 2014; Andrade et al. 2014; Nattel et al. 2014; Zipes 2014; Kirchhof et al. 2016). The main strategies include control of sinus rhythm or ventricular rate, antiarrhythmic drugs, imaging or catheter ablation among others.

Flutter ablation should be considered the first therapy for patients with troublesome symptoms, for those in whom ventricular rate control with drugs is suboptimal, and in those with left ventricular dysfunction because of persistent tachycardia. Long term success rates in prevention of recurrent atrial flutter are about 80% and 90% with a major complication rate of less than 0.5% (Hall & Todd 2006). However, the principal weakness of flutter ablation is the subsequent onset of AF (Hall & Todd 2006; Goel et al. 2013).

In the management of multifocal atrial tachycardia, the treatment of the underlying condition, eliminating stimuli such as hypoxia, acidosis, electrolyte disturbances, and hyperadrenergic state, is the most common therapy. However, rhythm conversion to sinus is almost never effective without treating the underlying disease state, and antiarrhythmic

agents are notoriously ineffective in multifocal tachycardia (Blomstrom-Lundqvist 2003). Slowing down the rate using AVN blocking agents may be more successful and nondihydropyridine calcium channel blockers are usually recommended as the drug of first choice for rate control (Goel et al. 2013).

When manage patients with AF, the major goals of treatment are symptom control, prevention of thromboembolic events, and tachycardia-induced cardiomyopathy and the two major strategies of management are rate control or rhythm control (Goel et al. 2013; Kirchhof et al. 2016). Rate control strategy ignores the patient's atrial rhythm but slowing down the ventricular response rate by means of drugs or AVN ablation via catheter ablation. The rhythm control strategy attempts to regulate the atrial rhythm by the use of antiarrhythmic agents or catheter ablation of atrial tissue to eliminate or isolate the arrhythmogenic foci. Hemodynamically stable patients with AF for more than two days or for an unknown period should be assessed for the presence of atrial thrombi. If thrombi are detected, anticoagulation with warfarin is recommended before electrical cardioversion is attempted. Patients with other supraventricular arrhythmias may be treated with  $\beta$ -blockers to disrupt reentrant pathways (Hebbar & Hueston 2002). Furthermore, the introduction of novel oral anticoagulants has provided clinicians with alternative options in managing patients with AF at moderate to high thromboembolic risk (Liew 2013).

The use of antiarrhythmic agents (such as flecainide, propafenone, amiodarone, sotalol, dronedarone) can be helpful in certain patients, but in general, their use is marked by lack or modest efficacy and poor side effect profile (Zipes 2014). Patients who are highly symptomatic from the arrhythmia rather than their heart rate or those in whom heart rate is difficult to control with AV node blocking agents, are best suited to these agents, although they may be proarrhythmic (Goel et al. 2013). In fact, the efficacy of these agents in maintaining sinus rhythm is approximately 50% to 60% at the end of the first year (AFFIRM 2002). The drug-related side effects include death (0.5%), torsades de pointes (0.7%), neuropathy (5.0%), and thyroid dysfunction in 3.3% (Calkins et al. 2009).

When initial medications are ineffective, catheter ablation of ectopic sites is the treatment option (Hebbar & Hueston 2002). Since the description of successful treatment of atrial arrhythmias by catheter ablation, techniques have evolved considerably. Catheter ablation attempts to isolate or eliminate the ectopic foci by the application of radiofrequency energy (radiofrequency ablation) or freezing (cryoablation) to destroy the atrial tissue (Goel et al. 2013; Andrade et al. 2014). The two principal techniques are PV isolation (Shah et al. 2000; Shah et al. 2002) and the left atrial circumferential ablation technique (Pappone et al. 2001). Results reported cure rates of up to 90% for patients with paroxysmal AF and slightly lower for patients with persistent AF, although rates in clinical practice were lower. Complication rates are also higher and an overall risk of significant complications of 6% arises including a 1% to 2% risk of cardiac tamponade and a 1.3% risk of PV stenosis (Cappato et al. 2005).

A major innovation in the practice of cardiac electrophysiology is due to the development of intra-procedural imaging techniques. They use multipolar diagnostic catheters

to simultaneous record and stimulate wider areas of activation easing the understanding and localization of arrhythmia circuits. However, it was the development of electroanatomical mapping (EAM) for the simultaneous recording of spatial information and electrical activity from electrodes placed on a catheter with cardiac imaging that have spurred the greatest advances (Andrade et al. 2014).

Recent developments in computational biology and bioengineering have also opened up exciting new possibilities in arrhythmia evaluation. The so-called ECG imaging uses a multitude of surface ECG recordings from leads embedded in a jacket to produce non-invasive 3-dimensional mapping. This technique tries to determine the arrhythmia mechanisms, the localization of ablation targets and guide therapeutic intervention (Rudy 2010). A related method uses invasive intracardiac basket mapping and mathematical algorithms to identify focal sources and reentrant rotors that underlie arrhythmogenesis (Martínez-Mateu et al. 2017).

The last model-based approaches (Nattel et al. 2014; Giffard-Roisin et al. 2016; Reich et al. 2016) may allow the understanding of the function of the heart in health and disease and the use of computational modelling and processing and machine learning techniques to diagnose these atrial arrhythmias non-invasively and to guide and personalize interventions. In this regard, (Laurent et al. 2010; Trayanova & Chang 2015) recognized that with the use of an atrial model, a better understanding of the degree of local capture by pacing could be achieved, which might have important implications for the development of pacing algorithms for atrial arrhythmia termination.

# CHAPTER 3

---

## Justification and objectives

*This chapter sets out the justification and the main hypothesis and aim for the present PhD thesis and describes the specific objectives defined to answer a set of clinical and technological questions related to atrial electrophysiology.*

### 3.1. Justification

Previous sections have been devoted to analyse the clinical and technological state of the art in the diagnosis and management of atrial arrhythmias. Bearing in mind the scientific background, the fundamentals that justify the objectives of the present PhD thesis are the following:

- a) The incidence and prevalence of atrial arrhythmias are very high, becoming one of the most important public health issues. Only considering common flutter, focal tachycardia and fibrillation, the number of new cases considering a population of 100000 persons/year reaches 88, 35 and between 21 and 41, respectively. On the other hand, the prevalence is currently increasing due to the greater ability to treat chronic cardiac disorders. In this sense, by 2030 between 14 and 17 million of AF patients are expected only in the European Union.
- b) Although these cardiac disorders are not life-threatening illnesses, the related comorbidities influence the most on both, the patients' quality of life and the rising of the health care expenditure in western countries. Currently, atrial flutter and AF hold together the highest risk for thromboembolic events while AF by itself remains one of the major causes of stroke, heart failure, sudden death, and cardiovascular morbidity in the world.
- c) ECG is still the gold standard in the diagnosis of atrial arrhythmias. However, some inherent conditions may make the diagnosis based on the ECG difficult. This may be due to the low amplitude of the atrial signals registered on the torso surface in comparison with the ventricular contribution and to the isoelectric or biphasic morphology in many torso leads. Aiming at overcoming such difficulties, new diagnosis techniques have raised, such as the electroanatomical mapping (invasive for the patient), the ECGi (very computationally expensive) or the BSPM (non-invasive but still not standardized in its use).

- d) The gold standard treatment of these cardiac disorders is based on the administration of antiarrhythmic drugs or on catheter ablation. Drugs are marked by lack or modest efficacy and poor side effect profile, while the invasive ablation procedures present an overall risk of significant recurrence rates and complications such as cardiac tamponade or pulmonary veins stenosis.
- e) The use of realistic multiscale human atrial-torso models together with the most advanced computational and signal processing techniques may allow simulating and understanding the cardiac electrical behaviour in health and disease. These models and simulations may help to shed some light on complex clinical questions, tackle the main clinical and technological shortcomings non-invasively and give shape to the concepts of *in-silico* medicine, digital patient and virtual physiological human.
- f) Clinical MRI scans may allow building patient-specific 3D geometric meshes. Human cell patch-clamp-based measurements on different atrial regions may allow personalizing the atrial APs. In the end, new data gathered from different scales may feed atrial models to help in its personalization and then in their use in the clinical domain.
- g) Computer simulations of the human heart are currently helping to improve the management of arrhythmias in several domains: anti-arrhythmia pacing for AF termination, drug cardiotoxicity effects beyond the single cell for pharmacological therapy, defibrillation threshold for implantable cardioverter defibrillator, ablation target prediction or arrhythmia risk prediction using new biomarkers.

## 3.2. Objectives

### 3.2.1. Main hypothesis

Multiscale atrial models may help to predict the electrical behaviour of the atria provided that they include the required anatomical and electrophysiological detail. Considering this premise, *our atrial-torso model can be used to non-invasively diagnose physiological and pathological atrial contributions and rhythms*.

### 3.2.2. General objective

Some clinical issues do remain currently unsolved though. How the different atrial regions effectively contribute to the genesis of the P-wave or how to effectively localize the atrial ectopic triggers to guide the ablation procedures non-invasively are questions that require further investigation.

The general objective of the present PhD thesis is *the creation and validation of a realistic three-dimensional multiscale human atrial-torso model, and the use of this model*

*to study the electrical sources at atrial scale, responsible for the potential distribution on the torso surface under physiological and arrhythmic conditions.*

### **3.2.3. Specific objectives**

The general objective is broken down into several specific objectives from the cellular level to the analysis of the potential distribution on the torso surface. More precisely, the specific objectives are the following:

- a) Modelling of the electrical differences in cellular and tissue properties across the atria to obtain characteristic atrial action potentials with realistic morphology in each atrial region.
- b) Modelling of the anatomical and histological properties at atrial scale to obtain a realistic activation/repolarization sequence.
- c) Modelling of the anatomical and electrical properties across the torso to realistically propagate the physiological and arrhythmic atrial activity and to be able to measure the ECG on the torso surface as well as the body surface distribution of the electrical activity.
- d) Understanding the contribution from specific atrial regions to the physiological P-waves as well as their local influence on the body surface potential maps and BSPM-derived biomarkers.
- e) Development of a pipeline to non-invasively localize atrial ectopic beats by defining new BSPM-derived biomarkers and using machine-learning techniques.



# CHAPTER 4

---

## Multiscale 3D model of the human atria

*This chapter describes the multiscale atrial model and the mathematical approach developed to model and simulate the physiological electrical propagation from the cell to the organ scale. A deep analysis of the existing human atrial models, at cellular, tissue and organ scales, will allow building and validating the new atrial model as the main outcome of this chapter.*

*The content of this chapter has been partially published in:*

**A. Ferrer, R. Sebastián, D. Sánchez-Quintana, J. F. Rodríguez, E. J. Godoy, L. Martínez, and J. Saiz,** “Detailed anatomical and electrophysiological models of human atria and torso for the simulation of atrial activation,” *PLoS One*, vol. 10, no. 11, p. e0141573, Jan. 2015

### 4.1. Existing human atrial models

A large number of biological processes takes place naturally at different scales. In the field of cardiac electrophysiology, cell, tissue and organ scales can be easily differentiated (Zhang et al. 2016). At the cellular scale, the ion exchange through the cell membrane is the process responsible for the generation of action potentials. At the same time, the anatomical and electrophysiological connection between different cells facilitates the spread of these APs through the myocardium allowing the contraction (systole) and relaxation (diastole) of the heart. From a macroscopic perspective, the heart could be considered as a sole source of potential capable of generating sufficient intensity signals to be recorded on the torso surface.

These three scales are, in reality, a simplified representation of the natural behaviour of the myocyte, the myocardium tissue and the atria. Therefore, they can be modelled to facilitate the understanding of the biological processes individually and as a whole interconnected organ. This type of analysis is well known as multiscale modelling (Figure 4.1). However, a multiscale model can only be considered as an acceptable representation of reality if it responds to a series of well-defined theoretical questions (Fish 2009)

such as the information that must be transferred between scales and the principles that must be fulfilled during the transfer process. Only giving answers to those questions, it will be possible to build up multiscale models able to reproduce cardiac electrophysiological behaviour and understand the process of electrical propagation from the myocyte to the torso surface.

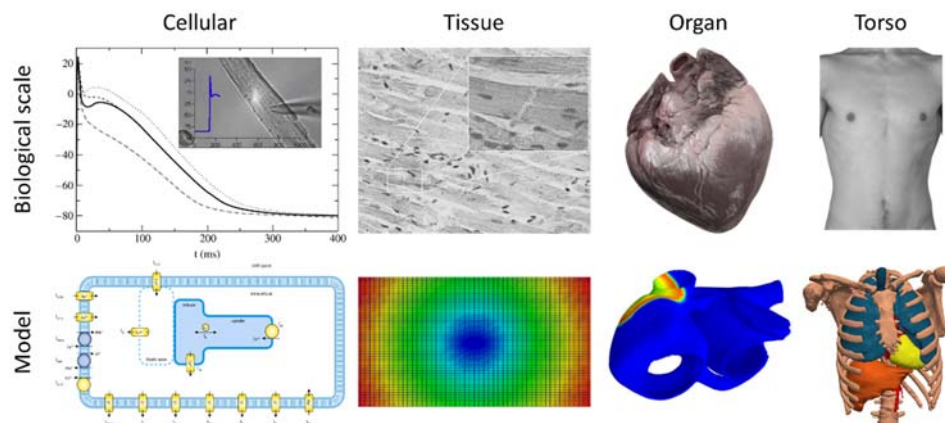


**Figure 4.1: Multiscale cardiac model**

#### 4.1.1. Models of atrial myocytes

The first model of cardiac action potential was developed more than 50 years ago (Noble 1960) and was based on previous studies (Hodgkin & Huxley 1952). Authors considered the cell membrane as a set of ion channels, i.e., proteins embedded with a small gate in its central region. This gate allowed or blocked the different ions going through depending on factors as the membrane potential, the time, the pH, the concentration of certain ions or the presence of specific drug molecules. When the channel was open, the ions of  $\text{Na}^+$ ,  $\text{K}^+$  or  $\text{Ca}^{2+}$  could go through the membrane pushed forward by diffusion forces (concentration gradients from both sides of the cell membrane) or by electric field.

Considering that the cell membrane divides the intracellular and the extracellular domains and that there are ionic carriers on both sides with the same capacity to cross over it, the membrane may be modelled with an equivalent electric circuit as the one shown in Figure 4.2.

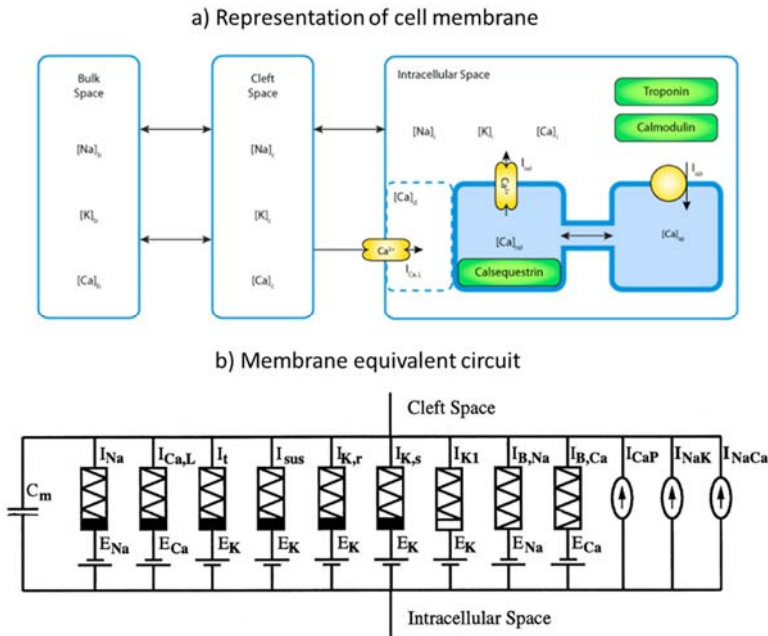


**Figure 4.2: Schematic representation of the mathematical human atrial cell model**

a) Fluid compartment model, including intracellular, cleft, and extracellular spaces; b) Electrical equivalent circuit (Nygren et al. 1998).

In this circuit,  $C_m$  is the capacity of the cell membrane with an approximate value of  $1\mu F/cm^2$ ,  $I_j$  represents the value of electrical conductance associated with different ions  $j$  (sodium, potassium, calcium, etc.) and  $E_j$  is the rest electrochemical potential or equilibrium for each ion  $j$ . This potential is defined by the Nerst equation:

$$E_j = \frac{RT}{zF} \cdot \ln \left( \frac{[C]_{ej}}{[C]_{ij}} \right) \quad \text{Equation 4.1}$$

where  $[C]_{ij}$  and  $[C]_{ej}$  are the concentration of the ion  $j$  in the intracellular and extracellular spaces respectively,  $R$  is the constant of gases ( $8.3144 \text{ J / mol K}$ ),  $T$  is the absolute temperature in Kelvin degrees,  $z$  is the amount of moles of electrons that participate in the reaction and  $F$  is the constant of Faraday ( $96500 \text{ C / mol}$ ). The membrane potential can then be calculated using Equation 4.2:

$$\frac{dV_m}{dt} = -\frac{1}{C_m} \cdot I_{ion} \quad \text{Equation 4.2}$$

where  $C_m$  is the capacity of the cell membrane and  $I_{ion}$  is the total amount of currents going through the membrane.

On the other hand, the current flowing across each channel can be represented by:

$$I_j = g_j \cdot (V_m - E_j) \quad \text{Equation 4.3}$$

in a way that:

$$I_{ion} = \sum_{j=1}^n g_j \cdot (V_m - E_j) + (I_P + I_E + I_B) \quad \text{Equation 4.4}$$

where  $V_m$  is the membrane potential,  $E_j$  is the equilibrium potential of the channel associated to the ion  $j$ ,  $g_j$  is the time-dependent value of conductance,  $I_P$  refers to the pumps (such as the  $\text{Ca}^{2+}$  and  $\text{Na}^+ \text{-K}^+$  pumps),  $I_E$  refers to the exchangers (such as the  $\text{Na}^+ \text{-Ca}^{2+}$  exchanger) both type of currents responsible for maintaining intracellular ion concentrations, and  $I_B$  refers to the background (leakage) currents (such as the  $\text{Na}^+$  and  $\text{Ca}^{2+}$  background currents). According to the Hodgkin and Huxley theory, the value of conductance  $g_j$  is given by the following equation:

$$g_j(t) = \theta_j \cdot \gamma_j \cdot f_j(t) \quad \text{Equation 4.5}$$

where  $\theta_j$  is the channel density related to ion  $j$ ,  $\gamma_j$  is the unitary conductance of these ion  $j$  channels and  $f_j(t)$  is the fraction of open channels at a given moment. Even though  $\theta_j$  and  $\gamma_j$  are specific to the types of cell and ion channel, the fraction of open channels  $f_j(t)$  depends on other factors such as voltage, concentration of intra and extracellular ion  $j$  or substances that can enhance or inhibit the behaviour of the channel. If the number of channels of the ion  $j$  is high, the fraction of open channels will be equal to the probability that just such a channel is open.

It is possible now to describe the mathematical equations that model the behaviour of any ion channel. To this end, it is necessary to introduce the concept of gate. Figure 4.3 schematically depicts how the gates already run:

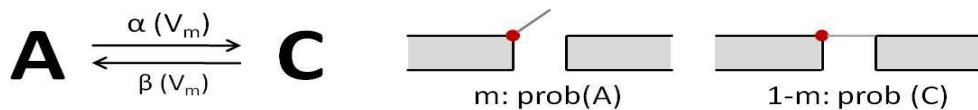


**Figure 4.3: Schematic representation of a gate**  
(Hodgkin & Huxley 1952).

According to the Hodgkin and Huxley's theory, each ion channel has a series of gates that open and close modulating the current passing through the channel. If the channel is completely open (open gate, A), then  $f_j(t) = 1$  and consequently  $g_j(t)$  is maximum. However, if the channel is closed (closed gate, C),  $f_j(t) = 0$  and  $g_j(t) = 0$  indicating that the ion channel does not allow the ions crossing.

This model also defines the rates of opening ( $\alpha$ ) and closing ( $\beta$ ) of the channel, what allows formulating the probability of opening the channel as:

$$\frac{dm}{dt} = \alpha \cdot (1 - m) - \beta \cdot m = \frac{m_\infty(V_m) - m(t)}{\tau_m(V_m)} \quad \text{Equation 4.6}$$

where  $m$  is the probability of opening the channel,  $m_\infty(V_m)$  is the stationary value corresponding to the probability of opening the channel for a given membrane potential and  $\tau_m(V_m)$  is the time constant of the channel activation. Using appropriate adjustment methods, expressions can be obtained for  $m_\infty(V_m)$  and  $\tau_m(V_m)$ :

$$m_\infty = \frac{\alpha(V_m)}{\alpha(V_m) + \beta(V_m)} \quad \text{Equation 4.7}$$

$$\tau_m = \frac{1}{\alpha(V_m) + \beta(V_m)} \quad \text{Equation 4.8}$$

A channel can have more than one gate of the same type, or gates of different types. The gate is called activation if it is opened while the membrane potential increases. However, if the gate tends to close when the potential increases, it is called inactivation.

Nevertheless, another approach, different from the one defined by Hodgkin and Huxley, has been gaining the attention from researchers over the past two decades. Advances in molecular biology have widened the knowledge on the structure and function of membrane ion channels (Carbonell-Pascual et al. 2016). Genetic mutations, for instance, can produce structural changes in the channels that modify their kinetic properties (Keating & Sanguinetti 1996; Sanguinetti & Tristani-Firouzi 2006; Tomaselli et al. 1995; Wilde & Brugada 2011). In order to introduce the effect of mutations in the models, Clancy and

Rudy abandoned the Hodgkin and Huxley formulation and adopted a new paradigm based on Markov chains (Clancy & Rudy 1999). In this newer approach, the authors used Markov model transitions to represent the voltage- and time-dependent state transitions of individual ion channels. The macroscopic channel conductance was then expressed as a function of the occupation of the open state. From this point of view, Markov models are versatile and powerful to reproduce the behaviour of ionic currents when genetic mutations are present. In fact, they have been used since then to describe non-mutant ion channels (Irvine et al. 1999; Clancy & Rudy 2001; Clancy & Rudy 2002; Silva & Rudy 2005) as well as drug effects (Romero et al. 2009; Zygmunt et al. 2011).

However, the adoption of a Markov formulation adds complexity in terms of parameter estimation. Usually, data from patch-clamp experiments used to formulate these mathematical models are noisy and difficult to analyse, something that makes the parameter fitting harder in this models compared to Hodgkin and Huxley. Although knowledge on the structure of the protein can help to choose an appropriate set of Markov model states, problems inherent to parameter estimation makes it almost impossible to determine which is the best structure of the Markov chain to define the ionic current formulation (Fink & Noble 2009).

The proof of concept to compare both mathematical formulations was carried out within our research group (Carbonell-Pascual et al. 2016). We presented a proof of concept of the validity of Hodgkin and Huxley formulation-based models of ionic currents to replicate the simulation results obtained with the more complex but computationally more demanding Markov model formulations in both wild-type and mutated cells. Both the static and dynamic properties of the APs were significantly unchanged when replacing a Markov formulation by a homologous Hodgkin and Huxley model. While the advantages of Markov models were no questioned, our results could lead to significantly reduced computational times when simulating multiscale 3D cardiac models and this was the main reason to use the Hodgkin and Huxley formulation in the present work.

From the first formulation of the (Hodgkin & Huxley 1952) model and the onset of the voltage clamp (Cole et al. 1991) and patch clamp (Hamill et al. 1981) techniques to experimentally measure the currents that cross the membrane, several cell models have been developed mainly focused on animal ventricles. The first model was published by (Beeler & Reuter 1977) and included the intracellular calcium dynamics in the calculation of the AP. Later on, (Luo & Rudy 1994a; Luo & Rudy 1994b) used experimental records to develop a model of pig myocyte. Afterwards, (Jafri et al. 1998) replaced the conventional calcium channel by calcium channel type L and a ryanodine receptor. Regarding this channel, (Williams et al. 2010) added a new type of model based on probabilistic Markov states (Fink & Noble 2009).

Among the human cell models, the ventricular myocytes are also more frequent. Among these, it can be highlighted the models proposed by (Priebe & Beuckelmann 1998; ten Tusscher et al. 2004; Iyer et al. 2004; Grandi et al. 2010).

Models of atrial myocyte have been studied since (Hilgemann & Noble 1987) developed a model of rabbit myocyte and (Earm & Noble 1990) mathematically studied its calcium dynamics. Other models were developed subsequently. Among them we can highlight the model of pacemaker for cells of frog proposed by (Rasmusson et al. 1990), the model of sinoatrial node cell developed by (Demir et al. 1994) or the model of (Lindblad et al. 1996) who proposed a model of rabbit cell membrane. The first models of human atrial myocytes were developed by (Courtemanche et al. 1998) and (Nygren et al. 1998) using experimental data. Recently, others authors have proposed new models based on theoretical or experimental studies. These models are based on potential blockers of the  $I_{Kr}$  current (Tsujimae et al. 2007), new insights into the repolarization dynamics (Malekár et al. 2009), the pathological processes related to AF (Grandi et al. 2011) or include a specific model of sarcoplasmic reticulum within the cell structure (Koivumäki et al. 2011). Several adaptations of these models include  $Na^+$  dependent regulation of  $I_{K1}$  and  $I_{K,Ach}$  (Voigt et al. 2013), the ryanodine receptor dysregulation and the SERCA2a inhibitor protein in patients with paroxysmal AF (Voigt et al. 2014) or incorporate the two-pore  $K^+$  current and its regulation in AF (Schmidt et al. 2015). The newest cardiomyocyte atrial model has been proposed by (Skibsbye et al. 2016) aiming to characterise how sodium channel inactivation affects refractoriness in human atria.

Future modelling studies related to atrial electrophysiology, arrhythmogenesis and therapeutic responses are likely to move beyond current whole-cell models by incorporating new data on sub-cellular architecture, macromolecular protein complexes, and localized ion-channel regulation by signalling pathways (Heijman et al. 2015).

#### **4.1.2. Models of atrial tissue and propagation**

The atrial cell models can be coupled anatomically and electrically for the development of tissue models as well as the whole atrial model allowing the simulation of the action potential propagation through the atrial myocardium. At tissue scale, this propagation must be defined not only in terms of the behaviour of the ionic currents with respect to the membrane potential but also in terms of how these currents flow from one cell to its neighbours. The appropriate way to conceptualize this binomial is using a reaction-diffusion model where the reactive part refers to the ionic currents, while the diffusive part defines the propagation between neighbouring cells.

Regarding the numerical methods, the first approaches based on the reaction-diffusion equation started from the premise that all the electric resistance in the tissue is due to the connection between neighbouring cells, and that the extracellular domain was a perfect conductor. Both the electrical coupling between cardiac myocytes and the conduction through the myocardial tissue could then be mathematically defined by means of a bidomain model of reaction-diffusion. Initially proposed by (Schmitt 1969), the mathematical formulation of this model began with previous works published by (Cracraft 1988; Spach et al. 1979; Geselowitz & Miller 1983; Plonsey & Barr 1987), while the

validation through experimental studies was initiated with the contributions by (Henriquez 1993).

The bidomain model considers the heart tissue composed of two domains, intracellular and extracellular, that spatially coexist. It is therefore necessary to define the ionic currents, the membrane potential and the extracellular potential (Henriquez 1993; Potse et al. 2006). The mathematical formulation of the model is based on the Ohm's law applied to the currents in the two domains, as shown by the following equations:

$$J_i = -\mathbf{M}_i \nabla V_i \quad \text{Equation 4.9}$$

$$J_e = -\mathbf{M}_e \nabla V_e \quad \text{Equation 4.10}$$

where  $J_i$  and  $J_e$  are the ionic current densities in the intra- and extracellular domains,  $\mathbf{M}_i$  and  $\mathbf{M}_e$  are the respective conductivity tensors and  $V_i$  and  $V_e$  are the potential on both sides of the membrane.

On the other hand, the cell membrane acts as a capacitor, compensating the load on both sides, so that the load accumulated at any time and at any point is zero:

$$\frac{\partial}{\partial t} (q_i + q_e) = 0 \quad \text{Equation 4.11}$$

where  $q_i$  and  $q_e$  are the charges in the intra and extracellular domains, respectively.

Since the current flow at each point must be a balance between the incoming and the outgoing current, the following expressions may be easily inferred, where the positive sign defines, by consensus, a current flowing from the intracellular to the extracellular space:

$$-\nabla \cdot J_i = \frac{\partial q_i}{\partial t} + \chi I_{ion} \quad \text{Equation 4.12}$$

$$-\nabla \cdot J_e = \frac{\partial q_e}{\partial t} - \chi I_{ion} \quad \text{Equation 4.13}$$

where  $I_{ion}$  is the current through the membrane and  $\chi$  is the area of the membrane per unit volume. From Equation 4.10 to Equation 4.13, we can deduce the equation for the current conservation, given by:

$$\nabla \cdot J_i + \nabla \cdot J_e = 0 \quad \text{Equation 4.14}$$

Replacing Equation 4.9 and Equation 4.10 in Equation 4.14, the following expression can be easily inferred:

$$\nabla \cdot (\mathbf{M}_i \nabla V_i) + \nabla \cdot (\mathbf{M}_e \nabla V_e) = 0 \quad \text{Equation 4.15}$$

The membrane potential  $V_m$  depends on both the potential difference between the intra and extracellular domains as on the membrane capacity according to the following equation:

$$V_m = \frac{q}{\chi C_m} = \frac{q_i - q_e}{2 \cdot \chi C_m} \quad \text{Equation 4.16}$$

Operating with Equation 4.11 and Equation 4.16, the following expression is deduced:

$$\chi C_m \cdot \frac{\partial V_m}{\partial t} = \frac{1}{2} \frac{\partial (q_i - q_e)}{\partial t} = \frac{\partial q_i}{\partial t} = - \frac{\partial q_e}{\partial t} \quad \text{Equation 4.17}$$

If this previous expression is replaced in Equation 4.12 and Equation 4.13 and we use the expressions given by Equation 4.9 and Equation 4.10, we arrive to the next equations:

$$\nabla \cdot (\mathbf{D}_i \nabla V_i) = \chi C_m \cdot \frac{\partial V_m}{\partial t} + I_{ion} \quad \text{Equation 4.18}$$

$$\mathbf{D}_i = \frac{\mathbf{M}_i}{\chi} \quad \text{Equation 4.19}$$

where  $\mathbf{D}$  is the diffusion vector. However, to achieve the equations that define the bidomain model as described by (Cracraft 1988), it is necessary to remove the dependency with respect  $V_i$ , and then:

$$\nabla \cdot (\mathbf{D}_i \nabla V) + \nabla \cdot (\mathbf{D}_i \nabla V_e) = C_m \cdot \frac{\partial V_m}{\partial t} + I_{ion} \text{ en } \Omega_H \quad \text{Equation 4.20}$$

$$\nabla \cdot (\mathbf{D}_i \nabla V) + \nabla \cdot ((\mathbf{D}_i + \mathbf{D}_e) \nabla V_e) = 0 \text{ en } \Omega_H \quad \text{Equation 4.21}$$

where  $\Omega_H$  represents the spatial domain occupied by the heart.

In order to solve these equations, it is necessary to define the boundary conditions assuming the heart is surrounded by a non-conductive medium. Starting from this hypothesis, the normal component of the intra- and extracellular currents must be equal to zero along the boundary,  $\partial\Omega_H$ , and then, the following boundary constrains must hold:

$$\mathbf{n} \cdot (\mathbf{D}_i \nabla V + \mathbf{D}_i \nabla V_e) = 0 \text{ en } \partial\Omega_H \quad \text{Equation 4.22}$$

$$\mathbf{n} \cdot \nabla(\mathbf{D}_e \nabla V_e) = 0 \text{ en } \partial\Omega_H \quad \text{Equation 4.23}$$

The system composed of Equation 4.20 to Equation 4.23, defines the bidomain model. Its mathematical resolution is very demanding computationally, so a series of simplifications are usually undergone limiting the problem to a unique domain (Henriquez & Papazoglou 1996). These simplifications are based on two assumptions:

- a) Variations in the extracellular potential are sufficiently small so variations in the transmembrane potential match with those in the intracellular domain.
- b) The effect that extracellular potential has on the transmembrane current is negligible, what allows to uncouple the equations of the bidomain model.

It can be therefore considered that the conductivity tensor presents equal anisotropy ratios, what means that  $\mathbf{D}_e = \lambda \cdot \mathbf{D}_i$ . Since  $\lambda$  is a scale factor,  $\mathbf{D}_e$  can be removed from Equation 4.20 and Equation 4.21 and rewritten as:

$$\nabla \cdot (\mathbf{D}_i \nabla V) + \nabla \cdot (\mathbf{D}_i \nabla V_e) = C_m \cdot \frac{\partial V}{\partial t} + I_{ion} \text{ en } \Omega_H \quad \text{Equation 4.24}$$

$$\nabla \cdot (\mathbf{D}_i \nabla V) + (1 + \lambda) \nabla \cdot (\mathbf{D}_i \nabla V_e) = 0 \text{ en } \Omega_H \quad \text{Equation 4.25}$$

Rearranging these two previous expressions and operating, the monodomain model can be defined by the following expression:

$$\nabla \cdot (\mathbf{D} \nabla V) = C_m \cdot \frac{\partial V}{\partial t} + I_{ion} \text{ in } \Omega_H \quad \text{Equation 4.26}$$

with a unique boundary condition given by:

$$\mathbf{n} \cdot \nabla(\mathbf{D} \nabla V) = 0 \text{ en } \partial\Omega_H \quad \text{Equation 4.27}$$

As can be appreciated, the numerical and computational complexity of the monodomain model is deeply lower than in the case of bidomain model. While this bidomain approach involves the resolution of a nonlinear parabolic equation coupled to an elliptic equation, the monodomain model is simpler. It can be solved by means of a parabolic partial differential equation that perfectly describes the reaction-diffusion phenomena. The reactive side comes defined by  $I_{ion}$  governed by the cellular model, while the diffusive part refers to the propagation of the action potential across the cardiac tissue.

Under this approach, the beginnings of atrial modelling were mainly focused on the development of models of uni- and bi-directional cardiac tissue with the interest of analysing the action potential propagation thought the atrial tissue. Based on this idea, and using 2D tissue models, previous studies analysed the anatomy of the pectinate muscles and its effect in the generation and maintenance of arrhythmias (Wu et al. 1998), the factors that mainly constrain the stability of the depolarization wavefront (Xie et al. 2002; Kneller et al. 2002) and the mechanisms that mainly facilitate the initiation and maintenance of re-entrant (Zhang et al. 2005; Pandit et al. 2005; Clayton & Taggart 2005).

When considering the 3D domain, continuous tissue models as the ones developed by (Vigmond et al. 2002; Vigmond et al. 2003; Plank et al. 2008; Wieser et al. 2008) integrate all the information about the distribution of gap junctions over the cell membranes as well as the fibre, sheet and other micro-structure organization in the cardiac tissue. Newer human tissue atrial models as the one developed by (Ashihara et al. 2012) and aimed at studying AF ablation have lately begun to represent fibrotic structural remodelling associated with persistent AF.

#### **4.1.3. Models of the human atrium**

Since factors such as atrial geometry, conduction velocity, anisotropy or fibre direction determine the propagation of the AP, the first anatomically realistic 3D atrial models started to emerge from year 1998, where all these data could be assimilated from clinical and histological samples.

Different approaches were used to understand and model the human atrium. On the one hand, spherical surface (generic) models such as those developed by (Gray & Jalife 1998; Vigmond et al. 2001; Blanc et al. 2001; Dokos et al. 2007) were used to study the role of specific anatomic structures on re-entry induction and maintenance as well as the mechanisms of AF. Based on a more realistic batrial structure of the human atrium, 3D surface models developed by (Virag et al. 2002; van Dam & van Oosterom 2003) allowed authors to investigate the dynamics of restitution-based AF using more realistic atrial sizes, conduction velocities and activation sequences. However, they do not incorporate complex anatomical structures, electrophysiological heterogeneity and/or fibre orientation. These properties were included, individually or in combination, in more realistic 3D volumetric human batrial models as the ones shown in Table 4.1, which is a revised updated version of the table in (Krüger 2012). The first model that considered

complex anisotropic anatomical structures and fibre directions was developed by (Harrild & Henriquez 2000). Later models such as those defined by (Seemann et al. 2006; Al Abed et al. 2010; Lu et al. 2011; Burdumy et al. 2012; Krueger et al. 2012; McDowell et al. 2012; Dongdong Deng et al. 2012) were developed emphasizing the electrophysiological heterogeneity or the fibre orientation to provide knowledge concerning the mechanisms of excitation and investigate how to model the atrial fibrosis.

However, the first atrial model which took into consideration both the anatomical and the electrophysiological properties from different atrial regions as well as the volumetric fibre direction was firstly developed in our research group by (Ruiz-Villa 2010), and validated by (Tobón 2010; Tobón et al. 2013). This model allowed evaluating the effect that different electrophysiological factors have on the wavefront propagation on atria in both sinus rhythm and arrhythmia. It also allowed simulating the efficiency that standard radiofrequency ablation procedures have on the treatment and finalization of atrial arrhythmias. Other recent models such as the one developed by (Jacquemet 2015) formulated and validated the current-dipole approach during sinus rhythm and atrial fibrillation to better understand and interpret the genesis of the P-wave and fibrillatory waves in relation to atrial anatomy. As can be seen in Table 4.1, with exception of two of these models (Al Abed et al. 2010; Gonzales et al. 2013), all the others included the models developed by (Courtemanche et al. 1998) or (Nygren et al. 1998) at the cellular scale and used the formulation of the monodomain model (Heidenreich et al. 2010) or cellular automation (Gerhardt et al. 1990) to propagate the APs through the atrial tissue scale.

**Table 4.1: Human batrial 3D multiscale models**

STUDY	SPECIES	COPARTMENTS	MESH TYPE	EPM	PROPAGATION	FIBERS	HETEROGENEITIES
Harrild et al. 2000	Human	Batrial	Hexahedral	NYG	Monodomain	Bundles	BB, CT, PM, IS, FO
Seemann et al. 2006	Visible Female	Batrial	Voxel	CRN	Monodomain	Bundles	BB, CT, PM, AVR, APG, SN
Abed et al. 2010	Visible Man	Batrial	Voxel	Generic	Monodomain	-	BB, CT, CS, APG
Lu et al. 2011	Human	4 chambers	Spheroidal	NYG	Cellular Automaton	-	BB, CT, PM, IS, FO
Burdumy et al. 2012	Human	Batrial	Voxel	CRN	Cellular Automaton	-	-
Krueger et al. 2012	Human	Batrial	Voxel	CRN	Monodomain	Volumetric	BB, CT, PM, IS, AVR, APG
McDowell et al. 2012	Human	Batrial	Tetrahedral	CRN	Monodomain	Mono Layer	-
Deng et al. 2012	Human	Batrial	Voxel	CRN	Monodomain	Volumetric	SAN, CT, PM, BB, IB, AVR
Tobon et al. 2013	Human	Batrial	Hexahedral	NYG	Monodomain	Volumetric	RA/PM, CT/BB, RAA, TV, LA, PV, LAA, MV
Gonzales et al. 2013	Human	Batrial	Cubic Hermite	n/p	Not Specified	Volumetric	-
Jacquemet V. 2015	Human	Batrial	Cubic	CRN	Monodomain	Volumetric	BB, CT, PM

## 4.2. Modelling atrial myocytes

One of the aims of the present PhD work has been to develop a new 3D atrial model that improves the previous ones (Ruiz-Villa 2010; Tobón 2010; Tobón et al. 2013).

Regional electrical differences in cellular properties across the atrium are critical characteristics for obtaining an atrial AP with realistic morphology and activation/repolarisation sequence. Since the starting point to model the human atria is the understanding

of its behaviour in realistic conditions, the cellular electrical activity was initially modelled using the Maleckar's ionic model (Maleckar et al. 2009) as an evolution of the Nygren ionic model (Nygren et al. 1998) used in (Tobón et al. 2013). The main reason is that Maleckar's model shows better long-term stability in terms of restitution properties and APD<sub>90</sub>. The stability of these dynamic properties is considered essential to develop and validate the regional physiological conditions. The AP produced by this model is characterized by a rest potential of -73mV, a maximum amplitude during depolarization phase above 40mV, and APD<sub>90</sub> of 199ms and a triangular morphology characteristic when considering atrial myocytes.

The first step before modelling the electrophysiological heterogeneity in the atrium is to stabilize the long-term behaviour of the model in physiological conditions. To do that, we performed several tests to quantify the influence of the mathematical ordinary differential equation (ODE) integrator, the length of the stimuli train (stabilization time) as well as the duration and amplitude of the stimulus. As can be seen in Figure 4.4, there were not differences in the AP simulated after a stimuli train of 10 seconds (BCL set to 1 second) when using the solver CVODE (red line) or the Forward Euler (blue line). Differences in AP when varying the stabilization time from 10 seconds to 600 seconds were negligible as depicted in Figure 4.5. However, the effect is significant when varying the duration and amplitude of the stimulus as can be seen in Figure 4.6. Indeed, while higher stimulus amplitudes produce quicker depolarization and higher amplitude in the APs, higher stimulus durations reduce both the AP amplitude and its depolarization velocity. However, the repolarization phase seems to remain unchanged.

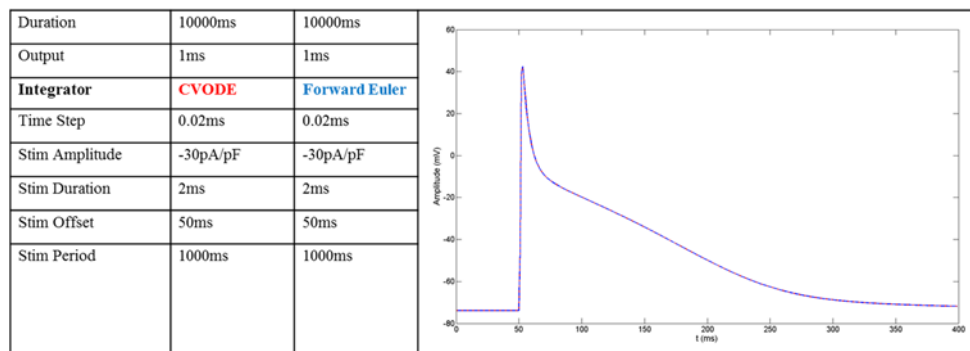


**Figure 4.4: Differences in the AP morphology when changing the ODE**  
CVODE (red line) and Forward Euler (blue line).

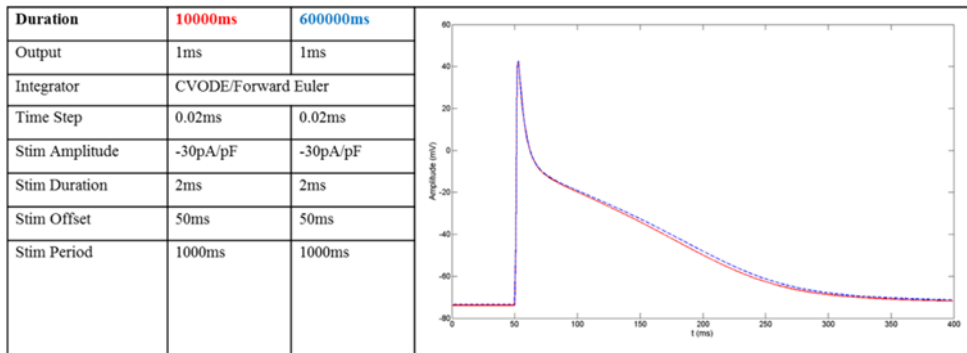


**Figure 4.5: Differences in the AP morphology when varying the stabilization time**  
10 seconds (red line) and 600 seconds (blue line).

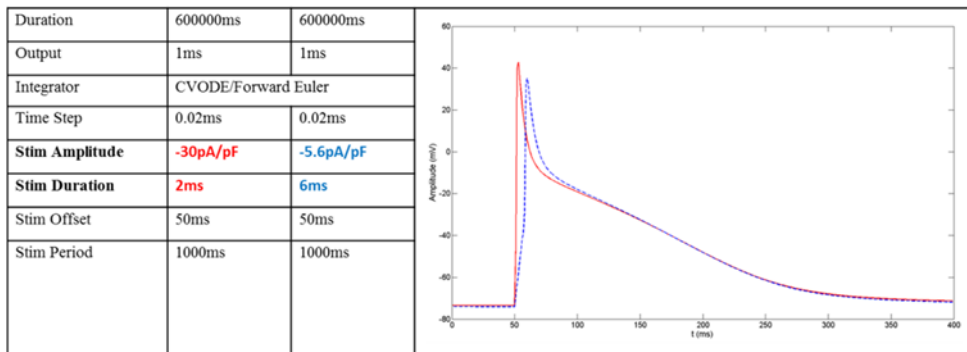


**Figure 4.6: Differences in AP morphology when varying duration and amplitude**  
-30pA/pF and 2ms (red line) and -5.6pA/pF and 6ms (blue line).

After all these tests, and considering the stabilization times defined in (Wilhelms et al. 2013) for the Maleckar's model, we applied a train of 3600 stimuli (1 ms of duration and 52 pA/pF of amplitude) at a basic cycle length (BCL) of 1000 ms. After stabilizing, an additional stimulus with the same BCL was applied to check whether intracellular concentrations of  $[Na^+]$ ,  $[K^+]$  and  $[Ca^{2+}]$  and APD<sub>90</sub> remained stable, obtaining a mean variation lower than the 2% millimolar measured instantly before the depolarization between the first and last stimulus within the last 60 stimuli.

Once the Maleckar's cellular model reached the steady state, next step allowed us to define the atrial electrophysiological heterogeneity under normal conditions. Since there exists a lack of availability of human tissue data, animal data has been used instead. Variations in AP morphology and duration between regions have been considered much more relevant than the absolute value of APD. Analysing experimental data within the

canine RA, myocytes from different regions show systematic variations in AP morphology and APD that reflect spatial variation in ionic current densities, with voltage- and time-dependent properties being constant across regions (Bartos et al. 2015). First studies were carried out by (Feng et al. 1998) who noted AP differences in isolated atrial cells from 4 regions in canine RA (CT, RAA, PM and AV rings) by using whole-cell patch-clamp technique. Authors showed main differences in three ionic currents  $I_{to}$ ,  $I_{CaL}$  and  $I_{Kr}$ . Experimental data by (Li et al. 2001) showed a shorter APD in canine LA compared with RA myocytes, which was attributed to larger  $I_{Kr}$  and resulted in a potential significance for determining the interatrial differences in basic electrophysiology. Additionally, (Cha et al. 2005) studied the ionic currents and APs in dogs finding differences between the PVs and cells at the LA free posterior wall. Considering then the differences between RA and LA, the 4 regions found in RA and the 2 regions in LA, a total of 8 different regions of both atria were finally considered, by following a similar procedure as the one described in previous computational works (Seemann et al. 2006; Tobón et al. 2013; Colman 2014). The maximum conductance of the three same ionic currents ( $I_{to}$ ,  $I_{CaL}$  and  $I_{Kr}$ ) was adjusted in tissues corresponding to RA-PM, CT-BB, RAA, TV ring, LA, PV, LAA and MV ring. This adjustment consisted in applying multiplicative factors, see Table 4.2, with respect to the default values in the Maleckar's model in order to increase or reduce the channel conductance, as previously done by (Sanchez et al. 2012). Main differences are visible in the  $APD_{90}$  produced by each model and compared with experimental values. The resulting characteristic APs are shown in Figure 4.7 for each of the eight regional cell models.

**Table 4.2: Ionic channel conductance and  $APD_{90}$  for the eight submodels**

Relative values for the ionic channel conductance in each model and the  $APD_{90}$  after stimulating the cell model during 60 minutes. Experimental values from canine and human cells are also included.

Ionic Conductance / model		RA, PM	CT, BB	RAA	TVR	LA	PV	LAA	MVR
Multiplicative factors	<b><math>g_{to}</math></b>	1.00	0.50	1.35	1.35	1.00	1.35	1.35	1.35
	<b><math>g_{CaL}</math></b>	1.00	1.00	1.00	0.80	0.67	0.67	0.67	0.53
	<b><math>g_{Kr}</math></b>	1.00	0.50	1.00	2.00	1.60	3.20	1.60	3.20
<b>Simulated <math>APD_{90}</math> (ms) BCL=1Hz</b>		<b>199.0</b>	<b>227.0</b>	<b>189.0</b>	<b>173.0</b>	<b>181.0</b>	<b>161.0</b>	<b>171.0</b>	<b>158.0</b>
Experim. APD (ms)	<b>APD<sub>95</sub></b> (Feng et al. 1998)	190.0±3	270.0±10	180.0±3	160.0±4				
	<b>APD<sub>90</sub></b> (Li et al. 2001)	170.9±4.3				152.9±4.3			
	<b>APD<sub>90</sub></b> (Cha et al. 2005)					200.0	178.0		
	<b>APD<sub>90</sub></b> (Dobrev et al. 2001)	207.0±18							

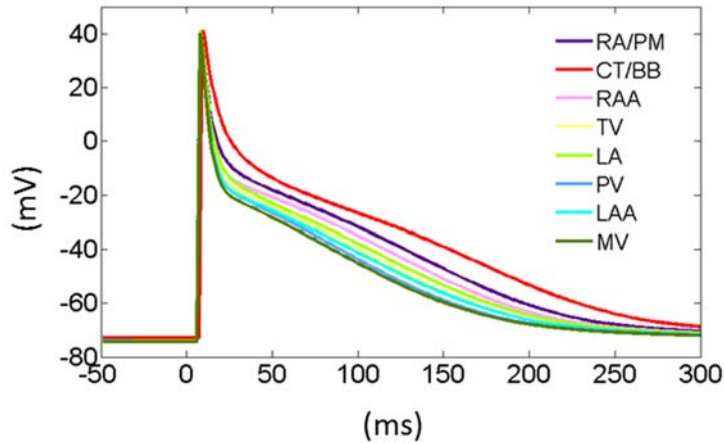


**Figure 4.7: Resulting characteristic APs produced by each subcellular model**

According to the maximum conductance of the three ion currents  $I_{to}$ ,  $I_{CaL}$  and  $I_{Kr}$ , the eight different regions correspond to RA, PM, CT, BB, TV, LA, PV, LAA and MV.

These variations between atrial regions can be easily understood in Figure 4.8 where green spheres represent regions in RA while the blue ones correspond to LA and percentage variations are highlighted.

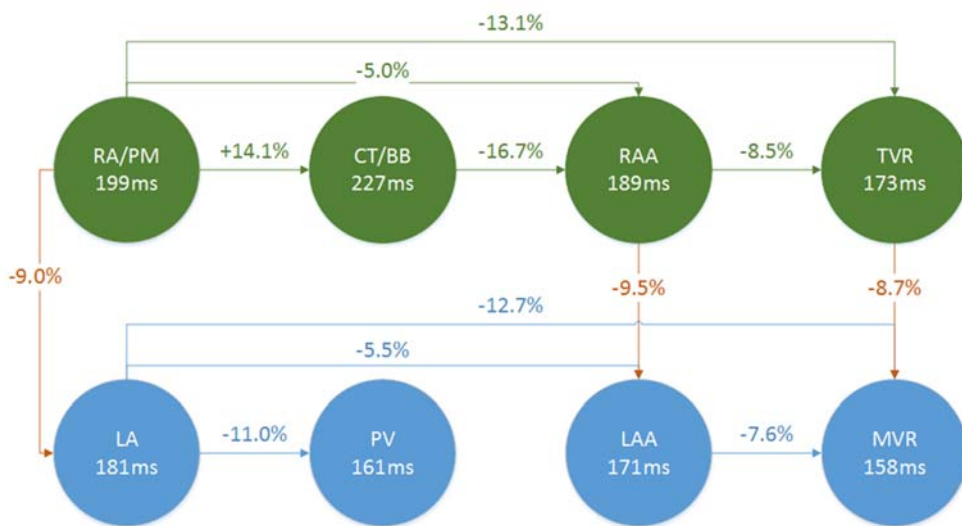


**Figure 4.8: Electrophysiological heterogeneity relative to the eight cellular submodels**  
Upper red spheres correspond to regions in RA while lower blue are relative to LA regions.

Only the model associated to the CT/BB showed some difficulties along the process to reach the steady state. The fact is that the sodium-calcium exchanger developed automatic excitability, see Figure 4.9, when increasing  $g_{CaL}$  due to an increase in the Calcium concentration. Actually, APs shown in this figure are produced when using as multiplicative factors 0.50 for  $I_{to}$ , 1.40 for  $I_{CaL}$  and 0.70 for  $I_{Kr}$ , stimulating the CT/BB model during 60 minutes and then removing the stimulus. It can be seen how the Calcium concentration keeps increasing gradually, what forces the NaCa exchanger to continue working and the overall potential threshold is rapidly overcome triggering the AP as a chain reaction.

As a consequence, this constrain prevented us to modify  $g_{CaL}$  and then forced the use of only the  $g_{to}$  and  $g_{Kr}$  to obtain the characteristic AP in both bundles (CT and BB) with the final values showed in Table 4.2.

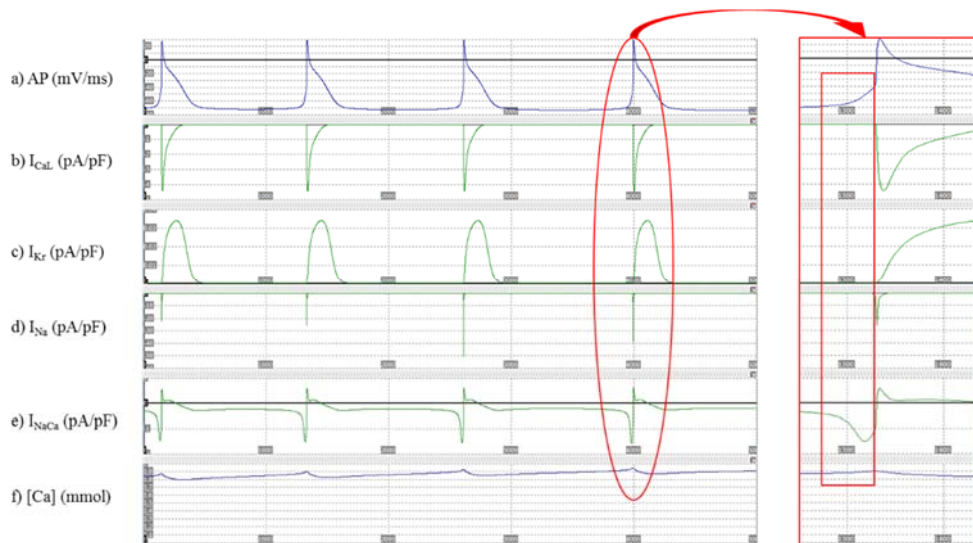


**Figure 4.9: Automatic excitability of the sodium-calcium exchanger**  
Produced when increasing  $g_{CaL}$  due to an automatic increase in the Calcium concentration.

### 4.3. Modelling atrial tissue

The atrial tissue was modelled by a 3D slab with  $50 \times 50 \times 3$  linear hexahedra with  $300 \mu\text{m}$  of spatial resolution, as can be seen in Figure 4.10. The main objective was to analyse the behaviour of the cellular models described in the previous section but at the tissue scale and characterize the conduction velocities and the activation times.

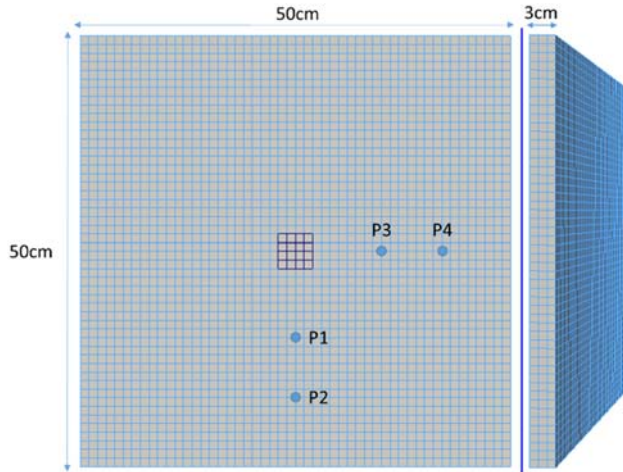


**Figure 4.10: Slab with 50x50x3 linear hexahedra with 300 µm of spatial resolution**

The conduction velocities in each atrial region were calculated by adjusting the longitudinal conductivities ( $\sigma_L$ ) and the anisotropy ratios ( $\sigma_T/\sigma_L$ ) in the slab model. The anisotropy ratio ( $\sigma_T/\sigma_L$ ) assigned to the BB, PM, CT and LFO (fast conducting structures) was considered very high (0.15), matching experimental observations with anisotropy ratios between 0.10 (Saffitz et al. 1994) and 0.21 (Spach et al. 1988). An anisotropy ratio of 0.35 was assigned to RA and LA tissue and of 0.50 to PV and CS regions (Seemann et al. 2006; Tobón et al. 2013). Finally, a ratio of 1.00 (isotropy) was assigned to IST, SAN and FO. With respect the longitudinal conductivities, the values assigned to each region are shown in Figure 4.11. Coherent with the anisotropy ratios, BB, PM, CT and LFO have the faster longitudinal conductivity values (0.0120 and 0.0088 S/cm pF). An intermediate value corresponds to CS (0.0078 S/cm pF) while lower values are assigned to PVs and Isthmus (0.0048 S/cm pF), RA and LA (0.0035 S/cm pF). The SAN is the region where the stimulus is applied and it does only need to trigger the activation of neighbouring tissue, so its conductivity is set to a very low value. Finally, FO is an isolating tissue and it has not been included in the figure since its conductivity is set to zero value.

Each atrial region was then characterized by three properties: cellular model, longitudinal conductivity and anisotropy ratio. Several simulations were then carried out to determine the tissue conduction velocity and the depolarization pattern for each region considering the following principles: Longitudinal direction: vertical; Transversal direction: horizontal; Simulation duration: 10ms; Stimulus duration and amplitude: 2ms and 100pA/pF; and conduction velocity: computed as the distance between P1 and P2 (equal to the distances from P3 to P4) divided by the time difference between the two local activation times (LATs).

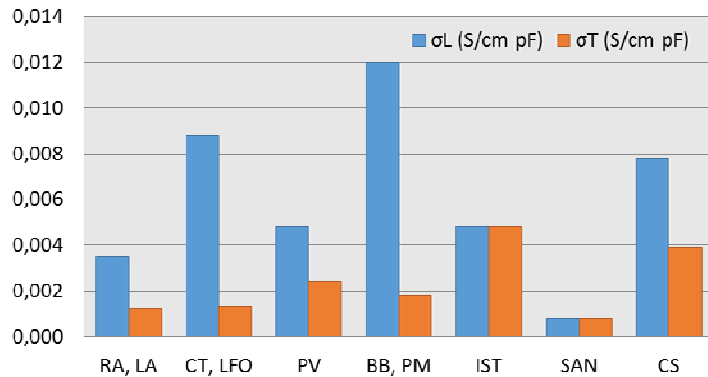


Figure 4.11: Conductivity (S/cm pF) for the eight atrial type of tissues

Figure 4.12 represents the four kind of activation patterns (LATs) computed from the simulations performed for each type of tissue. Thus, isotropic tissues like the isthmus are depolarized following the spherical propagation shown in panel a). On the other hand, lower anisotropic patterns associated to PVs and CS and tissues with intermediate anisotropy ratio corresponding to non-specific RA and LA regions depict, as can be seen in panels b) and c), higher longitudinal than transversal conduction velocity. Finally, the highest anisotropic ratios produce depolarization patterns as the one in panel d) and are associated to the preferential conduction bundles since they must quickly guide the wavefront along the RA by means of the CT and PM, and between atria through the BB and LFO.

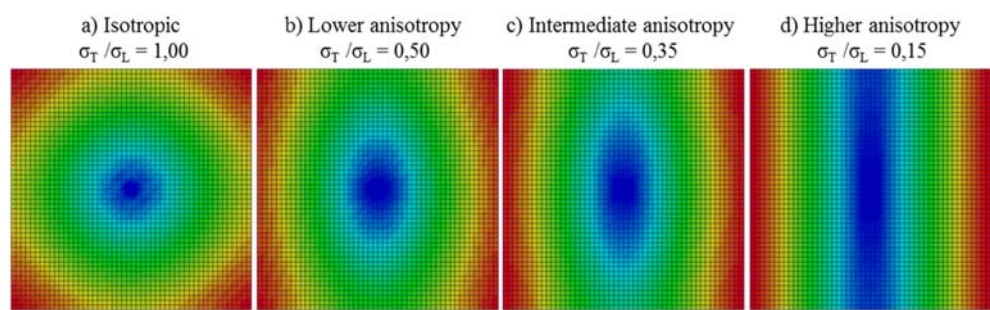


Figure 4.12: LATs computed from the simulations performed for each type of tissue.

a) isotropic tissue (isthmus); b) tissues with lower anisotropy ratio (PVs and CS); c) tissues with an intermediate value of anisotropy (RA and LA non-specific regions); d) highest values of anisotropy associated to CT, PM, BB and LFO.

Using these patterns, we were able to calculate the conduction velocities. Table 4.3 summarizes the results for each type of atrial tissue. Since the cellular model mainly modifies

the morphology of the AP during the repolarization phase, no changes in the activation patterns are visible when tissue properties are equal but cellular properties are different (as an example, cellular models corresponding to RA and RAA are different but both regions produce similar velocities at tissue scale).

**Table 4.3: Longitudinal and transversal conduction velocities for the atrial tissues**

	$\sigma L$ (S/cm pF)	$\sigma T$ (S/cm pF)	$\sigma T / \sigma L$	CVL (cm/s)	CVT (cm/s)
<b>RA, LA</b>	0,0035	0,0012	0,35	63,3	36,6
<b>CT, LFO</b>	0,0088	0,0013	0,15	99,5	38,7
<b>PV</b>	0,0048	0,0024	0,50	75,0	53,0
<b>BB, PM</b>	0,0120	0,0018	0,15	116,0	46,4
<b>IST</b>	0,0048	0,0048	1,00	76,6	76,6
<b>SAN</b>	0,0008	0,0008	1,00	27,7	27,7
<b>CS</b>	0,0078	0,0039	0,50	97,2	68,6
<b>FO</b>	0,0000	0,0000	1,00	0,0	0,0

As shown in Figure 4.13, the mean longitudinal conduction velocity varies from high values for BB, PM, CT, LFO and CS (from 99.5 to 116.0 cm/s), to intermediate values for PV and IST (from 75.0 to 76.6 cm/s) and lower values for RA and LA general tissue (63.3 cm/s). Note that these conductivity values obtained from the slab simulations must be subsequently fine-tuned in the atrial model to match atrial activation sequences and P-wave morphologies to experimental measurements (Lemery et al. 2007; Huo et al. 2014).

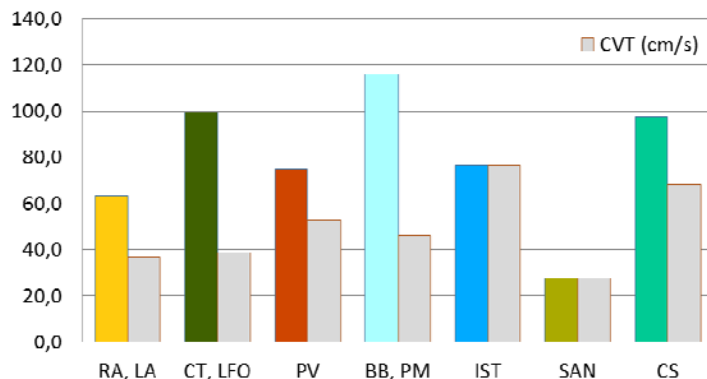


**Figure 4.13: Conduction Velocity (cm/s) associated to each type of atrial tissue**  
Coloured bars: regional longitudinal velocity; Greyish bars: regional transversal velocity (CVT)

## 4.4. Modelling the three-dimensional atria

### 4.4.1. Analysis of histological data

Atrial muscular fibre orientation has a major impact on the depolarization sequence since it defines the preferential conduction bundles across and between atria. In cardiac human models, local fibre orientation is usually mapped based on ex-vivo histological information (from an atlas human heart or by employing a rule-based approach) or on diffusion tensor image (DTI) (Trayanova & Chang 2015). Activation patterns from simulations in ventricles with the rule-based approach (Krueger et al. 2011; Dössel et al. 2012), the atlas-based approach (Vadakkumpadan et al. 2009) and DTI-derived fibre orientations are however nearly indistinguishable (Bayer et al. 2012). Unlike the ventricles, atria have a very complex geometry with a very thin wall. Recent findings carried out by (Pashakhanloo et al. 2016) who used DTI, demonstrated that the main features of atrial anatomy are mostly preserved although thickest sections could not be reliably imaged. Since the histological data still remains the gold standard, a ruled-based approached based on histology gathered over several years, is the base to define the muscular architecture in our model. In particular 30 formalin-fixed hearts from patients who died of non-cardiac causes were considered (Cabrera et al. 2008; Ho et al. 2012; Sánchez-Quintana et al. 2012; Sánchez-Quintana et al. 2013). This study was approved by the bioethical committee on human research (University of Extremadura, registration nº14/2015). The mean heart weight was  $375 \pm 25$  g. The hearts were dissected and prepared for light microscopy to perform the histological studies. Blocks of tissue encompassing various atrial regions were processed and serially sectioned at 12 or 15  $\mu\text{m}$  in sagittal or anteroposterior, frontal and transverse planes. Sections were stained at 1 mm intervals with Masson's trichrome (Cabrera et al. 2008). Photographs were taken using a stereo microscope equipped with a digital camera (Nikon SM 1500) and an image resolution of 300 pixels/inch.

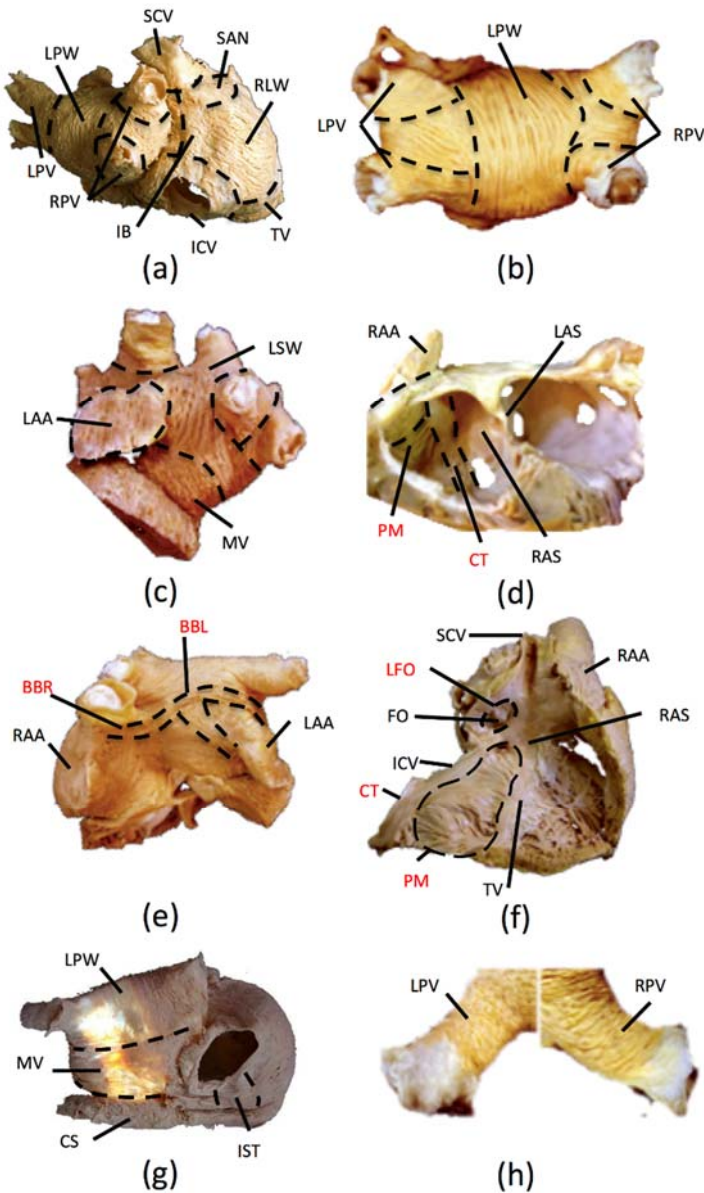


**Figure 4.14: Anatomical atrial regions and principal fibre direction**

a-h) Regions are delimited by dashed lines, displaying different atrial views with circumferential, longitudinal and oblique fibre directions. The preferential conduction axes are labelled in red colour. Panels b), c), d) and e) are adapted from (Ho et al. 2012; Sánchez-Quintana et al. 2013) under a CC BY license, with their permission, original copyright years 2012 and 2013.

The alignment of the myocardial fibres of the atria was studied by peeling away the epicardium and the endocardium to reveal the arrangement of the major muscular bundles that make up the walls of the atrial chambers. The macroscopic appearance of slender muscle bundles revealed three main orientations: circumferential, longitudinal, and oblique. Circumferential fibres were those parallel to the insertion of the tricuspid and mitral valves; longitudinal fibres were perpendicular to the circumferential fibres, and oblique fibres were at angles to both.

A total of 21 anatomical atrial regions were identified, and the principal direction of the fibres within each region was histologically analysed (Figure 4.14a-h). With the exception of views (b) and (h) which were common to 60% of the hearts studied, the fibre orientations shown in all the other views were observed in 80% of the hearts. In the RA, 12 regions were recognised: sinoatrial node (SAN), Crista Terminalis (CT), Bachmann's bundle (right part, BBR), intercaval bundle (IB), septum (RAS), lateral wall (RLW), right appendage (RAA), pectinate muscles (PM), isthmus (IST), superior (SCV) and inferior cava veins (ICV) and ring of the tricuspid valve (TV). In the LA, 8 regions were identified besides the left section of the Bachmann's bundle (BBL): superior wall (LSW), septum (LAS), left appendage (LAA), posterior wall (LPW), ring of the mitral valve (MV), right (RPV) and left pulmonary veins (LPV) and the coronary sinus (CS). In addition, the fossa ovalis (FO) and its limb (LFO), which connects the RA and the LA, were considered as one independent structure.

After defining the anatomical boundaries of the regions, the principal fibre orientation was determined by a rule-based algorithm (developed using Matlab R2015) with respect to the global coordinate system of the atria. This algorithm has four steps (see Figure 4.15). First, each region is defined by a main vector direction. Second, the cross product is computed between such vector and the normal vector to the external surface of each element belonging to that region. Third, each resulting tangent vector is projected on the external surface of the corresponding element. Finally, this unit projection is assigned to the centre of the corresponding element defining the longitudinal fibre direction.

Special emphasis was made on determining the morphology and location of the main conduction bundles. We observed three main structures: the CT, the PMs and the BB (Figure 4.14d-f, red labels). The CT runs transmural from the base of the SCV to the ICV with an average thickness of 3mm (Figure 4.14 d and f). The PMs were identified as tubular structures that run on the luminal surface, almost parallel to each other, with a thickness of 1-2 mm. A total of 15 to 34 PMs were observed to be distributed along the CT and extended towards the vestibule (Figure 4.14d), in agreement with previous studies (Hansson et al. 1998). The BB was identified as a longitudinal two-sided structure connecting both atria. Its right side (BBR) starts at the SAN and embraces the SCV towards the LA. In the left side (BBL), the BB is divided into two main axes that extend around the LAA from both sides (Figure 4.14e).

Some structures, such as the SCV, shown in Figure 4.15, and the ICV, the TV and the MV, the RPV and the LPV, and the CS showed a circumferential fibre orientation. RA

structures like the IB, the RLW and the RAA have homogeneously oriented fibres forming an approximate angle of 60° with respect to the CT, whereas RAS fibres are almost parallel to the CT. On the other hand, the IST fibres are parallel to those of the ICV and the TV. In the case of the LA, the fibres from the LAS are aligned parallel to their adjacent regions in the RAS (actually, there is only one septum with two faces separated by an isolating layer). Fibres from the LPW descend from the LSW perpendicularly to the fibres in the junction between the RPVs and the LPVs with the MV. Finally, the LAA, the most prominent structure in the LA, aligns its fibres perpendicularly to those in the LSW.

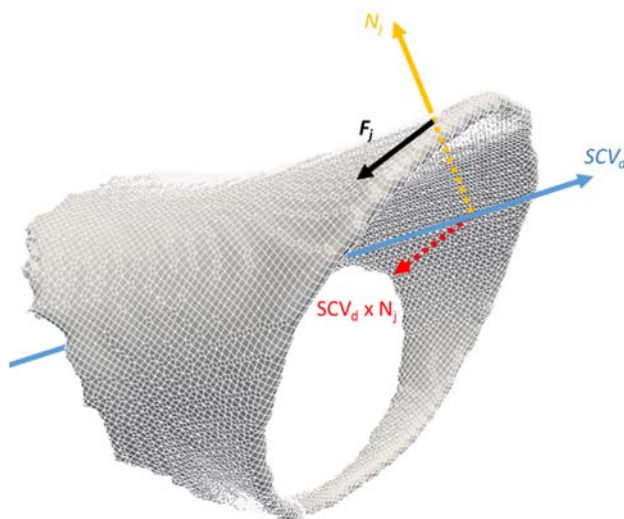
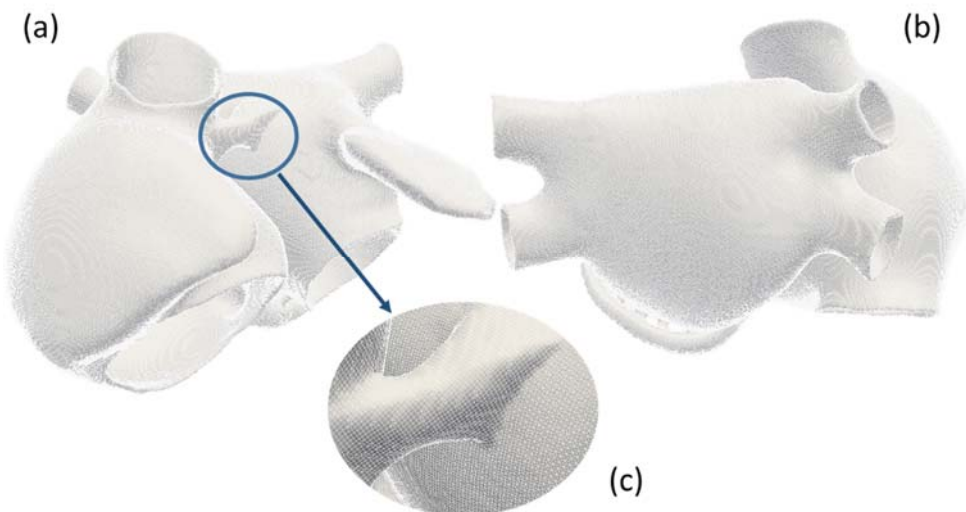


**Figure 4.15: Rule-based algorithm to assign fibre direction**

SCV<sub>d</sub> (blue line) is the main vector direction defining, as an example, the SCV region; N<sub>j</sub> (orange line) represents the normal vector associated to element j; SCV<sub>d</sub> × N<sub>j</sub> (red dotted line) is the cross product between both vectors; F<sub>j</sub> (black line) is the fibre orientation related to element j located at its centre and computed as the projection of SCV<sub>d</sub> × N<sub>j</sub> on the external surface of element j.

#### 4.4.2. Novel 3D atrial model

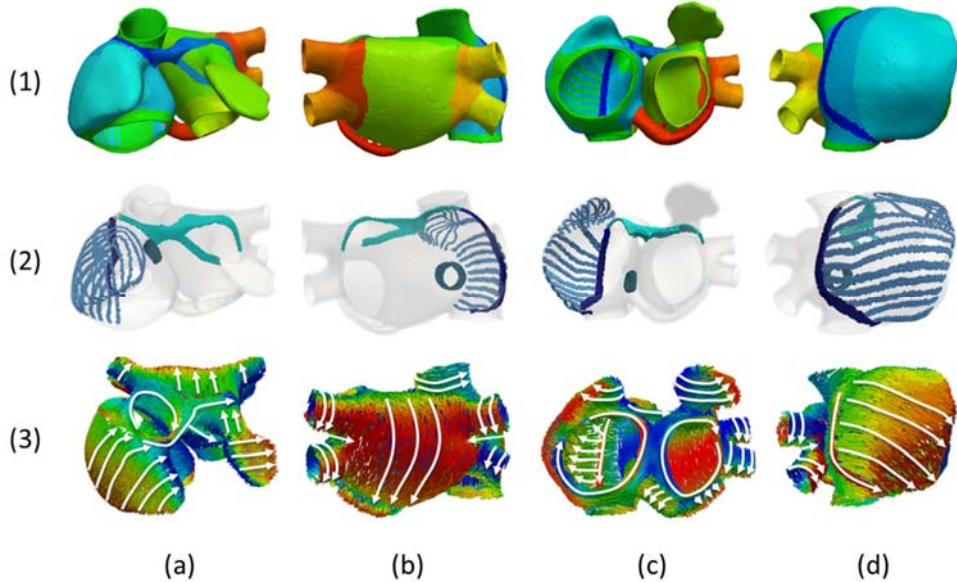
We have developed a novel atrial model that improves our previous 3D model of the human atria (Tobón et al. 2013). The new model, available at (RIUNET, <http://hdl.handle.net/10251/55150>), has enhanced the anatomical and functional heterogeneity and the detailed regional description of fibre direction. The resulting computational finite element model is a multi-layer mesh (see Figure 4.16) with a homogeneous wall thickness between 600 and 900 µm (754893 nodes and 515010 elements), built with linear hexahedral elements with a regular spatial resolution of 300 µm (as used at tissue scale).



**Figure 4.16: Atrial multi-layer mesh**

a) Frontal view; b) rear view; c) magnified view of the Bachmann's bundle region.

Following the histological analysis, the geometrical model was manually divided into 21 regions. However, for the detailed description of fibre orientation, some regions were further subdivided into a total of 53 sub-regions (Figure 4.17 row 1). The model also includes the preferential conduction bundles (Figure 4.17 row 2), which are the CT, PMs, BB with right (BBR) and left (BBL) sides and the LFO between both atria. From the information provided by the anatomical observations, the architecture of preferential bundles in the new model is the following: i) the CT runs down longitudinally from the SAN to the vestibule of the TV, with dimensions of 6 cm x 0.3 cm x 0.09 cm (length, width, intramural maximum thickness); ii) 10 PMs were included along the CT as parallel ridges that run on the endocardium of the RLW (Hansson et al. 1998). Their dimensions range from the smallest PM (1.7 cm x 0.15 cm x 0.06 cm) to the largest (4.5 cm x 0.3 cm x 0.06 cm). The septum spurium is an additional PM that branches out into nine smaller PMs (each 0.1 cm wide) covering the endocardial surface area of the RAA; iii) the antero-superior interatrial connection follows the tubular structure of the BB. The BBR section originates in the SAN and extends 3.5 cm towards the LA with a width varying between 0.2 and 0.9 cm. The BBL turns around the LAA splitting in two branches. First branch (2 cm x 0.3 cm) extends towards the lower face of the LAA, and the second one (3 cm x 0.6 cm) extends around the LAA on its upper side, following the experimental observations and other previous results (Ho & McCarthy 2010).

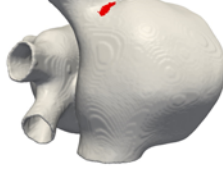


**Figure 4.17: Properties of the novel 3D atrial model**

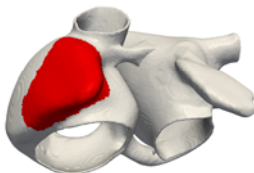
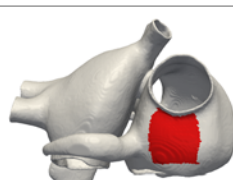
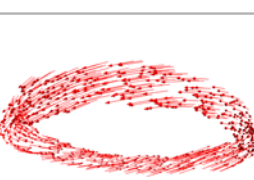
Row (1) show in colours the division in 21 atrial regions; Row (2) shows preferential conduction bundles; Row (3) shows principal fibre direction; Columns correspond to a) Frontal view; b) rear view; c) inferior view; and d) right lateral view.

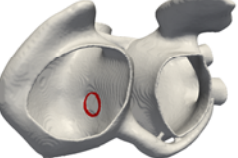
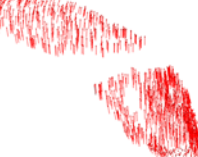
Atrial fibre orientation was analysed in detail to determine the number and location of regions with a common fibre organization (Figure 4.17 row 3). As can be seen in Figure 4.17, the BB (row 3, column a), CT and PMs (row 3, column c) and the RLW (row 3, column d) match the histological observations (Figure 4.14). It is important to note that several neighbouring regions show large differences in the principal direction of their fibres and thus strongly influence the propagation of the electrical wavefront. These include CT vs RLW, CT vs PMs, RLW vs TV, BBL vs LSW, and LPW vs base of LPV and vs RPV. All the anatomical and electrophysiological properties corresponding to each atrial region are described in detail in the following Table 4.4.

**Table 4.4: Atrial regions and main electrophysiological cellular and tissue properties**

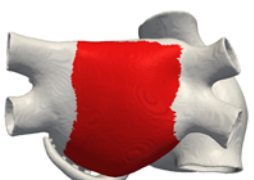
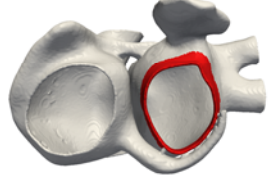
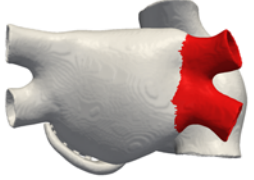
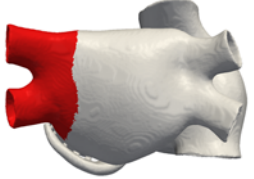
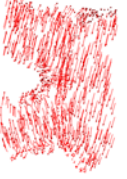
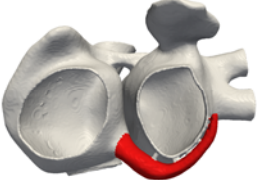
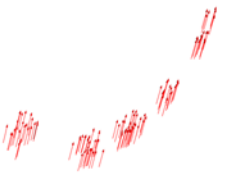
Nº	REGION	PROPERTY	VALUE	FIBRE DIRECTION	
					
1	SAN	Nº ELE	659		
		Sub-regions	--		
		V (mm <sup>3</sup> )	17,8		
		MODEL	RA		
		MATERIAL	SAN		
		CV <sub>L</sub>	27,7		
		CV <sub>T</sub>	27,7		
		LAT <sub>INI</sub> (ms)	0		
		LAT <sub>END</sub> (ms)	3		
2	CT	Nº ELE	5867		
		Sub-regions	--		
		V (mm <sup>3</sup> )	158,4		
		MODEL	CT		
		MATERIAL	CT		
		CV <sub>L</sub>	100,0		
		CV <sub>T</sub>	38,9		
		LAT <sub>INI</sub> (ms)	3		
		LAT <sub>END</sub> (ms)	60		
3	BBR BBL	Nº ELE	15227		
		Sub-regions	6		
		V (mm <sup>3</sup> )	411,1		
		MODEL	BB		
		MATERIAL	BB		
		CV <sub>L</sub>	116,7		
		CV <sub>T</sub>	46,5		
		LAT <sub>INI</sub> (ms)	3		
		LAT <sub>END</sub> (ms)	72		
3	BB (Insulating)	Nº ELE	4430		
		Sub-regions	2		
		V (mm <sup>3</sup> )	119,6		
		MODEL	--		
		MATERIAL	--		
		CV <sub>L</sub>	0		
		CV <sub>T</sub>	0		
		LAT <sub>INI</sub> (ms)	0		
		LAT <sub>END</sub> (ms)	0		
4	IB	Nº ELE	25732		
		Sub-regions	--		
		V (mm <sup>3</sup> )	694,8		
		MODEL	RA		
		MATERIAL	RA		
		CV <sub>L</sub>	63,3		
		CV <sub>T</sub>	36,6		
		LAT <sub>INI</sub> (ms)	3		
		LAT <sub>END</sub> (ms)	60		
5	RAS	Nº ELE	48977		
		Sub-regions	--		
		V (mm <sup>3</sup> )	1322,4		
		MODEL	RA		
		MATERIAL	RA		
		CV <sub>L</sub>	63,3		
		CV <sub>T</sub>	36,6		
		LAT <sub>INI</sub> (ms)	20		
		LAT <sub>END</sub> (ms)	95		

Chapter 4

Nº	REGION	PROPERTY	VALUE	FIBRE DIRECTION	
6	RLW	Nº ELE	40932		
		Sub-regions	--		
		V (mm <sup>3</sup> )	1105,2		
		MODEL	RA		
		MATERIAL	RA		
		CV <sub>L</sub>	63,3		
		CV <sub>T</sub>	36,6		
7	RAA	LAT <sub>INI</sub> (ms)	18		
		LAT <sub>END</sub> (ms)	85		
		Nº ELE	27740		
		Sub-regions	--		
		V (mm <sup>3</sup> )	749,0		
8	PM	MODEL	RAA		
		MATERIAL	RA		
		CV <sub>L</sub>	63,3		
		CV <sub>T</sub>	36,5		
		LAT <sub>INI</sub> (ms)	20		
		LAT <sub>END</sub> (ms)	75		
		Nº ELE	15259		
9	IST	Sub-regions	10		
		V (mm <sup>3</sup> )	412,0		
		MODEL	PM		
		MATERIAL	PM		
		CV <sub>L</sub>	115,4		
		CV <sub>T</sub>	46,3		
		LAT <sub>INI</sub> (ms)	15		
10	SCV	LAT <sub>END</sub> (ms)	75		
		Nº ELE	9023		
		Sub-regions	--		
		V (mm <sup>3</sup> )	243,6		
		MODEL	RA		
		MATERIAL	IST		
		CV <sub>L</sub>	76,6		
11	ICV	CV <sub>T</sub>	76,6		
		LAT <sub>INI</sub> (ms)	75		
		LAT <sub>END</sub> (ms)	96		
		Nº ELE	19121		
		Sub-regions	--		
		V (mm <sup>3</sup> )	516,3		
		MODEL	RA		

Nº	REGION	PROPERTY	VALUE	FIBRE DIRECTION	
12	TV	Nº ELE	15194		
		Sub-regions	--		
13	LFO (Insulating)	V (mm <sup>3</sup> )	410,2		
		MODEL	TV		
14	FO (Insulating)	MATERIAL	RA		
		CV <sub>L</sub>	63,3		
15	LSW	CV <sub>T</sub>	36,5		
		LAT <sub>INI</sub> (ms)	64		
16	LAS	LAT <sub>END</sub> (ms)	109		
		Nº ELE	4654		
17	NO FIBRES DIRECTION	Sub-regions	--		
		V (mm <sup>3</sup> )	125,7		
18	LAA	MODEL	RA		
		MATERIAL	LFO		
19	FO (Insulating)	CV <sub>L</sub>	99,1		
		CV <sub>T</sub>	38,6		
20	NO FIBRES DIRECTION	LAT <sub>INI</sub> (ms)	48		
		LAT <sub>END</sub> (ms)	80		
21	FO (Insulating)	Nº ELE	6357		
		Sub-regions	--		
22	NO FIBRES DIRECTION	V (mm <sup>3</sup> )	171,6		
		MODEL	--		
23	FO (Insulating)	MATERIAL	--		
		CV <sub>L</sub>	0,0		
24	NO FIBRES DIRECTION	CV <sub>T</sub>	0,0		
		LAT <sub>INI</sub> (ms)	NA		
25	FO (Insulating)	LAT <sub>END</sub> (ms)	NA		
		Nº ELE	19007		
26	NO FIBRES DIRECTION	Sub-regions	2		
		V (mm <sup>3</sup> )	513,2		
27	FO (Insulating)	MODEL	LA		
		MATERIAL	LA		
28	NO FIBRES DIRECTION	CV <sub>L</sub>	63,3		
		CV <sub>T</sub>	36,6		
29	FO (Insulating)	LAT <sub>INI</sub> (ms)	38		
		LAT <sub>END</sub> (ms)	81		
30	NO FIBRES DIRECTION	Nº ELE	37094		
		Sub-regions	--		
31	FO (Insulating)	V (mm <sup>3</sup> )	1001,5		
		MODEL	LA		
32	NO FIBRES DIRECTION	MATERIAL	LA		
		CV <sub>L</sub>	63,3		
33	FO (Insulating)	CV <sub>T</sub>	36,6		
		LAT <sub>INI</sub> (ms)	40		
34	NO FIBRES DIRECTION	LAT <sub>END</sub> (ms)	83		
		Nº ELE	31711		
35	NO FIBRES DIRECTION	Sub-regions	2		
		V (mm <sup>3</sup> )	856,2		
36	FO (Insulating)	MODEL	LAA		
		MATERIAL	LA		
37	NO FIBRES DIRECTION	CV <sub>L</sub>	63,3		
		CV <sub>T</sub>	36,5		
38	FO (Insulating)	LAT <sub>INI</sub> (ms)	64		
		LAT <sub>END</sub> (ms)	125		

Chapter 4

Nº	REGION	PROPERTY	VALUE	FIBRE DIRECTION	
17	LPW	Nº ELE	61325		
18	MV	Nº ELE	21476		
19	RPV	Nº ELE	30588		
20	LPV	Nº ELE	45026		
21	CS	Nº ELE	21873		
	CS (Unions)	Nº ELE	611		

#### 4.4.3. Multiscale anisotropic vs isotropic atrial activation

The electrophysiological heterogeneity represented by the eight stabilized cellular models as well as the tissue conduction velocities were coupled into the 3D atrial model as depicted in Figure 4.18.

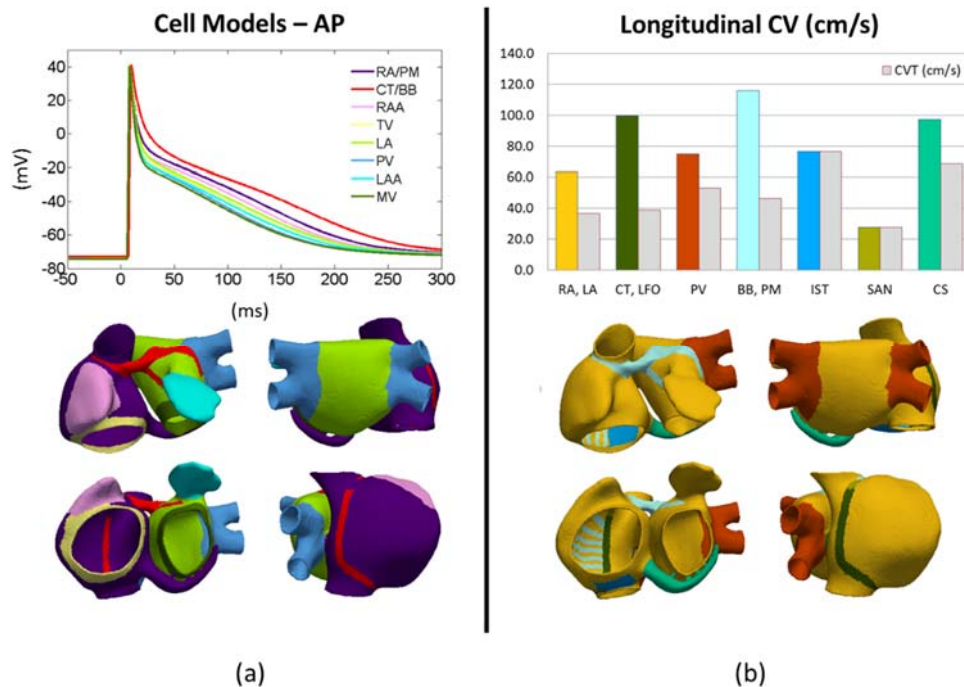


**Figure 4.18: Cellular and tissue properties of the atrial model**

a) Action potentials produced by each cell model (top) and the atrial regions to which each model has been assigned labelled by colour (bottom); b) Longitudinal (coloured) and transversal (grey) tissue conduction velocities (top) and the corresponding atrial regions colour coded (bottom).

Before carrying out the simulations at organ scale, it was necessary to determine the threshold current for exciting the 3D atrial tissue. Figure 4.19 shows the compromise between stimulus duration and its amplitude for the three scales (cell, slab and whole atrium) using the Maleckar's model without varying any ionic conductance. Daily practice recommends selecting a stimulus with the minimum duration to avoid a decrease in the depolarization slope and with a higher amplitude than the one corresponding to its threshold. For this reason, we used a stimulus of 1ms and 52pA/pF to trigger cells, 2ms with 100pA/pF at tissue scale when simulating the slab and 2ms with 30pA/pF when simulating the whole atrial model.

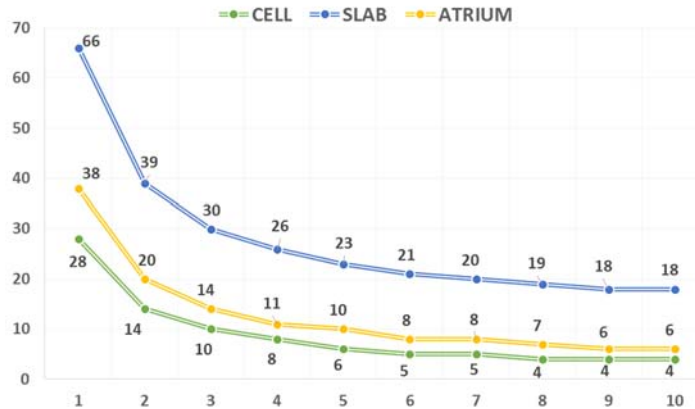


**Figure 4.19: Threshold current required for triggering the models**  
At cellular scale (green line), tissue scale (blue line) and organ scale (yellow line).

Physiological simulation at atrial scale consisted of 10 stimuli with a frequency of 1 Hz, amplitude of 30 pA/pF and duration of 2 ms applied to the SAN region to reach the steady-state in 3D and to smooth differences between neighbouring regions. This simulation was then validated analysing first the differences in APD<sub>90</sub> between atrial regions across the three scales and afterwards comparing the simulated activation pattern with experimental patterns measured by (Lemery et al. 2007). APD<sub>90</sub> in the atrium was computed from an AP measured at one single node within each region. As shown in Figure 4.20, the smaller value of APD<sub>90</sub> occurs at cellular scale due to there is no cellular coupling modifying the repolarization phase. On the other hand, and considering that both, the slab and the whole atrium are indeed 3D tissues and that the slab has the thickest wall width, its repolarization phase slows down and therefore its APD<sub>90</sub> is higher than in the atrial scale. Finally, the tissue coupling of the RA regions smooths the APD<sub>90</sub> differences probably due to the fibres are align in a continuous way. However, differences in APD<sub>90</sub> in the LA are kept from the cellular to the atrial scale may be due to the highest variations in conduction velocities and fibre directions.

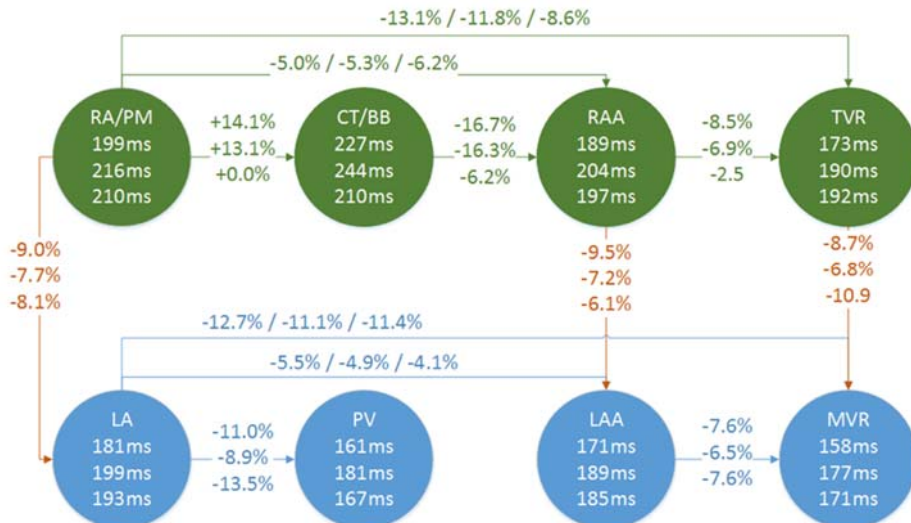


**Figure 4.20: APD<sub>90</sub> differences between cellular, tissue slab and atrial scale**  
Analysis of the inter-region electrophysiological heterogeneity.

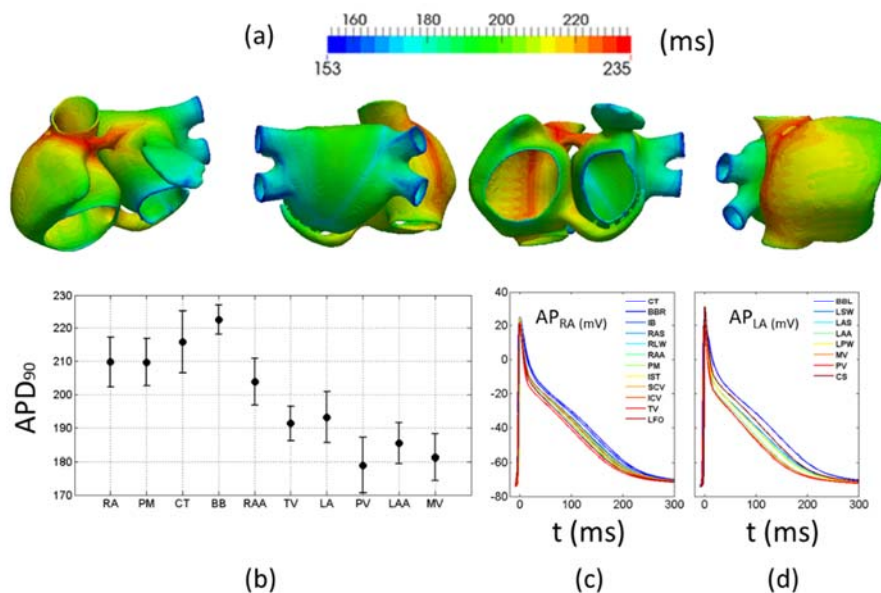


**Figure 4.21: Spatial variability of APD<sub>90</sub> across the atrium**  
(a) Represents the colour-coded distribution from minima (blueish colours) to maxima value (reddish colours); (b) represents the mean APD<sub>90</sub> and its first standard deviation. Panels c) and d) show the AP morphology registered at nodes located in RA and LA respectively.

Figure 4.21a shows the spatial variability of APD<sub>90</sub>, which ranges from the lowest values at the PVs (153 ms) to the highest at the BB (235 ms). Figure 4.21b shows the mean APD<sub>90</sub> and first standard deviation ( $\sigma$ ) for each atrial region where minimum mean values correspond again to the PVs ( $178.9 \pm 8.2$  ms), whereas maximum mean values are from the BB ( $222.4 \pm 4.3$  ms) as expected. Dispersion within each region ranges from  $\sigma = \pm 9.3$  ms (CT) to  $\sigma = \pm 4.3$  ms (BB). The relationship between APDs from each region at organ scale (Figure 4.21 panels c) and d)) was maintained when compared to cellular scale, although the smoothing effect mentioned before was again observed as expected due to the tissue coupling.

The second phase in the validation process was carried out analysing the activation sequence and comparing the results with experimental measures performed by (Lemery et al. 2007). Figure 4.22 shows the isochronal map for the last stimulus applied (the tenth). After the SAN is depolarized ( $t = 0$  ms, dark blue regions), the CT, the BBR, the IB and the SCV simultaneously start their respective depolarisations (light blue regions). The activation descends rapidly through the CT towards the ICV for 57 ms (arrow 1) activating sequentially the PMs and the endocardial wall of the IB. This activation pattern produces a triangular wavefront that spreads from CT to TV through the RLW and the RAA for 85 ms (arrow 2). The right side of the atrial septum (RAS) is activated by the IB at  $t = 20$  ms, (light blue regions), which allows a second wavefront to spread with lower conduction velocity from CT towards TV (arrow 3). Both wavefronts (arrows 2 and 3) collide in the TV, the last RA region activated, and thus produce the last activation time registered in the RA at  $t = 109$  ms (reddish regions).

The activation moves through the BBR from the RA to the LA (arrow 4), registering the first activated point in the LA at  $t = 38$  ms (light blue regions in Figure 4.22). As can be seen, the original LA wavefront splits up into two parts, which facilitates the rapid depolarization of the LSW and regions around the LAA. The left side of the atrial septum (LAS) is partially activated by the BBL (arrow 5) and partially by the LFO 10 ms later (not visible in the figure). These LA activations produce four wavefronts at  $t = 64$  ms, as can be observed in the figure, which advance simultaneously towards the MV (arrow 5), the union between the superior and inferior RPV (arrow 6), the LPW (arrow 7) and the LAA (arrow 8).

The LAA shows a slow conduction velocity, since the depolarization wavefront travels perpendicularly to the local fibre direction, taking 61 ms to be completely depolarized. In the posterior wall, the LPW depolarization sequence depends on two wavefronts, one arriving from the LSW (arrow 7) and the other crossing the RPV (arrow 6). This causes a diagonal wavefront (arrow 9) that electrically sweeps the posterior wall from the superior RPV towards the inferior LPV for 64 ms.

The CS (arrow 10) is depolarized together with the LPW but with a slower conduction velocity due to the circular fibre direction. The latest activation time registered in the atria corresponds to  $t = 132$  ms and is concurrent with the latest activation of the CS.

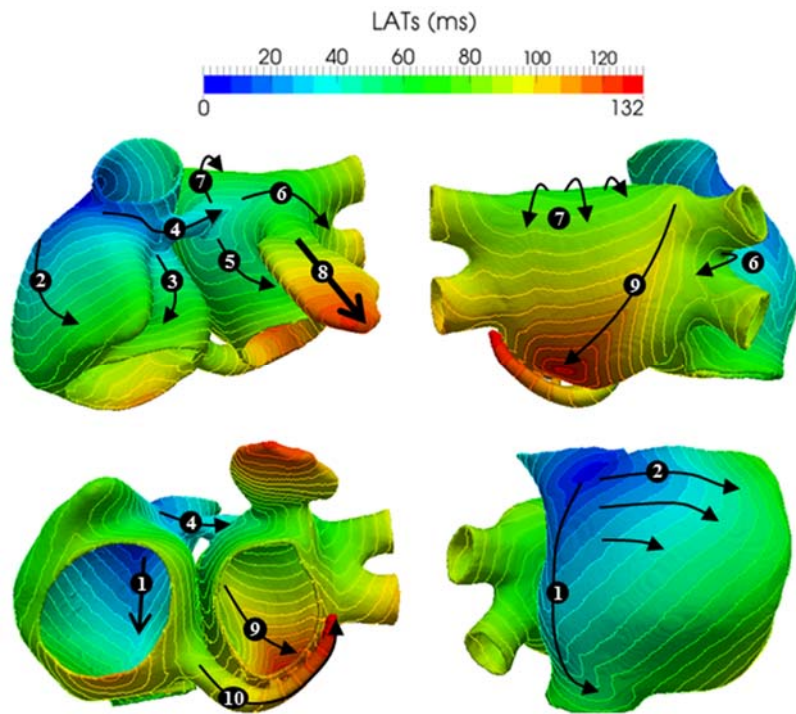


**Figure 4.22: Atrial LATs produced by the anisotropic atria with fibre orientation**

All the atrial activation time instants that define the first and last activation of each region are already included in Table 4.4. Figure 4.23 shows snapshots of the atrial activation sequence, and the comparison between the simulated activation times at different time instants of the atria with the experimental data (in red) reported by (Lemery et al. 2007). The overall depolarization process is slightly slower in the simulation, although the activation sequence and all the simulated activation times are within experimental ranges.

The last step in the analysis of the atrial activation sequence consisted in quantifying the contribution of the fibre orientation by means of comparing the previous results with the atrial activation obtained from an isotropic atrial model. Tissue heterogeneity and longitudinal conduction properties were kept identical for both models, but the anisotropy ratio was fixed to 1:1 for the whole atrium. Figure 4.24 shows the differences in local activation times (LAT) between both configurations. Positive differences (reddish colours) correspond to regions that activate earlier in the isotropic model, whereas negative (bluish colours) correspond to regions that activate earlier in the anisotropic model. Since longitudinal conductivity and heterogeneity are equal in both models, the activation sequences seem similar, although the wavefront spreads out almost circularly from the

SAN in the isotropic model, thereby the depolarization times registered are considerably lower in specific parts of the atria. The strongest effect produced by the isotropic model is the increase in the wavefront velocity in these regions, where it advances mainly perpendicular to the longitudinal fibre direction, such as the atrial appendages (RAA and LAA), the TV and the lower right area of the LPW. In the isotropic model the latest activation times are  $t = 94$  ms and  $t = 112$  ms for the RA and the LA respectively, 12.5% and 15.2% faster than in the anisotropic atrial propagation.

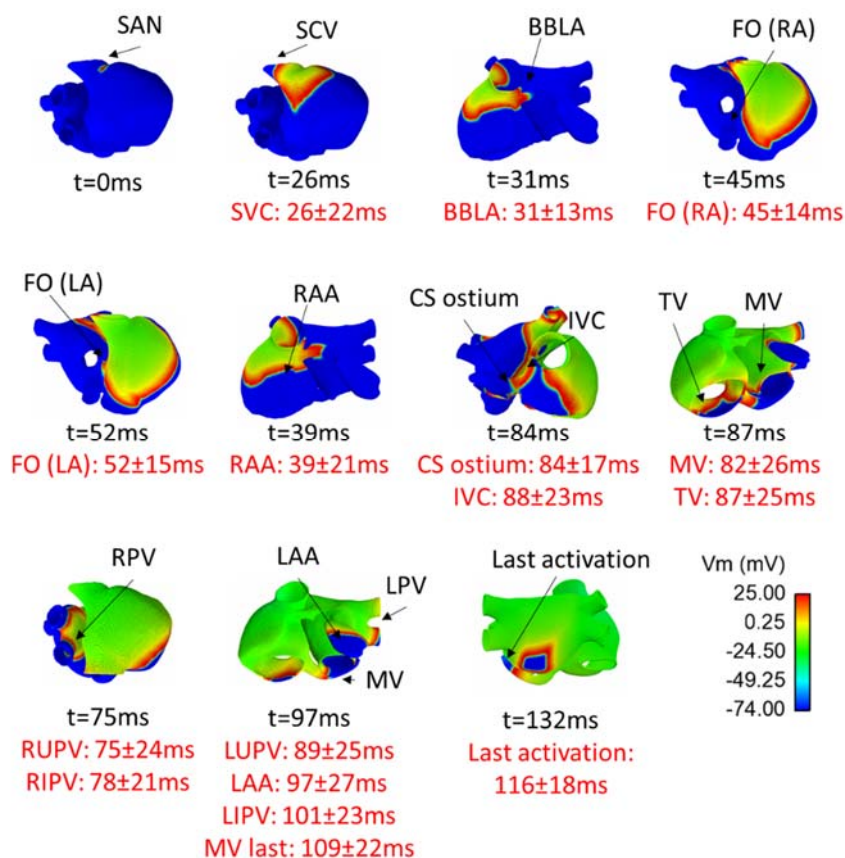


**Figure 4.23: Atrial depolarization sequence**

Snapshots of the atrial activation and comparison of the simulated activation times at different points of the atria with the experimental activation times (in red) reported by (Lemery et al. 2007).

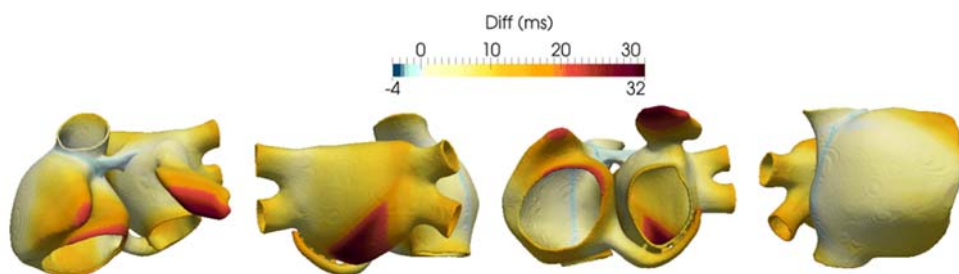


**Figure 4.24: LAT differences between anisotropic and isotropic atrial model**

## 4.5. Discussion

This chapter presents a new detailed multiscale computer model for the study of atrial electrical activation. Eight different models were adjusted on the cellular scale, allowing us to generate APs personalised to different types of atrial tissues. On the organ scale, an anatomo-functional atrial model was developed including the specialized anatomical structures of the atria, cellular and tissue electrophysiological heterogeneity, with detailed descriptions of fibre orientation. As previous human-based (Seemann et al. 2006; Al Abed et al. 2010; Lu et al. 2011; Burdumy et al. 2012; Krueger et al. 2012; McDowell et al. 2012; Dongdong Deng et al. 2012; Tobón et al. 2013; Gonzales et al. 2013; Jacquemet 2015) as well as animal-based studies (Ridler et al. 2006; Zhao et al. 2012; Aslanidi et al. 2013), we decided not to consider the variability of the atrial wall thickness and its contribution to the P-wave morphology aiming at analysing the isolated effect of fibre direction, electrophysiological heterogeneity and tissue conductivity on the signals registered on the atrial and body surfaces.

### 4.5.1. Multiscale anatomical and electrophysiological atrial model

The multiscale atrial-torso model presented here improves in a number of properties with respect our original computational atrial model (Tobón et al. 2013). Next paragraphs intend to describe such improvements and the key strengths of the new model.

Regarding the atrial mesh quality, hexahedral voxels were used with higher homogeneous spatial resolution (0.3 mm), similarly as in (Aslanidi et al. 2012; Burdumy et al. 2012; Krueger et al. 2012; Jacquemet 2015). Thanks to the high quality and regularity of the mesh, the stability of numerical computations is guaranteed (Lamata et al. 2013).

Secondly, since the conduction bundles influence the most on the atrial activation sequence, particular emphasis must be placed on the modelling of these structures. In this regard, the number and size of PMs of the specialized anatomical atrial structures were redefined according to histological observations, covering the endocardial surface of RLW and RAA, from the CT to the vestibule of the TV. Additionally, the BB was lengthened to join the SAN in the RA and to hug the LAA on its left side (Cabrera & Sánchez-Quintana 2013). Although the newest models already included these conduction bundles

(Krueger et al. 2012; Jacquemet 2015; McDowell et al. 2015), they were not particularly focused on modelling neither the realistic anatomy of the PMs nor its special properties associated to the fibre orientation, conduction velocity or anisotropy ratios of the PMs.

With respect to global tissue anisotropy, the whole atrium was divided into 21 anatomical structures and 53 sub-regions in order to improve the local control of fibre orientation, mainly at the conduction structures (CT, PM and both sides of BB). The fibre orientation of several regions was updated with respect to our previous model, to agree with descriptions extracted from new histological data. Since models of the human atrial anatomy must be build purpose specific, the highly specialized division of this atrial structure allow the fine-tuning of the microscopic properties and then makes it easier to adapt this model to other macroscopic objectives. However, when models are macroscopically designed from its conception as happens with (Jacquemet 2015; McDowell et al. 2015), their use to check an hypothesis other than the one for which they were built is rather difficult.

Fourthly, with respect to the cellular AP, the basic model was changed from Nygren et al. (Nygren et al. 1998) used in our previous model to Maleckar et al. (Maleckar et al. 2009), since Maleckar's model shows long-term stability in terms of restitution properties and APD<sub>90</sub>. The majority of the previous models (Aslanidi et al. 2012; Burdumy et al. 2012; Krueger et al. 2012; Jacquemet 2015; McDowell et al. 2015) use however (Courtemanche et al. 1998). The main reason is based on the fact that previous models aimed to study atrial fibrillation and this requires basic cycle lengths below the normal rhythm. Under pathological conditions, the behaviour of the Courtemanche's model is much more stable than the Nygren's or Maleckar's models. However, this does not happen under normal atrial behaviour in which case the AP characteristics are much more similar to experimental measurements. The stability of these dynamic properties was then considered essential to develop and validate the eight regional cell models in physiological conditions (RA/PM, CT/BB, RAA, TVR, LA, PV, LAA and MVR). All these cellular models reach steady state after approximately 10 min, although the stabilization process was carried out for 60 min, allowing a robust usage at both the cell and tissue scales for investigation of the human atria (Wilhelms et al. 2013).

Finally, with respect to tissue conductivity, different values of longitudinal conductivity and anisotropy ratios were defined as a function of the atrial region (RA/LA, CT/LFO, PV, BB/PM, IST, SAN, CS and the isolating layers of FO and inside BB). A limited number of experimental studies provide values of conduction velocities from healthy subjects in sinus rhythm, with measurements in only a few human atrial structures (Hansson et al. 1998; Kojodjojo et al. 2006; Fedorov et al. 2010). The conduction properties presented here were then compared and validated against experimental atrial conduction velocities. Results showed that simulations provided ranges between 63.3 cm/s and 116.0 cm/s and they matched well with the mean experimental conduction velocities. (Hansson et al. 1998) measured values close to 88±9 cm/s, (Fedorov et al. 2010) provided ranges between 70-90 cm/s through the RA free wall or 120-140 cm/s through the CT

while (Kojodjojo et al. 2006) quantified mean RA and LA values of  $70.2 \pm 9.9$  and  $77.0 \pm 10.8$  cm/s respectively. Much like to tissue anisotropy, regional conduction velocities are of high relevance when modelling the normal behaviour of the atrium. Our model, unlike other previous models (Krueger et al. 2012; Jacquemet 2015; McDowell et al. 2015), has been also designed to consider conductivity at microscopic scale making easy to adapt this property to any other pathological and macroscopic condition.

#### **4.5.2. Multiscale atrial simulations**

After coupling the cellular models in 3D, differences in AP morphology were registered when simulating and comparing the AP at both levels. These changes, due to the electrical coupling between myocytes, equalize ionic loads and relax the border effects between regions, producing a reduction in the maximum AP amplitude and subtle differences in APD<sub>90</sub>. When considering all action potentials recorded from each atrial region, the APD<sub>90</sub> value ranges from  $178.9 \pm 8.2$  ms in the PVs to  $222.4 \pm 4.3$  ms in the BB, with a total maximum variability between regions of 56 ms, slightly lower than the variability produced by differences at the cellular scale (66 ms between the same regions, see Table 4.2). For the RA and the PM, the APD<sub>90</sub> (199 ms) is similar to values measured in human subjects ( $207.0 \pm 18$  ms) at the same BCL of 1 Hz (Dobrev et al. 2001). The models for the CT, the BB, the RAA and the TV regions were adjusted to match the experimentally observed APD<sub>90</sub> ratios between different atrial regions within the RA. The ratios obtained in the models were: +14.4% for CT/BB, -5.0% for RAA and -13.1% for TV, which have been experimentally reported as +42.1%, -5.3% -15.8%, respectively (Feng et al. 1998). Our LA model has an APD<sub>90</sub> ratio of -9.0% with respect to RA/PM versus an experimental observation of -10.5% (Li et al. 2001), and a -11.0% reduction of the PV versus the LA as observed by (Cha et al. 2005). Due to the lack of physiological data related to the LA, a similar variation between the RA and the LA was applied to the LAA with respect to the RAA (-9.5%) and the MVR with respect to the TVR (-8.7%).

The final multiscale atrial model produces an activation sequence that matches experimental local activation times. Thus, the first LA activation, produced through the BB, and the latest RA and LA activation times at 38 ms, 109 ms and 132 ms, respectively, are within the experimental ranges given by  $31 \pm 13$  ms,  $93 \pm 17$  ms and  $116 \pm 18$  ms respectively registered at the same locations (Lemery et al. 2007). This is the common approach followed in other computational models (Dong-dong Deng et al. 2012; Krueger et al. 2013; Colman 2014).

Using this new multiscale model, we analysed the influence of the atrial tissue fibre orientation. Our results showed that an isotropic atrial tissue (without considering fibre direction) influences the mean effective velocity and the depolarization pattern, making the depolarization wavefront arrives between 2 and 4 ms earlier at BB and CT but 32ms later at LAA and LPW. These changes are mainly dependent on the degree of alignment between the local direction of fibres in a particular region and the direction in which the depolarization wavefront enters that region. The transversal direction of the fibres in

RAA, TV and LAA therefore slowed down the advance of the wavefront in the anisotropic model. However, in the case of the right inferior LPW, the increase is mainly due to a new wavefront crossing the LFO region and depolarizing the LIPV and inferior LPW faster. The final effects of isotropy on the atrial activation sequence were in agreement with the findings of Roberts et al. (Roberts et al. 1979), who experimentally analysed the interdependence between fibre direction, conduction velocity and potential generated by a depolarization wave, concluding that fibre direction has major effects on all of these variables. This analysis was carried out by using a different setup than the one used in previous studies (Krüger 2012; Zhao et al. 2012), whose aim was to analyse the combined effect of fibre isotropy and homogeneous atrial conductivity. However, we only used an anisotropy ratio of 1:1, keeping the specific tissue heterogeneity in order to isolate the effect produced by fibre orientation. The results showed in the present work are then encouraging since they numerically quantify the specific effect of anisotropy in a realistic human multiscale atrial model.

## **4.6. Limitations**

Mathematically, the most recurrent simplification is the following:

- a) The bidomain model to simulate atrial activity, which considers current flows in both intra-and extracellular domains, is still the most widely used approach to solve the forward problem in cardiac electrophysiology. However, since computational costs are significantly expensive, a common simplification in which only the intracellular space is represented allows the use of the monodomain approach to compute the membrane and extracellular potentials faster.

Anatomically, the atrial scale also present some simplifications:

- a) The atrial mesh is a highly improved version of the first model published by (Harrild & Henriquez 2000). Since the main objectives of the present thesis is the study of the atrial activity at the torso surface, this atrial model was meshed considering a monolayer wall. On the other hand, although the main conduction bundles have been included and validated (BB, CT, the ring of FO or the CS) new insights into the atrial histology unveil that might exist additional bundles between the CT and the FO and CS.
- b) Although the atrial mesh was validated using experimental studies, there exist numerous sources of inter-patient variability and uncertainty in the models formulation that could impact the results and then the use of these models in the clinical practice (Mirams et al. 2016).

Some additional electrophysiological simplifications have also been considered:

- a) At cellular level, to eight different models of atrial myocytes have been modelled with specific action potentials. These models have been validated using experimental data. However, there are not enough experimental studies on humans and some of them were carried out on animals. In those cases, we have used published ratios between regions

instead of the absolute values of, for instance, APD<sub>90</sub> or restitution curves. However, realistic properties of the APs in human atrial myocytes across the atrium would force to adjust our regional models.

b) Conduction velocities at tissue level were adjusted by using the slab instead of the atrial mesh as a whole. Although the atrial depolarization and repolarization sequences were validated using experimental studies, a more realistic measurement of the longitudinal and transversal velocities should be carried out on the atrial model.



# CHAPTER 5

---

## Genesis of P-waves: contribution from atrial regions

*This chapter presents the torso model developed and the mathematical techniques that allow propagating the atrial signals through the torso up to its surface. A careful review of previous human torso models guides the building of the new torso model that has been adapted to the atrial model already designed in chapter 4. The multi-scale atrial-torso model is used to understand the body surface potential maps under physiological conditions and how the different atrial regions are responsible for the main P-wave characteristics.*

*The content of this chapter has been partially published in:*

**A. Ferrer, R. Sebastián, D. Sánchez-Quintana, J. F. Rodríguez, E. J. Godoy, L. Martínez, and J. Saiz,** “Detailed anatomical and electrophysiological models of human atria and torso for the simulation of atrial activation,” *PLoS One*, vol. 10, no. 11, p. e0141573, Jan. 2015

**A. Ferrer, R. Sebastian, J.F. Rodriguez, C. Tobon, J. Saiz.** *Modelling of Human Torso for the Study and Characterization of Atrial Arrhythmias. Cardiac Physiome*, San Diego, 2013

**A. Ferrer, R. Sebastian, J. F. Rodriguez, C. Tobon, M. Guillem, E. J. Godoy, and J. Saiz,** “Computational Simulation and Analysis of 3D Body Surface Potential Patterns Generated by Common Atrial Arrhythmias,” in *Computing in Cardiology*, 2013, pp. 919–922.

### 5.1. Existing human torso models

First torso models (Frank, 1955) intended to analyse isopotential lines and the movement of the cardiac electrical dipole on the surface of a human torso (see Figure 5.1a). Since then, there has been an increasing interest in building realistic human torso models. Later computational approaches developed by (Rudy & Plonsey 1980; Abboud et al. 1991; Leon & Horacek 1991) tried to represent a finite, homogeneous and isotropic space without considering the specific anatomical and electrical properties of tissues and organs.

Those authors studied the variations of surface potentials only due to changes in a volumetric conductor geometry such the one shown in Figure 5.1b.

From the time of these rudimentary models, more realistic approaches allowed to mathematically tackle the forward problem in cardiac electrophysiology with a twofold objective. On one hand, to improve the model geometry using magnetic resonance images (MRI), computed tomography or ultrasounds. On the other hand, to include the electrophysiological heterogeneities and anisotropies associated to organs and tissues. The model developed by (MacLeod et al. 1991) was the first in considering these properties and was built using 116 MRI from one single subject. Additionally, it included tissue heterogeneities associated to skin, muscles, bones, blood vessels or fat as well as specific conductivity values from organs such as lungs and heart.

Later on, (Weixue and Ling, 1996) developed an anatomically little realistic torso model (see Figure 5.1c) but more electrically efficient in terms of computation than previous models. This surface model consisted in 412 nodes and 820 triangular elements and included the surfaces corresponding to lungs, blood, muscles and the whole heart. More recently, this model was used by (Aslanidi et al. 2011; Colman et al. 2011) to compute the potential time series on the torso surface and to localize the origin of atrial arrhythmias by analysing the P-wave morphology.

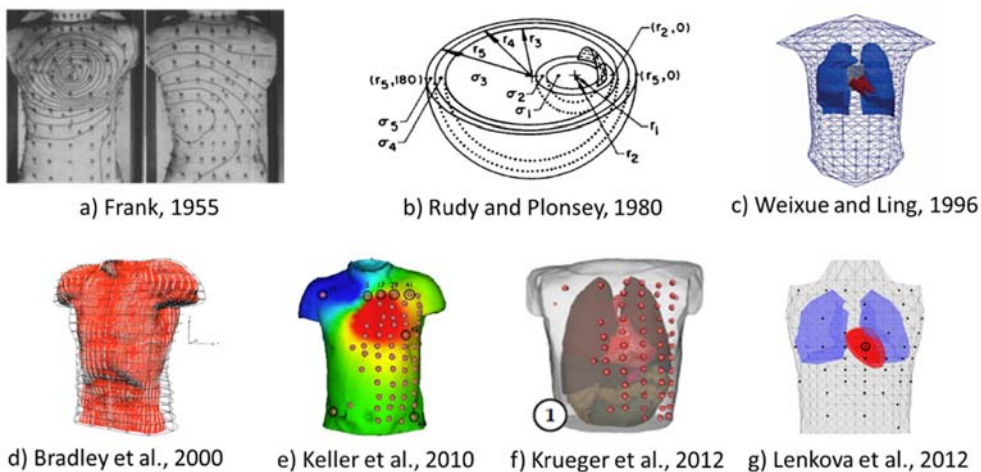


**Figure 5.1: Examples of previous existing human torso models**

Using the complete anatomically detailed three-dimensional database of representations of the normal male and female human bodies (Ackerman 1992) and the improved segmentation and meshing techniques based on boundary or finite elements, it is possible to

find in the literature more realistic computational torso models. For example, (Sachse et al., 2000) provided a 3D anatomical model of the whole human body with 370 millions of cubic voxels, a spatial resolution of  $1\text{mm}^3$  and myocardial fibre direction. Afterwards, investigations carried out by (Bradley et al. 2000; Bauer et al. 2009; Keller et al. 2010; Weber, Luik, et al. 2011) and centred on the human torso models (see Figure 5.d and 1e) allowed a deep analysis of the effect of electrical conductivities introduced by organs and tissues.

Over the last years, the evolution in the electrophysiological modelling of both, the human atrium and the torso has been focused on improving the personalized diagnostics and treatment of patients suffering from atrial arrhythmias. In this sense, one of the first methods used to build human-specific torso models was firstly proposed by (Bradley et al. 1997; Bradley et al. 2000) who investigated how to fit geometric data of the human torso obtained from MRIs, with high-order bicubic Hermite surface elements. More recently, the inhomogeneous volumetric models proposed by (Krueger et al. 2012; Lenkova et al. 2012) allowed to adapt the shape of the torso models (see Figure 5.f and 1g) to different patient morphologies. These authors tried to mathematically address the inverse problem and then to determine the mechanisms associated to changes in the activation patterns and cardiac rhythms.

## 5.2. Modelling the Human Torso

The dataset required to build our new 3D torso model was obtained from the online open repository stored at the Centre for Integrative Biomedical Computing (CBIC) from University of Utah (MacLeod et al. 1991). Data in this repository had been already anonymised and made available to the research community. The complete systematic process followed to build the new torso model is shown in Figure 5.2 and the final model is made freely available for the research community through the repository owned by the Polytechnic University of Valencia (RIUNET, <http://hdl.handle.net/10251/55150>).

The primary source of geometrical information for this model was then the set of 116 transverse magnetic resonance images, recorded at 5 mm separation, of the entire thorax of a single subject. From the previous grey-level threshold segmentation of these MRIs carried out by (MacLeod et al. 1991), we built the torso model following a three-step approach as depicted in Figure 5.2.

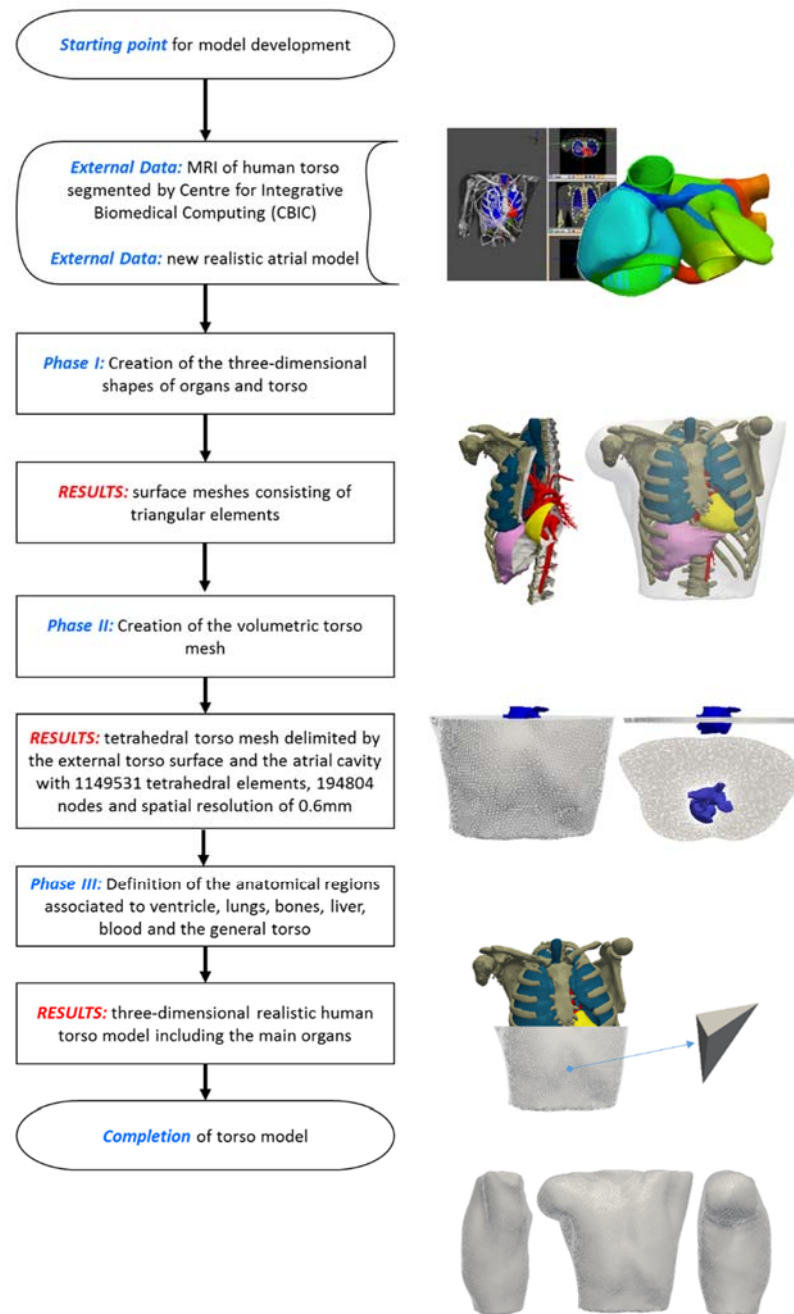
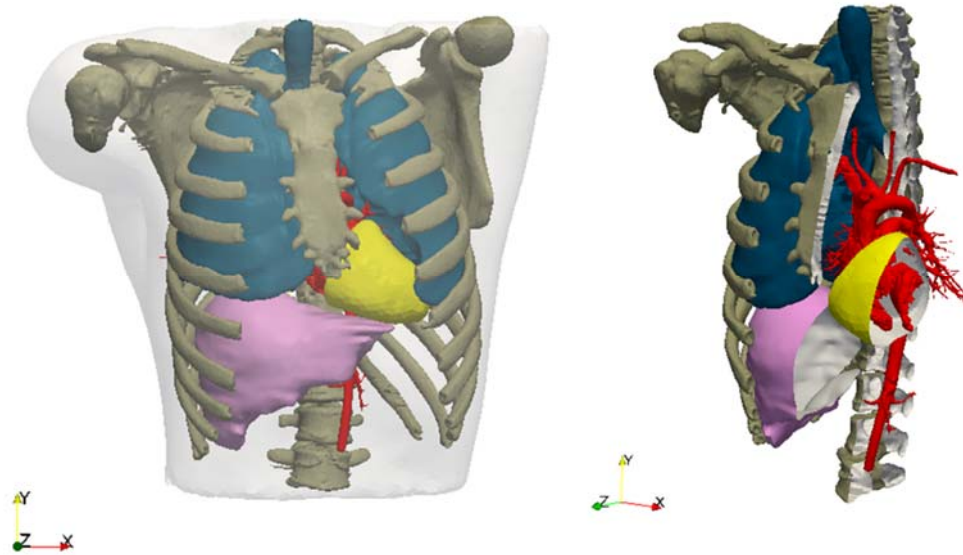


Figure 5.2: Building process of the human torso model

Phase I: Creation of the three-dimensional surfaces of organs and torso

The isosurfaces of the principal organs in the torso (myocardium, bones, liver, lungs, blood and chest) were obtained from a labelled MRI dataset. Following, they were manually corrected, remeshed and smoothed using the software Remesh 2.1 in order to obtain the enough uniformity and density of triangular elements. It was fundamental to correct intersection between regions and elements as well as mesh holes. The individual surfaces corresponding to each organ and the chest were then combined and converted into a single surface model in vtk (visual toolkit) format using the software Paraview 3.12.

In this process, the original atrial model belonging to the segmented torso was removed and replaced by our detailed anatomical atrial model by rigid registration. Since the torso model must be built and adapted to our new multi-scale atrial model (see chapter 4), the whole vtk torso mesh was relocated by using Paraview 3.12 to perfectly match and be lined up with the atrium. Final surfaces are shown in Figure 5.3.



**Figure 5.3: Surface meshes**

Left panel shows the whole torso mesh including myocardium, bones, liver, lungs, blood and chest. Right panel shows a transversal cut of the organ meshes.

Phase II: Creation of the volumetric torso mesh

The torso was segmented by using the Seg3D software (Cibc 2013) and meshed with tetrahedral elements by TetGen (Si & Gärtner 2005). The resulting solid mesh had 190804 nodes and 1149531 tetrahedral elements with a spatial resolution of 0.6 mm. The

tetrahedral elements of the torso that overlapped with the atrial myocardium were highly refined to increase the number of nodes at which the extracellular potential had to be calculated. In this refinement process, a set of 33905 additional torso nodes was included at a constant distance from the atrial boundary (0.8 mm) to reduce mathematical errors in the approximation of the extracellular potentials. The volumetric torso mesh is shown in Figure 5.4.

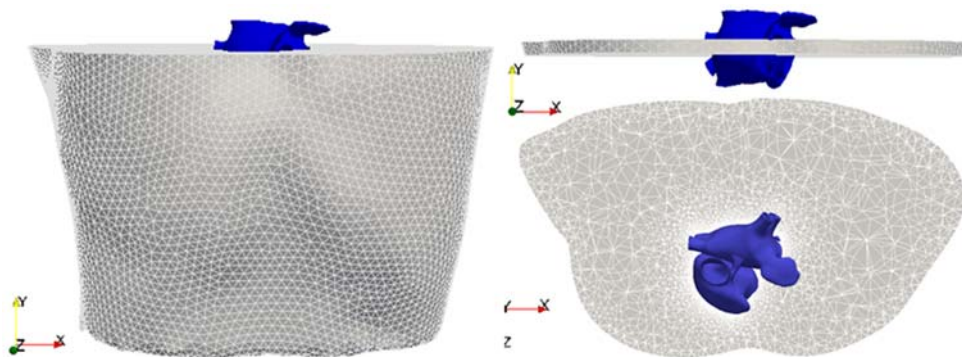


**Figure 5.4: Tetrahedral torso mesh**  
In blue, the atrial model.

Phase III: Definition of the anatomical regions associated to the organs

Each element of the model was then automatically labelled as lung, bone, liver, ventricle, blood, or general torso. The labelling algorithm determines first the centroid of each element. Then, it localizes each centroid with respect the surface meshes that delimit each organ. If the centroid is within a specific organ, then the corresponding element is labelled accordingly. Otherwise, the element is labelled as general torso. It is important to highlight that a single tetrahedron cannot be labelled twice so each of them have a unique identifying label and then they are unique within the torso mesh. The final torso mesh is shown in Figure 5.5.

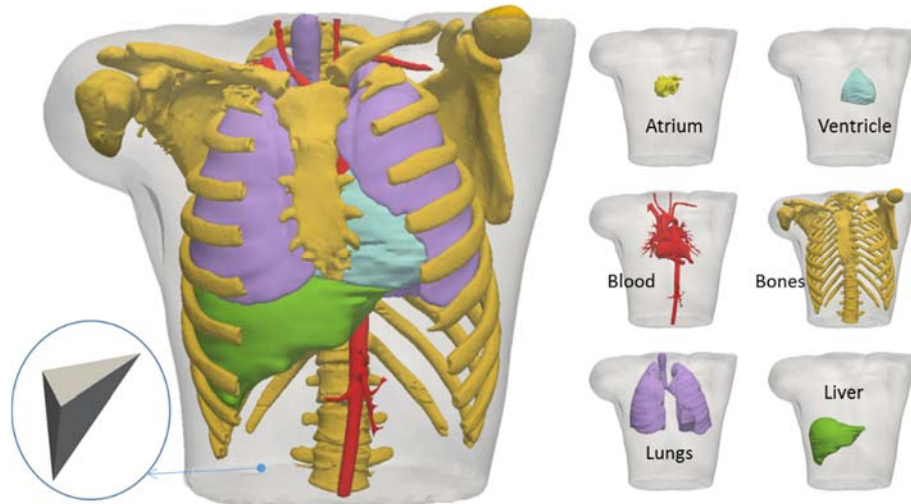


**Figure 5.5: Tetrahedral torso model including the most relevant organs**  
 i) Ventricle (light blue,), ii) bones (orange), iii) liver (green), iv) lungs (purple), v) blood (red) and v) chest (transparent white).

Other types of tissues such as fat and skeletal muscles have not been included. In the case of fat, we have considered that it mainly affects the amplitude of the signal at the torso surface so it might be mathematically corrected. On the other hand, since there is not enough experimental data regarding the orientation of muscular fibres in the torso, it seems very much cautious not to include this type of tissue.

This assignment is used to assign the corresponding organ conductivity to each region as reported in previous studies (MacLeod et al. 1991; C. Gabriel et al. 1996; Klepfer et al. 1997; Bradley et al. 2000; Bressler & Ding 2006; E. Poletti D. Fiorin & Ruggeri 2009). In this way, the new anisotropic torso model has the following conductivities: i) myocardium (4.589 mS/cm), ii) bone (0.200 mS/cm), iii) liver (0.277 mS/cm), iv) lungs (0.389 mS/cm), v) chest (2.390 mS/cm) and vi) blood (7.000 mS/cm). As can be seen in Table 5.1, all of these values are within experimental ranges.

**Table 5.1: Experimental and model values of tissue conductivities**

Anatomical Region	Model conductivities (mS/cm)	Experimental conductivities (mS/cm)	References
Myocardium (ventricles)	4.590	5.00	(Bradley et al., 2000)
		0.60~4.00	(Miklavčič et al., 2006)
		0.53~4.83	(Gabriel et al., 1996a, Keller et al., 2010)
Lungs	0.389	0.54	(MacLeod et al. 1991)
		0.50	(Bradley et al., 2000)
		0.24~0.90	(Miklavčič et al., 2006)
		0.39	(Bauer et al., 2010)
Bones	0.200	0.39	(Gabriel et al., 1996a, Keller et al., 2010)
		0.10~0.60	(MacLeod et al. 1991)
		0.20	(Miklavčič et al., 2006)
Blood	7.000	0.05~0.60	(Gabriel et al., 1996a, Keller et al., 2010)
		4.30~7.00	(Miklavčič et al., 2006)
		7.00	(Gabriel et al., 1996a, Keller et al., 2010)
Liver	0.277	4.35~10.0	(Gabriel et al., 1996a, Keller et al., 2010)
		0.23~2.00	(Miklavčič et al., 2006)
		0.28	(Gabriel et al., 1996a, Keller et al., 2010)
General Torso	2.390	0.28~2.00 2.39 2.20	(Klepper et al., 1997) (Bradley et al., 2000)

### 5.3. Propagation of atrial rhythms

The electrical propagation of APs in the atrium was mathematically described in chapter 4, section 4.1.2 (Equations 4.26 and 4.27) representing the monodomain model:

$$\nabla \cdot (\mathbf{D} \nabla V) = C_m \cdot \frac{\partial V}{\partial t} + I_{ion} \text{ in } \Omega_H$$

$$\mathbf{n} \cdot (\mathbf{D} \nabla V) = 0 \text{ in } \partial \Omega_H$$

where  $D$  was the equivalent conductivity tensor,  $V$  the transmembrane potential,  $I_{ion}$  the transmembrane ionic current that depends on the cellular model,  $C_m$  the membrane capacitance and  $\Omega_H$  was the heart domain.

After performing atrial simulations and obtaining the transmembrane potential,  $V_m$ , the next step forward needs to introduce the constraints governing the propagation of the electrical potential between the atrial and torso models. There exist two possibilities in the literature. The first one considers the heart and the torso completely coupled and then the limits impose to the heart-torso interface  $\partial\Omega_{H-T}$  are those defined by (Krassowska & Neu 1994; Pullan et al. 2005; Sundnes et al. 2006) as follows:

$$V_e = V_T \text{ en } \partial\Omega_{H-T} \quad \text{Equation 5.1}$$

$$\mathbf{D}_e \nabla V_e \cdot \mathbf{n} = \mathbf{D}_T \nabla V_T \cdot \mathbf{n} \text{ en } \partial\Omega_{H-T}, \quad \text{Equation 5.2}$$

where  $\mathbf{D}_e$  and  $V_e$  represent the conductivity tensor and the potential in the extracellular domain while  $\mathbf{D}_T$  and  $V_T$  represent the heterogeneous conductivity tensor and the extracellular potential propagated through the torso.

The second approach considers that the heart and the torso are completely uncoupled electrically (Boulakia et al. 2010). In this way, replacing Equation 5.2 with Equation 5.3 as defined by (Potse et al. 2006) the electrical feedback from the torso to the heart can be disregarded:

$$\mathbf{D}_e \nabla V_e \cdot \mathbf{n} = 0 \text{ en } \partial\Omega_{H-T}. \quad \text{Equation 5.3}$$

Once these boundary Dirichlet conditions between the heart and the torso are defined using any of the previous approaches, it is necessary to calculate the potential propagating through the torso up to its surface. Under quasi-stationary conditions (Malmivuo & Plonsey 1995), the torso volume can be considered as an isolated and passive conductor. Hence, the propagation of the extracellular potential throughout the torso is governed by the Laplace equation across the whole torso domain  $\Omega_T$  and then it is subjected to homogeneous Neumann boundary conditions:

$$\nabla \cdot (\mathbf{D}_T \nabla V_T) = 0 \text{ in } \Omega_T \quad \text{Equation 5.4}$$

$$\mathbf{n}_T \cdot (\mathbf{D}_T \nabla V_T) = 0 \text{ in } \partial\Omega_T \quad \text{Equation 5.5}$$

where  $\Omega_T$  represents the torso domain and  $\partial\Omega_H$  its external surface. Equation 5.5 constrains the torso surface stating that no electrical current can flow from the torso surface outwards.

### 5.3.1. The heat transfer equation

The system defined by Equation 5.3 to Equation 5.5 simplifies the propagation through the torso volume and can be solved using the heat transfer equation. Heat transfer in a rigid body can be easily obtained from the energy equation given by the following expression:

$$\int_v \rho \dot{u} \cdot dv = \int_s -\mathbf{q} \cdot \mathbf{n} \cdot dS + \int_v r \cdot dv \quad \text{Equation 5.6}$$

where  $\rho$  is the body density,  $u$  is the internal energy per unit of mass ( $J \cdot Kg^{-1}$ ),  $\mathbf{q}$  is the heat flow vector in the body surface  $S$  ( $W \cdot m^2$ ),  $\mathbf{n}$  is the normal and  $r$  represents a heat source per unit of volume  $v$ . The negative sign in the surface integral means that a heat flow entering to the system increases the internal energy and then the body temperature.

The body heat flow can be divided in i) heat flow produced by conduction trough the body ( $\mathbf{q}_K$ ), ii) convective heat due to the heat exchange between the body surface and the external environment ( $\mathbf{q}_h$ ), and iii) heat flow due to the radiation again between the body surface and the external environment ( $\mathbf{q}_R$ ). In this way,  $\mathbf{q}$  and Equation 5.6 may be rewritten as follows:

$$\int_v \rho \dot{u} \cdot dv = \int_s -(\mathbf{q}_K + \mathbf{q}_h + \mathbf{q}_R) \cdot \mathbf{n} \cdot dS + \int_v r \cdot dv \quad \text{Equation 5.7}$$

Using the Divergence Theorem to the surface integral related to  $\mathbf{q}_K$  and the Fourier's Law, the following equation can be inferred:

$$\mathbf{q}_K = -\mathbf{k} \cdot \nabla T \quad \text{Equation 5.8}$$

where  $\mathbf{k}$  is the conduction tensor given in ( $W \cdot m^{-1} \cdot K^{-1}$ ), and  $\nabla(\cdot)$  is the gradient operator. Hence, Equation 5.7 can be once more rewritten as:

$$\int_v \rho \dot{u} \cdot dv = \int_v (\nabla \cdot (\mathbf{k} \cdot \nabla T) + r) dv - \int_{S_q} (\mathbf{q}_h + \mathbf{q}_R) \cdot \mathbf{n} \cdot dS \quad \text{Equation 5.9}$$

The surface integral has been constrained to  $S_q$  aiming to differentiate the surface  $S_T$  where the temperature  $T$  is already specified, from the surface where convective or radiant heat flow is given,  $S = S_q \cup S_T$ .

In absence of mechanical work, the exchange of internal energy is proportional to the exchange in temperature  $T$  and this can be translated into:

$$C_p = \frac{\partial u}{\partial T} \quad \text{Equation 5.10}$$

where  $C_p$  is the specific heat given in ( $\text{J} \cdot \text{Kg}^{-1} \cdot \text{K}^{-1}$ ). We can now combine Equation 5.9 and Equation 5.10 to obtain the following expression:

$$\int_v \left( \rho C_p \cdot \frac{\partial T}{\partial t} - \nabla \cdot (\mathbf{k} \cdot \nabla T) - r \right) \cdot d\mathbf{v} = - \int_{S_q} (\mathbf{q}_h + \mathbf{q}_R) \cdot \mathbf{n} \cdot dS \quad \text{Equation 5.11}$$

In this expression, the volume integral represents the heat transfer equation while the surface integral refers to the boundary and the resting state conditions. We can now rewrite this Equation 5.11 using differential equations:

$$\rho C_p \cdot \frac{\partial T}{\partial t} - r = \nabla \cdot (\mathbf{k} \cdot \nabla T) \text{ in } v \quad \text{Equation 5.12}$$

$$\mathbf{q}_h = h(T - T_f) \text{ in } S_h \quad \text{Equation 5.13}$$

$$\mathbf{q}_R = \epsilon(T^4 - T_\infty^4) \text{ in } S_R \quad \text{Equation 5.14}$$

$$T = T_0 \text{ in } S_T \quad \text{Equation 5.15}$$

Equation 5.13 and Equation 5.14 define the convective and radiant heat flow respectively, while Equation 5.15 represents the prescribed temperature.

When comparing this equations system with the one corresponding to the monodomain model, a quick analogy can be pointed out:

$$\rho C_p = C_m \quad \text{Equation 5.16}$$

$$-r = \chi I_{ion} \quad \text{Equation 5.17}$$

$$\mathbf{k} = \mathbf{D} \quad \text{Equation 5.18}$$

### 5.3.2. The Finite Elements Method

In order to solve the previous equations system, it is necessary to use the variational form of Equation 5.12. Considering that  $\partial T = 0$  in all the points where  $T$  is already prescribed, Equation 5.12 can be multiplied by  $\partial T$  and integrated within the whole volume using the following expression:

$$\int_v f \nabla g \cdot dv = \int_S (fg) \mathbf{n} dS - \int_v g \nabla f \cdot dv \quad \text{Equation 5.19}$$

in order to get the final expression:

$$\begin{aligned} \int_v \rho C_p \cdot \partial T \cdot \frac{\partial T}{\partial t} dv &= \int_v (\nabla \partial T \cdot (\mathbf{k} \cdot \nabla T) + r \partial T) \cdot dv \\ &- \int_{S_q} \partial T (\mathbf{q}_h + \mathbf{q}_R) \cdot \mathbf{n} dS \\ &- \int_{S_T} \partial T \cdot (\mathbf{k} \cdot \nabla T) \cdot \mathbf{n} dS \end{aligned} \quad \text{Equation 5.20}$$

Like the case of atrial propagation through the myocardium, it is necessary to perform a spatial and temporal discretization to solve Equation 5.20. The spatial discretization requires the introduction of interpolation functions for the temperature  $T$ . Then,  $T$  uses the expression  $T = N_i T_i$  for  $i = 1 \dots n$  where  $N_i$  are the interpolation functions,  $T_i$  is the temperature at node  $i$  and  $n$  is the total number of nodes within the mesh of finite elements. Considering also an implicit integration of Equation 5.20, the following expression can be easily deduced:

$$\begin{aligned} \partial T_i \int_v \rho C_p N_i \cdot \frac{N_j T_j^{k+1} - N_j T_j^k}{\Delta t} dv \\ &= -\partial T_i \left[ \int_v \nabla N_i \cdot \mathbf{k}^{k+1} \cdot \nabla N_j \cdot dv \right] T_j^{k+1} \\ &+ \partial T_i \int_v r^{k+1} N_i dv \\ &- \partial T_i \int_{S_q} N_i \cdot (\mathbf{q}_h + \mathbf{q}_R) \cdot \mathbf{n} dS \end{aligned} \quad \text{Equation 5.21}$$

where  $k$  refers to the time  $t^k$  and the surface integral on  $S_T$  has been removed since it is easily satisfied by using the formulation itself. For the monodomain approach and using Equation 5.12 to Equation 5.18, the Equation 5.21 can be replaced by Equation 5.22:

$$\begin{aligned} \partial T_i \int_v C_m N_i \cdot \frac{N_j T_j^{k+1} - N_j T_j^k}{\Delta t} d\nu \\ = -\partial T_i \left[ \int_v \nabla N_i \cdot D^{k+1} \cdot \nabla N_j \cdot d\nu \right] T_j^{k+1} \\ - \partial T_i \int_v I_{ion}^k N_i d\nu \end{aligned} \quad \text{Equation 5.22}$$

These equations can be solved using the operator splitting method (as in the case of the atrial propagation) using two steps:

Step 1: using  $V_i^k$  as resting state condition,  $V_i^*$  can be determined as follows:

$$V_i^* = V_i^k - \Delta t \cdot I_{ion}(V_i^k, t^k). \quad \text{Equation 5.23}$$

Step 2: using  $V_i^*$ ,  $V_i^{k+1}$  can be computed as:

$$\begin{aligned} \partial T_i \int_v C_m N_i \cdot \frac{N_j T_j^{k+1} - N_j T_j^k}{\Delta t} d\nu \\ = -\partial T_i \left[ \int_v \nabla N_i \cdot D^{k+1} \cdot \nabla N_j \cdot d\nu \right] T_j^{k+1} \end{aligned} \quad \text{Equation 5.24}$$

As can be seen, the propagation through the torso simplifies even more the monodomain approach when it considers a single and stationary heat transfer problem with adiabatic conditions in the torso surface and the temperature (variable representing the electrical potential) prescribed in the atrium-torso interface. In this situation, Equation 5.24 can be simplified a bit more giving rise to the equation that describes the propagation of the electrical potential through the torso model:

$$-\partial T_i \left[ \int_v \nabla N_i \cdot \mathbf{k}^{k+1} \cdot \nabla N_j \cdot dv \right] T_j^{k+1} = 0 \text{ en } \Omega_T \quad \text{Equation 5.25}$$

$$T = T_0 \text{ en } \partial\Omega_T, \quad \text{Equation 5.26}$$

where  $\mathbf{k}^{k+1} = \mathbf{D}$  is the conductance per unit length and  $T$  is the variable being sought.

The fundamentals driving the heat transfer process are two: i) the energy in each material is proportional to the temperature, the density and the specific heat referred to the specific material; ii) the heat transfer across boundaries is proportional to the conductivity, the temperature gradient in each region and the contact surface between regions (Ii & Herod 1997). The system defined by Equation 5.25 and Equation 5.26 describes the propagation of electrical potential through the finite elements of the torso mesh. The solution is then the potential value in each torso surface lead (P-waves) or the potentials registered at every single node of the torso (BSPM) for each time instant.

Some previous authors such as (Sachse 2004; Pullan et al. 2005; Sundnes et al. 2006) have simulated cardiac electrophysiology without considering the reaction-diffusion models to compute the ECG. However, other studies carried out by (Lines et al. 2003; Potse et al. 2003; Trudel et al. 2004; Keller et al. 2007; Potse et al. 2009) already considered the bidomain or monodomain approaches, although only (Potse et al. 2003; Potse et al. 2009) provided the final simulations of the standard ECG leads.

We have solved the monodomain model using the operator splitting numerical scheme with the ELVIRA software (Heidenreich et al. 2010) and a constant time step of  $dt = 0.02$  ms. The Laplace equations, governing the propagation of the extracellular potentials throughout the torso, was solved using ABAQUS (Dassault Systèmes Simulia Corp.). Under these conditions, we are able to obtain the potential for all the nodes in the torso domain every 1 ms. The volumetric conductor thus might allow us to study the potential maps at the surface where P-waves and surface potential maps are registered, but also inside the torso.

#### 5.4. Body Surface Potential Maps (BSPM)

The distribution of potentials on the torso at different time points of the atrial activation is shown in Figure 5.6 on coronal and axial planes where the characteristic electrical dipole is clearly visible. During SAN depolarization ( $t = 0$  ms, not shown in the figure) the atria and torso remain in a resting state. At  $t = 26$  ms there is a visible dipole located on the upper right quadrant of the frontal chest (Figure 5.6b). For the following 44 ms the dipole slightly rotates towards the lower left quadrant and then backwards (at  $t = 70$  ms) until it completely disappears from the surface when the RA is almost depolarized (at  $t = 93$  ms). This rotation is clearly visible in the axial plane (Figure 5.6c). Atrial depolarization produces the maximum potential registered on the torso surface at  $t = 45$

ms, when the atrial wavefront is travelling across the RLW and the RAS towards the upper side of the TV, and the interatrial wavefront starts the activation of the LA through the BB. At  $t = 70$  ms, the electrical propagation flows towards the isthmus on the RA, and the left superior wavefront on the LA splits into three different directions (see also Figure 4.22 in chapter 4, arrows 5 to 7), causing a dipole rotation and forcing higher potentials towards the posterior side of the torso. At  $t = 93$  ms, the RA is almost depolarized but some regions in the LA such as the LAA, the MV, the CS and the LPV are still in a resting state. From then until  $t = 132$  ms the potentials registered on the surface start decreasing, as can be observed in Figure 5.6b-c.

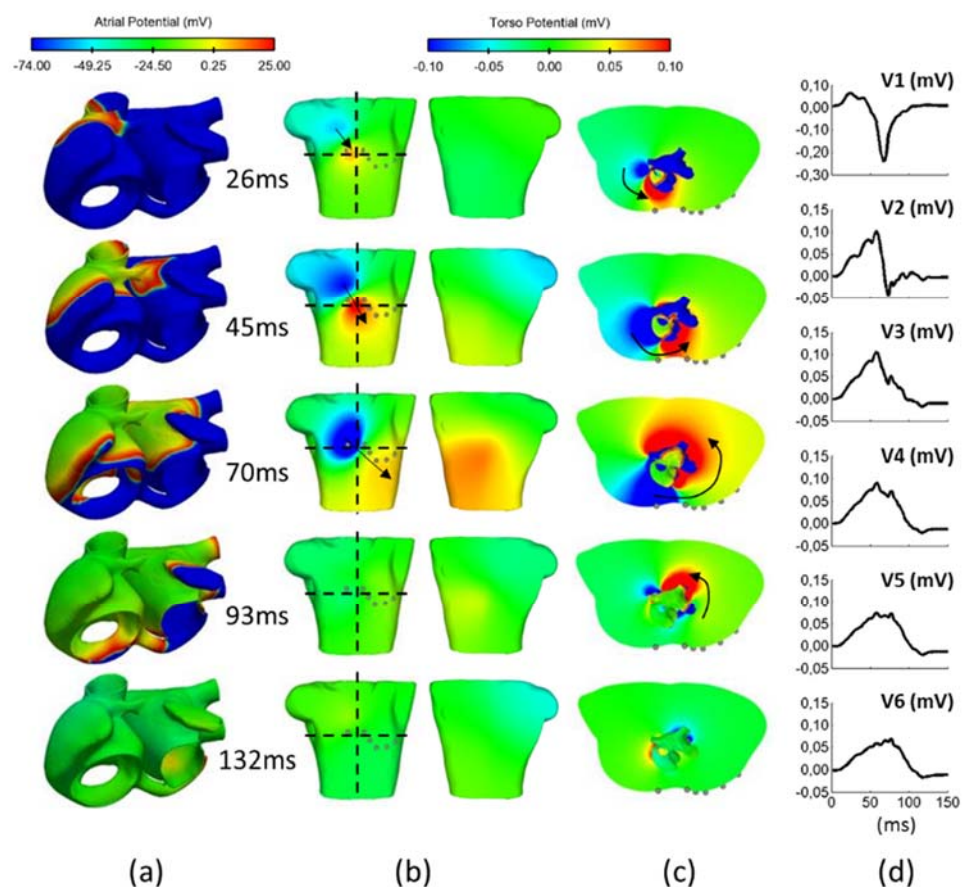


**Figure 5.6: Body surface potential maps over time**  
 a) Atrial activation sequence at characteristic time points (first contact with BB at  $t = 26$ ms; starting depolarization of LA at  $t = 45$ ms; rotation of the atrial wavefront at  $t = 70$ ms; final RA depolarization

from  $t = 93\text{ms}$ ; latest LA depolarization time at  $t = 132\text{ms}$ ); b) Torso frontal (left) and rear (right) surface displaying the electrical dipole at the same instants; c) Axial torso plane at the V1 and V2 height; d) P-wave (mV) registered at the precordial leads V1 to V6.

P-waves with negative single-phase are obtained on the upper right chest (Figure 5.6d) precordial lead V1, while positive single-phases appear on the lower anterior torso precordial leads V3 to V6. Biphasic waveforms with initial positive deflection are observed from leads on the central and upper parasternal region (Figure 5.6d, precordial lead V2).

#### **5.4.1. Study of the P-wave across the torso surface**

We performed a deeper signal analysis computing the Root Means Square (RMS) on the whole BSPM (from now on B-RMS) to obtain additional information on the P-wave signal magnitude and its morphology (Figure 5.7). Next paragraphs focus on analysing regional characteristics of the P-waves.

The signals registered within the dotted square at the central position (high B-RMS values around  $0.031 \text{ mVrms}$ ) correspond to the region of maxima potentials and have very similar biphasic morphology ( $0.35 \text{ mVpp}$ ). The main characteristic of all the P-waves within this square lies in their biphasic morphologies with a turning point from positive to negative potentials at  $t = 70 \text{ ms}$ . This morphology is due to the rotation of the electrical dipole (see Figure 4.22 in chapter 4).

P-waves in the upper right quadrant (dotted circle) also have the highest values of B-RMS, but show monophasic patterns with high negative amplitude ( $0.22 \text{ mVpp}$ ). A negative to positive change in the signal slope is observed in all the signals registered within this circle at  $t = 70 \text{ ms}$ , also produced by the rotation of the electrical dipole.

P-waves from the upper left quadrant (dotted diamond) and the lower right panel (dotted star) present low values of B-RMS ( $0.002 \text{ mVrms}$ ) and a very noisy monophasic morphology with low amplitude ( $0.04 \text{ mVpp}$  and  $0.03 \text{ mVpp}$ , respectively) what prevented us from inferring useful information related to atrial activation.

Finally, in the lower left quadrant (dotted triangle), we registered P-waves with medium values of B-RMS, indicating once again signals with sufficient monophasic amplitude ( $0.10 \text{ mVpp}$ ) to be considered useful information. As in the previous cases, the double peak at  $t = 70 \text{ ms}$  (M-shaped morphology) represents the rotation of the electrical dipole.

Potential B-RMS distribution in the rear torso was also analysed (Figure 5.7b) and similar conclusions were reached. Only signals registered on the green area of the rear central (dotted square) and lower quadrants (dotted triangle and star) allowed noise-free signals to be analysed.

This analysis allows us to predict the areas on the torso surface in which P-waves have enough amplitude and sufficiently well-defined morphology to be considered as sources of information for clinical decisions. Based on these results, we define the frontal upper

right and the frontal and rear lower left quadrants as the best sites to register P-wave signals. The blue coloured areas can thus be discarded in the analysis of the whole BSPM.

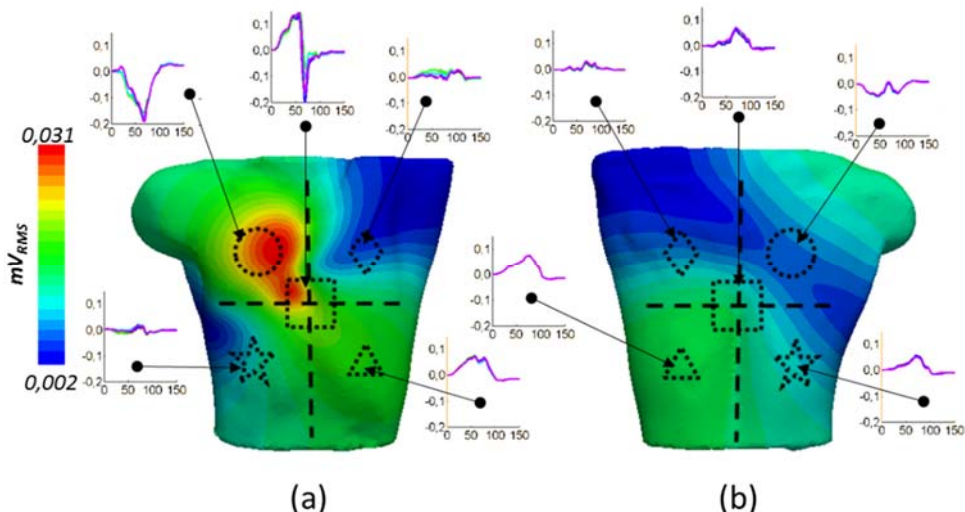


**Figure 5.7: Spatial information from the potential root mean square (B-RMS)**  
a) Frontal and b) rear torso views. Geometric forms in each quadrant represent the torso area where the displayed P-waves are registered (units: mV vs ms).

#### 5.4.2. Study of determinants for the P-wave characteristics

In this multi-scale validation process of physiological atrial activation and its propagation through the torso, it is important not only to analyse the signals on the torso surface, but also to find the conditions that determine the amplitude, duration and morphology of the P-waves. Two main effects must therefore be taken into consideration: i) the atrial anisotropy produced by the distribution of the atrial fibres and ii) the influence of the torso as a volumetric conductor. The individual effects on the P-wave morphology produced by changes in these two properties are shown in Figure 5.8. The left panel shows differences between anisotropic (black line) and isotropic (red line) atrial propagation (see also Figure 4.24 in chapter 4). The main changes produced by an isotropic atrial model when registering at the unipolar precordial or standard leads (only shown V3, V6 and the standard lead III) are: a) reduction of P-wave duration (-38% measured on V3); b) increase of P-wave maximum amplitude (37% measured on V3); and c) simultaneous depolarization of the RA and the LA, which causes differences in the activation patterns with erratic morphologies.

In Figure 5.8 right panel, we analyse differences in P-wave morphology considering: a) a complete heterogeneous torso model, and b) the torso as a homogenous and infinite volumetric conductor. The P-wave produced using the homogenous volumetric approach (red line) differs from the heterogeneous approach (black line) in three significant aspects: a) reduction of P-wave duration (-43% measured on V3); b) reduction of P-wave amplitude (-56% measured on V3) opposite to the effect produced by isotropy; and c) morphological changes.

These results reveal the importance of considering muscle fibre directions in the atrial model and tissue conductivities in the torso model. Both properties significantly influence the amplitude, duration and morphology of P-waves.

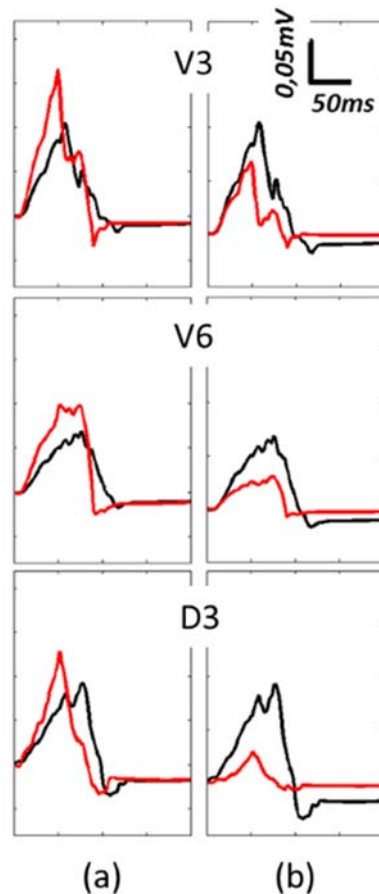


**Figure 5.8: Effects of the tissue heterogeneity in the P-wave morphology**

- a) Differences between anisotropic (black line) and isotropic (red line) atrial tissue propagation using a complete torso model; b) Differences between a complete torso model with heterogeneous electrical conductivities and the heat transfer equation (black line) and P-waves registered considering a homogeneous and infinite torso approach using the equation of extracellular potentials (red line).

## 5.5. Contribution of individual atrial regions to normal atrial behaviour

### 5.5.1. Study of regions with greatest impact on P-wave morphology

Figure 5.6 and Figure 5.7 showed that maximum potential values and B-RMS produced by the whole atrium are registered in the centre of the torso frontal surface. However, one of the biggest challenges for cardiac electrophysiologists lies in to assess individual contributions from each region of the atria to the complete ECG morphology. Although it is practically unfeasible to divide and individualize the atrial activation sequence produced by each of the anatomical atrial structures, the use of electrophysiological modelling may help to understand how different tissues contribute to the genesis of the BSPM and the P-wave of the ECG.

As it was possible to isolate the contribution of each atrial region by masking the electrical contribution of other regions, we analysed the individual contribution to the B-RMS potential and corresponding P-wave produced by each atrial region in sinus rhythm. Figure 5.9a shows the torso surface area in which the different atrial regions present their maximum contribution to B-RMS maxima.

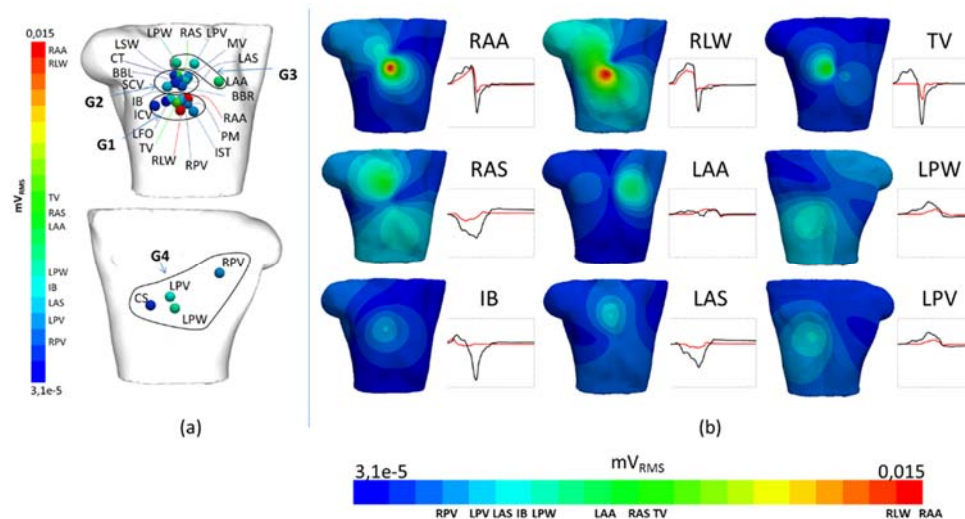


**Figure 5.9: Contribution from individual atrial regions to the P-wave**

a) Location of the maximum value of potential RMS produced from each atrial structure; b) B-RMS patterns (mV<sub>RMS</sub>) from the individual atrial structures with the highest contributions. Also displayed

the P-waves (mV vs ms) registered at the point with maximum potential RMS value (red line) compared with the total P-wave (black line) registered at the same node.

Four spatial clusters can be identified. The G1 group, localized at the lowest position of the frontal torso, encloses the contributions from RAA, RLW, TV, IB, PM, IST, RPV, LFO and ICV. The highest values are produced by RAA and RLW, as can be confirmed in Figure 5.9b from the amplitude of the individual P-wave (in red) related to the total P-wave (in black and produced by the whole atrium) registered at the same node. The G2, at the middle position, groups contributions from RAS, LAS, LSW, CT, BBL, SCV, BBR and MV. The G3 group, at the upper position, shows contributions from LAA, LPW and LPV. Finally, the G4 clusters contributions from LPW, LPV, RPV and CS, all of them regions with better registry on the back.

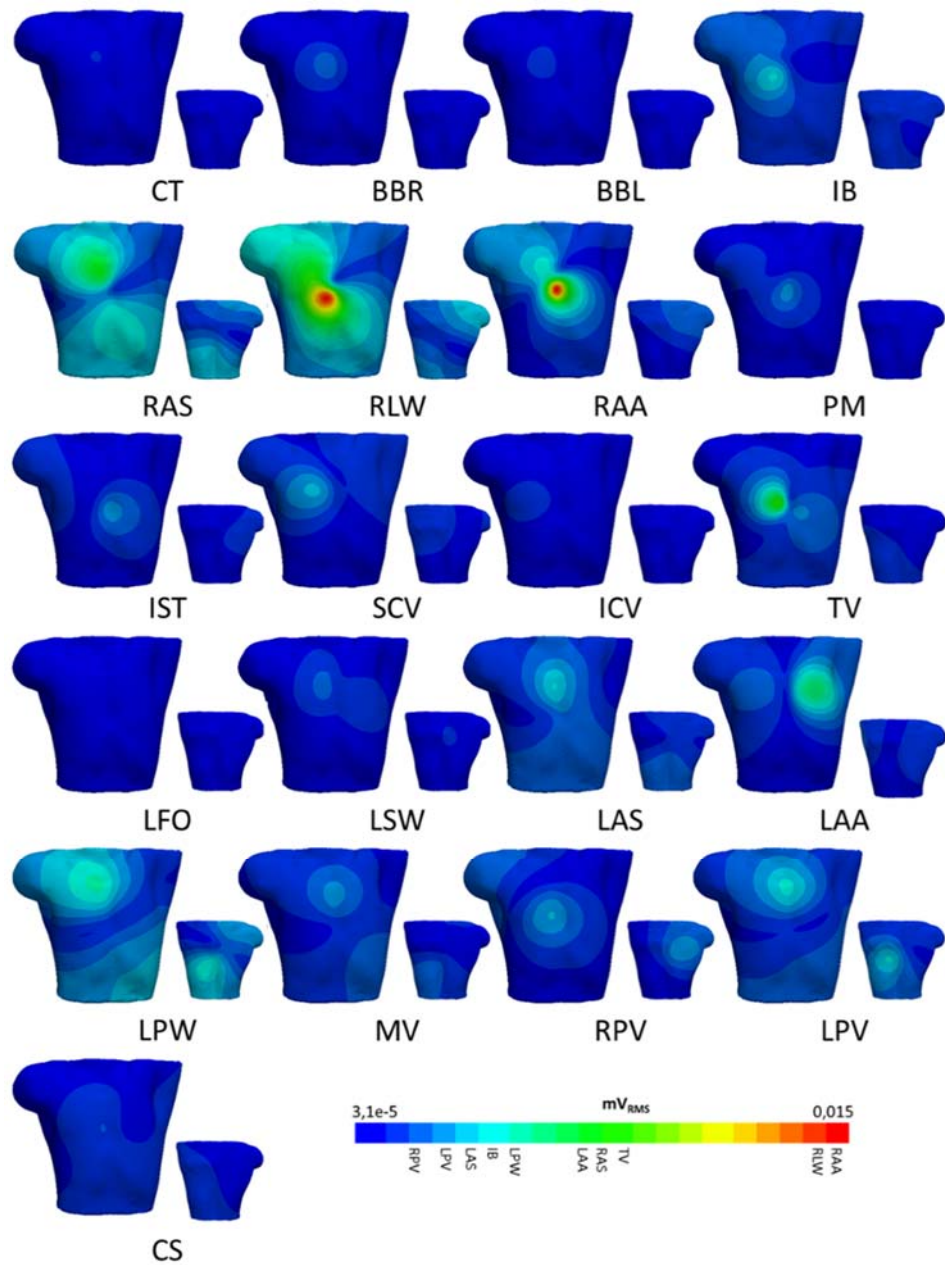


**Figure 5.10: Body surface RMS maps from the 21 individualized atrial regions**

It is worth noting that only nine atrial regions (RAA, RLW, TV, RAS, LAA, IB and LAS on the frontal view, and LPW and LPV on the rear view) produce a significant potential contribution when considering the whole range of potential RMS and the B-RMS maps from each region. This can be observed in Figure 5.9b, where coloured maps show very high (red) to medium (green) RMS values. The other 12 atrial structures shown in Figure 5.10 produce individual homogeneous body maps with RMS (blueish) values lower than 20% of the maximum contribution when considering the whole atrium.

Figure 5.11a shows the potential RMS patterns obtained by adding the contribution of the previous nine regions with the greatest impact on the P-wave, which are responsible for the 89% of the total contribution produced by the 21 regions. The other 12 structures, Figure 5.11b, are responsible for the remaining 11%, suggesting that the morphology of the total P-wave in sinus rhythm depends mainly on these 9 nine identified regions (even when they only represent the 65% of the total atrial volume).

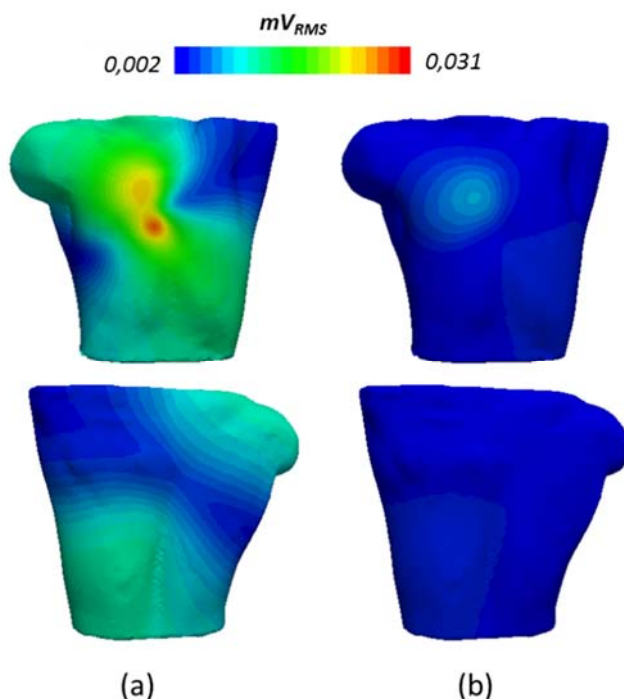


**Figure 5.11: Added contribution from atrial regions with highest and lowest impact**  
 a) Effective contribution of the 9 regions jointly responsible for the 89% of the total contribution (RAA, RLW, TV, RAS, LAA, LPW, IB, LAS and LPV); b) Effective contribution from the remaining 12 regions responsible for the 11% of the total contribution.

### **5.5.2. Study of individual impact on electrocardiographic leads**

These individual contributions were also analysed with respect to different positions of the electrocardiographic leads. Figure 5.12 shows the signals registered in precordial leads V3 and V6, the standard lead III, and on the rear side N2, N5 and N8 (see red points for the specific localization on the torso surface and Figure 5.13 and Figure 5.14 for the remaining leads).

The P-waves (black lines) produced by the complete atrial depolarization at different standard locations are displayed in Figure 5.12a (torso front) and Figure 5.12c (torso back). The contribution from the RA structures (solid red line) and the contribution from the LA structures (dotted red line) are also depicted in the figure. Figure 5.12b (torso front) and Figure 5.12d (back) show only those individual regions whose contributions mainly determine the RA and the LA total waveforms, with a maximum amplitude larger than 30% of the maximum P-wave amplitude.

In the case of V3, and similarly to V1 and V2 (see Figure 5.13 and Figure 5.14), the RA contribution is significantly higher than LA and determines the P-wave morphology. Within RA, the V3 waveform is mainly determined by the RLW and the RAA (blue lines) and the same occurs with lead V2. In the case of V1, the TV and the RLW contributions determine the waveform. For the LA, no individual region contributes more than 30% and therefore the LA waveform is the result of a number of small contributions. The behaviour of the other three precordial leads is similar to the behaviour observed for V6 in Figure 5.12 (see Figure 5.13 and Figure 5.14 for V4 and V5).

In V6, the RA morphology is mainly determined by the RLW (blue line), but no particular region defines the LA. However, the P-wave is the result of comparable contributions from both atria, where RA dominates the first part of the wave (until  $t = 70$  ms) while LA starts dominating from then to the end.

Finally, when registering Einthoven leads, the resulting P-wave depends on the specific lead. However, it must be noticed that both atria overlap their effects to produce M-shaped complexes with the inflection time at  $t = 70$  ms. In the case of the standard lead III (D3), no individual region from RA determines the RA waveform and only LPW (orange line) appears to significantly contribute to LA morphology. However, standard lead I (D1) is defined by the contributions of RLW plus LAA, and Einthoven lead II (D2) from those produced by RLW, RAS and LPW.

We also showed in Figure 5.9 and Figure 5.10 that LPW, RPV, LPV and CS produced their maximum potential on the back, where the contribution from LA structures is much higher. This is also consistent with the results in Figure 5.12d, in which, as we move towards the area of the biggest contribution, P-wave amplitude increases and the atrial structures responsible for the P-wave signal are mainly from the LA. Thus, the LPV and the LPW are the only regions defining the morphology at the central and lower rear leads N5 and N8. Figure 5.13 to Figure 5.16 show the electrical signals registered on eighteen leads on the frontal and rear view of the torso surface.

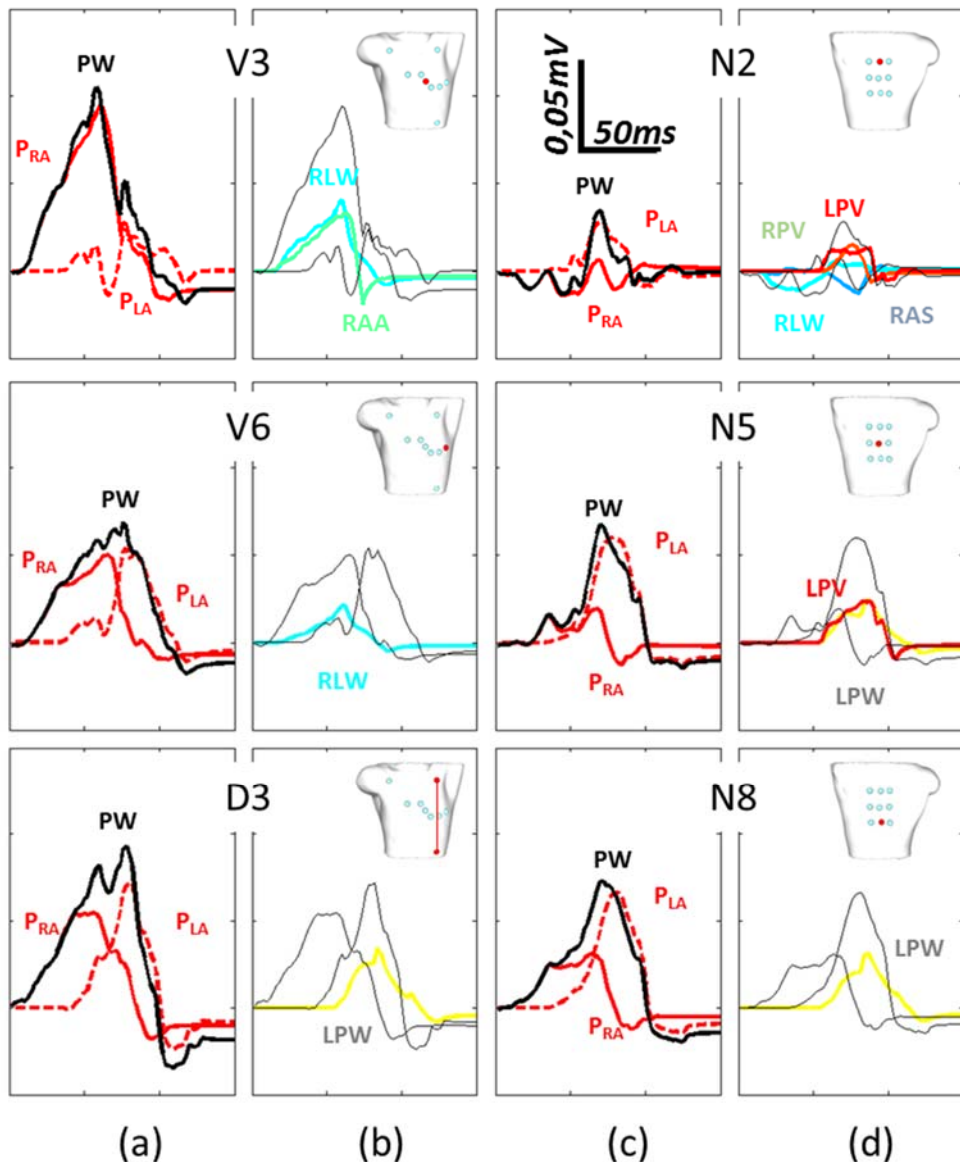


**Figure 5.12: P-waves registered on precordial and standard leads (V3, V6 and D3)**  
 Panels a) and c) represent the P-wave produced by the whole atria depolarization (black line), the contribution from the RA structures (continuous red line) and the contribution from the structures in LA (dotted red line). Panels b) and d) show only those individual regions with maximum amplitude of at least the 30% of the maximum P-wave amplitude registered at the frontal and rear sides.

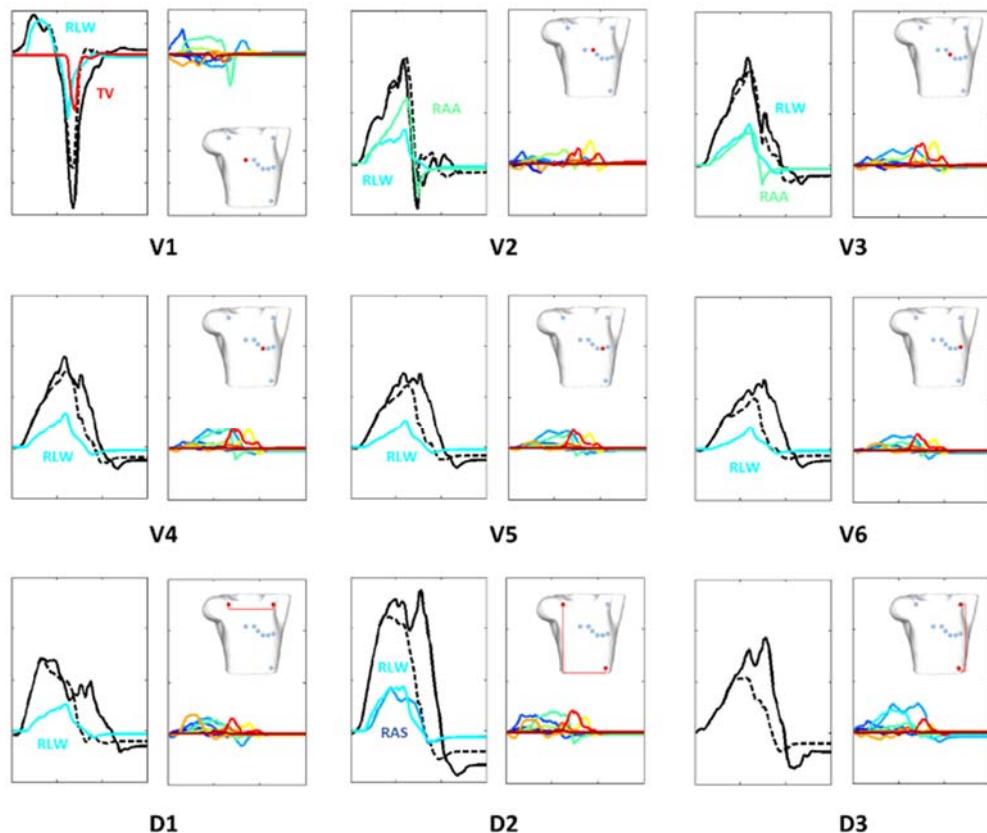


**Figure 5.13: P-waves produced by the RA structures**

Precordial V1 to V6 leads. Standard I (D1), II (D2) and III (D3) leads. For each lead: left panel shows the standard P-wave (continuous black line), the P-wave produced by the RA (dotted black line) and the P-waves produced by individual structures with a contribution higher than 30% of the total P-wave maximum amplitude (coloured lines); right panel shows the individual P-waves from RA structures below that 30% (the remaining atrial structures).

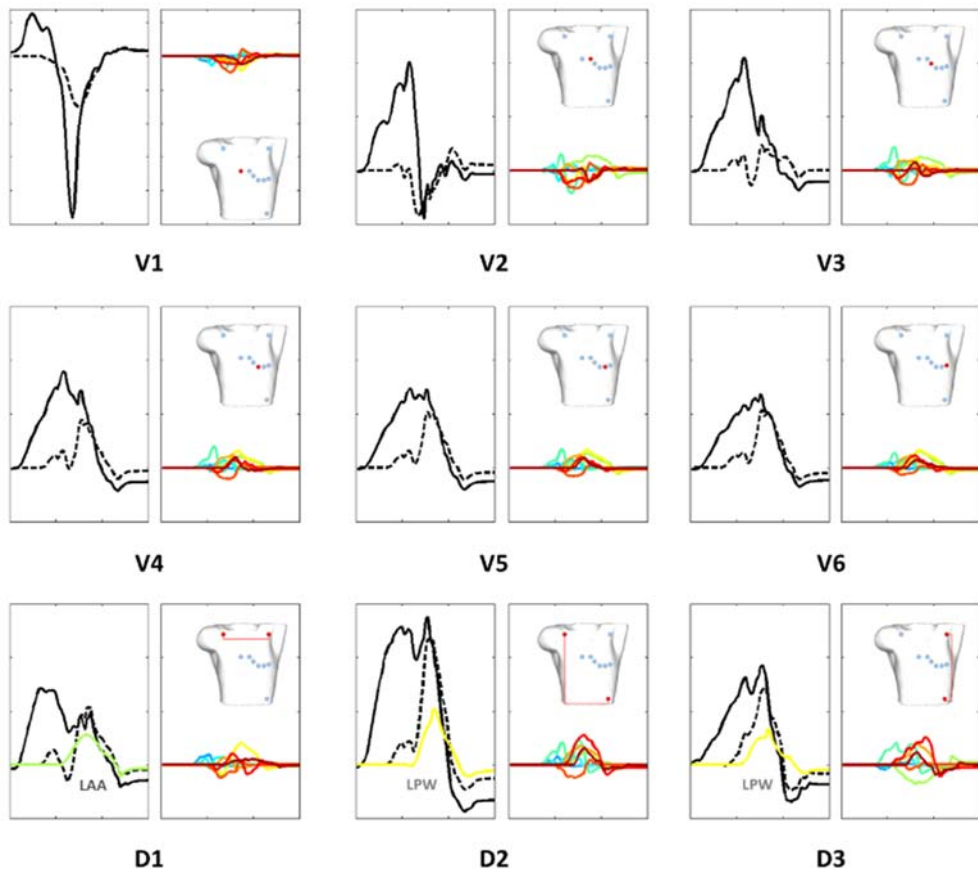


**Figure 5.14: P-waves produced by the LA structures**

Precordial V1 to V6 leads. Standard I (D1), II (D2) and III (D3) leads. For each lead: left panel shows the standard P-wave (continuous black line), the P-wave produced by the LA (dotted black line) and the P-waves produced by individual structures with a contribution higher than 30% of the total P-wave maximum amplitude (coloured lines); right panel shows the individual P-waves from LA structures below that 30% (the remaining atrial structures).

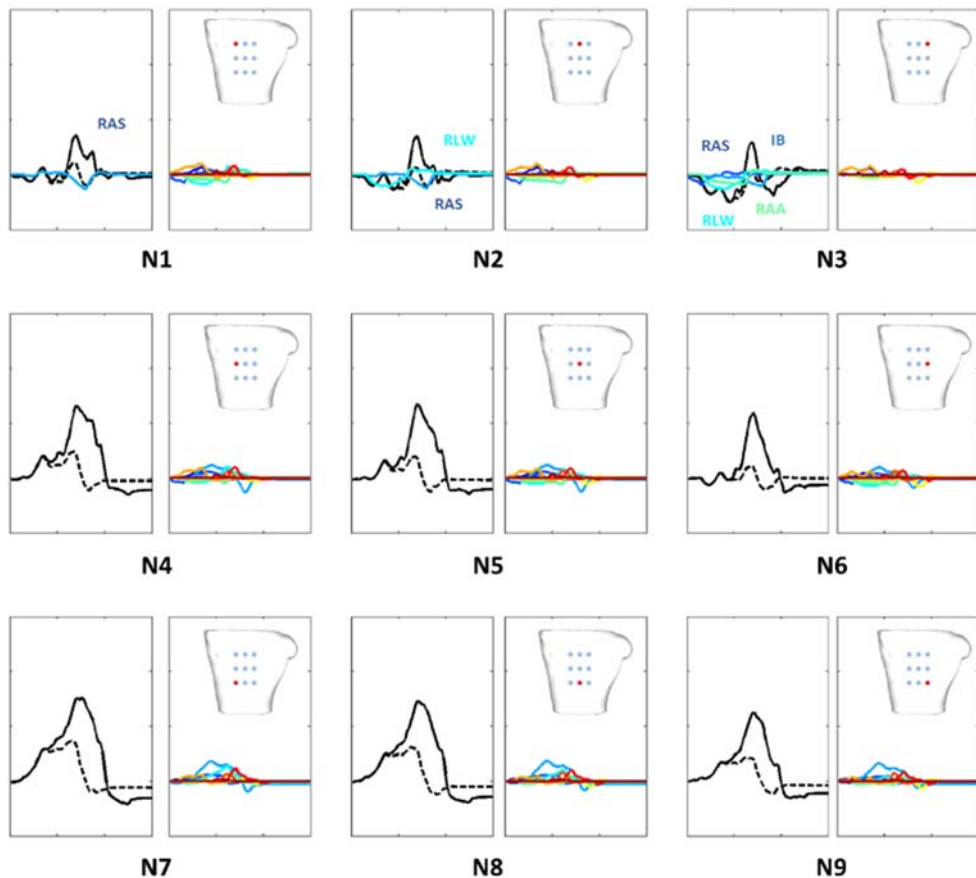


**Figure 5.15: P-waves produced by the RA structures registered on the rear torso**

For each lead: left panel shows the standard P-wave (continuous black line), the P-wave produced by the RA (dotted black line) and the P-waves produced by individual structures with a contribution higher than 30% of the total P-wave maximum amplitude (coloured lines); right panel shows the individual P-waves from RA structures below that 30% (the remaining atrial structures).

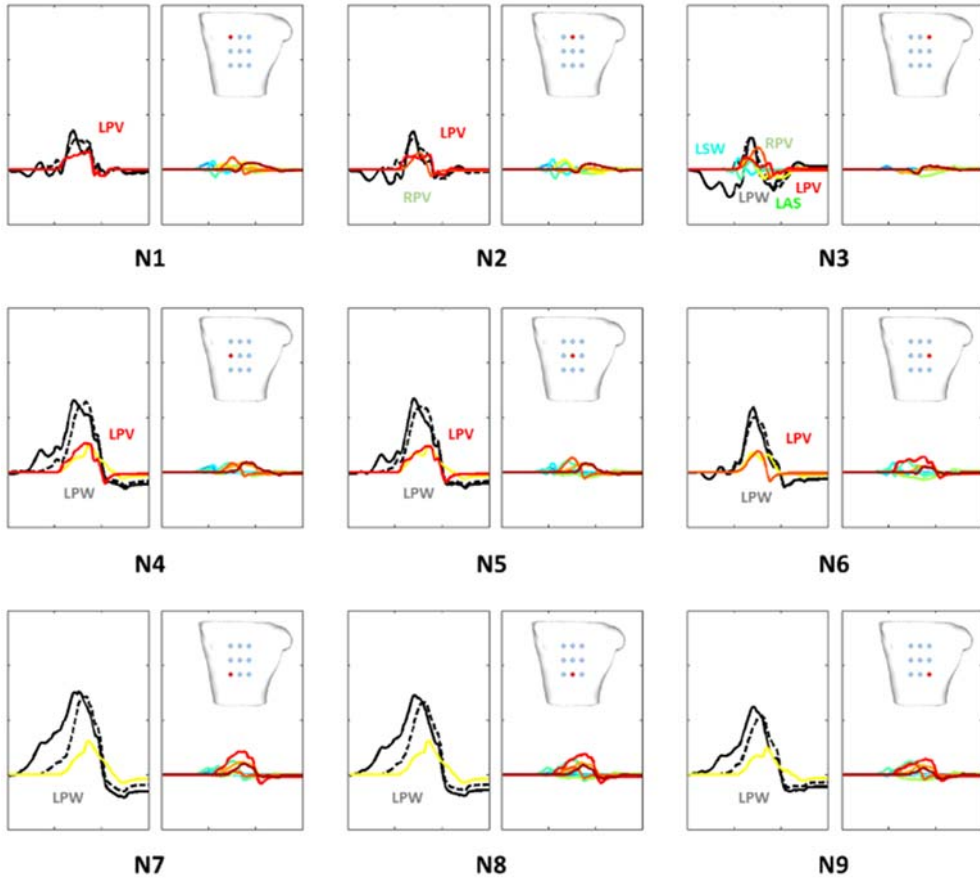


**Figure 5.16: P-waves produced by the LA structures registered on the rear torso**

For each lead: left panel shows the standard P-wave (continuous black line), the P-wave produced by the LA (dotted black line) and the P-waves produced by individual structures with a contribution higher than 30% of the total P-wave maximum amplitude (coloured lines); right panel shows the individual P-waves from LA structures below that 30% (the remaining atrial structures).

## 5.6. Discussion

This chapter presents a new detailed computer torso model fitted to the atrial model described in chapter 4, giving rise to a novel and realistic multi-scale atrial-torso model. A fast systematic pipeline to build the torso model was developed and the most standard approach based on the concept of heat transfer was used to compute the electrical wave-front propagation. This integrated model may allow simulating the atrial electrical activity while it propagates through the torso to its surface. Therefore, facilitating the use of

this computational atrial-torso model for clinical applications such as those devoted to the guidance and planning of electrophysiological therapies in patients suffering from atrial arrhythmias.

This kind of torso models has been used to deal with both, the forward and the inverse problems in electrocardiography. Both approaches pursue the same answers in regards the mechanisms and origin of atrial arrhythmias. During the present decade, there have been a number of works based on both, the analysis of the P-wave and torso surface potentials (Keller et al. 2010; Weber, Luik, et al. 2011; Krueger et al. 2012; Lenkova et al. 2012; Alday et al. 2015; Perez Alday et al. 2016) and on the electrocardiographic imaging ECGi (Rudy 2010; Wang et al. 2012; Shah et al. 2014; Figuera et al. 2016). Since the inverse problem is still very computational expensive, studies based on BSPM and BSPM-derived biomarkers remains the reasonable approach to non-invasively analyse atrial activity under physiological and pathological conditions.

### **5.6.1. Realistic torso model**

The influence of the torso model on the volumetric propagation of the atrial activation and on the morphology of the resulting P-waves and BSPM was analysed. The first computational torso models considered the chest as a finite, homogeneous and isotropic conductor and did not take into account changes produced by tissues and organs (Rudy & Plonsey 1980; Abboud et al. 1991; Leon & Horacek 1991). The first model that considered the different electrical tissue properties (skin, fat, muscle, bone and vessels) and organs (lungs and heart) was developed by (MacLeod et al. 1991), who used 116 MRIs from a single patient. Subsequent studies (van Dam & van Oosterom 2005; Keller et al. 2010; Keller et al. 2011) were able to predict changes in forward-calculated body surface potential maps (BSPMs) caused by variations in tissue conductivities. More recent torso models (Lenkova et al. 2012; Krueger et al. 2012) tried to adapt the anatomical form of the torso to different types of patients, aiming to deal with the inverse problem in electrocardiography.

The new torso model developed in the present thesis includes all these previous elements: a realistic population-based anatomy derived from image sequences, the most influential organs with realistic conductivity values. The new model makes it possible not only to study surface maps, but also volumetric maps, which can help in the understanding of the influence on P-wave morphology of: atrial fibre direction, electrophysiological tissue heterogeneity, local atrial conductivity and anisotropy, and organ conductivities.

Our results show that realistic atrial fibre orientation and heterogeneous torso models are essential characteristics of multi-scale models when they are used to simulate human atrial and torso behaviours.

### **5.6.2. Body Surface Potential Maps and P-waves**

In clinical practice it is rather difficult to acquire electro anatomical maps (EAMs) simultaneously to BSPMs, and impossible for healthy subjects. Furthermore, only limited

data on BSPM is available in clinical routine. This is due to the relative novelty of BSPM, the lack of consensus in the number and position of leads in experimental BSPM (M. Guillem et al. 2009) and the difficulty in interpreting such a large amount of information (van der Graaf et al. 2014). The enhanced spatial resolution provided by the multiple electrode system provides more detailed information on temporal and spatial distributions of cardiac electrical activity than the standard 12-lead electrocardiography (Zarychta et al. 2007; Fereniec et al. 2011; Safdarian et al. 2013). Also, as it has been already stated, understanding BSPM during normal cardiac excitation should also serve as the baseline for understanding abnormal cardiac electrical activity and rhythm disorders of the heart (Ramanathan et al. 2006).

The use of computational modelling techniques and the specific atrial-torso multi-scale model developed here may help not only to understand normal atrial excitation and how this electrical sequence physiologically propagates through the torso, but also i) to study the volumetric and superficial effect produced by the excitation of the complete atrium and also those effects produced by individual atrial structures; and ii) to rapidly infer morphological information on the superficial P-waves in any lead.

We have shown that, when considering anisotropy, physiological atrial depolarization produces a standard electrical pattern on the BSPM different from that produced when fibre orientation is neglected (Figure 5.8) and comparable to those experimentally measured by (Lian et al. 2002; Ramanathan et al. 2006; Kozlíková 2007; Robles De Medina et al. 2014). In this situation, a dipolar distribution characterizes the surface potential maps with negative and positive time integral distributions localized in the frontal upper right and lower left quadrants, respectively. This general behaviour is also in agreement with previous computational atrial-torso models (Aslanidi et al. 2011; Krueger et al. 2013; Rodrigo et al. 2014). However, these previous models used a simplified torso anatomy or considered only a limited number of organs what may influence the pathway followed by the electrical wavefront and then the morphology of the signals registered at the torso surface.

Additionally, the use of the finite elements method (FEM) instead of the boundary elements method (BEM) to simulate electrical propagation allowed us to analyse the surface maps (Figure 5.6b) and to understand how BSPM is formed from the propagation of the electrical wavefront through the torso volume (van der Graaf et al. 2014). We analysed the volumetric propagation by means of slices of the torso from multiple axial views (Figure 5.6c) and studied the spatio-temporal volumetric distribution of the electrical dipole. In this way, it was possible to determine the specific region of the atrium responsible for the negative and positive potentials in the frontal and rear views of the torso. On the frontal view, negative values were mainly produced by CT/IB while positive were produced by RLW/RAA. When analysing the rear view, positive potentials start appearing from  $t=70$  ms mainly dominated by the LSW, LPW and LPV.

We also analysed the P-wave at individual torso leads by means of the root mean square (RMS) value, to simplify the analysis of the spatial and morphological variations of the

P-wave and BSPM (Gozolits et al. 2002; Lux et al. 2014). This method therefore allowed us to extract information from the total P-wave morphology, duration and amplitude by observing the RMS distribution map (Figure 5.7). The expected P-wave morphologies, such as those registered at specific areas of the torso surface with positive and negative single-phases, as well as biphasic or M-shaped complexes, are in agreement with experimental measurements. In this regard, results reported by (Lian et al. 2002) revealed that P waves were uniphasically negative over the right upper chest whereas uniphasically positive over the inferior anterior torso. Biphasic waveforms with initial positive deflection were sensed from electrodes along the upper parasternal region. In addition, M-shaped complexes over the left upper chest and notches in left inferior channels were observed. (Huo et al. 2014) concluded that there exists a causal association between the P-wave morphology and duration and the major atrial conduction routes. Our results reveal that the M-shaped complexes are mainly produced at the inflexion time at  $t = 70$  ms when the wavefront goes through the BB and breaks down giving rise to three individual wavefronts which depolarize the LA following three different directions.

This approach also made it possible to study the individual RMS patterns (Figure 5.9 and Figure 5.10) and the individual pseudo P-waves (Figure 5.12 to Figure 5.16) produced by individual atrial regions when their contributions were registered on the torso surface. Results revealed that, although the distance between a recording lead on the torso surface and a given atrial region is an important determinant of the potential RMS recorded, other factors such as wavefront direction has its main effect on the polarity of the signal. Our RMS study also shows that only 9 regions are responsible for almost 90% of the total atrial contribution to the RMS torso surface pattern (Figure 5.11), while two regions of RA (RLW and RAA) and two of LA (LPW and LPV) are mainly responsible for almost the total P-wave morphology. To the best of our knowledge, no previous experimental or computational studies have been able to evaluate the associations between individual atrial structures and the genesis of the P-wave and related body surface maps.

## 5.7. Limitations

Our computational torso model involves a number of unavoidable simplifications in their conceptualization and implementation and must be bear in mind.

Mathematically, the most recurrent simplification is the following:

a) The finite elements formulation is the most extended method to numerically solve the electrical propagation of the atrial activity trough discretized spatial domains such as the human torso. The torso is usually conceptualized as a passive domain and then, the heat transfer equation is the most extended approach to compute the propagation through it. This simplification pursues to find the temperature field (equivalent to the electrical potential) and the heat fluxes in a material domain (the volumetric torso mesh) given a set of a boundary conditions (at the torso surface) and initial conditions (at the atrial region).

Anatomically, the torso scale also presents some simplifications:

- a) The human torso was meshed including those tissue conductivities (organs) that mostly influence the electrical propagation. However, both the fat and the muscular fibres could additionally impact the wavefront while it is travelling through the torso. On the other hand, the original atrium corresponding to the original torso mesh was replaced by our detailed atrial model. Although both meshes are perfectly aligned and integrated, a slight impact could this have on the measurements of the ECG and BSPM.
- b) Although the torso mesh was validated using experimental studies, there exist numerous sources of inter-patient variability and uncertainty in the model formulation that could impact the results and then the use of this model in the clinical practice (Mirams et al. 2016).

Some additional electrophysiological simplifications must be also bear in mind:

- a) The electrical contribution from those isolating atrial tissues, such as the body of the FO and interior layer of the Bachmann's Bundle, to the computation of the P-wave has been disregarded at the time of the interpolating the atrial activity to the initial conditions for the torso propagation. This help to avoid the contribution of the resting potential at which these nodes are kept on the final ECG. However, those isolating layers could be better modelled as a saline solution acting as a current sink or directly they could be removed from the model.
- b) The whole set of torso surface nodes (14157) were used to analyse both, the BSPM and the BSPM-derived biomarkers. This provides a vast and valuable amount of information. However, it is not clinically feasible to register the ECG nor the BSPM in such number of leads what might lead to misinterpretations.
- c) The interpretation of the results is more difficult when considering the very much multifactorial and variable clinical environment. The feasibility and transferability of the tool and methodology to the clinical practice should then be considered in future work.

# CHAPTER 6

---

## Non-invasive localization of atrial ectopic beats

*This chapter capitalizes on the main outcomes of chapters 4 and 5 aiming to non-invasively localize atrial ectopic beats. New BSPM-derived biomarkers are defined and machine-learning techniques are used to cluster and classify focal atrial tachycardia from the body surface distribution of such biomarkers.*

*The content of this chapter has been sent to publish in:*

**A. Ferrer-Albero, E. J. Godoy, M. Lozano, L. Martínez-Mateu, F. Atienza, J. Saiz, and R. Sebastian,** “Non-invasive localization of atrial ectopic beats by using simulated body surface P-wave integral maps,” *PLoS One*, 2017. Under revision.

*and has been partially published in:*

**A. Ferrer-Albero, E. J. Godoy, R. Sebastian, L. Martínez, and J. Saiz,** “Analysis of *in silico* Body Surface P-wave Integral Maps show important differences depending on the connections between Coronary Sinus and Left Atrium,” in *Computing in Cardiology*, 2016, vol. 43, pp. 1–4.

### 6.1. Existing approaches to localize atrial ectopic triggers

The non-invasive localization of atrial ectopic foci during focal atrial tachycardia is complex to determine. Methods based on either standard 12-lead electrocardiograms (ECG) or body surface potential maps (BSPM) have not shed sufficient light on how to accurately correlate ectopic focus locations with the distribution of potential and P-wave characteristics on the torso surface. This limitation results in longer intra-operative invasive mapping procedures, which could lead to suboptimal localization and ablation of focal triggers. The last consequence is an increased recurrence rate of ablation procedures to stop the arrhythmia.

From the early 70’s, several approaches have been proposed to localize ectopic foci in the atria. The first studies in humans consisted in pacing the atria at different sites to analyse the morphology, time sequence and polarity of P-waves (Harris et al. 1968;

Massumi et al. 1969; Leon et al. 1970) using the standard 12-lead ECG. Unfortunately, the usability of the standard 12-lead ECG for such analysis is poor due to the number of P-waves with low amplitude or isoelectric morphology. In the late 90's, some studies increased the number of body surface electrodes and focused on studying the body surface potential distribution (Mirvis 1980; Kawano et al. 1983; Kawano et al. 1989; Ishihara et al. 1997) or the body surface integral P-wave maps (BSPIMs) (SippensGroenewegen et al. 1998; Gerstenfeld et al. 2000; SippensGroenewegen et al. 2004; Groenewegen 2004) during controlled atrial pacing. Those approaches provided dense maps of P-wave signals, triggered from stimulation catheters placed at a few sites inside the atria that allowed characterising the signals and analysing their distribution on the torso surface. More recently, a combination of BSPM with surface wavefront propagation maps (M. S. Guillem et al. 2009), and with the spatial evolution of the electrical dipole (Giacopelli et al. 2012) have been proposed to get an insight into the determination of the ectopic focus origin that maintains the arrhythmia and the dynamics of the dipole of atrial depolarization prior to the ablation procedure. However, none of those approaches based on the forward problem have provided an efficient and systematic method to localize the specific origin of the ectopic excitation.

Recent studies have focused on designing and validating algorithms based on P-wave polarity that used 12-lead (Kistler et al. 2006; Colman et al. 2011) or 64-lead recordings (Alday et al. 2015) for identifying the origin of ectopic sites that were artificially induced from a pacing catheter in the atrium. Those procedures showed a general good accuracy for detecting the site of some ectopic foci. However, their accuracy decreases again when bi-phasic P-waves are present in many leads (Alday et al. 2015).

Computational tools have also been proposed to help in the localization of ectopic foci. For instance, the electrocardiographic imaging (ECGi) allows estimating the electric activity of the heart by solving the inverse problem, i.e., it reconstructs maps of epicardial potentials from data measured on the body surface. This method has evolved from the first non-human study in the late 90's where a dog heart was paced at different sites on the ventricles (Rudy & Burnes 1999) to clinical applications for the diagnostics of focal ventricular tachycardia (Intini et al. 2005), the characterization of epicardial atrial pathological activation (Cuculich et al. 2010) or the guidance of atrial fibrillation ablation (Lim et al. 2015). Further methods propose to build a database of simulated BSPM combined with machine learning techniques to predict the localization of ventricular ectopic triggers (Giffard-Roisin et al. 2016), or the use of machine learning techniques to classify cardiac excitation patterns during atrial fibrillation using a cross-validated SVM (Reich et al. 2016).

Taking advantage of the methodologies and results provided by these previous studies, we use the detailed anatomical and electrophysiological multi-scale atrial-torso model already developed in chapters 4 and 5, together with similar machine learning techniques (Kernel regressions and SVM) to develop a pipeline in order to cluster and classify BSPM-derived biomarkers into groups associated with ectopic atrial sites. The goal is

two-fold. Firstly, to spatially clustering ectopic atrial foci into clearly differentiated atrial regions based on the analysis of the biomarker patterns that they display. Secondly to classify new patterns into the previously well-defined clusters (related to atrial sites). Finally, to provide a virtual population of 58 *in-silico* normalized reference BSPM-derived biomarkers to gain insight into the different patterns computed by stimulating across both atria.

## **6.2. Improvements of the multi-scale 3D atrial-torso model**

### ***6.2.1. Cellular scale***

The first version of our three-dimensional model of the human atria was already described in chapter 4. This atrial finite element model consisted of a multi-layer hexahedral mesh with: i) homogeneous wall thickness; ii) specific fibre direction in 21 atrial regions; iii) electrophysiological heterogeneity modelled by adjusting  $I_{to}$ ,  $I_{CaL}$  and  $I_{Kr}$  in the Maleckar's model (Maleckar et al. 2009) in eight different regions between both atria; and iv) tissue heterogeneity modelled by specific conduction velocities and anisotropy ratios. Regarding the torso, already described in chapter 5, it was developed by using the open access and anonymized repository made available online by the Centre for Integrative Biomedical Computing (CBIC) from University of Utah (MacLeod et al. 1991). This model consisted of a tetrahedral mesh with the main organs (lungs, bones, liver, ventricle, blood pools, and flesh) and with specific conduction properties each.

We have enhanced this detailed multiscale atrial-torso model to incorporate more realistic electrophysiology properties at cellular and tissue scales and to improve the interpolation between the atrial and torso scales. The new anatomical atrial domain consists of a 3D mesh with 754893 nodes and 515005 linear hexahedral elements, with the same wall thickness in the range of (~600 - 900  $\mu\text{m}$ ) and a regular spatial resolution of 300  $\mu\text{m}$ . Similar to previous studies (Aslanidi et al. 2011; Dössel et al. 2012; Tobón et al. 2013), we have kept the homogeneous wall thickness in order to reduce the mesh size and computational load. This property is expected to slightly influence the simulations. However, since we look for the relationship between BSPM-derived biomarkers and the atrial ectopic sites, it seems likely that increasing the atrial wall thickness homogeneously will not affect such association.

For this study, the Courtemanche-Ramírez-Nattel ionic model for human atrial electrophysiology (Courtemanche et al. 1998) has been used instead of the Maleckar's model (Maleckar et al. 2009) used in our previous studies (chapters 4 and 5). The main reason is that the Maleckar's model under BCLs below 1Hz self-stimulates the cell even if no external stimulus is applied. These circumstances motivated the generation of new cellular sub-modes based on the Courtemanche's model, following the same procedure that was used previously. In this regard, nine different cellular sub-models have been derived from its original formulation to account on the heterogeneous AP morphologies in the atria under normal physiological conditions. We have also split the BB in its right

(BBRA) and left (BBLA) sides with specific cellular properties improving the repolarization phase in the LA (Martínez-Mateu et al. 2017). Final multiplicative factors applied to the maximum conductance of the same three ionic currents ( $I_{to}$ ,  $I_{CaL}$  and  $I_{Kr}$ ) are shown in Table 6.1 as well as the values of  $APD_{90}$  measured at a  $BCL=1000ms$  and  $BCL=500ms$ .

**Table 6.1: Multiplicative factors and APD associated to each sub-model**

Multiplicative factors related to each ionic channel conductance and APD after 1 minute of stimulation at  $BCL=1000ms$  and  $BCL=500ms$ .

Ionic Conductance / model	RA, PM	CT, BBRA	BBLA	RAA	TV	LA	PV	LAA	MV
<b>g<sub>to</sub></b>	1.00	1.00	1.00	0.68	1.00	1.00	1.00	0.68	1.00
<b>g<sub>CaL</sub></b>	1.00	1.67	1.67	1.00	0.67	1.00	1.00	1.00	0.67
<b>g<sub>Kr</sub></b>	1.00	1.00	1.60	1.00	1.53	1.60	2.20	1.60	2.44
Simulated APD <sub>90</sub> (ms) BCL=1Hz	295.0	311.0	264.0	278.0	227.0	256.0	227.0	278.0	193.0
Simulated APD <sub>90</sub> (ms) BCL=2Hz	266.0	295.0	253.0	252.0	197.0	230.0	204.0	230.0	170.0

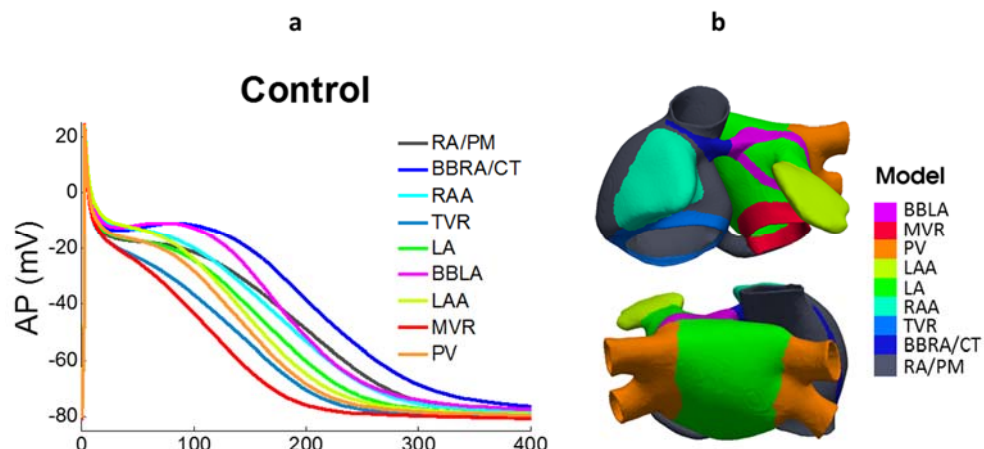


**Figure 6.1: AP's morphologies and distribution across the atria**

a) Resulting characteristic APs produced by each cellular sub-model, according to the maximum conductance of the three ion currents  $I_{to}$ ,  $I_{CaL}$  and  $I_{Kr}$ . The nine different regions correspond to RA/PM, CT/Right BB, RAA, TV ring, LA, Left BB, LAA, MV ring and PVs; b) Distribution of the cellular sub-models across both atria. Published in (Martínez-Mateu et al. 2017).

APs were recorded after 1 minute of stimulation at both cycle length using a pulse amplitude and duration of 28 pA/pF and 2 ms, respectively. The APD variation among regions was again similar to experimental observations (Feng et al. 1998; Li et al. 2001; Cha et al. 2005). In this way, the APD in the CT region was longer than in the RA region, which in turn was longer than in the TV, RAA and LA regions. Within the LA, the APD was shorter in the PV region than in the LA region. The AP's morphology provided from the nine cellular sub-models at a BCL=1000ms are shown in Figure 6.1a. Afterwards, the nine cellular sub-models were assigned to the nodes in the 3D geometrical model, following the distribution shown in Figure 6.1b.

### 6.2.2. Tissue and atrial scale

At tissue scale, the atrial model has also been fine-tuned (Martínez-Mateu et al. 2017) similarly as it was already described in chapter 4. For this study, nine types of atrial tissue have been modelled splitting the CT and the ring of the FO into two different types of atrial tissues. Thus, tissue conductivities in each atrial region were adjusted as shown in Table 6.2 to match the activation sequences to the experimental data (Lemery et al. 2007).

**Table 6.2: Longitudinal and transversal conduction velocities for atrial tissues**

	$\sigma L$ (S/cm pF)	$\sigma T$ (S/cm pF)	$\sigma T / \sigma L$
<b>RA, LA</b>	0,0030	0,0010	0,35
<b>CT</b>	0,0085	0,0013	0,15
<b>LFO</b>	0,0075	0,0075	1,00
<b>PV</b>	0,0017	0,0008	0,50
<b>BB, PM</b>	0,0075	0,0011	0,15
<b>IST</b>	0,0015	0,0015	1,00
<b>SAN</b>	0,0008	0,0008	1,00
<b>CS</b>	0,0060	0,0030	0,50
<b>FO</b>	0,0000	0,0000	1,00

Another relevant improvement has been carried out at tissue level in the CS-LA bridges since clinical and histological studies have shown the relevance of the striated myocardial muscles along its sleeve, connecting CS with the LA myocardium (Chauvin et al. 2000; Saremi et al. 2011). In that sense, the longitudinal conductivity on the first two proximal bridges has been increased up to (0.006 S/cm · pF) representing 7.5 times with respect to the four distal junctions (0.0008 S/cm · pF) to allow the wavefront to run at different velocities through these connections and reproduce a more realistic CS-LA

propagation. Grounds on which this change are based are duly justify in section 6.4.3. Considering all these improvements at cellular and tissue scales, the final atrial activation sequence is as shown in Figure 6.2.

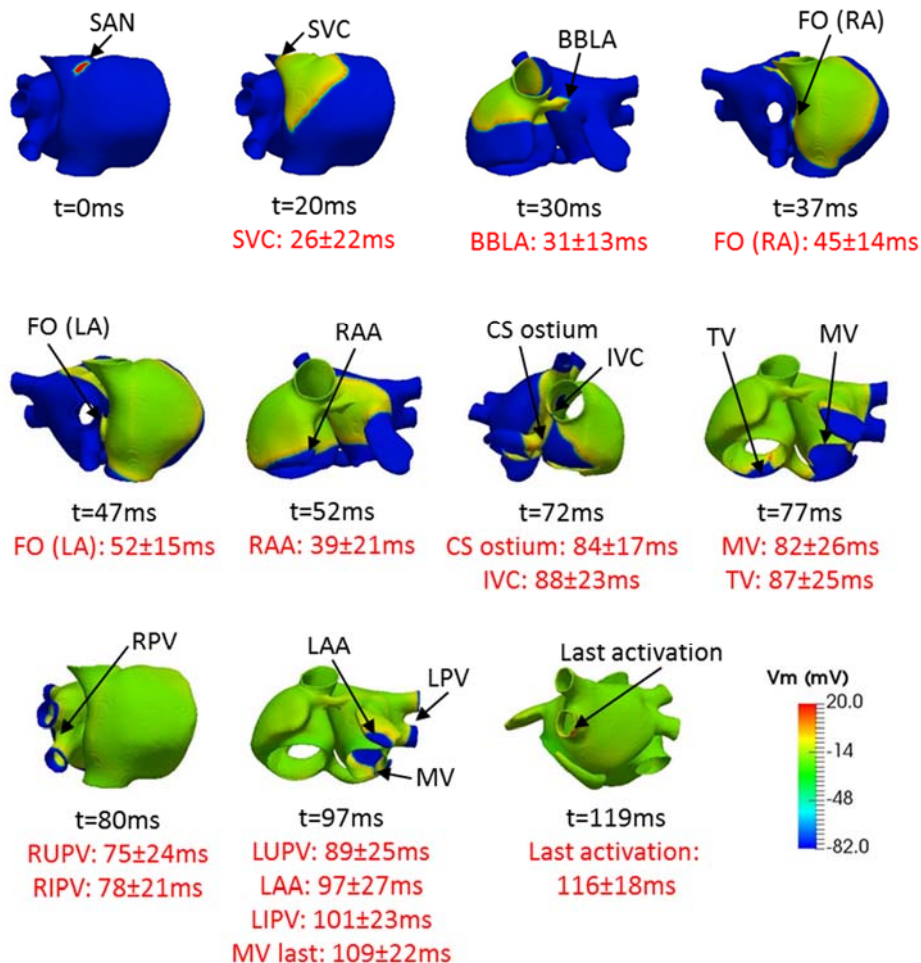


**Figure 6.2: Atrial depolarization sequence**

Snapshots of the atrial activation as described in (Martínez-Mateu et al. 2017) and comparison of the simulated activation times at different points of the atria with the experimental activation times (in red) reported by (Lemery et al. 2007).

### **6.2.3. Torso scale**

The torso model has also been improved with respect the previous version developed and used in chapter 5. Specifically, it has been re-meshed to increase the density of nodes in the region that overlaps the atrial model, improving the interpolation from transmembrane voltages computed at atrial scale to the finite-element tetrahedron model of the torso and then the coupling among both models. Instead of increasing the density at a constant distance of 0.8mm as it was done in the previous version, 64172 additional nodes were included in the area that overlapped the atrial myocardium, as shown in Figure 6.3. The resulting volumetric torso mesh has 254976 nodes and 1554255 tetrahedral elements. The spatial resolution ranges now from 0.5 mm on the atrial region to 5.8 mm on the torso surface. The number and tissue properties associated to the organs within the torso remain identical as in the previous version (atria, lung, bone, liver, ventricle, blood, and general torso).

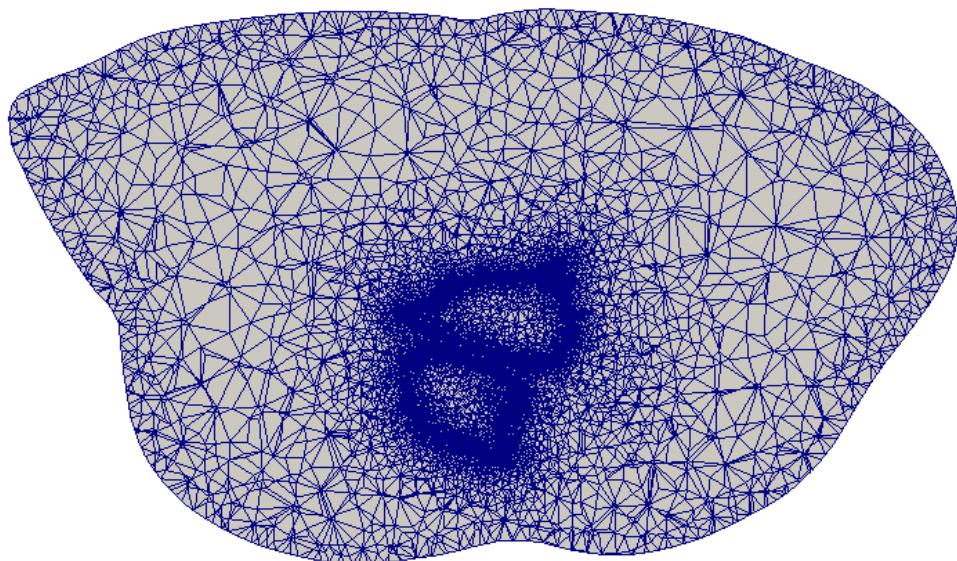


**Figure 6.3: Transversal cut of the torso, at the height where the atrium is placed**  
It is shown how the spatial resolution changes from the atrial region to the torso surface.

## **6.3. Biophysical simulations of focal atrial tachycardia**

### **6.3.1. Triggering sites of atrial ectopic beats**

First clinical studies that performed ectopic pacing in humans (Harris et al. 1968; Massumi et al. 1969; Leon et al. 1970) stimulated in only 5-9 atrial sites (RIPV, RSPV, LSPV, LAA, free RA and LA walls, CS, LAA and ICV). Afterwards, the number of sites

was increased to 34 divided into both atria (SippensGroenewegen et al. 1998; Gerstenfeld et al. 2000; SippensGroenewegen et al. 2004) providing experimental patterns on the torso surface. However, the most recent studies (Kistler et al. 2006; Cuculich et al. 2010; Colman et al. 2011; Alday et al. 2015; Lim et al. 2015) have not increased the number of the triggering sites and still stimulate in well-known locations (CT, BB, PM, AVR, SVC, IVC, CS os, RAA, PM, RPV, LPV, MV, LAA, CS, and RA and LA septum).

Since more accurate information on the specific trigger originating atrial tachycardia is needed, our atrial model was paced at the sinoatrial node (SAN), and at 57 distributed transmural ectopic foci (one at a time), placed along the RA and the LA. In this regard, a set of 17 sites on RA (R1 to R17) and 14 sites of LA (L1 to L14) were defined (see blue sites in Figure 6.4) following experimental studies (SippensGroenewegen et al. 1998; SippensGroenewegen et al. 2004) with the main aim of validating the results of the present work. This group of triggering sites will be referred as validation set.

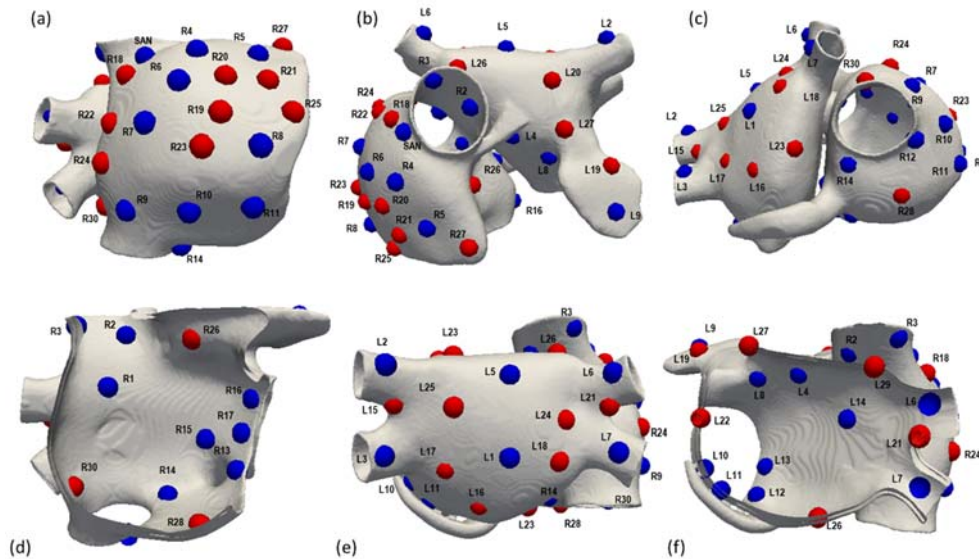


**Figure 6.4: Localization of the 58 ectopic focus sites (including the SAN)**  
Blue points labelled as R1 to R17 and L1 to L14 are the ectopic sites belonging to the validation set.  
Red points labelled as R18 to R30 and L15 to L27 represent the additional ectopic locations to cover the atrial walls.

The additional 26 sites (13 on each atrium) were selected to cover the whole RA (R18 to R30) and LA (L15 to L27) walls and to increase the size of the training set that will feed

in the machine-learning algorithms for ectopic foci location (see red sites in Figure 6.4). The specific anatomical locations are summarized in Table 6.3.

**Table 6.3: Anatomical sites of the 58 foci (including the SAN)**

Sites are grouped by RA and LA segment locations. The first 17 and 14 sites on RA and LA respectively (31 sites in total) were located at the same positions used in previous experimental studies (SippensGroenewegen et al. 1998; Gerstenfeld et al. 2000; SippensGroenewegen et al. 2004). The additional 13 sites on each atrium (26 sites in total) were selected to cover the whole atrial walls.

RA Segment location	Experimental Ectopic Sites	Additional Ectopic Sites
Sinoatrial node	SAN	
Crista Terminalis		R18
Intercaval Bundle	R9	R22, R24, R30
Right Septum	R1, R15	R26
Right Wall	R4, R6, R7, R8, R10, R11, R12	R19, R20, R23, R25
Right Appendage	R5	R21, R27
Isthmus	R14	R28
Superior Cava Vein	R2, R3	
Tricuspid Valve	R13, R16, R17	R29
LA Segment location	Experimental Ectopic Sites	Additional Ectopic Sites
Left Bachmann Bundle	L4, L8	L22
Left Superior Wall		L26, L27
Left Septum	L14	
Left Appendage	L9	L19
Posterior Wall	L1, L5	L16, L17, L18, L20, L23, L24, L25
Mitral Valve	L10, L11, L12, L13	
Right Pulmonary Veins	L6, L7	L21
Left Pulmonary Veins	L2, L3	L15

### **6.3.2. Computation of extracellular potentials**

The electrical propagation in the atria was computed by solving the reaction-diffusion mono-domain Equations 4.26 and 4.27 with the finite element method (Heidenreich et al. 2010). It was deeply described in chapter 4, section 4.1.2.

$$\nabla \cdot (\mathbf{D} \nabla V) = C_m \cdot \frac{\partial V}{\partial t} + I_{ion} \text{ in } \Omega_H$$

$$\mathbf{n} \cdot (\mathbf{D} \nabla V) = 0 \text{ in } \partial \Omega_H$$

However, the extracellular potentials ( $V_e$ ) were computed by an approximation of the bidomain model instead of using the approximation to the heat transfer equation used in chapter 5 (section 5.3.1). This change aims to optimize the propagation phenomenon between the atrial and the torso scales. In fact, when working with multiscale systems the common approach separates the lower and the upper scales solving each of them separately. The main fundamentals of this approach is that upper scale (in this case the torso) is often modelled at macroscopic level while the lower scale (related to the atria) is much more microscopically designed and this could lead to a weak coupling between scales. However, we have highly improved the density of nodes in the torso that overlaps the atrial myocardium increasing the spatial resolution to 0.5 mm, which ensures a smooth coupling between scales. Hence, the bidomain approach can be used to solve the whole system equation, from the atria (using the monodomain simplification) to the torso.

For this purpose, we firstly interpolated the transmembrane potentials ( $V$ ) obtained in the atrial hexahedral mesh to nodes in the tetrahedral torso mesh overlapping the atrial myocardium. Secondly, the extracellular potential was computed by solving the bidomain model (Keller et al. 2010; Martinez et al. 2016) described by Equation 6.1, using the finite elements method and the Dirichlet and Neumann boundary conditions (Weber, Keller, et al. 2011).

$$\nabla \cdot (\mathbf{D}_i \nabla V) + \nabla \cdot ((\mathbf{D}_i + \mathbf{D}_e) \nabla V_e) = 0 \quad \text{Equation 6.1}$$

where  $D$  is the equivalent conductivity tensor,  $D_i$  and  $D_e$  are the volume-averaged conductivity tensors of the intra- and extracellular domains,  $I_{ion}$  was the transmembrane ionic current that depends on the cellular model,  $C_m$  is the membrane capacitance and,  $\Omega_H$  is the heart domain.

### 6.3.3. Stimulation protocol for triggering ectopic beats

To reach a steady-state, we simulated 20 continuous beats with an amplitude of 28pA/pF, a duration of 2ms, and a basic BCL of 500ms, stimulating at the SAN area (1180 equidistant nodes with a spatial resolution of 300μm), which stabilized the whole 3D atrium and smoothed differences between neighbouring regions. Following, from the steady-state conditions, a simulation was performed for each ectopic site by delivering a single square pulse with 2 ms of duration and 28 pA/pF of amplitude on a circular area comprising an average of 542 equidistant nodes with the same spatial resolution. Since we did not include electrical remodelling, the shortest APD for our model was 170ms

(MV), which is longer than the whole atrial activation. This fact warranties that a second ectopic beat cannot start an activation sequence until the whole atria is completely depolarized.

## 6.4. Biomarkers to interpret focal atrial tachycardia

### 6.4.1. Study of biomarkers on the torso surface

Simulated BSPMs were registered at the torso surface mesh (14157 virtual leads) for each ectopic focus as shown in Figure 6.5a and Figure 6.5b (BSPM snapshot at the time  $t=43\text{ms}$  computed by stimulating at L1 location, see Figure 6.4). The dotted square encircles the region of interest, i.e., the frontal and rear regions where electrodes may be placed to register relevant P-wave electrocardiographic signals as those shown in Figure 6.5c. In this panel, blue line corresponds to the P-wave signal registered at the precordial lead V3 (highlighted as a white point in panel a) when the ectopic focus is paced at site L1, and red line refers to the P-wave registered at the same lead when stimulating at the SAN. Differences between both waves were as expected since principal wavefronts direction change depending on the triggering site.

Several indicators (maxima and minima values of P-wave, root mean square RMS, area under the P-wave and the product between RMS and the P-wave integral) derived from BSPM and P-waves have been considered to find out the biomarker or feature that best clusters and predicts the ectopic foci origin, using machine-learning techniques. Among all these biomarkers, maxima and minima values of P-wave signals did not show good performance mainly because these values depend on the local signal polarity. On the other hand, root means square (RMS), as the most common parameter to avoid the dependence with respect to the signal polarity, was used in order define those regions at the torso surface that mostly concentrate the signal. The main shortcoming with this index is that important information related to the course of the wavefront direction is lost.

After interpreting the information unveiled by each indicator, we choose the P-wave integral map. This integral map represents the area under the P-wave, between the zero line and the curve outlined from the P-wave onset to its offset. These two fiducial points are defined as the time at which the atrial depolarization starts from the ectopic focus and the time at which the latest atrial node is already depolarized, respectively. The body surface P-wave integral maps (BSPiM) are then displayed as a static body surface map that summarizes P-wave signals recorded at each lead. Figure 6.5d shows the BSPiM derived from the simulated BSPM corresponding to the ectopic focus placed at site L1.

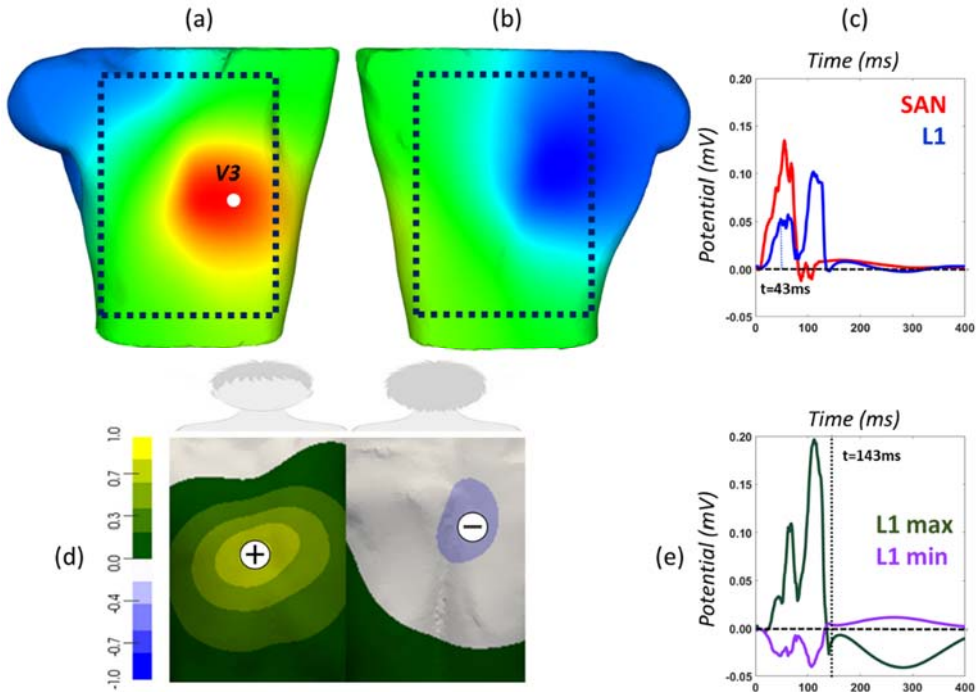


**Figure 6.5: Simulated BSPMs and integral map (BSPiM) computed at the torso surface**

Torso model (including the atria and the additional regions) showing an example of the frontal (a) and rear (b) views of the Body Surface Potential Map (BSPM) at time  $t=43\text{ms}$ , delivering the ectopic beat at site L1. The dotted square represents the approximate area of the frontal and rear surface where electrographic signals may provide useful information; (c) morphology of the P-wave (potential versus time) registered at the precordial lead V3 (highlighted as a white sphere in (a) in sinus rhythm (red line) and when stimulating ectopic L1 (blue line); d) Characteristic P-wave integral map (BSPiM) (left). Greenish to yellowish area represents positive P-waves registered at any lead of this area (see green P-wave line in panel (e) registered at the position with maximum integral value), and greyish to blueish region means negative P-waves (see purple P-wave line in panel (e) registered at the position with the minimum integral value); e) Dashed horizontal baseline represents the division between positive and negative potentials. Dotted vertical line defines the duration of the P-wave defined as the latest atrial depolarization time for each simulation ( $t=143\text{ms}$  in the case of L1).

Normalized maximum and minimum BSPiM values are indicated on the map with symbols plus and minus, and the corresponding P-waves registered at V3 lead are shown in Figure 6.5e. The position of these extrema is relevant since they summarize the resultant direction of the electrical dipole. It is important to highlight that BSPiM overcomes the shortcomings related to other indexes. In fact, BSPiM considers all the information, i.e., a) the signal polarity (green to yellow areas indicate mainly positive signals while grey to purple areas mean negative P-waves); b) the regions where the energy is mostly concentrated (yellow and purple areas); and c) the atrial wavefront direction (positive P-

waves located at the frontal torso surface indicating that the atrial wavefront moves from the LA free posterior wall towards the frontal atrial side, when considering the L1 trigger site).

A combined indicator calculated by multiplying the RMS map by the BSPiM was additionally considered (highlighting those regions with maximum energy contribution within the positive and negative integral regions). However, it did not improve results (not shown) with respect to using BSPiM alone and it was finally disregarded. Therefore, only the indicator computed as the time-integral map (BSPiM) was finally used to correlate the location of the ectopic beat with the pattern obtained at the torso surface.

#### **6.4.2. Validation of body surface P-wave integral maps (BSPiM)**

The full atrial-torso model was firstly validated by comparing the simulated BSPiMs validation set (R1 to R17 and L1 to L14) to equivalent experimental activations measured by (SippensGroenewegen et al. 1998; Gerstenfeld et al. 2000; SippensGroenewegen et al. 2004). These clinical studies describe the use of BSPiM as a non-invasive method to identify the region of atrial tachycardia origin prior to catheter ablation using 62-lead sites superimposed over the human torso and a dataset of individual paced P-wave integral maps in 22 patients with normal cardiac anatomy. Their main result was a database consisting of 34 mean paced P-wave integral maps, 17 from each atrium.

Figure 6.6a shows the LATs obtained by stimulating the atrial model at different locations of the RA (R2, R5, R9, R12 and R17) and LA (L1, L4, L9, L10 and L14). All the remaining simulations belonging to the validation set are depicted in Figure 6.7 and Figure 6.8. The total atrial activation time for simulations activated by ectopic foci placed in the RA ranges from 111ms (R2, at the medial wall of the SCV) to 180ms (R11, at the lateral lower wall of RA). As expected, ectopic foci at RA produce wavefronts moving leftwards and entering the LA through the BB, FO and CS. However, the movement is rightwards when the ectopic foci are delivered in the LA. In this last case, the activation times range from 111ms (L4, localized in the left side of the BB) to 173ms (L9, placed in the LAA). It is worth highlighting how the architecture of the striated myocardial muscle connections between CS and LA strongly affects the main entrance pathway for the depolarization wavefront initiated in the low LA. Proof thereof is the fact that these bridges allow the electrical wavefront to enter the RA through the CS and depolarize both atria upwards.

For each simulated ectopic activation, the normalized BSPiM was computed at the torso surface as displayed in Figure 6.6b (for all the others sites belonging to the validation set, see Figure 6.7 and Figure 6.8). These simulated BSPiMs were analysed and compared to the experimental integral patterns published in (SippensGroenewegen et al. 1998; Gerstenfeld et al. 2000; SippensGroenewegen et al. 2004) and reproduced in Figure 6.6c.

When comparing each pair of simulated-experimental patterns, it can be noticed that both match in terms of distribution of positive and negative values of the P-wave integral as well as in the position of the maxima and minima values.

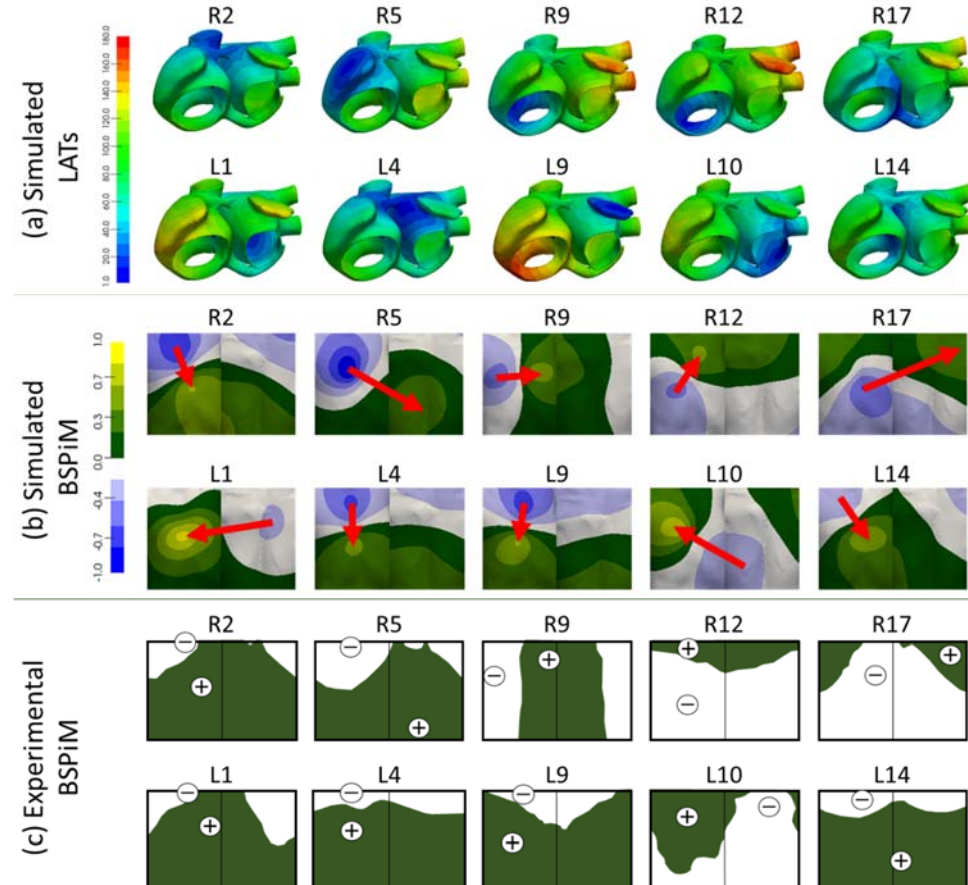


**Figure 6.6: Comparison between simulated and experimental BSPiMs**

(a) Simulated Local Activation Times (LATs) computed when the ectopic sites are located at different positions of the RA (2, 5, 9, 12 and 17) as defined in (SippensGroenewegen et al. 1998) and locations of the LA (1, 4, 9, 10 and 14) as defined in (SippensGroenewegen et al. 2004). Bluish colour corresponds to  $t=0\text{ms}$  and reddish colours correspond to the latest activation time. Time is given in milliseconds; (b) Simulated normalized Body Surface P-wave Integral Maps (BSPiM) computed at the 14.157 nodes of the torso surface for each ectopic focus. Bluish colours correspond to the most negative while yellowish correspond to the most positive integral values. Red arrows represent the position of the minima towards maxima integral values; (c) Experimental integral patterns reproduced from the originals published by SippensGroenewegen et al. White colour means negative integrals (equivalent to the blueish range for the simulated BSPiM) while green colour means positive integrals (equivalent to the greenish to yellowish range for the simulated BSPiM).

In the RA, three different patterns can be observed depending on the direction of the vector that links the minimum and maximum values (see Figure 6.6b, upper row and Figure 6.7 and Figure 6.8 for all the others sites). These patterns are: i) downwards for ectopic foci originated at the upper face of this RA (R2 and R5), ii) upwards for ectopic foci placed near the TV (R12 and R17), and iii) left-sided for ectopic foci originated at the lower atrial backside (R9). The same trend is observed in the experimental patterns that even match the position of the maxima and minima values of the integral (see Figure 6.6c, upper row and Figure 6.7 and Figure 6.8 for all the others sites). In the case of ectopic sites placed in the LA (see Figure 6.6b, lower row), atrial activation is mostly influenced by the conduction pathways between both atria. Thus, when the wavefront first arrives to the RA through the BB and FO (L4, L9 and L14), the simulated BSPiMs are positively signed on the medium and lower torso. However, when the wavefront enters the RA through the CS (L1 and more visibly in L10) the BSPiM changes and mainly shows positive values on the frontal torso. Similar patterns and location of the maxima and minima values are again observed experimentally (see Figure 6.6c, lower row), except in the case of L1 where the most negative value produced by our simulation is shifted from the frontal to the rear side on the torso model. When analysing the position of the L1 maxima and minima values, it can be observed that the position of the maximum positive is correct while its minimum negative value is moved from the expected frontal upper position to the posterior medium area. If we try to find other ectopic sites that produce the most negative value at that frontal upper area, but keeping a similar position for the positive maximum, we might find R2, R26, L4, L15, L19, L20, L22, L25, L26 or L27. These sites are shifted leftmost and a bit further up with respect L1. Probably, placing L1 nearer L25, the position of its extrema values would be improved while keeping its BSPiM. Despite this case, the overall distribution of the integral values across the torso surface shows similar patterns for the whole validation set of simulated and experimental BSPiM.

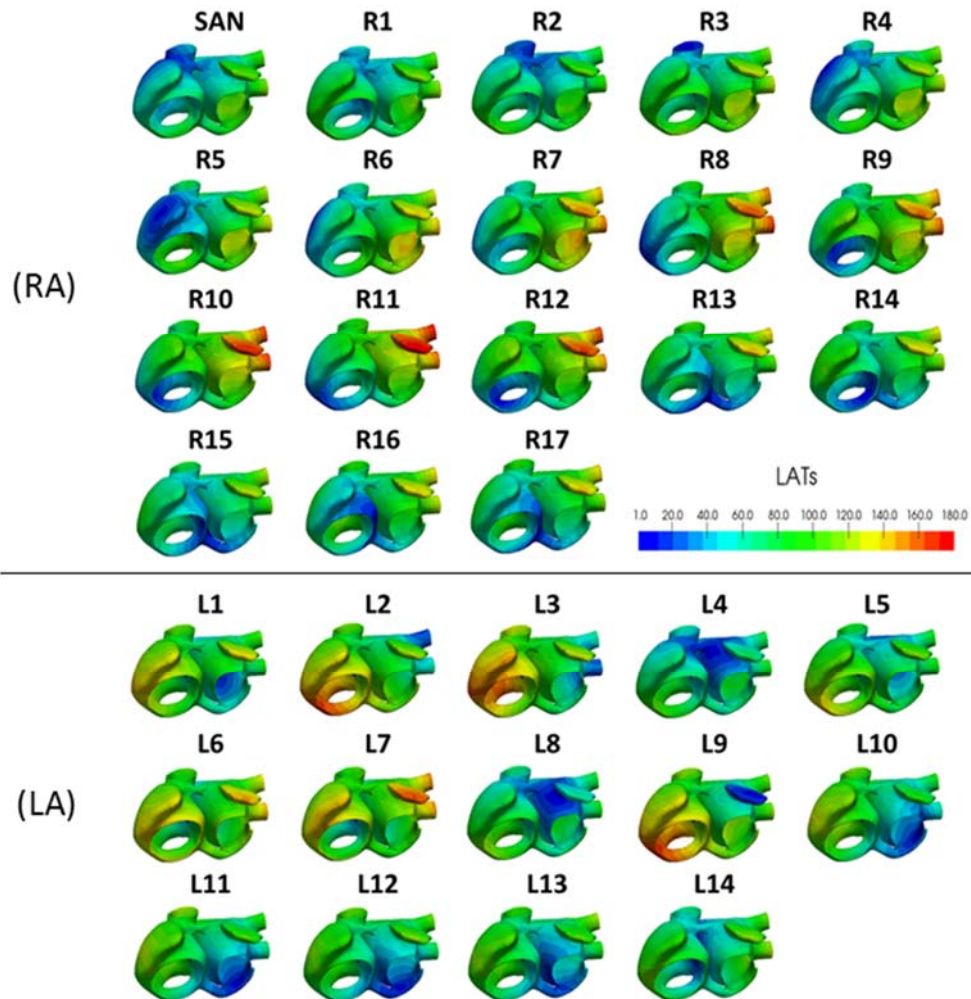


**Figure 6.7: Simulated LATs by activating the SAN, the 17 RA and the 14 LA sites**  
Upper panel: RA sites; Lower panel: LA sites. Bluish colours correspond to  $t=0\text{ms}$  and reddish colours correspond to the latest activation time.

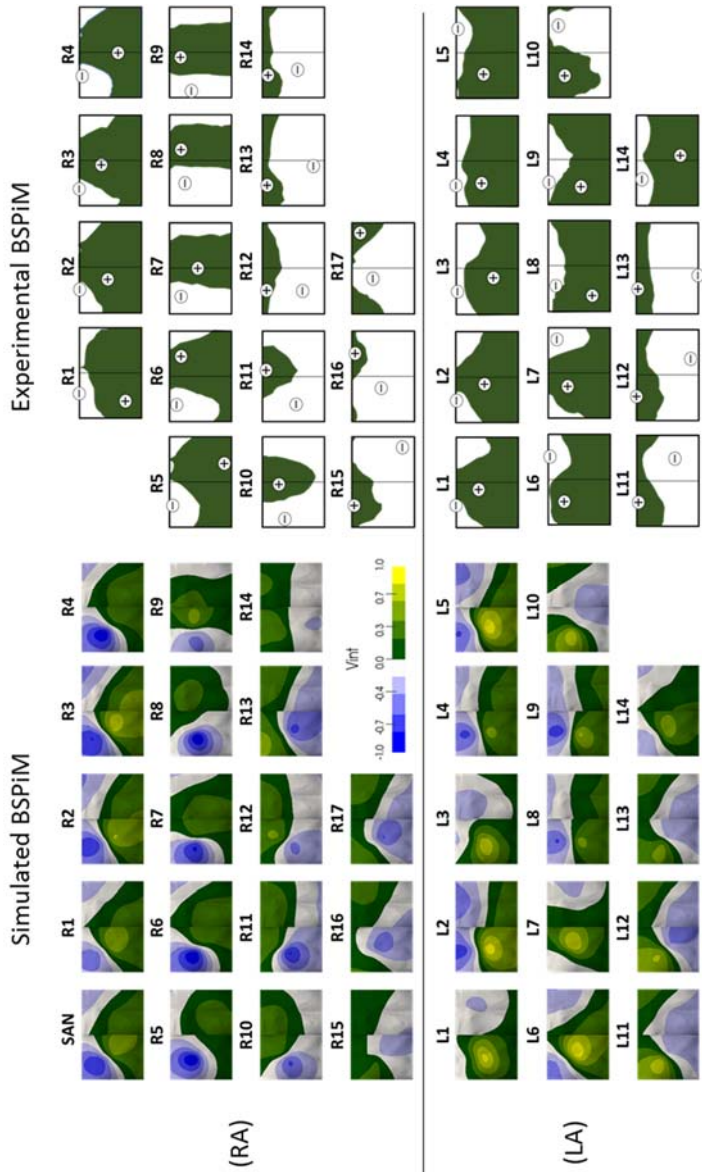


**Figure 6.8: Simulated and experimental BSPiMs for the whole validation set**

Left panel: Simulated normalized Body Surface P-wave Integral Maps (BSPiM) computed at the torso surface for each ectopic foci belonging to the validation set. Bluish colour means the most negative integral value and yellowish means the most positive integral value; Right panel: Experimental integral patterns reproduced from the originals computed by SippensGroenewegen et al. White colour means negative P-waves (equivalent to the white to blue range for the simulated BSPiM) while green colour means positive P-waves (equivalent to the green to yellow range for the simulated BSPiM).

The second validation test for the model consisted of analysing and comparing the morphology of the P-wave signals in specific leads as carried out experimentally by (Kistler et al. 2006), who also stimulated in different sites on the RA and LA. Figure 6.9 compares simulated (left panel) vs experimental (right panel) leads V1, V3 and V5 registered when the ectopic foci were placed in the CS, CT, TV, atrial appendages RAA and LAA and PVs. Among the whole dataset of 57 in-silico ectopic foci plus the SAN, those localized nearer the experimental sites were chosen in order to compare equivalent simulated-experimental P-wave morphologies. In general, the P-wave polarity and morphology closely followed similar trends in the experimental and simulated domains for the three leads and for all the anatomic sites tested. Examples of this similar behaviour for the simulated-experimental pairs are: i) the pair R27-RAA shows a negative V1 while V3 and V5 are isoelectric; ii) the pair L3-LIPV shows a noteworthy morphology in V1, that is a characteristic double peak, also reproduced by the equivalent simulation L3; iii) in the case of L30-CS body, V1 is positively signed in both, simulated and experimental leads, while V3 is isoelectric and V5 slightly negative in both domains. All the remaining simulated P-waves registered at the same leads for the 57 ectopic foci and the SAN are shown in Figure 6.10 and Figure 6.11. In general, the morphology described by all the P-waves at the three leads, and for all the simulations, is coherent with the position of the corresponding ectopic focus. Besides, sites placed around the same atrial region also produce P-waves with similar trend.

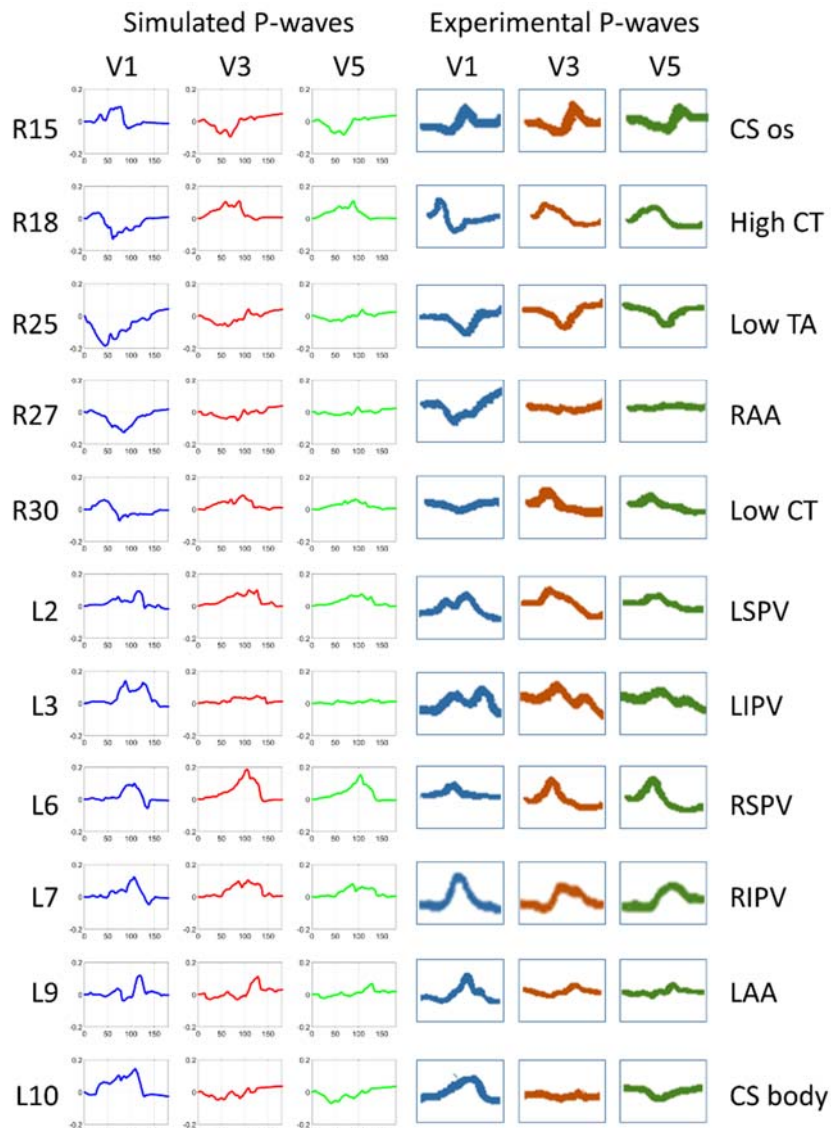


**Figure 6.9: P-wave morphology in simulated and experimental precordial leads**

Left panel (simulations): P-wave registered at V1 (blue), V3 (red) and V5 (green) from the RA simulations 15, 18, 25, 27 and 30 and from the LA simulations 2, 3, 6, 7, 9 and 10; Right panel (experimental data): P-waves reproduced from the experimental recordings by Kistler et al [in] at the same sites as used to simulate. Experimental stimulated regions: Ostium and Body of the Coronary Sinus (CS os and CS body), Higher and Lower crista terminalis (High and Low CT), Lower region of the Tricuspid Annulus (Low TA), Right and Left atrial appendages (RAA and LAA), Left and Right and Superior and Inferior Pulmonary Veins (LSPV, RSPV, LIPV, RIPV).

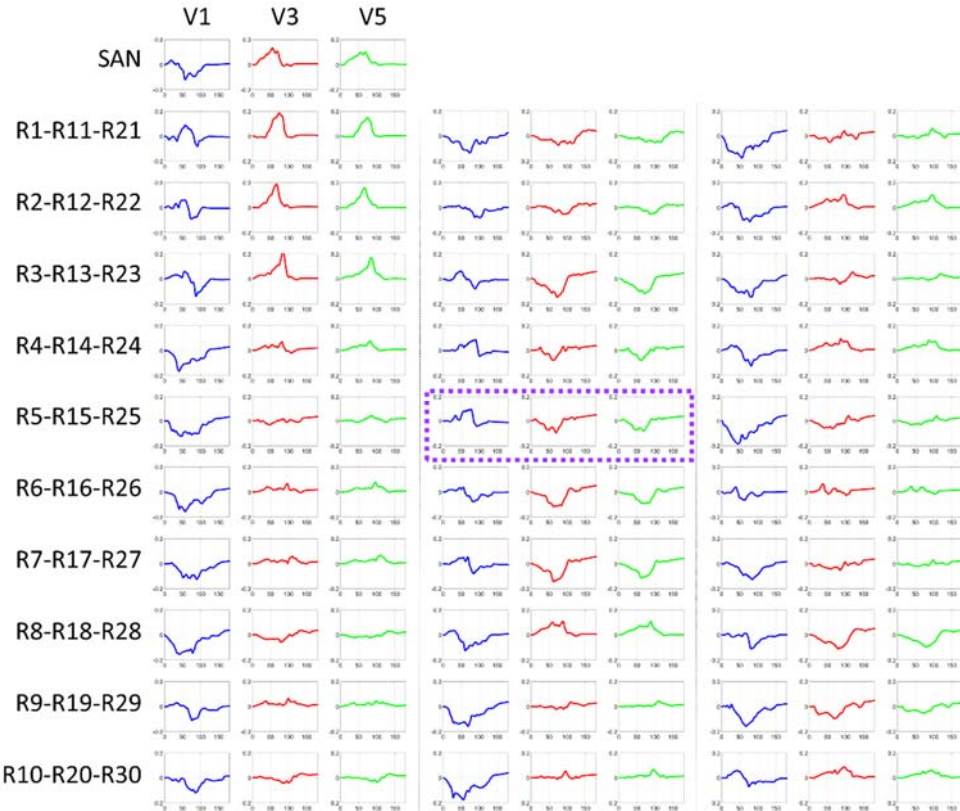


**Figure 6.10: P-wave morphologies registered for the 30 ectopic sites on the RA**

Position of precordial leads on the torso surface and P-wave morphology registered at V1 (blue), V3 (red) and V5 (green). The dotted purple square, for example, identifies the P-waves registered at V1, V3 and V5 produced by the ectopic site R15.

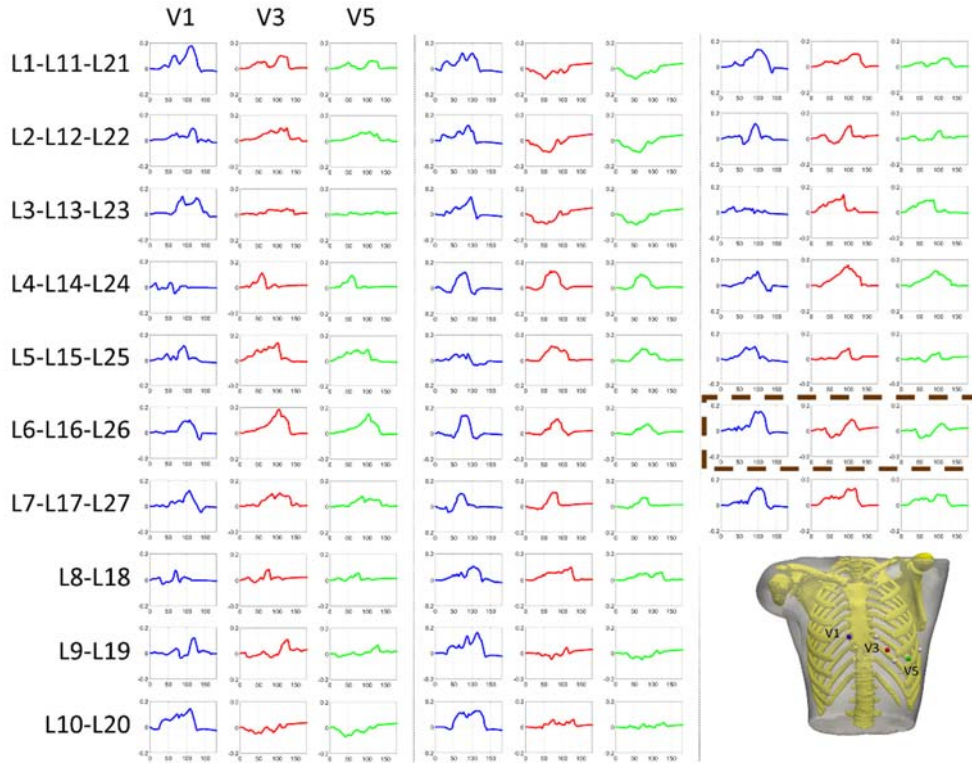


**Figure 6.11: P-wave morphologies registered for the 27 ectopic sites on LA**

Position of precordial leads on the torso surface and P-wave morphology registered at V1 (blue), V3 (red) and V5 (green). The dotted purple square, for example, identifies the P-waves registered at V1, V3 and V5 produced by the ectopic site L26.

#### 6.4.3. Influence of the CS-LA bridges on the BSPiMs

The electrical connections between the atrial CS and the LA myocardium have an effect on the overall atrial activation pattern and the P-wave morphology. Important differences in BSPiM were observed depending on the presence or absence of CS-LA electrical connections. Furthermore, when these junctions exist, the patterns slightly differ among themselves depending on their distal or proximal location with respect to the ostium of the CS.

As it was already introduced in previous section 6.2.2, several clinical studies of the human atria have histologically shown the existence of striated myocardial muscle at discrete locations along the sleeve of the CS that electrically connects CS and the LA myocardium (Chauvin et al. 2000; Saremi et al. 2011). The anatomy of these interatrial connections and their location have been previously shown as having high variability

between patients. This leads to strong differences in the pathway followed by the atrial depolarization wavefront (Chauvin et al. 2000) and influences the BSPiM.

In order to analyse this effect, pacing sites were selected as shown in Figure 6.12 row 1: low LA, at the farthest point from the ostium of CS, considering the CS-LA electrical junction activated (Figure 6.12a) or blocked (Figure 6.12b); low LA, at the closest point from the ostium, considering the CS-LA electrical junction activated (Figure 6.12c) or blocked (Figure 6.12d).

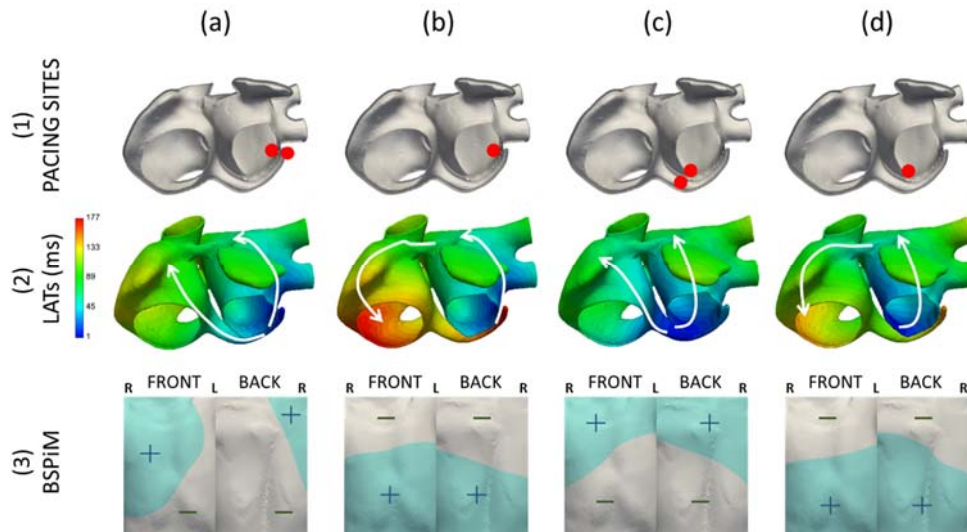


**Figure 6.12: In-silico simulations when foci are paced in distal and proximal LA sites**

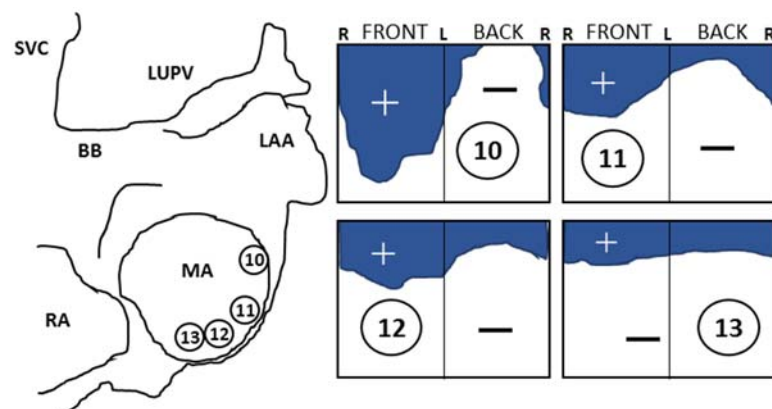
Row (1): Double-red dots represent a bridge between CS and LA myocardium, (a, c). Single-red dots, (b, d), represent the lack of CS-LA connections. Row (2): LATs for each configuration with arrows showing the direction of the depolarization wavefront. Row (3): In-silico BSPiMs. Bluish areas represent positive signed BSPiMs while greyish areas represent those with negative signed BSPiMs. R and L identify the right and left sides of the frontal and rear views of the torso surface.

Figure 6.12 row (2) displays the LATs produced by each configuration. Figure 6.12a shows how the wavefront propagation starts depolarizing the LA upwards but entering very fast to the RA through the CS and then depolarizing upwards this atrium almost simultaneously. Figure 6.12b outlines the same depolarization profile for LA, but in the opposite direction in the case of RA since the wavefront enters through the BB instead of using the CS-LA junctions. Similar effect is shown when the pacing site is near the ostium of CS. When the CS-LA junction is electrically activated (see Figure 6.12c) both atria depolarize upwards thanks to the fast connection between LA and RA. However,

when this bridge is blocked (d), the two atria depolarize in opposite direction as happens in configuration (b).

In-silico BSPiMs shown in Figure 6.12 row (3) represent the same frontal and rear views of the torso surface as described in Figure 6.5. The BSPiM produced when the potential wavefront enters through distal muscular CS-LA connections (a), shows that P-wave morphology is positively signed mainly on the right side of the torso surface corresponding to the frontal-superior side and to the right-superior corner at the back. However, when the wavefront does not find distal muscular CS-LA bridges (b), the positive P-wave integral pattern appears on the inferior part of the torso in its both faces. Simulations with proximal CS-LA connections (c) show patterns inverted with respect to the configuration without them (d). The patterns associated to models with no proximal or distal CS-LA connections (b, d) are similar among themselves but opposite to the configurations when bridges CS-LA (a, c) are activated.

In-vivo clinical BSPiMs described in (SippensGroenewegen et al. 2004; Groenewegen 2004) show similar behaviour. In these experimental studies, the authors recorded sixty-two-lead body surface ECG recordings during LA pace mapping in 22 patients with normal cardiac anatomy. The results obtained when pacing at low LA are depicted in Figure 6.13 for points 10 to 13. The farthest point from the ostium of CS corresponds to the site number 10, which BSPiMs is highly similar to our pattern showed in Figure 6.12, row 3(a). Furthermore, the sites from 11 to 13 describe a positive signed integral map on the superior part of frontal and rear part of the torso surface while it is negative underneath. These three patterns closely match our in-silico BSPiMs depicted in Figure 6.12, row 3(c).



**Figure 6.13: In-vivo clinical BSPiMs**

Reproduced from the originals published in (SippensGroenewegen et al. 2004; Groenewegen 2004). Bluish areas represent positive signed P-wave integrals while whitish are negative signed. R and L identify the right and left sides of the frontal and rear views of the torso surface.

## 6.5. Clustering and classification of atrial ectopic foci from BSPiM

### 6.5.1. Methodological pipeline

We designed the pipeline depicted in Figure 6.14 with the aim of training a system to identify the region from which an ectopic focus is triggered from the corresponding BSPiMs. First, BSPiMs are calculated from the biophysical simulation of the ectopic foci. Following BSPiMs are clustered into groups, from now on ectopic clusters (EC), which number is defined by the user. Finally, the BSPiMs and their group numbers are used to train a system based on support vector machine that has to be able to classify non-observed BSPiMs into their corresponding groups.

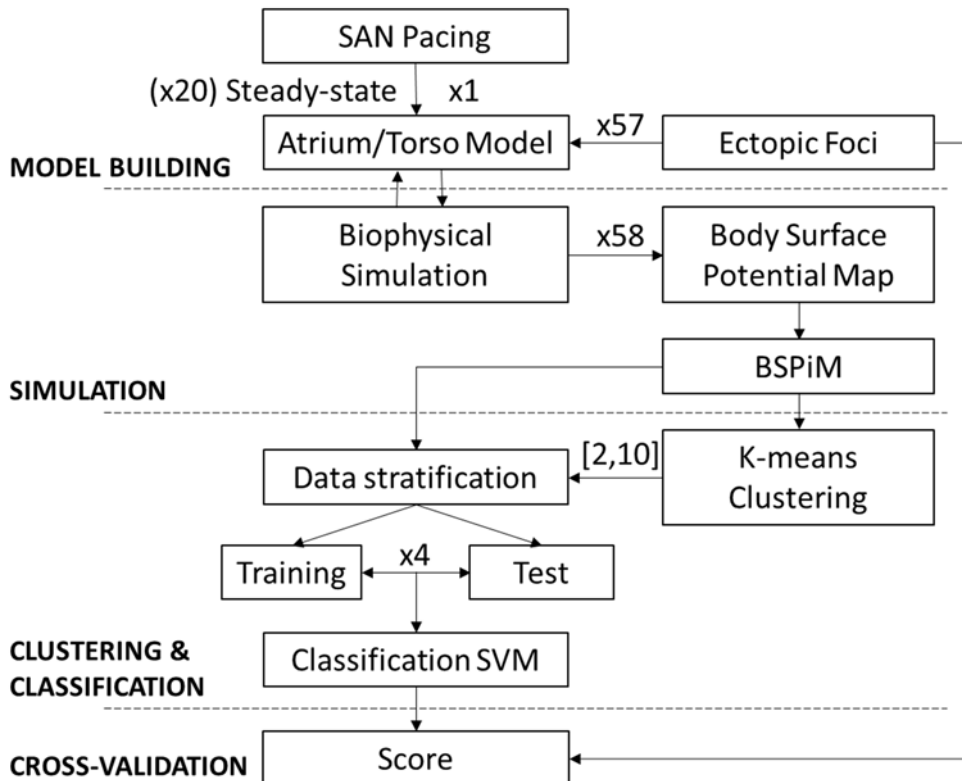


**Figure 6.14: Methodological pipeline to cluster and classify ectopic foci**

The atrial-torso model was built up and stabilized in sinus rhythm. Afterwards, 57 new biophysical simulations were carried out stimulating at 57 additional ectopic foci in order to compute the corresponding BSPMs and BSPiMs. Machine learning techniques were used to firstly cluster these ectopic sites into spatial and well-defined atrial regions and to secondly be able to prospectively classify and predict the location of new sites with high accuracy.

We aim to find the EC, i.e. the atrial region, where an ectopic focus is paced, instead of its exact location, since the EC is more affordable and robust from a clinical perspective. To build the ECs we first computed the BSPiM corresponding to each ectopic focus and defined this map as its feature vector. Therefore, our training set has 58 feature vectors (57 ectopic foci plus the sinus node activation) with a size of 14157 torso FEM nodes each, where BSPiM was calculated. Then, we seek to validate the following hypothesis: ectopic foci localized close/near from each other in the atria would produce similar BSPiM patterns. Therefore, clustering BSPiMs would produce ECs that define non-intersected regions.

The clustering algorithms chosen were K-means (Hartigan 1989) and EM (Expectation maximization) (Bishop 2006). We provided both models (K-means, EM) with the training set (R1 to R30 and L1 to L27) and split it into different ECs, i.e., k values from 2 to 10. Once the ECs were established, we validated their compactness and checked for intersections between groups.

Next, to validate the quality of the clusters obtained for different number (k) of ECs we used, as a performance oriented metric, a classification procedure. We chose a multiclass Support Vector Machine classifier to classify the samples, i.e., the ectopic foci, considering the ECs obtained in the training phase. The aim in this second phase was to evaluate the resultant classification models using cross-validation (CV), which let us know the capability to correctly classify new samples into distinct groups. We used a stratified N-fold CV where the training set was split into N smaller sets called “folds”. Folds are selected so that the mean response value is approximately equal in all of them. This means that each fold will contain the same proportions of ectopic foci from each EC, and all the ectopic foci will be tested. The final score for the classifier is computed as the average for all the folds. In this work, we considered 4 folds, which leave 75% of samples for training and 25% of samples for testing in each fold.

### **6.5.2. BSPiMs clustering and database**

We checked whether our initial hypothesis held, which proposed that close/near ectopic foci in the atria should produce similar BSPiMs. For this purpose, we used the whole dataset of 58 triggers aiming at covering the whole atrial tissue. The 26 additional BSPiMs were computed making up a database with 58 BSPiMs (including those belonging to the validation set and the SAN stimulation).

Figure 6.15 displays the patterns corresponding to the additional 26 ectopic foci. The same three kinds of patterns can be observed for the sites placed in the RA (upper panel): i) downwards (R18, R20, R21, R22, R26 and R27) for foci originated from the upper side of this atrium, ii) upwards (R28) for ectopic foci placed near the TV, and iii) leftwards (R19, R23, R24, R25, R29 and R30) for ectopic foci originated in the medial lower side. In the case of ectopic sites in the LA (lower panel) these patterns show again distributions similar to the ones showed in Figure 6.6: i) downwards (L15, L19, L20, L21, L22, L24, L25, L26 and L27) with ectopic sites localized in the upper half of the LA

forcing the wavefront to enter the RA through the BB and FO, and ii) rightwards (L16, L17, L18 and L23) indicating the atrial depolarization wavefront enters the RA through the CS from sites placed in the lower rearward of the LA.

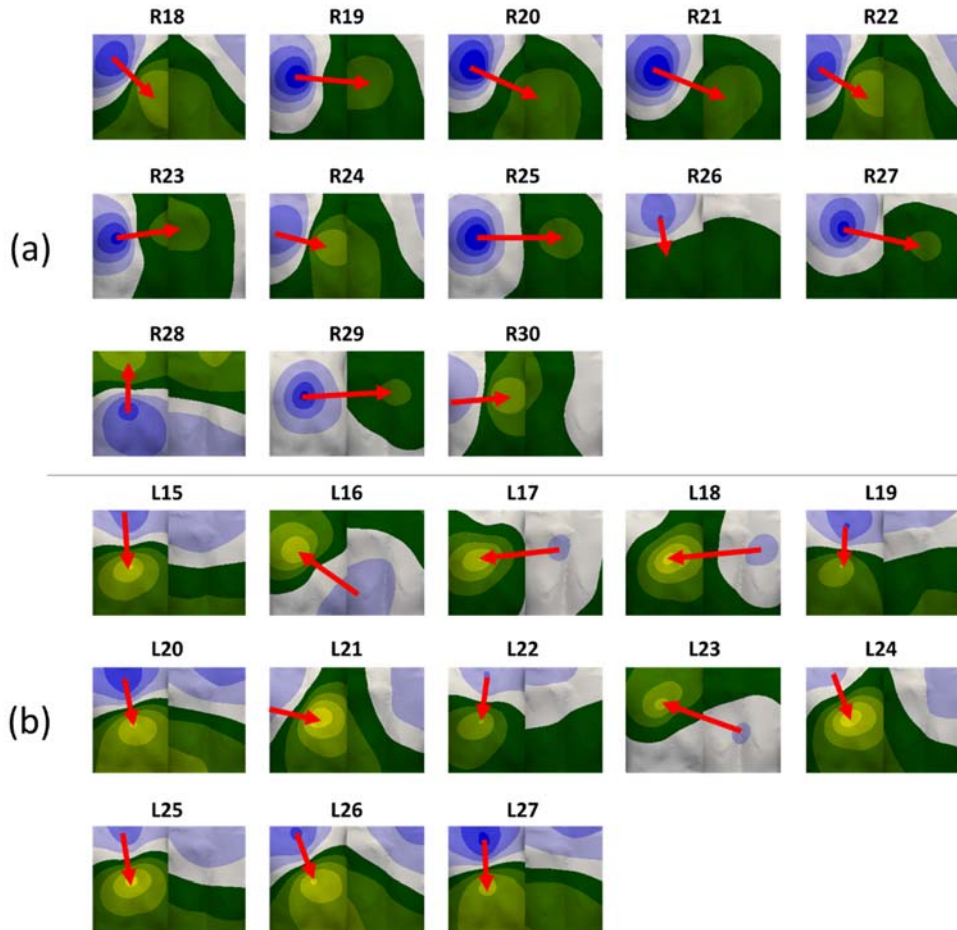


**Figure 6.15: Simulated normalized additional BSPiMs**

BSPiMs have been computed at the torso surface for the 26 additional ectopic foci stimulated at a) RA (R18 to R30), and b) LA (L15 to L27). Normalization was carried out based on the maximum range of P-wave integral considering the 58 different BSPiMs.

The dataset of BSPiMs was then clustered into ECs by K-means and EM algorithms, in order to group ectopic foci that produce statistically similar and well-defined BSPiMs. Both algorithms produced almost the same results for all the ECs. Figure 6.16 shows an

exemplary BSPiM from each EC (upper row with coloured circles corresponds to individual cluster IDs) for each k (number of ECs in which the whole database of 58 BSPiMs is split). Additionally, Figure 6.17 displays these clusters, computed by using the K-means algorithm for different values of k (all the foci belonging to the same group have the same colour ID previously defined by the coloured circles in Figure 6.16).

For k=2 the dataset is divided in two different groups. The first one shows the positive signed integral values in the lower and leftmost side of the frontal and rear torso (e.g. R1, Figure 6.16 blue EC), and corresponds to ectopic sites localized in the upper part of both atria (blue points in Figure 6.17 corresponding to blue-k2-0 in Table 6.4). The other cluster shows the opposite, i.e., positive values at the upper and rightmost side of the torso (e.g. L13, Figure 6.16 red EC) and corresponds to ectopic sites in the region closer to the TV and MV (red points in Figure 6.17 corresponding to red-k2-1 in Table 6.4).

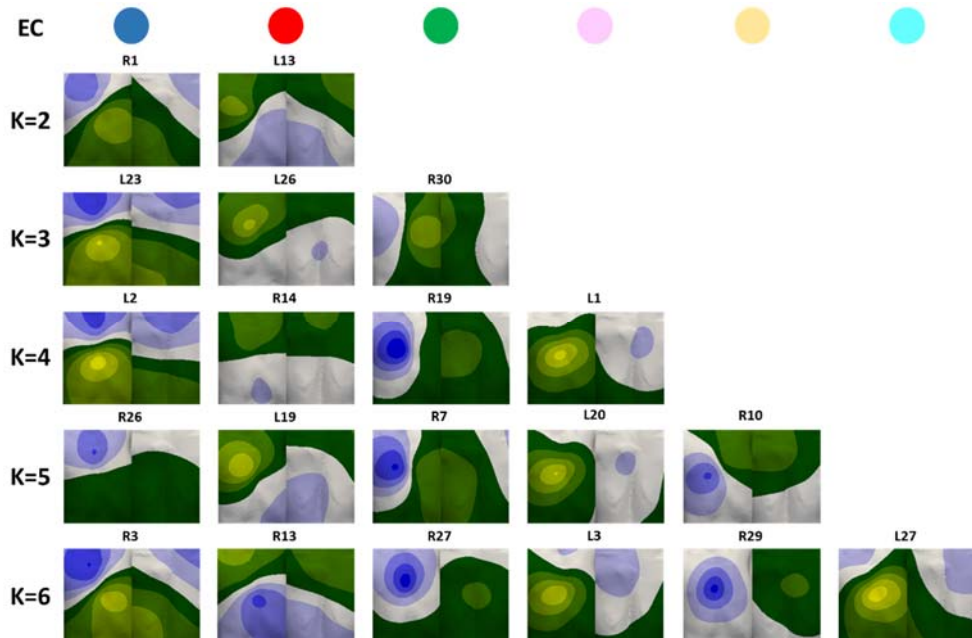


**Figure 6.16: Exemplary BSPiMs included in the ECs**

For different number of clusters (k) from 2 to 6. A single pattern belonging to each coloured class for each k is displayed.

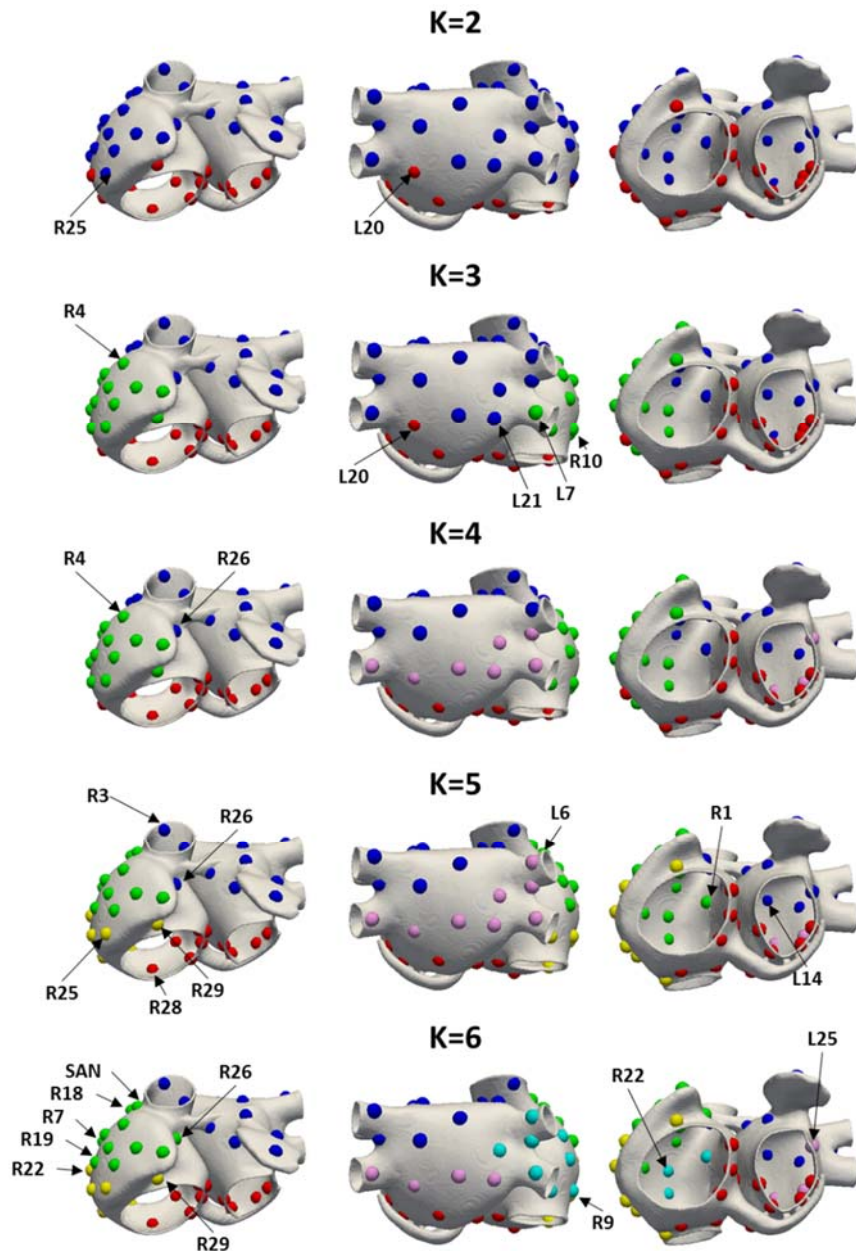


**Figure 6.17: Clustering of the BSPiMs**

57 patterns of BSPiM (30 from RA and 27 from LA) plus the SAN using the K-means algorithm on the torso surface nodes where K is the number of pre-defined ECs. For each K, all the foci belonging to the same EC have the same colour.

**Table 6.4: Classification of BSPiMs**

For each K, left column shows the colour and number of each EC resulting from the clustering step while right column shows the classification results identifying the ectopic site that is not well classified with the colour of the correct group, to which it really belongs.

	K=2 0,97 ( $\pm 0,02$ SEM)	K=3 0,92 ( $\pm 0,03$ SEM)	K=4 0,96 ( $\pm 0,02$ SEM)	K=5 0,85 ( $\pm 0,08$ SEM)	K=6 0,82 ( $\pm 0,06$ SEM)
R9	0	0	0	1	1
R30	0	0	0	1	0
R23	0	0	0	1	1
R25	0	1	0	1	5
R22	0	0	0	2	2
R24	0	0	0	2	0
R4	0	0	2	0	2
R5	0	0	0	2	2
R6	0	0	0	2	3
R7	0	0	0	2	3
R19	0	0	0	2	3
R20	0	0	0	2	3
R21	0	0	0	2	3
R27	0	0	0	2	3
L7	0	0	2	3	0
R2	0	0	2	0	0
R3	0	0	2	0	2
L2	0	0	2	0	0
L4	0	0	2	0	0
L5	0	0	2	0	0
L8	0	0	2	0	0
L9	0	0	2	0	0
L18	0	0	2	0	0
L22	0	0	2	0	0
L23	0	0	2	0	0
L28	0	0	2	0	0
L29	0	0	2	0	0
L30	0	0	2	0	0
R26	0	0	2	0	2
R1	0	0	2	0	0
SAN	0	0	2	0	2
R18	0	0	2	0	3
L6	0	0	2	0	0
L25	0	0	2	3	0
L14	0	0	2	3	2
L24	0	0	2	3	0
L27	0	0	2	3	0
L1	0	0	2	3	4
L3	0	0	2	3	4
L21	0	0	2	3	4
R8	1	1	0	2	1
R10	1	1	0	1	1
R29	1	1	0	2	1
R11	1	1	1	1	1
R12	1	1	1	1	1
R13	1	1	1	1	3
R14	1	1	1	1	3
R15	1	1	1	1	3
R16	1	1	1	1	3
R17	1	1	1	1	3
R28	1	1	1	1	1
L10	1	1	1	1	3
L11	1	1	1	1	3
L12	1	1	1	1	3
L13	1	1	1	1	3
L19	1	1	1	1	3
L26	1	1	1	1	3
L20	1	0	1	2	4

For  $k=3$ , BSPiMs associated with blue and red ECs remain almost unchanged with respect to patterns with  $k=2$  (Figure 6.16). The new green EC shows positive integral values all along the left side of the torso on both, the front and back (e.g. R30). The fact is that, as depicted in Figure 6.17, blue- $k2-0$  mainly divides itself into two classes giving rise to the clusters in the right (green- $k3-0$ ) and left (blue- $k3-2$ ) atria including the septum and the superior cava vein. Interestingly, red- $k3-1$  previously associated with the lower side of both atria only suffers a very slight movement of the borders between the three classes.

If we continue increasing the number of groups to  $k=4$ , the green EC with  $k=3$  splits up giving rise to a pattern with positive integral values further backwards as is the case of R19 and new (pink) EC where the positive values are mainly computed at the frontal torso surface. In the atria (Figure 6.17), the new yellow class when  $k=5$  is the result of splitting the green and red ECs ( $k=4$ ) giving rise to this new EC localized in the lower right side of the RA.

Finally, when  $k=6$  class subdivision starts mixing up ectopic foci from previous pink, green and yellow groups ( $k=5$ ) and the identification of the area is slightly difficult as can be seen in the lower row of Figure 6.17.

When the number of classes ( $k$ ) increases beyond 6, it is difficult to clearly assign some of the BSPiMs into ECs since the number of ectopic foci within each class starts decreasing significantly (see for example the 5 sites within the pink EC and the 7 sites within the yellow EC) and the size of the spatial region is considerably reduced not allowing to clearly differentiate P-wave integral patterns among clusters.

### **6.5.3. Prospective classification of ectopic foci**

Considering the ECs defined during the previous clustering phase, we study the accuracy of a learning algorithm to classify ectopic foci into the ECs. We use support vector machines (SVM) with a radial basis function to learn the BSPiM patterns and their associated ECs. Following, the classification accuracy is determined by a 4-folds stratified cross-validation (CV). Results are shown in Table 6.4. For each fold, around 13-17 ectopic foci with representatives of all classes are used for testing the system, and the remaining for training the SVM. High values of accuracy imply that the majority of the ectopic sites are properly classified, while lower values highlight that some sites are assigned to clusters to which they do not really belong.

For  $k=2$ , only 2 out of 58 sites (R25 and L20 highlighted in Table 6.4 and Figure 6.17) were wrongly classified and the final accuracy of the classifier was 97%. As can be observed in Figure 6.17, these two foci are located at the border between both ECs so they might belong to any of the classes. When  $k=3$ , there are 5 out of 58 sites at the border between ECs wrongly classified (R4, R10, L7, L20 and L21) resulting in a lower accuracy (92%). For  $k=4$ , the ectopic sites classified incorrectly are R4 and R26 bringing again the accuracy to higher values (96%). For these previous clustering and classifica-

tion results, and mainly when  $k=2$  and  $k=4$ , the results in terms of accuracy can be considered excellent (higher than 95%). However, when  $k$  is 5 and 6 the accuracy decreases below 90%, what means that more ectopic sites are being wrongly classified. As  $k$  increases, the number of ectopic foci in each EC decreases, the classifier is not able to discriminate BSPiMs and the accuracy falls under 80%.

Given our training set of 58 BSPiM, 4 ECs is the optimum number of clusters, dividing the atria into four regions as depicted in Table 6.4 and Figure 6.17: i) top left (blue-k4-0) including SVC, BB, LSW, LAA, superior side of the LPW, LSPV and RSPV, ii) bottom right and left (red-k4-1) mainly including TV, MV, IVC and IST, iii) further right (green-k4-2) including RLW and RAA and IB, and iv) bottom back left (pink-k4-3) including LIPV, RIPV and lower side of the LPW.

## 6.6. Discussion

In this chapter, we present an enhanced multi-scale atrial-torso model that allows generating BSPMs and validating BSPiMs, which are exploited by machine learning techniques to associate BSPM-derived biomarkers with the location of atrial foci in cases of focal atrial tachycardia. Given prospective BSPiM, our computational pipeline is able to predict from which atrial region was the focal atrial tachycardia triggered with an accuracy over 95% (considering between 2 and 4 regions). We additionally provide a database with 58 simulated BSPiM patterns with 14157 samples computed by placing the ectopic foci across both atria.

### 6.6.1. Computational modelling and validation

In the 3D atrial model, the adjustment of the connections of the proximal and distal CS-LA bridges have improved the realism of wavefront propagation between both regions, compared to our previous model. In fact, the majority of the existing atrial models (Harrild & Henriquez 2000; Seemann et al. 2006; Lu et al. 2011; Krueger et al. 2011; Burdumy et al. 2012; Aslanidi et al. 2013; Krueger et al. 2012; McDowell et al. 2012; Dongdong Deng et al. 2012) do not to include the CS and only a few (Tobón et al. 2013; Jacquemet 2015) considered this region. The effect that these bridges have on the P-wave morphology and the P-wave integral patterns is remarkable in some configurations. For instance, they fully determine the pathway followed by the depolarization wavefront when an ectopic focus is localized in the low LA. Proof thereof is the fact that when the bridges are blocked, the wavefront enters the RA through the BB and FO depolarizing the LA upwards and the RA downwards affecting the morphology of the P-wave and therefore altering the BSPiM. However, when these junctions are activated, both atria depolarized upwards. The BSPiMs computed with this last configuration are very much alike the experimental ones by (SippensGroenewegen et al. 2004; Groenewegen 2004) and helped us to validate the model.

The two-step validation process compares first our simulated validation set of 31 BSPiMs, concerning ectopic triggers placed in R1 to R17 and L1 to L14, with experimental integral patterns (SippensGroenewegen et al. 1998; Gerstenfeld et al. 2000; SippensGroenewegen et al. 2004; Groenewegen 2004) and afterwards compares some of our P-wave morphologies with experimental signals (Kistler et al. 2006). The results confirmed that our atrial-torso model is accurate since simulated patterns match the experimental measurements. This allowed us to increase the number of ectopic foci covering the whole atrial walls and build up a database of 58 BSPiMs to feed in the machine-learning algorithms for ectopic foci localization.

#### ***6.6.2. Clustering and classification of BSPiM***

Among the BSPM-derived biomarkers tested to non-invasively cluster atrial ectopic sites, the BSPiMs provided the best results in terms of localizing ectopic atrial triggers. This biomarker takes into account the main characteristics of the P-wave signal and atrial depolarization: morphology, atrial depolarization wavefront and potential distribution towards and on the torso surface. The clusters obtained by using K-means (or EM) algorithm were not intersected and defined anatomical atrial regions so that they could be useful to guide clinicians during invasive interventions like radiofrequency ablation of ectopic sites. When the number of ECs considered is between 2 and 4, the clusters of BSPiMs are clearly differentiable. As the number of ECs increases, the new classes do not provide clearly distinguishable patterns probably because the number of ectopic sites within those new classes is very low.

Beyond the good performance of the clustering process, the results obtained from the classification phase are also very promising. In this regard, the wrongly classified ectopic sites when the number of ECs is between 2 and 4 are always localized at the borders between classes and the accuracy in classifying raises up to 97%. However, as the number of ECs increases, the classification errors also increase thereby reducing the accuracy to values below 90%. Technically, this may be due again to the fact that the number of ectopic sites within each cluster is dramatically reduced (sometimes below 6 sites) and the classifier, which only uses 75% of available sample for training, has not enough information to correctly assign the patterns to the pre-defined clusters. As can be observed in Table 6.4, those cluster with fewer samples show larger misclassification rates. This could be overcome increasing the database of feature vectors mapping the atria with additional trigger ectopic sites. We will extend our database in the future to test whether our methodology can improve the classification rates for larger number of clusters.

#### ***6.6.3. Previous studies***

All the experimental studies based on the analysis of the ECG and BSPM (Harris et al. 1968; Massumi et al. 1969; Leon et al. 1970; Mirvis 1980; Kawano et al. 1983; Kawano et al. 1989; Ishihara et al. 1997; Giacopelli et al. 2012) highlighted the need to localize the origin of the ectopic foci non-invasively. They provided a first-hand knowledge of the changes on P-wave characteristics and potential distribution on the torso surface

when the atrial tachycardia origins at different atrial regions. These studies drew interesting conclusions: i) P-wave morphology in lead V1 was the most informative for the diagnosis of left atrial rhythms (Harris et al. 1968); ii) when depolarization starts from a focus within the RA and CS, the resultant P-waves consistently assumed an orientation determined by the site of stimulation (Leon et al. 1970); and iii) P-wave dipole evolution may correlate the dipole trajectory with specific RA-paced regions (Giacopelli et al. 2012), but when the ectopic site is placed in the LA, the poles changed its position and amplitude very fast giving rise to big jumps forward and backwards. However, several shortcomings prevented authors from clearly relating torso surface electrical phenomena to atrial myocardial events: a) the techniques used were not much accurate mainly with P-waves with low amplitudes or isoelectric in surface leads; b) it was always emphasized the necessity of using intracardiac intervention to measure the atrial depolarization times; and c) the isopotential map characterized by a single maximum and/or a single minimum did not show a direct correlation with the origin of the atrial ectopic foci.

Our results already confirm all these experimental conclusions. In this way, patterns produced by ectopic sites localized in the RA are very much clear and easily clustered and classified than those produced from the LA. The main reason is that bridges from RA towards LA define a coherent movement of the wavefront always leftwards. However, the path followed by this depolarization wavefront is extremely dependent on the interatrial bridges on the opposite direction (from LA towards RA) and then patterns are completely different depending on the RA tissue in being firstly depolarized (from the BB, the FO or the CS).

Short time after BSPM arose as an integral part of the mapping protocol during radiofrequency catheter ablation procedures, the use of BSPiM shed much more light on how to noninvasively determine the arrhythmogenic target region for ablation using a single beat analysis approach (SippensGroenewegen et al. 1998; Gerstenfeld et al. 2000; SippensGroenewegen et al. 2004; Groenewegen 2004). In this regard, our BSPiMs and those patterns experimentally obtained pacing at upper and lower regions of the RA showed similar trends with respect to i) the opposite positions of the maxima and minima extremes, ii) the rotation of the P-wave forces as pacing site moves downwards and iii) the movement of the zero-line contour between segments (equivalent to our ECs). Coherent results have also been obtained from our simulated and the experimental P-wave integral patterns when the ectopic triggers are localized in the LA, always dependent on the firstly-activated bridge between LA and RA. Exceptionally, BSPiMs computed when pacing sites are placed at the FO are very similar to patterns obtained by pacing at other LA sites and therefore there is no certainty about the unique origin of the ectopic focus (SippensGroenewegen et al. 2004). Although these experimental studies provided 34 mean maps (17 from each atrium), authors concluded that it is complex to differentiate among those patterns localized close to each other, as it is the case, for example, of experimental R1 and R2, R7 to R9, R12 to R14, L1 to L3 or L11 to L12. This experimental inter-pattern similarity led us to conclude that our spatial ECs are much more representative of specific atrial regions responsible for triggering ectopic foci.

On the other hand, results provided by other techniques such as ECGi during experimental atrial pacing in humans (Rudy & Burnes 1999; Intini et al. 2005; Cuculich et al. 2010) and in patients with paroxysmal or persistent atrial fibrillation (Lim et al. 2015), could determine specific triggering sites (mainly lateral RA and PVs from Non-PV) on the basis of earliest activation and localization of the potential minimum and maximum. However, the authors were not able to distinguish between, for example, upper from lower PVs, RA from LA or these two from the atrioventricular rings. Experimental ECGi presents three main shortcomings. First, it is highly dependent on the inherent atrial signal quality, as it is the case for ECG or BSPM, leading to discard many leads with low signal to noise ratio. Second, it reconstructs potentials only on the atrial epicardial surface, ignoring effects of the myocardial atrial wall. That requires an imaging study and the reconstruction of the atrial and torso 3D domains, which is highly complex and time consuming. Third, some regions remain difficult to image like interatrial septum, the left PVs and the LAA ridge. All this may lead to incorrect computational assumptions that can influence the reconstruction of the atrial potentials. From our results can be inferred that P-wave integral is a more robust biomarker against low quality P-wave signals since the area under the signal is a simple mathematical computation independent on the signal amplitude or morphology. Furthermore, the whole atrial wall is always taken into consideration to compute the forward BSPiM and then to inversely cluster and classify ectopic foci on the atrial wall.

When analysing computational approaches, there are relevant studies that have provided interesting results. In this regard, a simple decision tree algorithm was firstly constructed using experimental P-waves (Kistler et al. 2006) and posteriorly used with computational models (Colman et al. 2011) for the identification of the anatomic triggering atrial sites based on the P-wave morphology. This algorithm was able to correctly identify the focus in 93% of the experimental cases while the accuracy decreased to an average of 85% (and even lower with bi-phasic P-waves) with their simulation results. Based on the morphology, authors grouped triggering sites in a) CT overlapped sometimes with right PVs, b) TV together with RAA; c) CS ostium overlapped with LAS, d) perinodal together with RAS, e) left PVs together with LAA, f) MV and g) CS body. Interestingly, our results show a higher accuracy above 95% without intersecting critical clusters such us those including PVs, CT or CS.

A more recent algorithm was developed (Alday et al. 2015) to obtain the triggering site of the stimulus from a 64-lead ECG system with a success rate of 93%. The authors divided both the torso and the atria in 8 quadrants and used the P-wave polarity to quantify the differences in morphology. All these computational approaches assumed however, predefined areas what might lead to a bias when interpreting the results, and found the same problems associated with bi-phasic or irregular P-waves. Our methodology overcomes this bias by using clustering algorithms that allow a first natural pooling of the BSPiMs without any initial constrain or starting point.

These approaches based on the use of single algorithms have evolved to the recent and more complex combinations between computational models and machine learning techniques. Previous studies based on machine learning techniques mainly focused on predicting ventricular pacing sites (Giffard-Roisin et al. 2016) and on classifying cardiac excitation patterns during atrial fibrillation on tissue patches (Reich et al. 2016). In (Giffard-Roisin et al. 2016) a set of features obtained from simulated BSPM signals are learned using Kernel Ridge Regression, including: position of the global extremum, the absolute potential of the global extremum, the sign of the global extremum, or the number of zero crossings. On the contrary, we use support vector machine regression (SVM), and choose a single feature, the BSPiM, from a set of features analysed such as maximum, minimum, and integral maps. Another difference is that in (Giffard-Roisin et al. 2016) they try learn and predict the full ventricular activation time, whereas we associate each BSPiM to a class, that is related to focal ectopic location. In (Reich et al. 2016), they choose also as a learning algorithm a multiclass SVM, but to differentiate between fibrillation activation patterns and classify them into 4 groups (plane waves, ectopic focus (spherical wave), rotor (spiral wave) and block). We only work with patterns derived from focal atrial tachycardia, and therefore we do not recognize other types of arrhythmias. The applications and goals of other works that use machine-learning techniques are very different to ours, and therefore comparing their accuracies will not provide useful information.

## **6.7. Limitations**

Inter-patient variability is always a common clinical problem when diagnosing atrial arrhythmias what may prevent physicians to draw general conclusions. The use of computational models may lead to similar shortcomings unless they are based on proper virtual population cohort. This fact led us to validate our simulations using a database of 34 experimental mean P-wave integrals from 22 patients. Additionally, we propose the use of the normalized BSPiM as a robust biomarker against small or local variations of the P-wave morphology. However, additional work must be done to build a larger set of representative atrial-torso models, and to check the accuracy of the machine-learning pipeline in presence of fibrotic areas or uncommon atrial morphologies.

Current commercial BSPM systems are equipped with around 256 electrodes or less, which is a small number compared to the 14157 electrodes that includes our torso surface. Additional work should be carried out to reduce the number of leads and define the optimal surface ECG electrode set in terms of number and position on the torso surface to obtain similar clustering and classification results. Having a sufficiently large number of ectopic samples for training the system, the accuracy could be improved even increasing the number of ectopic atrial regions in which the atria is divided, which could improve clinical usefulness.

Finally, our methodology allows classifying prospective BSPiMs into predefined groups associated to atrial regions of different sizes. Therefore, differently to other techniques

such as ECGi, we cannot provide a spatial accuracy in our predictions, since the ectopic beat could be anywhere in the region, and region size changes depending on the number of clusters considered.

# CHAPTER 7

---

## General Conclusions

The general objective of the present PhD thesis was the creation and validation of a realistic three-dimensional multi-scale human atrial-torso model to study the relationship between the electrical sources in the atria and the potential distribution on the torso surface under physiological and arrhythmic conditions. From our results, we can conclude that our multi-scale model is an accurate tool that allows studying the propagation of the electrical activity in the atria under physiological and pathological situations and determining the relationship between the local and global effects of pathological substrate from a given region of the atria and the potential distribution on the torso surface. The outcome is therefore a promising framework for quantifying the specific effect of pathological regions and characterising typical scenarios linked to arrhythmic episodes.

The general objective was broken down into several specific objectives to cover the understanding from the cellular scale to the macroscopic analysis on the torso surface. Our findings related to each specific objective are summarized below:

***Modelling of the electrical differences in cellular and tissue properties across the atria to obtain characteristic atrial action potentials with realistic morphology in each atrial region.***

The atrial model built in this thesis includes the most relevant properties at cellular and tissue levels published in the literature. First, electrophysiological heterogeneity was considered through different cellular sub-models with long-term stability in terms of APD<sub>90</sub> and restitution properties to guarantee the stability of numerical computations. The Maleckar's model is a good base model when the BCL is 1Hz so this was the choice to understand the physiological behaviour of the atrial activity. However, once the BCL falls to tachycardia rhythms, the Maleckar's model self-stimulates and the Courtemanche's model was chosen as the best alternative to model the cellular heterogeneity. The AP associated to specific atrial regions in both cases was validated using experimental, whenever possible, human or animal data or results from computational studies. Related to the tissue scale, a simple high spatial resolution mesh was developed to accurately adjust the conduction velocities and anisotropy for each of the atrial regions.

***Modelling of the anatomical and histological properties at atrial scale to obtain a realistic activation/repolarization sequence.***

The full 3D atrial model was built on the basis of a previous model developed by our research group. An in-depth analysis of experimental histological studies was carried out and a rule-based algorithm was developed to assign the fibre orientation to the different atrial regions. An improvement has been included along the course of this thesis in order to include the most recent knowledge on the conduction pathways between both atria, mainly in the region of the coronary sinus. This improvement is of high relevance when studying focal atrial tachycardia mainly when the ectopic triggers are localized in the left atrium since the pattern described by the depolarization wavefront is very much dependent on the CS-LA bridges. Electrical properties at tissue scale were fine-tuned at atrial scale and the activation patterns was validated using experimental data. The main outcome is a multi-scale atrial model useful to the study of atrial behaviour under physiological and pathological conditions.

***Modelling of the anatomical and electrical properties across the torso to realistically propagate the physiological and arrhythmic atrial activity and to be able to measure the ECG on the torso surface as well as the body surface distribution of the electrical activity.***

The torso was built from MRI scans including the most relevant tissue conductivities affecting the generation of body surface and volumetric potentials as well as the P-wave morphologies. A relevant improvement was also carried out at torso level along the course of this thesis. It was based on the increase of the spatial resolution of the torso mesh in the area surrounding the atria. The highest the resolution the better the overlap between the atrial myocardium and the torso scales. Based on this, the bidomain approach was used instead of the heat transfer equation in order to compute the electrical propagation of the atrial activity through the torso model.

***Understanding the contribution from specific atrial regions to the physiological P-waves as well as their local influence on the body surface potential maps and BSPM-derived biomarkers.***

The simulations carried out using this multi-scale model allowed us to identify the contributions from different parts of the atria and determine their influence on the generation of the P-wave, body surface potential and RMS maps. From the results obtained, we concluded that RAA and RLW are the most influential atrial regions on the torso frontal surface under physiological conditions, due to their size, location and orientation. Furthermore, as P-wave signals in the rear side of the torso surface were mainly produced by LA activation (specifically by the LPW and PVs) their influence could be easily analysed independently.

Using this multiscale model, it was revealed that the best places for recording P-waves are the frontal upper right and the frontal and rear left quadrants of the torso. Our results also suggest that only nine regions (of the twenty-one structures in which the atrial tissue was divided) made the most significant contribution to the BSPM and determine the main P-wave characteristics.

***Development of a pipeline to non-invasively localize atrial ectopic beats by defining new BSPM-derived biomarkers using machine-learning techniques.***

After the previous-mentioned improvements of the atrial and torso models, a database with 58 simulations of focal atrial tachycardia (FAT) was built and new BSPM-derived biomarkers were analysed. From the results obtained, we conclude that the body surface P-wave integral map (BSPiM) is the best biomarker to summarize the atrial activation pattern since it considers all the relevant information: a) the signal polarity; b) the regions where the energy is mostly concentrated; and c) the atrial wavefront direction.

Furthermore, the methodological approach used in this study is the first in using unsupervised clustering and classifying techniques to localize atrial triggering sites in FAT, providing promising and useful results for physicians. In this regard, our validated atrial-torso multi-scale model has been used to produce different BSPMs in-silico, together with K-means clustering algorithms and classifying models based on multiclass support vector machine (SVM). From the results obtained, we concluded that ectopic foci with similar BSPiMs naturally cluster into differentiated non-intersected atrial regions and that prospective patterns could be correctly classified with an accuracy of 97% when considering 2 clusters and 96% when this number increases up to 4. Our results also suggest that an increase in the number of clusters is feasible at the cost of decreasing accuracy.

Although the classification capability with reduced spatial information should be investigated in future studies, these promising results could encourage physicians to use the BSPiMs as non-invasive biomarker and machine learning techniques to guide, for example, the radiofrequency ablation procedure or any other invasive procedure to restore patients to sinus rhythm.



# Annex I

---

## Future research work

The ultimate goal beyond the present thesis is to be able to accurately diagnose complex atrial arrhythmias and its specific triggering sites and mechanisms non-invasively by only analysing the potential distribution on the torso surface. Current limitations described in chapters 4 to 6 point out the necessity of improving the 3D multiscale atrial-torso model and the methodology in some aspects. In this regard, the future work from now on will try to solve the following issues:

**Consider the heterogeneous volume of the atrial wall.** An uncertainty degree must be bear in mind when analysing our results since the atrial wall has remained homogeneous in all the simulations carried out in this thesis. One could expect slight changes regarding the regions that mainly contribute to the P-wave when considering heterogeneous thickness since thicker regions will impact much more on the ECG morphology. The potential distribution on the torso surface as well as the patterns computed from our studies could also experiment changes. It is then necessary to adapt the wall thickness in both atria and remesh the atrial model to compare our current results with the new simulations and quantify the specific effect of the atrial wall thickness.

**Develop patient-specific atrial-torso models to ease a patient-specific diagnose and treatment.** The coupling between our atrial and torso scales has been carried out with high accuracy. However, atria and torso meshes should be segmented from a unique human or population cohort so the final model is much more realistic. On the other hand, inter- and intra-patient variability related to the cellular, tissue and organ scales should be considered. Understanding for example variations in the size and bifurcation of PVs, the CS-LA bridges or in the inter-atrial conduction bundles can be useful for the application of ablation lesions to patients suffering from atrial arrhythmias. It is therefore recommended to use additional clinical images to build a complete human atrial-torso model.

**Increase the number of ectopic atrial triggering sites within our database.** Our results suggested that an increase in the number of atrial clusters is feasible at the cost of decreasing accuracy. However, it is expected that increasing the number of sites and then the number of BSPiMs in our database, the machine-learning pipeline will provide a high

number of clusters with a highly accurate classification of prospective cases. It is therefore necessary to seed the atrial wall with more triggering sites carefully localized with a high spatial resolution.

**Reduce the number of leads considered to build the BSPM.** All our patterns have been built considering the 14157 nodes of the torso surface. However, this is not feasible in clinical practice. It is essential to build maps from up to 256 torso surface nodes and check if they reproduce the clustering and classification results with similar accuracy.

**Check the accuracy of the machine-learning pipeline in presence of other cardiac disorders.** Our simulations focused on studying focal atrial tachycardia. However, it is also very interesting for clinicians to be able to cluster and classify not only focal sites but also pathological substrates related to fibrotic areas, macro-reentrant arrhythmias or paroxysmal and permanent fibrillatory rhythms. The understanding gained during the present research work encourage us in the near future to first consider electrical atrial remodelling and fibrotic patches and second to simulate atrial fibrillation to try to reproduce our promising results with similar accuracy.

## Annex II

# List of scientific publications

### Contributions derived from this Thesis

International Journals:

- 1 **A. Ferrer**, R. Sebastián, D. Sánchez-Quintana, J. F. Rodríguez, E. J. Godoy, L. Martínez, and J. Saiz, “Detailed anatomical and electrophysiological models of human atria and torso for the simulation of atrial activation,” PLoS One, vol. 10, no. 11, p. e0141573, Jan. 2015
- 2 **A. Ferrer-Albero**, E. J. Godoy, M. Lozano, L. Martínez-Mateu, F. Atienza, J. Saiz, and R. Sebastian, “Non-invasive location of atrial ectopic beats by using Body Surface P-wave integral Maps,” PLoS One, 2017. Under revision

Conference papers:

- 1 **A. Ferrer**, R. Sebastian, J. F. Rodriguez, C. Tobon, and J. Saiz, “Modeling of Human Torso for the Study and Characterization of Atrial Arrhythmias,” in Cardiac Physiome, 2013.
- 2 **A. Ferrer**, R. Sebastian, J. F. Rodriguez, C. Tobon, M. Guillem, E. J. Godoy, and J. Saiz, “Computational Simulation and Analysis of 3D Body Surface Potential Patterns Generated by Common Atrial Arrhythmias,” in Computing in Cardiology, 2013, pp. 919–922.
- 3 **A. Ferrer-Albero**, E. J. Godoy, R. Sebastian, L. Martínez, and J. Saiz, “Analysis of in-silico Body Surface P-wave Integral Maps show important differences depending on the connections between Coronary Sinus and Left Atrium,” in Computing in Cardiology, 2016, vol. 43, pp. 1–4.

### Contributions related to this Thesis

International Journals:

- 1 D. Calvo, F. Atienza, J. Saiz, L. Martinez, P. Avila, J. Rubin, B. Herreros, A. Arenal, J. Garcia-Fernandez, **A. Ferrer**, R. Sebastian, P. Martinez-Camblor, J.

*List of scientific publications*

---

- Jalife, and O. Berenfeld, “Ventricular Tachycardia and Early Fibrillation in Patients with Brugada Syndrome and Ischemic Cardiomyopathy Show Predictable Frequency-Phase Properties on the Precordial ECG Consistent with the Respective Arrhythmogenic Substrate,” *Circ. Arrhythmia Electrophysiol.*, vol. 8, no. 5, pp. 1133–1143, Oct. 2015.
- 2 B. Carbonell-Pascual, E. Godoy, **A. Ferrer**, L. Romero, and J. M. Ferrero, “Comparison between Hodgkin-Huxley and Markov formulations of cardiac ion channels.” *J. Theor. Biol.*, vol. 399, pp. 92–102, Apr. 2016.
- 3 L. Martínez-Mateu, L. Romero, **A. Ferrer-Albero**, R. Sebastián, J. F. Rodríguez Matas, J. Jalife, O. Berenfeld, and J. Saiz, “Factors Affecting Basket Catheter Detection of Real and Phantom Rotors in the Atria: A Computational Study,” *Circ. Arrhythm. Electrophysiol.*, p. Manuscript submitted, 2017. Under revision
- Conference papers:
- 1 E. Godoy, M. Lozano, **A. Ferrer**, J. Saiz, and R. Sebastian, “Optimal surface ECG electrode set for prediction of atrial ectopic foci region,” in *Computational and Mathematical Biomedical Engineering*, 2017, no. April, pp. 206–209.
- 2 Martínez L, Romero L, **Ferrer A**, Jalife J, Berenfeld O, Saiz J, et al. Effect of Multi-Electrode Configurations on Accuracy of Rotor Detection in the Atria. Computing in Cardiology. 2016. pp. 2–5. doi:10.22489/CinC.2016.312-412

---

## References

- Abboud, S., Berenfeld, O. & Sadeh, D., 1991. Simulation of high-resolution QRS complex using a ventricular model with a fractal conduction system. Effects of ischemia on high-frequency QRS potentials. *Circulation research*, 68(6), pp.1751–1760.
- Al Abed, A. et al., 2010. An anatomically realistic 3D model of atrial propagation based on experimentally recorded action potentials. *2010 Annual International Conference of the IEEE Engineering in Medicine and Biology Society, EMBC'10*, pp.243–246.
- Ackerman, M., 1992. The visible human project of the National Library of Medicine. *Medinfo*, 92, pp.366–370.
- AFFIRM, 2002. A Comparison of Rate Control and Rhythm Control in Patients with Atrial Fibrillation (AFFIRM). *N Engl J Med*, 347(23), pp.1825–1833.
- Akcay, M. et al., 2007. Prominent Crista Terminalis: As An Anatomic Structure Leading to Atrial Arrhythmias and Mimicking Right Atrial Mass. *Journal of the American Society of Echocardiography*, 20(2), p.197.e9-197.e10.
- Alday, E.A.P. et al., 2015. A New Algorithm to Diagnose Atrial Ectopic Origin from Multi Lead ECG Systems - Insights from 3D Virtual Human Atria and Torso. *PLoS Computational Biology*, 11(1), p.e1004026.
- Almendral, J. et al., 2014. Update on arrhythmias and cardiac pacing 2013. *Revista española de cardiología (English ed.)*, 67(4), pp.294–304.
- Almendral, J. & Huerta, E.M., 2001. Guías de práctica clínica de la Sociedad Española de Cardiología en arritmias cardíacas R. E. Cardiol, ed. ... *Española De Cardiología*, p.54; 307-367.
- Anderson, R.H. & Cook, A.C., 2007. The structure and components of the atrial chambers. *Europace : European pacing, arrhythmias, and cardiac electrophysiology : journal of the working groups on cardiac pacing, arrhythmias, and cardiac cellular electrophysiology of the European Society of Cardiology*, 9 Suppl 6(suppl 6), p.vi3-9.
- Andrade, J.G., Rivard, L. & Macle, L., 2014. The Past, the Present, and the Future of Cardiac Arrhythmia Ablation. *Canadian Journal of Cardiology*, 30(12), pp.S431–S441.

---

*References*

- Ashihara, T. et al., 2012. The role of fibroblasts in complex fractionated electrograms during persistent/permanent atrial fibrillation: Implications for electrogram-based catheter ablation. *Circulation Research*, 110(2), pp.275–284.
- Aslanidi, O. et al., 2011. 3D virtual human atria: A computational platform for studying clinical atrial fibrillation. *Progress in Biophysics and Molecular Biology*, 107(1), pp.156–168.
- Aslanidi, O. V. et al., 2013. Application of micro-computed tomography with iodine staining to cardiac imaging, segmentation, and computational model development. *IEEE Transactions on Medical Imaging*, 32(1), pp.8–17.
- Aslanidi, O. V. et al., 2012. Virtual tissue engineering of the human atrium: Modelling pharmacological actions on atrial arrhythmogenesis. *European Journal of Pharmaceutical Sciences*, 46(4), pp.209–221.
- Atienza, F. et al., 2009. Real-time dominant frequency mapping and ablation of dominant frequency sites in atrial fibrillation with left-to-right frequency gradients predicts long-term maintenance of sinus rhythm. *Heart Rhythm*, 6(1), pp.33–40.
- Bachmann, G., 1916. The inter-auricular time interval. *American Journal of Physiology -- Legacy Content*, 41(3), pp.309–320.
- Barr, R.C. & Plonsey, R., 1984. Propagation of excitation in idealized anisotropic two-dimensional tissue. *Biophysical journal*, 45(6), pp.1191–1202.
- Bartos, D.C., Grandi, E. & Ripplinger, C.M., 2015. Ion Channels in the Heart. In *Comprehensive Physiology*. Hoboken, NJ, USA: John Wiley & Sons, Inc., pp. 1423–1464.
- Bauer, S. et al., 2009. How do tissue conductivities impact on forward-calculated ECGs? An efficient prediction based on principal component analysis. *IFMBE Proceedings*, 25(4), pp.641–644.
- Bayer, J.D. et al., 2012. A novel rule-based algorithm for assigning myocardial fiber orientation to computational heart models. *Annals of Biomedical Engineering*, 40(10), pp.2243–2254.
- Beeler, G.W. & Reuter, H., 1977. Reconstruction of the action potential of ventricular myocardial fibres. *The Journal of physiology*, 268(1), pp.177–210.
- Bellemare, F., Jeanneret, A. & Couture, J., 2003. Sex differences in thoracic dimensions and configuration. *American Journal of Respiratory and Critical Care Medicine*, 168(3), pp.305–312.
- Bellemare, J.F. et al., 2001. Thoracic dimensions at maximum lung inflation in normal subjects and in patients with obstructive and restrictive lung diseases. *Chest*, 119(2), pp.376–386.
- Benardeau, A. et al., 1996. Contribution of Na<sup>+</sup>/Ca<sup>2+</sup> exchange to action potential of human atrial myocytes. *Am J Physiol*, 271(3 Pt 2), pp.H1151-61.

- Bishop, C.M., 2006. *Patterns Recognition and Machine Learning* Springer-V.,
- Bjorck, S. et al., 2013. Atrial fibrillation, stroke risk, and warfarin therapy revisited: A population-based study. *Stroke*, 44(11), pp.3103–3108.
- Blanc, O. et al., 2001. A computer model of human atria with reasonable computation load and realistic anatomical properties. *IEEE Transactions on Biomedical Engineering*, 48(11), pp.1229–1237.
- Blomstrom-Lundqvist, C., 2003. *ACC/AHA/ESC Guidelines for the Management of Patients With Supraventricular Arrhythmias\*--Executive Summary: A Report of the American College of Cardiology/American Heart Association Task Force on Practice Guidelines and the European Society of Cardiology 2003/10/18.*
- Bommer, W. et al., 1979. Determination of right atrial and right ventricular size by two-dimensional echocardiography. *Circulation*, 60(1), pp.91–100.
- Boulakia, M. et al., 2010. Mathematical modeling of electrocardiograms: A numerical study. *Annals of Biomedical Engineering*, 38(3), pp.1071–1097.
- Bradley, C.P., Pullan, A.J. & Hunter, P.J., 1997. Geometric modeling of the human torso using cubic Hermite elements. *Annals of biomedical engineering*, 25(1), pp.96–111.
- Bradley, C.P., Pullan, a J. & Hunter, P.J., 2000. Effects of material properties and geometry on electrocardiographic forward simulations. *Annals of biomedical engineering*, 28(7), pp.721–741.
- Bressler, S.L. & Ding, M., 2006. Wiley Encyclopedia of Biomedical Engineering : Event-Related Potentials. In *Psychiatry research*. John Wiley & Sons, Inc., pp. 1–8.
- Burdumy, M. et al., 2012. Comparing measured and simulated wave directions in the left atrium a workflow for model personalization and validation. *Biomedizinische Technik*, 57(2), pp.79–87.
- Burton, B.M. et al., 2011. A toolkit for forward/inverse problems in electrocardiography within the SCIRun problem solving environment. *Proceedings of the Annual International Conference of the IEEE Engineering in Medicine and Biology Society, EMBS*, 2011, pp.267–270.
- Busscher, I. et al., 2010. Comparative anatomical dimensions of the complete human and porcine spine. *European Spine Journal*, 19(7), pp.1104–1114.
- Cabrera, J.A. et al., 2008. The architecture of the left lateral atrial wall: A particular anatomic region with implications for ablation of atrial fibrillation. *European Heart Journal*, 29(3), pp.356–362.
- Cabrera, J.A. & Sánchez-Quintana, D., 2013. Cardiac anatomy: what the electrophysiologist needs to know. *Heart (British Cardiac Society)*, 99(6), pp.417–31.
- Cabrera, J. a et al., 1998. The architecture of the atrial musculature between the orifice of the inferior caval vein and the tricuspid valve: the anatomy of the isthmus. *Journal of cardiovascular electrophysiology*, 9(11), pp.1186–1195.

## References

---

- Calkins, H. et al., 2009. Treatment of atrial fibrillation with antiarrhythmic drugs or radiofrequency ablation: Two systematic literature reviews and meta-analyses. *Circulation: Arrhythmia and Electrophysiology*, 2(4), pp.349–361.
- Cappato, R. et al., 2005. Worldwide survey on the methods, efficacy, and safety of catheter ablation for human atrial fibrillation. *Circulation*, 111(9), pp.1100–1105.
- Carbonell-Pascual, B. et al., 2016. Comparison between Hodgkin-Huxley and Markov formulations of cardiac ion channels. *Journal of theoretical biology*, 399, pp.92–102.
- Carley, S.D., 2003. Beyond the 12 lead: Review of the use of additional leads for the early electrocardiographic diagnosis of acute myocardial infarction. *Emergency Medicine*, 15(2), pp.143–154.
- Cassola, V.F. et al., 2011. Standing adult human phantoms based on 10th, 50th and 90th mass and height percentiles of male and female Caucasian populations. *Physics in medicine and biology*, 56(13), pp.3749–3772.
- Cha, T.J. et al., 2005. Atrial tachycardia remodeling of pulmonary vein cardiomyocytes: Comparison with left atrium and potential relation to arrhythmogenesis. *Circulation*, 111(6), pp.728–735.
- Chandler, N. et al., 2011. Computer Three-Dimensional Anatomical Reconstruction of the Human Sinus Node and a Novel Paranodal Area. *Anatomical Record*, 294(6), pp.970–979.
- Chandrasekhar, H.V.M.D. & Chandrasekhar, A.J.M.D., 2012. Radiological Anatomy of Heart and Vessels in Thorax. Available at: <http://www.meddean.luc.edu>.
- Chauvin, M. et al., 2000. The anatomic basis of connections between the coronary sinus musculature and the left atrium in humans. *Circulation*, 101, pp.647–652.
- Chen, S.A. et al., 1994. Sustained atrial tachycardia in adult patients. Electrophysiological characteristics, pharmacological response, possible mechanisms, and effects of radiofrequency ablation. *Circulation*, 90(3), pp.1262–78.
- Chugh, S.S. et al., 2014. Worldwide epidemiology of atrial fibrillation: A global burden of disease 2010 study. *Circulation*, 129(8), pp.837–847.
- Cibc, 2013. Seg3D: Volumetric Image Segmentation and Visualization. Scientific Computing and Imaging Institute (SCI), Download from: <http://www.seg3d.org>.
- Clancy, C.E. & Rudy, Y., 2001. Cellular consequences of HERG mutations in the long QT syndrome: Precursors to sudden cardiac death. *Cardiovascular Research*, 50(2), pp.301–313.
- Clancy, C.E. & Rudy, Y., 1999. Linking a genetic defect to its cellular phenotype in a cardiac arrhythmia. *Nature*, 400(6744), pp.566–569.
- Clancy, C.E. & Rudy, Y., 2002. Na<sup>+</sup> Channel Mutation That Causes Both Brugada and Long-QT Syndrome Phenotypes: A Simulation Study of Mechanism. *March*, 89(105), pp.1208–1213.

- Clayton, R.H. et al., 2011. Models of cardiac tissue electrophysiology: Progress, challenges and open questions. *Progress in Biophysics and Molecular Biology*, 104(1–3), pp.22–48.
- Clayton, R.H. & Taggart, P., 2005. Regional differences in APD restitution can initiate wavebreak and re-entry in cardiac tissue: a computational study. *Biomedical engineering online*, 4(1), p.54.
- Coffey, J.L., Cristy, M. & Warner, G.G., 1981. Specific absorbed fractions for photon sources uniformly distributed in the heart chambers and heart wall of a heterogeneous phantom. *Journal of nuclear medicine : official publication, Society of Nuclear Medicine*, 22(1), pp.65–71.
- Cohen, G.I. et al., 1995. Reference values for normal adult transesophageal echocardiographic measurements. *Journal of the American Society of Echocardiography : official publication of the American Society of Echocardiography*, 8(3), pp.221–230.
- Cole, W.C., McPherson, C.D. & Sontag, D., 1991. ATP-regulated K<sup>+</sup> channels protect the myocardium against ischemia/reperfusion damage. *Circulation research*, 69(3), pp.571–581.
- Colilla, S. et al., 2013. Estimates of current and future incidence and prevalence of atrial fibrillation in the U.S. adult population. *American Journal of Cardiology*, 112(8), pp.1142–1147.
- Colman, M., 2014. *Mechanisms of Atrial Arrhythmias*. Cham: Springer International Publishing.
- Colman, M.A. et al., 2011. Correlation between P-wave morphology and origin of atrial focal tachycardia-insights from realistic models of the human atria and torso. *IEEE Transactions on Biomedical Engineering*, 58(10 PART 2), pp.2952–2955.
- Cormier., R.E. et al., 1990. *Clinical Methods: The History, Physical, and Laboratory Examinations* 3rd editio. Walker HK, W. Hall, & J. Hurst, eds., Butterworth Publishers.
- Courtemanche, M., Ramirez, R.J. & Nattel, S., 1998. Ionic mechanisms underlying human atrial action potential properties: insights from a mathematical model. *The American journal of physiology*, 275(1 Pt 2), pp.H301-21.
- Cracraft, J., 1988. *Deep-history biogeography: Retrieving the historical pattern of evolving continental biotas*. Massachusset Institute of Technology, Cambridge, MA.
- Cranefield, P., 1977. Action Potentials, Afterpotentials, and Arrhythmias. *Circulation research*, 41(4), pp.415–423.
- Cuculich, P.S. et al., 2010. Noninvasive characterization of epicardial activation in humans with diverse atrial fibrillation patterns. *Circulation*, 122(14), pp.1364–1372.
- van Dam, P.M. & van Oosterom, A., 2003. Atrial excitation assuming uniform propagation. *Journal of cardiovascular electrophysiology*, 14(10 Suppl), pp.S166–S171.

## References

---

- van Dam, P.M. & van Oosterom, A., 2005. Volume conductor effects involved in the genesis of the P wave. *Europace*, 7(SUPPL. 2), pp.S30–S38.
- Dawodu, A.A. et al., 1996. The shape of human atrial action potential accounts for different frequency-related changes in vitro. *International Journal of Cardiology*, 54(3), pp.237–249.
- DeLand, F.H. & North, W. a, 1968. Relationship between liver size and body size. *Radiology*, 91(6), pp.1195–1198.
- Demir, S.S. et al., 1994. A mathematical model of a rabbit sinoatrial node cell. *The American journal of physiology*, 266(3 Pt 1), pp.C832–C852.
- Deng, D. et al., 2012. An image-based model of the whole human heart with detailed anatomical structure and fiber orientation. *Computational and Mathematical Methods in Medicine*, 2012, p.891070.
- Deng, D. et al., 2012. Simulation of biatrial conduction via different pathways during sinus rhythm with a detailed human atrial model. *Journal of Zhejiang University SCIENCE B*, 13(9), pp.676–694.
- Dobrev, D. et al., 2001. Molecular basis of downregulation of G-protein-coupled inward rectifying K(+) current ( $I(K,ACh)$ ) in chronic human atrial fibrillation: decrease in GIRK4 mRNA correlates with reduced  $I(K,ACh)$  and muscarinic receptor-mediated shortening of action potentials. *Circulation*, 104(21), pp.2551–2557.
- Doiny, D. & Merino, J.L., 2013. Atrial Flutter: Common and Main Atypical Forms. *E-Journal of Cardiology Practice*, 11(14), pp.1–8.
- Dokos, S., Cloherty, S.L. & Lovell, N.H., 2007. Computational model of atrial electrical activation and propagation. *Annual International Conference of the IEEE Engineering in Medicine and Biology - Proceedings*, (1), pp.908–911.
- Dössel, O. et al., 2012. Computational modeling of the human atrial anatomy and electrophysiology. *Medical & Biological Engineering & Computing*, 50(8), pp.773–799.
- E. Poletti D. Fiorin, E.G. & Ruggeri, a, 2009. World Congress on Medical Physics and Biomedical Engineering, September 7 - 12, 2009, Munich, Germany. In O. Dössel & W. C. Schlegel, eds. Springer Berlin Heidelberg, pp. 137–140.
- Earm, Y.E. & Noble, D., 1990. A model of the single atrial cell: relation between calcium current and calcium release. *Proceedings of the Royal Society of London. Series B, Containing papers of a Biological character. Royal Society (Great Britain)*, 240(1297), pp.83–96.
- Van Eck, H.J.R., Kors, J.A. & Van Herpen, G., 2003. The Elusive U Wave: A Simple Explanation of Its Genesis. *Journal of Electrocardiology*, 36(SUPPL.), pp.133–137.
- Einthoven, W., Fahr, G. & De Waart, A., 1950. On the direction and manifest size of the variations of potential in the human heart and on the influence of the position of the

- heart on the form of the electrocardiogram. *American Heart Journal*, 40(2), pp.163–211.
- Fedorov, V. et al., 2010. Optical mapping of the isolated coronary-perfused human sinus node. *Journal of the American College of Cardiology*, 56(17), pp.1386–1394.
- Feng, J. et al., 1998. Ionic mechanisms of regional action potential heterogeneity in the canine right atrium. *Circulation research*, 83(5), pp.541–551.
- Fereniec, M. et al., 2011. Risk assessment of ventricular arrhythmia using new parameters based on high resolution body surface potential mapping. *Medical science monitor : international medical journal of experimental and clinical research*, 17(3), p.MT26-T33.
- Ferrero, J., Saiz, J. & Arnau, A., 1994. *Bioelectrónica, señales bioeléctricas* Universidad Politécnica de Valencia, ed.,
- Figueras, C. et al., 2016. Regularization techniques for ECG imaging during atrial fibrillation: A computational study. *Frontiers in Physiology*, 7(OCT), pp.1–17.
- Fink, M. & Noble, D., 2009. Markov models for ion channels: versatility versus identifiability and speed. *Philosophical transactions. Series A, Mathematical, physical, and engineering sciences*, 367(1896), pp.2161–2179.
- Finlay, D.D. et al., 2005. Mining for diagnostic information in body surface potential maps: a comparison of feature selection techniques. *Biomedical engineering online*, 4, p.51.
- Furberg, C.D. et al., 1994. Prevalence of atrial fibrillation in elderly subjects (the Cardiovascular Health Study). *The American journal of cardiology*, 74(3), pp.236–241.
- Gabor, D. & Nelson, C. V., 1954. Determination of the resultant dipole of the heart from measurements on the body surface. *Journal of Applied Physics*, 25(4), pp.413–416.
- Gabriel, C., Gabriel, S. & Corthout, E., 1996. The dielectric properties of biological tissues: I. Literature survey. *Physics in medicine and biology*, 41(11), pp.2231–2249.
- Gabriel, S., Lau, R.W. & Gabriel, C., 1996. The dielectric properties of biological tissues: II. Measurements in the frequency range 10 Hz to 20 GHz. *Physics in medicine and biology*, 41(11), pp.2251–2269.
- Gerhardt, X., Schuster, X. & Tyson, X., 1990. A Cellular Automation Model of Excitable Media Including Curvature and Dispersion. *Science*, 247, p.1563.
- Gerstenfeld, E.P. et al., 2000. Derivation of an optimal lead set for measuring ectopic atrial activation from the pulmonary veins by using body surface mapping. *Journal of electrocardiology*, 33 Suppl, pp.179–185.
- Geselowitz, D.B. & Miller, W.T., 1983. A bidomain model for anisotropic cardiac muscle. *Annals of Biomedical Engineering*, 11(3–4), pp.191–206.
- Ghali, W.A. et al., 2005. Atrial flutter and the risk of thromboembolism: A systematic review and meta-analysis. *American Journal of Medicine*, 118(2), pp.101–107.

## References

---

- Giacopelli, D. et al., 2012. Spatial pattern of P waves in paroxysmal atrial fibrillation patients in sinus rhythm and controls. *PACE - Pacing and Clinical Electrophysiology*, 35(7), pp.819–826.
- Giffard-Roisin, S. et al., 2016. Non-Invasive Personalisation of a Cardiac Electrophysiology Model from Body Surface Potential Mapping. *IEEE Transactions on Biomedical Engineering*, 9294(c), pp.1–1.
- Goel, R., Srivathsan, K. & Mookadam, M., 2013. Supraventricular and Ventricular Arrhythmias. *Primary Care - Clinics in Office Practice*, 40(1), pp.43–71.
- Gonzales, M.J. et al., 2013. A three-dimensional finite element model of human atrial anatomy: New methods for cubic Hermite meshes with extraordinary vertices. *Medical Image Analysis*, 17(5), pp.525–537.
- Gozolits, S. et al., 2002. Global P Wave Duration on the 65-Lead ECG: Single-Site and Dual-Site Pacing in the Structurally Normal Human Atrium. *Journal of Cardiovascular Electrophysiology*, 13(12), pp.1240–1245.
- van der Graaf, A.W.M. et al., 2014. Noninvasive Imaging of Cardiac Excitation: Current Status and Future Perspective. *Ann. Noninvasive Electrocardiol.*, p.n/a-n/a.
- Granada, J. et al., 2000. Incidence and predictors of atrial flutter in the general population. *Journal of the American College of Cardiology*, 36(7), pp.2242–2246.
- Grandi, E. et al., 2011. Human atrial action potential and Ca<sup>2+</sup> model: sinus rhythm and chronic atrial fibrillation. *Circ Res*, 109(9), pp.1055–1066.
- Grandi, E., Pasqualini, F.S. & Bers, D.M., 2010. A novel computational model of the human ventricular action potential and Ca transient. *Journal of Molecular and Cellular Cardiology*, 48(1), pp.112–121.
- Gray, R.A. & Jalife, J., 1998. Ventricular fibrillation and atrial fibrillation are two different beasts. *Chaos (Woodbury, N.Y.)*, 8(1), pp.65–78.
- Groenewegen, A.S., 2004. Non-invasive localization and treatment of focal atrial fibrillation.
- Guerra, J.M. & Cinca, J., 2007. Ritmo sinusal normal. Nuevos conceptos anatómicos y fisiológicos del nódulo sinusal. Corriente If. *Revista Española de Cardiología*, 7(Supl.D), pp.26–31.
- Guillem, M. et al., 2009. How many leads are necessary for a reliable reconstruction of surface potentials during atrial fibrillation? *IEEE Transactions on Information Technology in Biomedicine*, 13(3), pp.330–340.
- Guillem, M.S. et al., 2009. Surface Wavefront Propagation Maps: Non-invasive characterization of atrial flutter circuit. *International Journal of Bioelectromagnetism*, 11(1), pp.22–26.
- Gulrajani, R.M., 1998. The Forward and Inverse Problems of Electrocardiography. *IEEE Engineering in Medicine and Biology*, 17(5), pp.84–122.

- Guyton, A., 1987. *Physiology of the human body* 5th ed., Philadelphia: Saunders.
- Haim, M. et al., 2015. Prospective National Study of the Prevalence, Incidence, Management and Outcome of a Large Contemporary Cohort of Patients With Incident Non-Valvular Atrial Fibrillation. *J Am Heart Assoc.*, 4(1), p.e001486.
- Haïssaguerre, M. et al., 2009. Spontaneous Initiation of Atrial Fibrillation by Ectopic Beats Originating in the Pulmonary Veins. <http://dx.doi.org.prxy4.ursus.maine.edu/10.1056/NEJM19980903391003>, 339(10), pp.659–666.
- Hall, M.C.S. & Todd, D.M., 2006. Modern management of arrhythmias. *Postgraduate medical journal*, 82(964), pp.117–25.
- Halligan, S.C. et al., 2004. Brief Communication The Natural History of Lone Atrial Flutter. *Annals of Internal Medicine*, pp.265–269.
- Hamill, O.P. et al., 1981. Improved patch-clamp techniques for high-resolution current recording from cells and cell-free membrane patches. *Pflügers Archiv European Journal of Physiology*, 391(2), pp.85–100.
- Hansson, a. et al., 1998. Right atrial free wall conduction velocity and degree of anisotropy in patients with stable sinus rhythm studied during open heart surgery. *European Heart Journal*, 19(2), pp.293–300.
- Harada, a et al., 1996. Atrial activation during chronic atrial fibrillation in patients with isolated mitral valve disease. *The Annals of thoracic surgery*, 61(1), pp.104-111-112.
- Harrild, D. & Henriquez, C., 2000. A computer model of normal conduction in the human atria. *Circulation research*, 87(7), pp.E25–E36.
- Harris, B.C. et al., 1968. Left Atrial Rhythm: Experimental Production in Man. *Circulation*, 37(6), pp.1000–1014.
- Hartigan, J.A., 1989. *Clustering Algorithms*,
- Hebbar, A.K. & Hueston, W.J., 2002. Management of common arrhythmias: Part I. Supraventricular arrhythmias. *American Family Physician*, 65(12), pp.2479–2486.
- Heidenreich, E.A. et al., 2010. Adaptive macro finite elements for the numerical solution of monodomain equations in cardiac electrophysiology. *Annals of Biomedical Engineering*, 38(7), pp.2331–2345.
- Heijman, J. et al., 2015. Computational models of atrial cellular electrophysiology and calcium handling , and their role in atrial fibrillation. *Journal of physiology*, Accepted (, pp.1–40.
- Henriquez, C.S., 1993. Simulating the electrical behavior of cardiac tissue using the bidomain model. *Critical reviews in biomedical engineering*, 21(1), pp.1–77.
- Henriquez, C.S. & Papazoglou, A.A., 1996. Using computer models to understand the roles of tissue structure and membrane dynamics in arrhythmogenesis. *Proceedings of the*

## References

---

- IEEE, 84(3), pp.334–354.
- Hilgemann, D.W. & Noble, D., 1987. Excitation-contraction coupling and extracellular calcium transients in rabbit atrium: reconstruction of basic cellular mechanisms. *Proceedings of the Royal Society of London. Series B, Containing papers of a Biological character. Royal Society (Great Britain)*, 230(1259), pp.163–205.
- Hiraoka, A. et al., 1998. Structural Characteristics of Koch's Triangle in Patients with Atrioventricular Node Reentrant Tachycardia. *Hiroshima Journal of Medical Sciences*, 47(1), pp.7–15.
- Ho, S.Y. et al., 1999. Anatomy of the left atrium: implications for radiofrequency ablation of atrial fibrillation. *Journal of cardiovascular electrophysiology*, 10(11), pp.1525–1533.
- Ho, S.Y., Cabrera, J.A. & Sanchez-Quintana, D., 2012. Left atrial anatomy revisited. *Circulation: Arrhythmia and Electrophysiology*, 5(1), pp.220–228.
- Ho, S.Y. & McCarthy, K.P., 2010. Anatomy of the left atrium for interventional electrophysiologists. *PACE - Pacing and Clinical Electrophysiology*, 33(5), pp.620–627.
- Hodgkin, a L. & Huxley, a F., 1952. A quantitative description of membrane current and its application to conduction and excitation in nerve. *Journal of Physiology*, 127, pp.500–544.
- Hoekema, R., Uijen, G. & Van Oosterom, a., 1999. The number of independent signals in body surface maps. *Methods of Information in Medicine*, 38(2), pp.119–124.
- Huo, Y. et al., 2014. P-wave characteristics and histological atrial abnormality. *Journal of Electrocardiology*, 47(3), pp.275–280.
- Ii, E.M.H. & Herod, J. V, 1997. Linear Methods of Applied Mathematics. , (c).
- Ilnicki, T., 1987. *Electrophysiological and Mechanical Measurements in Human and Rabbit Atria [microform]*, Thesis (M.Sc.)--University of Calgary.
- Intini, A. et al., 2005. Electrocardiographic imaging (ECGI), a novel diagnostic modality used for mapping of focal left ventricular tachycardia in a young athlete. *Heart Rhythm*, 2(11), pp.1250–1252.
- Irvine, L. a, Jafri, M.S. & Winslow, R.L., 1999. Cardiac sodium channel Markov model with temperature dependence and recovery from inactivation. *Biophysical journal*, 76(4), pp.1868–1885.
- Ishihara, H. et al., 1997. The isopotential body surface atrial maps in healthy children of different age groups. *Japanese circulation journal*, 51((5)), pp.520–6.
- Iyer, V., Mazhari, R. & Winslow, R.L., 2004. A computational model of the human left-ventricular epicardial myocyte. *Biophysical journal*, 87(3), pp.1507–1525.
- Jacquemet, V., 2015. Modeling left and right atrial contributions to the ECG: A dipole-current source approach. *Computers in Biology and Medicine*, 65, pp.192–199.

- Jafri, M.S., Rice, J.J. & Winslow, R.L., 1998. Cardiac Ca<sup>2+</sup> dynamics: the roles of ryanodine receptor adaptation and sarcoplasmic reticulum load. *Biophysical journal*, 74(3), pp.1149–1168.
- Jalife, J., 2003. Rotors and spiral waves in atrial fibrillation. *Journal of cardiovascular electrophysiology*, 14(7), pp.776–780.
- January, C.T., Chau, V. & Makielinski, J.C., 1991. Triggered activity in the heart: cellular mechanisms of early after-depolarizations. *Eur Heart J*, 12 Suppl F, pp.4–9.
- Kalman, J.M. et al., 1998. “Cristal tachycardias”: Origin of right atrial tachycardias from the crista terminalis identified by intracardiac echocardiography. *Journal of the American College of Cardiology*, 31(2), pp.451–459.
- Kannel, W.B. et al., 1982. Epidemiologic features of chronic atrial fibrillation: the Framingham study. *The New England journal of medicine*, 306(17), pp.1018–1022.
- Kawano, S. et al., 1989. Body surface maps of ectopic P waves originating in the left atrium in the dog. *Journal of Electrocardiology*, 22(1), pp.27–43.
- Kawano, S., Sawanobori, T. & Hiraoka, M., 1983. Human body surface mapping during atrial depolarization in normal and diseased subjects. *Journal of Electrocardiology*, 16(2), pp.151–159.
- Keating, M.T. & Sanguinetti, M.C., 1996. Molecular genetic insights into cardiovascular disease. *Science*, 272(5262), pp.681–685.
- Keller, D.U.J. et al., 2007. Computer based modeling of the congenital long-QT 2 syndrome in the Visible Man torso: From genes to ECG. *Annual International Conference of the IEEE Engineering in Medicine and Biology - Proceedings*, 2007, pp.1410–1413.
- Keller, D.U.J. et al., 2011. Impact of physiological ventricular deformation on the morphology of the T-wave: A hybrid, static-dynamic approach. *IEEE Transactions on Biomedical Engineering*, 58(7), pp.2109–2119.
- Keller, D.U.J. et al., 2010. Ranking the influence of tissue conductivities on forward-calculated ecgs. *IEEE Transactions on Biomedical Engineering*, 57(7), pp.1568–1576.
- Kirchhof, P. et al., 2016. 2016 ESC Guidelines for the management of atrial fibrillation developed in collaboration with EACTS. *Europace*, 18(11), pp.1609–1678.
- Kistler, P.M. et al., 2006. P-Wave Morphology in Focal Atrial Tachycardia. Development of an Algorithm to Predict the Anatomic Site of Origin. *Journal of the American College of Cardiology*, 48(5), pp.1010–1017.
- Kitzman, D.W. et al., 1988. Age-related changes in normal human hearts during the first 10 decades of life. Part II (Maturity): A quantitative anatomic study of 765 specimens from subjects 20 to 99 years old. *Mayo Clinic proceedings. Mayo Clinic*, 63(2), pp.137–146.
- Kléber, A., Janse, M. & Fast, V., 2001. Normal and abnormal conduction in the heart. In *Comprehensive Physiology*. John Wiley & Sons, Inc.

---

*References*

- Klepfer, R.N., Johnson, C.R. & Macleod, R.S., 1997. The effects of inhomogeneities and anisotropies on electrocardiographic fields: A 3-D finite-element study. *IEEE Transactions on Biomedical Engineering*, 44(8), pp.706–719.
- Kneller, J. et al., 2002. Cholinergic atrial fibrillation in a computer model of a two-dimensional sheet of canine atrial cells with realistic ionic properties. *Circulation research*, 90(9), pp.E73–E87.
- Koivumäki, J.T., Korhonen, T. & Tavi, P., 2011. Impact of sarcoplasmic reticulum calcium release on calcium dynamics and action potential morphology in human atrial myocytes: A computational study. *PLoS Computational Biology*, 7(1), p.e1001067.
- Kojodojo, P. et al., 2006. Age-Related Changes in Human Left and Right Atrial Conduction. *Journal of cardiovascular electrophysiology*, pp.10–15.
- Kowey, P.R., 2011. Novel Therapeutic Targets for Antiarrhythmic Drugs. *Circulation*, 123(7), pp.e241–e242.
- Kozlíková, K., 2007. P-wave body surface isointegral maps in children and in young adults. *Physiological research / Academia Scientiarum Bohemoslovaca*, 56 Suppl 1, pp.S123–S128.
- Kramer, G.H. et al., 2012. Linear Dimensions and Volumes of Human Lungs Obtained From Ct Images. *Health Physics*, 102(4), pp.378–383.
- Krassowska, W. & Neu, J.C., 1994. Effective boundary conditions for syncytial tissues. *IEEE Transactions on Biomedical Engineering*, 41(2), pp.143–150.
- Kratzer, W. et al., 2003. Factors affecting liver size: a sonographic survey of 2080 subjects. *Journal of ultrasound in medicine: official journal of the American Institute of Ultrasound in Medicine*, 22(11), pp.1155–1161.
- Krijthe, B.P. et al., 2013. Projections on the number of individuals with atrial fibrillation in the European Union, from 2000 to 2060. *European Heart Journal*, 34(35), pp.2746–2751.
- Krueger, M.W. et al., 2013. In-silico modeling of atrial repolarization in normal and atrial fibrillation remodeled state. *Medical and Biological Engineering and Computing*, 51(10), pp.1105–1119.
- Krueger, M.W. et al., 2011. Modeling atrial fiber orientation in patient-specific geometries: A semi-automatic rule-based approach D. Metaxas & L. Axel, eds. *Lecture Notes in Computer Science (including subseries Lecture Notes in Artificial Intelligence and Lecture Notes in Bioinformatics)*, 6666 LNCS, pp.223–232.
- Krueger, M.W. et al., 2012. Personalization of atrial anatomy and electrophysiology as a basis for clinical modeling of radio-frequency ablation of atrial fibrillation. *IEEE Transactions on Medical Imaging*, 32(1), pp.73–84.
- Krüger, M., 2012. *Personalized Multi-Scale Modeling of the Atria*. Karlsruher Institut für Technologie (KIT).

- Krzyminiewski, R. & Grajek, M., 2005. Numerical enlargement of signal resolution of records ECG. In *Medical Physics Proceedings of the jointly held Congresses ICMP 2005 14th International Conference of Medical Physics of the International Organization for Medical Physics (IOMP), European Federation of Organizations in Medical Physics (EFOMP) and the Ger.* Nuremberg, Germany, Biomedizinische Technik, pp. 275–276.
- Lamata, P. et al., 2013. Quality metrics for high order meshes: Analysis of the mechanical simulation of the heart beat. *IEEE Transactions on Medical Imaging*, 32(1), pp.130–138.
- Laurent, U. et al., 2010. Optimizing local capture of atrial fibrillation by rapid pacing: Study of the influence of tissue dynamics. *Annals of Biomedical Engineering*, 38(12), pp.3664–3673.
- Lee, J. & Fynn, S., 2015. P Wave Morphology in Guiding the Ablation Strategy of Focal Atrial Tachycardias and Atrial Flutter. *Current Cardiology Reviews*, 11(2), pp.103–110.
- Lemery, R. et al., 2007. Normal atrial activation and voltage during sinus rhythm in the human heart: An endocardial and epicardial mapping study in patients with a history of atrial fibrillation. *Journal of Cardiovascular Electrophysiology*, 18(4), pp.402–408.
- Lemery, R., Guiraudon, G. & Veinot, J.P., 2003. Anatomic description of Bachmann's Bundle and its relation to the atrial septum. *American Journal of Cardiology*, 91(12), pp.1482–1485.
- Lenkova, J., Svehlikova, J. & Tysler, M., 2012. Individualized model of torso surface for the inverse problem of electrocardiology. *Journal of Electrocardiology*, 45(3), pp.231–236.
- Leon, D.F. et al., 1970. Right atrial ectopic rhythms. Experimental production in man. *The American Journal of Cardiology*, 25(1), pp.6–10.
- Leon, L.J. & Horacek, B.M., 1991. Computer-Model of Excitation and Recovery in the Anisotropic Myocardium .3. Arrhythmogenic Conditions in the Simplified Left-Ventricle. *Journal of Electrocardiology*, 24(1), pp.33–41.
- Lesh, M.D. et al., 1996. The role of atrial anatomy in clinical atrial arrhythmias. *Journal of Electrocardiology*, 29(SUPPL.), pp.101–113.
- Li, D. et al., 2001. Potential ionic mechanism for repolarization differences between canine right and left atrium. *Circulation research*, 88(11), pp.1168–1175.
- Lian, J. et al., 2002. Body surface Laplacian mapping of atrial depolarization in healthy human subjects. *Medical & biological engineering & computing*, 40(6), pp.650–659.
- Liew, R., 2013. Almanac 2013: cardiac arrhythmias and pacing. *Heart (British Cardiac Society)*, 99(19), pp.1398–1407.
- Lim, H.S. et al., 2015. Noninvasive mapping to guide atrial fibrillation ablation. *Cardiac*

---

*References*

---

- Electrophysiology Clinics*, 7(1), pp.89–98.
- Lindblad, D.S. et al., 1996. A model of the action potential and underlying membrane currents in a rabbit atrial cell. *The American journal of physiology*, 271(4 Pt 2), pp.H1666–H1696.
- Lines, G.T. et al., 2003. Mathematical models and numerical methods for the forward problem in cardiac electrophysiology. *Computing and Visualization in Science*, 5(4), pp.215–239.
- Lu, W. et al., 2011. A computer model based on real anatomy for electrophysiology study. *Advances in Engineering Software*, 42(7), pp.463–476.
- Luo, C.H. & Rudy, Y., 1994a. A dynamic model of the cardiac ventricular action potential. I. Simulations of ionic currents and concentration changes. *Circulation research*, 74(6), pp.1071–1096.
- Luo, C.H. & Rudy, Y., 1994b. A dynamic model of the cardiac ventricular action potential. II. Afterdepolarizations, triggered activity, and potentiation. *Circulation research*, 74(6), pp.1097–1113.
- Lux, R.L. et al., 1978. Limited lead selection for estimation of body surface potential maps in electrocardiography. *IEEE transactions on bio-medical engineering*, 25(3), pp.270–276.
- Lux, R.L. et al., 2014. The application of root mean square electrocardiography (RMS ECG) for the detection of acquired and congenital long QT syndrome. *PLoS ONE*, 9(1), pp.1–9.
- MacLeod, R., Johnson, C. & Ershler, P., 1991. Construction of an Inhomogeneous Model of the Human Torso for Use in Computational Electrocardiography. *IEEE Engineering in Medicine and Biology Society 13th Annual International Conference*, p.pages 688–689.
- Maleckar, M.M. et al., 2009. K<sup>+</sup> current changes account for the rate dependence of the action potential in the human atrial myocyte. *American journal of physiology. Heart and circulatory physiology*, 297(4), pp.H1398–H1410.
- Malmivuo, J. & Plonsey, R., 1995. *Bioelectromagnetism: Principles and Applications of Bioelectric and Biomagnetic Fields* R. Plonsey, ed., New York : Oxford University Press.
- Marbán, E., 2002. Cardiac channelopathies. *Nature*, 415(6868), pp.213–218.
- Martínez-Mateu, L. et al., 2017. Factors Affecting Basket Catheter Detection of Real and Phantom Rotors in the Atria: A Computational Study. *Circulation. Arrhythmia and electrophysiology*, p.Manuscript submitted.
- Martinez, L. et al., 2016. Are multi-electrode arrays able to differentiate anatomical from functional reentries in an excitable sheet? *Computing in Cardiology*, 42, pp.865–868.
- Massumi, R.A. et al., 1969. Time sequence of right and left atrial depolarization as a guide to the origin of the P waves. *Am J Cardiol*, 24(1), pp.28–36.

---

References

- Matsuyama, T.A. et al., 2004. Anatomical diversity and age-related histological changes in the human right atrial posterolateral wall. *Europace*, 6(4), pp.307–315.
- McDowell, K.S. et al., 2012. Methodology for patient-specific modeling of atrial fibrosis as a substrate for atrial fibrillation. *Journal of Electrocardiology*, 45(6), pp.640–645.
- McDowell, K.S. et al., 2015. Virtual electrophysiological study of atrial fibrillation in fibrotic remodeling. *PLoS ONE*, 10(2), pp.1–16.
- Meek, S. & Morris, F., 2002. ABC of clinical electrocardiography. Introduction. I-Leads, rate, rhythm, and cardiac axis. *BMJ (Clinical research ed.)*, 324(7334), pp.415–418.
- Miller, J.M. & Zipes, D.P., 2011. *Diagnosis of Cardiac Arrhythmias* 9th ed. Ph.,
- Mirams, G.R. et al., 2016. White paper: Uncertainty and variability in computational and mathematical models of cardiac physiology. *The Journal of physiology*, epub aheea, pp.1–33.
- Mirvis, D.M., 1980. Body surface distribution of electrical potential during atrial depolarization and repolarization. *Circulation*, 62(1), pp.167–173.
- Moe, G.K., 1962. On the multiple wavelet hypothesis of atrial fibrillation. *Arch.Int.Pharmacodyn.Ther.*, 140, pp.183–188.
- Nattel, S. et al., 2014. New Directions in Cardiac Arrhythmia Management: Present Challenges and Future Solutions. *Canadian Journal of Cardiology*, 30(12), pp.S420–S430.
- Negoescu, R.M., 1991. Shift Of Sinoatrial True Pacemaker Under Autonomic Drive In Man. In *Proceedings of the Annual International Conference of the IEEE Engineering in Medicine and Biology Society Volume 13: 1991*. pp. 2321–2322.
- Noble, D., 1960. Cardiac action and pacemaker potentials based on the Hodgkin-Huxley equations. *Nature*, 188(4749), pp.495–497.
- Nygren, a et al., 1998. Mathematical model of an adult human atrial cell: the role of K<sup>+</sup> currents in repolarization. *Circulation research*, 82(1), pp.63–81.
- Nygren, a., Leon, L.J. & Giles, W.R., 2001. Simulations of the human atrial action potential. *Philosophical Transactions of the Royal Society A: Mathematical, Physical and Engineering Sciences*, 359(1783), pp.1111–1125.
- Onundarson, P.T. et al., 1987. Chronic atrial fibrillation--epidemiologic features and 14 year follow-up: a case control study. *European heart journal*, 8(5), pp.521–527.
- Orejarena, L. a et al., 1998. Paroxysmal supraventricular tachycardia in the general population. *Journal of the American College of Cardiology*, 31(1), pp.150–157.
- Pandit, S. V et al., 2005. Ionic determinants of functional reentry in a 2-D model of human atrial cells during simulated chronic atrial fibrillation. *Biophysical journal*, 88(6), pp.3806–3821.
- Pappone, C. et al., 2001. Atrial Electroanatomic Remodeling After Circumferential

---

*References*

---

- Radiofrequency Pulmonary Vein Ablation: Efficacy of an Anatomic Approach in a Large Cohort of Patients With Atrial Fibrillation. *Circulation*, 104(21), pp.2539–2544.
- Pashakhanloo, F. et al., 2016. Myofiber architecture of the human atria as revealed by submillimeter diffusion tensor imaging. *Circulation: Arrhythmia and Electrophysiology*, 9(4), p.e004133.
- Pedron-Torrecilla, J., 2010. *Implementación y estudio de métodos numéricos para la resolución del problema directo e inverso de la electrocardiografía : modelado de la actividad eléctrica en la superficie del torso*. Universidad Politécnica de Valencia.
- Pedrote-Martínez, A. et al., 2016. 15th Official Report of the Spanish Society of Cardiology Working Group on Electrophysiology and Arrhythmias (2015). *Revista Española de Cardiología*, 69(11), pp.1061–1070.
- Perez Alday, E.A. et al., 2016. Comparison of electric- and magnetic- cardiograms produced by myocardial ischemia in models of the human ventricle and torso. *Computing in Cardiology*, 42, pp.517–520.
- Plank, G. et al., 2008. From mitochondrial ion channels to arrhythmias in the heart: computational techniques to bridge the spatio-temporal scales. *Philosophical transactions. Series A, Mathematical, physical, and engineering sciences*, 366(1879), pp.3381–409.
- Plonsey, R. & Barr, R.C., 1984. Current flow patterns in two-dimensional anisotropic bisyncytia with normal and extreme conductivities. *Biophysical journal*, 45(3), pp.557–571.
- Plonsey, R. & Barr, R.C., 1987. Mathematical modeling of electrical activity of the heart. *Journal of electrocardiology*, 20(3), pp.219–226.
- Potse, M. et al., 2006. A comparison of monodomain and bidomain propagation models for the human heart. *Annual International Conference of the IEEE Engineering in Medicine and Biology - Proceedings*, 1, pp.3895–3898.
- Potse, M., Dube, B. & Gulrajani, R.M., 2003. ECG simulations with realistic human membrane, heart, and torso models. In *Proceedings of the 25th Annual International Conference of the IEEE Engineering in Medicine and Biology Society (IEEE Cat. No.03CH37439)*. pp. 70–73.
- Potse, M., Dubé, B. & Vinet, A., 2009. Cardiac anisotropy in boundary-element models for the electrocardiogram. *Medical and Biological Engineering and Computing*, 47(7), pp.719–729.
- Priebe, L. & Beuckelmann, D.J., 1998. Simulation study of cellular electric properties in heart failure. *Circulation research*, 82(11), pp.1206–1223.
- Pullan, A.J., A Cheng, L.K. & A Buist, M.L., 2005. *Mathematically Modelling the Electrical Activity of the Heart: From Cell to Body Surface and Back Again*, World Scientific Publishing Co. Pte. Ltd.

- Ramanathan, C. et al., 2006. Activation and repolarization of the normal human heart under complete physiological conditions. *Proceedings of the National Academy of Sciences of the United States of America*, 103(16), pp.6309–6314.
- Rasmusson, R.L. et al., 1990. A mathematical model of a bullfrog cardiac pacemaker cell. *The American journal of physiology*, 259(2 Pt 2), pp.H352–H369.
- Reich, C. et al., 2016. Classification of cardiac excitation patterns during atrial fibrillation. *Current Directions in Biomedical Engineering*, 2(1), pp.161–166.
- Reig, J. et al., 1997. Étude Morphologique De La Fosse Ovale Et Bases Anatomiques Du Cathétérisme Transseptal. *Surgical and Radiologic Anatomy*, 19(5), pp.279–282.
- Ridler, M. et al., 2006. Action potential duration gradient protects the right atrium from fibrillating. *Annual International Conference of the IEEE Engineering in Medicine and Biology - Proceedings*, 1, pp.3978–3981.
- Roberts, D.E., Hersh, L.T. & Scher, a M., 1979. Influence of cardiac fiber orientation on wavefront voltage, conduction velocity, and tissue resistivity in the dog. *Circulation research*, 44(5), pp.701–712.
- Robles De Medina, E.O. et al., 2014. Morphology of Ectopic Right Atrial Activation Body Surface Mapping During Pacing at Multiple Sites in the Human Atrium: P-Wave Body Surface Mapping During Pacing at Multiple Sites in the Human Atrium P-Wave Morphology of Ectopic Right Atrial Activation. *Circulation*, 97(4), pp.369–380.
- Rodrigo, M. et al., 2014. Body surface localization of left and right atrial high-frequency rotors in atrial fibrillation patients: A clinical-computational study. *Heart Rhythm*, 11(9), pp.1584–1591.
- Romero, L. et al., 2009. The relative role of refractoriness and source-sink relationship in reentry generation during simulated acute ischemia. *Annals of Biomedical Engineering*, 37(8), pp.1560–1571.
- Rudy, Y., 2010. Noninvasive imaging of cardiac electrophysiology and arrhythmia. *Annals of the New York Academy of Sciences*, 1188, pp.214–221.
- Rudy, Y. & Burnes, J.E., 1999. Noninvasive electrocardiographic imaging. *Annals of Noninvasive Electrocardiology*, 4(3), pp.340–359.
- Rudy, Y. & Plonsey, R., 1980. A comparison of volume conductor and source geometry effects on body surface and epicardial potentials. *Circulation research*, 46(2), pp.283–291.
- Ruiz-Villa, C., 2010. *Estudio de la vulnerabilidad a reentrantas a través de modelos matemáticos y simulación de la aurícula humana*. Universidad Politécnica de Valencia.
- Sachse, F.B., 2004. *Computational cardiology: modeling of anatomy, electrophysiology, and mechanics*, University of Utah.
- Safdarian, N. et al., 2013. Rule-based Method for Extent and Localization of Myocardial Infarction by Extracted Features of ECG Signals using Body Surface Potential Map

---

*References*

---

- Data. *J Med Signals Sens*, 3(3), pp.129–138.
- Saffitz, J.E. et al., 1994. Tissue-specific determinants of anisotropic conduction velocity in canine atrial and ventricular myocardium. *Circulation research*, 74(6), pp.1065–1070.
- Sánchez-Quintana, D. et al., 2013. Standardized review of atrial anatomy for cardiac electrophysiologists. *Journal of Cardiovascular Translational Research*, 6(2), pp.124–144.
- Sánchez-Quintana, D. et al., 2002. The terminal crest: morphological features relevant to electrophysiology. *Heart (British Cardiac Society)*, 88(4), pp.406–411.
- Sánchez-Quintana, D. et al., 2012. Triggers and anatomical substrates in the genesis and perpetuation of atrial fibrillation. *Current cardiology reviews*, 8(4), pp.310–26.
- Sanchez, C. et al., 2012. Ionic modulation of atrial fibrillation dynamics in a human 3D atrial model. In *Computing in Cardiology*. pp. 137–140.
- Sanchez, C., 2014. *Multiscale Analysis of Atrial Fibrillation Mechanisms*.
- Sanguinetti, M.C. & Tristani-Firouzi, M., 2006. hERG potassium channels and cardiac arrhythmia. *Nature*, 440(7083), pp.463–469.
- Saoudi, N. et al., 2001. A classification of atrial flutter and regular atrial tachycardia according to electrophysiological mechanisms and anatomical bases: A statement from a joint expert group from the working group of arrhythmias of the European society of cardiology and the . *European Heart Journal*, 22(14), pp.1162–1182.
- Saremi, F. et al., 2011. Posterior Interatrial Muscular Connection between the Coronary Sinus and Left Atrium: Anatomic and Functional Study of the Coronary Sinus with Multidetector CT. *Radiology*, 260(3), pp.671–679.
- Schmidt, C. et al., 2015. Upregulation of K<sub>2P</sub> 3.1 K<sup>+</sup> Current Causes Action Potential Shortening in Patients With Chronic Atrial FibrillationCLINICAL PERSPECTIVE. *Circulation*, 132(2), pp.82–92.
- Schmitt, O.H., 1969. *Biological information processing using the Concept of interpenetrating domains* ed K. N. Leibovic, ed., Springer-Verlag New York .
- Seemann, G. et al., 2006. Heterogeneous three-dimensional anatomical and electrophysiological model of human atria. *Philosophical transactions. Series A, Mathematical, physical, and engineering sciences*, 364(1843), pp.1465–1481.
- Selthofer, R. et al., 2006. Morphometric analysis of the sternum. *Collegium antropologicum*, 30(1), pp.43–47.
- Sethi, N.J. et al., 2017. The effects of rhythm control strategies versus rate control strategies for atrial fibrillation and atrial flutter: a protocol for a systematic review with meta-analysis and Trial Sequential Analysis. *Systematic reviews*, 6(1), p.47.
- Shah, A.J. et al., 2014. Non-invasive ECG mapping to guide catheter ablation. *Journal of Atrial Fibrillation*, 7(3), pp.32–38.

- Shah, D., Haïssaguerre, M. & Jaïs, P., 2002. Current perspectives on curative catheter ablation of atrial fibrillation. *BMJ: British Medical Journal*, 87(2), pp.6–8.
- Shah, D.C. et al., 2000. Electrophysiologically guided ablation of the pulmonary veins for the curative treatment of atrial fibrillation. *Annals of medicine*, 32(6), pp.408–416.
- Shahidi, a. V., Savard, P. & Nadeau, R., 1994. Forward and inverse problems of electrocardiography: Modeling and recovery of epicardial potentials in humans. *IEEE Transactions on Biomedical Engineering*, 41(3), pp.249–256.
- Si, H. & Gärtner, K., 2005. *Meshing piecewise linear complexes by constrained delaunay tetrahedralizations*,
- Silva, J. & Rudy, Y., 2005. Subunit interaction determines IKs participation in cardiac repolarization and repolarization reserve. *Circulation*, 112(10), pp.1384–1391.
- SippensGroenewegen, A. et al., 1998. Body surface mapping of atrial arrhythmias: Atlas of paced P wave integral maps to localize the focal origin of right atrial tachycardia. *Journal of Electrocardiology*, 31(SUPPL.), pp.85–91.
- SippensGroenewegen, A. et al., 2004. Potential role of body surface ECG mapping for localization of atrial fibrillation trigger sites. *Journal of Electrocardiology*, 37(SUPPL.), pp.47–52.
- Skibbsbye, L. et al., 2016. Refractoriness in human atria: Time and voltage dependence of sodium channel availability. *Journal of molecular and cellular cardiology*, 101, pp.26–34.
- Spach, M.S. et al., 1979. Extracellular potentials related to intracellular action potentials during impulse conduction in anisotropic canine cardiac muscle. *Circulation research*, 45(2), pp.188–204.
- Spach, M.S., Dolber, P.C. & Heidlage, J.F., 1988. Influence of the passive anisotropic properties on directional differences in propagation following modification of the sodium conductance in human atrial muscle. A model of reentry based on anisotropic discontinuous propagation. *Circulation research*, 62(4), pp.811–832.
- Spach, M.S., Dolber, P.C. & Sommer, J.R., 1985. Discontinuous propagation: an hypothesis based on known cardiac structural complexities. *International journal of cardiology*, 7(2), pp.167–174.
- Sunderman, F.W. & Boerner, F., 1950. Normal Values in Clinical Medicine. *Academic Medicine*, 25(2), p.159.
- Sundnes, J. et al., 2006. *Computing the electrical activity in the heart*, Springer-Verlag.
- T.B Moeller, E.R., 2007. *Pocket Atlas of Sectional Anatomy - Computed Tomography and Magnetic Resonance Imaging - Volume I e III* 3rd editio., Germany.
- Tang, C.W. et al., 1995. Use of P wave configuration during atrial tachycardia to predict site of origin. *Journal of the American College of Cardiology*, 26(5), pp.1315–1324.

---

*References*

- Thibodeau, G.A., Patton, K.T. & Elsevier, S., 2007. *Anatomía y Fisiología* 6<sup>a</sup> edición., University of Winsconsin - River FallsSt. Charles Community College.
- Tobón, C. et al., 2013. A Three-Dimensional Human Atrial Model with Fiber Orientation. Electrograms and Arrhythmic Activation Patterns Relationship. *PLoS ONE*, 8(2), p.e50883.
- Tobón, C. et al., 2012. Dominant frequency and organization index maps in a realistic three-dimensional computational model of atrial fibrillatio. *Europace*, 14(SUPPL. 5), pp.9–11.
- Tobón, C. et al., 2008. Reentrant mechanisms triggered by ectopic activity in a three-dimensional realistic model of human atrium. A computer simulation study. *Computers in Cardiology*, 35(April), pp.629–632.
- Tobón, D.C., 2010. *Modelización y evaluación de factores que favorecen las arritmias auriculares y su tratamiento mediante técnicas quirúrgicas. Estudio de simulación.* Universidad Politécnica de Valencia.
- Tomaselli, G.F. et al., 1995. A mutation in the pore of the sodium channel alters gating. *Biophysical journal*, 68(5), pp.1814–27.
- Trayanova, N.A. & Chang, K.C., 2015. How computer simulations of the human heart can improve anti-arrhythmia therapy. *The Journal of physiology*, 0(November 2014), pp.1–20.
- Trudel, M.C. et al., 2004. Simulation of QRST integral maps with a membrane-based computer heart model employing parallel processing. *IEEE Transactions on Biomedical Engineering*, 51(8), pp.1319–1329.
- Tsujimae, K. et al., 2007. Frequency-dependent effects of various IKr blockers on cardiac action potential duration in a human atrial model. *American journal of physiology. Heart and circulatory physiology*, 293(1), pp.H660–H669.
- Tung, L., 1978. A bi-domain model for describing ischemic myocardial d-c potentials.
- ten Tusscher, K.H.W.J. et al., 2004. A model for human ventricular tissue. *American journal of physiology. Heart and circulatory physiology*, 286(4), pp.H1573–H1589.
- Vadakkumpadan, F. et al., 2009. Image-Based Estimation of Myocardial Fiber Orientations for Patient-Specific Models of Cardiac Electrophysiology. *Heart Rhythm*, 6(11), pp.1688–1688.
- Vigmond, E.J. et al., 2003. Computational Tools for Modeling Electrical Activity in Cardiac Tissue. *Journal of Electrocardiology*, 36(SUPPL.), pp.69–74.
- Vigmond, E.J., Aguel, F. & Trayanova, N.A., 2002. Computational techniques for solving the bidomain equations in three dimensions. *IEEE Transactions on Biomedical Engineering*, 49(11), pp.1260–1269.
- Vigmond, E.J., Ruckdeschel, R. & Trayanova, N.A., 2001. Reentry in a morphologically realistic atrial model. *Journal of Cardiovascular Electrophysiology*, 12(9), pp.1046–

- 54.
- Virag, N. et al., 2002. Study of atrial arrhythmias in a computer model based on magnetic resonance images of human atria. *Chaos*, 12(3), pp.754–763.
- Voigt, N. et al., 2014. Cellular and molecular mechanisms of atrial arrhythmogenesis in patients with paroxysmal atrial fibrillation. *Circulation*, 129(2), pp.145–156.
- Voigt, N. et al., 2013. Impaired Na<sup>+</sup>-dependent regulation of acetylcholine-activated inward-rectifier K<sup>+</sup> current modulates action potential rate dependence in patients with chronic atrial fibrillation. *Journal of Molecular and Cellular Cardiology*, 61, pp.142–152.
- Waktare, J.E.P., 2002. Atrial fibrillation. *Circulation*, 106(1), pp.14–16.
- Waldo, a L. et al., 1977. Entrainment and interruption of atrial flutter with atrial pacing: studies in man following open heart surgery. *Circulation*, 56(5), pp.737–745.
- Waller, a. D., 1889. On the Electromotive Changes Connected with the Beat of the Mammalian Heart, and of the Human Heart in Particular. *Philosophical Transactions of the Royal Society B: Biological Sciences*, 180(0), pp.169–194.
- Wang, K. et al., 1995. Architecture of atrial musculature in humans. *British heart journal*, 73(6), pp.559–565.
- Wang, Y. et al., 2012. Noninvasive Electroanatomic Mapping of Human Ventricular Arrhythmias Using ECG Imaging (ECGI). *Sci Transl Med*, 3(98).
- Wang, Z., Fermini, B. & Nattel, S., 1993. Sustained depolarization-induced outward current in human atrial myocytes. Evidence for a novel delayed rectifier K<sup>+</sup> current similar to Kv1.5 cloned channel currents. *Circulation research*, 73(6), pp.1061–1076.
- Weber, F.M., Luik, A., et al., 2011. Conduction velocity restitution of the human atrium–An efficient measurement protocol for clinical electrophysiological studies. *IEEE Transactions on Biomedical Engineering*, 58(9), pp.2648–2655.
- Weber, F.M., Keller, D.U.J., et al., 2011. Predicting tissue conductivity influences on body surface potentials. An efficient approach based on principal component analysis. *IEEE Transactions on Biomedical Engineering*, 58(2), pp.265–273.
- Weigner, M.J. et al., 1999. Left atrial appendage anatomy and function: short term response to sustained atrial fibrillation. *Heart (British Cardiac Society)*, 82(5), pp.555–558.
- Wellens, H.J.J., 2002. Contemporary management of atrial flutter. *Circulation*, 106(6), pp.649–652.
- Wieser, L. et al., 2008. A finite element formulation for atrial tissue monolayer. *Methods of Information in Medicine*, 47(2), pp.131–139.
- Wilde, A.A.M. & Brugada, R., 2011. Phenotypical manifestations of mutations in the genes encoding subunits of the cardiac sodium channel. *Circulation Research*, 108(7), pp.884–897.
- Wilhelms, M. et al., 2013. Benchmarking electrophysiological models of human atrial

---

*References*

- myocytes. *Frontiers in Physiology*, 3 JAN(January), p.487.
- Williams, G.S.B. et al., 2010. Models of cardiac excitation-contraction coupling in ventricular myocytes. *Mathematical Biosciences*, 226(1), pp.1–15.
- Wu, T.J. et al., 1998. Role of pectinate muscle bundles in the generation and maintenance of intra-atrial reentry: potential implications for the mechanism of conversion between atrial fibrillation and atrial flutter. *Circulation research*, 83(4), pp.448–462.
- Xie, F. et al., 2002. Electrical refractory period restitution and spiral wave reentry in simulated cardiac tissue. *American journal of physiology. Heart and circulatory physiology*, 283(1), pp.H448–H460.
- Yanowitz, F.G., 2012. Introduction to ECG Interpretation v8.0. Available at: <http://library.med.utah.edu/kw/ecg/AELOutlineJuly2010.pdf>.
- Yasuura, K., 1981. A relation between forward and inverse problems on electrocardiography. *Japanese circulation journal*, 45(11), pp.1310–1311.
- Zarychta, P. et al., 2007. Body Surface Potential Mapping for Detection of Myocardial Infarct Sites. , (figure 4), pp.181–184.
- Zhang, H. et al., 2005. Competitive interactions between ectopic foci and reentry in virtual human atrium. *Computers in Cardiology*, 32, pp.73–76.
- Zhang, Y. et al., 2016. Multi-scale Modeling of the Cardiovascular System: Disease Development, Progression, and Clinical Intervention. *Annals of Biomedical Engineering*, 44(9), pp.2642–2660.
- Zhao, J. et al., 2012. An image-based model of atrial muscular architecture effects of structural anisotropy on electrical activation. *Circulation: Arrhythmia and Electrophysiology*, 5(2), pp.361–370.
- Zipes, D.P., 2014. Antiarrhythmic therapy in 2014: Contemporary approaches to treating arrhythmias. *Nature Publishing Group*, 12(2), pp.68–69.
- Zipes, D.P. & Jalife, J., 2004. *Cardiac Electrophysiology: From Cell to Bedside, Fifth Edition* 5th editio., Saunders.
- Zoni-Berisso, M. et al., 2014. Epidemiology of atrial fibrillation: European perspective. *Clinical Epidemiology*, 6, p.213.
- Zygmunt, a. C. et al., 2011. Mechanisms of atrial-selective block of Na<sup>+</sup> channels by ranolazine: I. Experimental analysis of the use-dependent block. *AJP: Heart and Circulatory Physiology*, 301(4), pp.H1606–H1614.

---

# Curriculum Vitae



**Ana Ferrer Albero** obtained her BEng in Communications Engineering from the Polytechnic University of Valencia, Spain, in 2000. Later, she was acknowledged as European Engineer from the European Federation of National Engineering Association in 2005. Finally, she obtained her MSc. in Biomedical Engineering from the University of Valencia and the Polytechnic University of Valencia in 2012. Afterwards, she has worked as researcher on the topic of computational modelling and simulation as well as on biosignal processing in the field of cardiac electrophysiology.

She has more than 10 years of experience working on project management for multi-national companies in the sector of Communications and Electronic Systems. Since 2010, she is senior project manager in the field of Health, leading the Unit of International Research Programs at the Biomedical Information Science Research Group of the Institute for the Applications of Advanced Information and Communication Technologies (ITACA – UPV), later on at the Foundation for the Promotion of Biomedical Research (FISABIO) and up today at the Health Research Institute (INCLIVA – University Clinic Hospital of Valencia).